



**Università degli Studi di Parma**  
**Dipartimento di Ingegneria Civile, dell'Ambiente, del Territorio e Architettura**

**Dottorato di Ricerca in Forme e Strutture dell'Architettura**

(ICAR 08 - ICAR 09 - ICAR 10 - ICAR 14 - ICAR17 - ICAR 18 - ICAR 19 – ICAR 20- MAT 02)

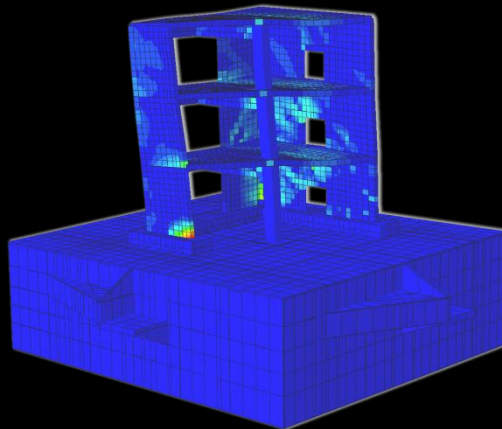
**XXVIII Ciclo**

**Alessandro Stocchi**

**Seismic Response Assessment of RC Wall Structures.  
Applications of Non-Linear Finite Element Modelling Techniques.**

ICAR 09

*Valutazione della risposta sismica di strutture a parete in CA.  
Applicazioni di tecniche di modellazione non lineari agli elementi finiti.*



Tutor: prof. Ivo Iori  
Co-tutor: prof.ssa Beatrice Belletti

Coordinatore del Dottorato: prof. Aldo De Poli





**Università degli Studi Di Parma**  
**Dipartimento di Ingegneria Civile, dell'ambiente, del Territorio e Architettura**

**Dottorato di Ricerca in Forme e Strutture dell'architettura**

(ICAR 08 - ICAR 09 - ICAR 10 - ICAR 14 - ICAR17 - ICAR 18 - ICAR 19 – ICAR 20- MAT 02)

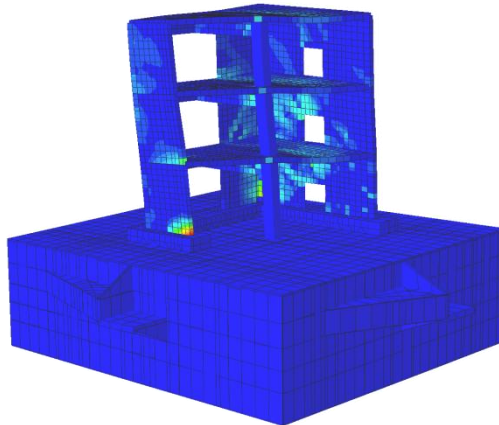
**XXVIII Ciclo**

**Alessandro Stocchi**

**Seismic Response Assessment of RC Wall Structures.  
Applications of Non-Linear Finite Element Modelling Techniques.**

ICAR 09

*Valutazione della risposta sismica di strutture industriali a parete in CA.  
Applicazioni di tecniche di modellazione non lineari agli elementi finiti.*



Tutor: prof. Ivo Iori  
Co-tutor: prof.ssa Beatrice Belletti

Coordinatore del Dottorato: prof. Aldo De Poli





**UNIVERSITÀ DEGLI STUDI DI PARMA**

**DIPARTIMENTO DI INGEGNERIA CIVILE, DELL'AMBIENTE, DEL TERRITORIO E ARCHITETTURA**

**DOTTORATO DI RICERCA IN FORME E STRUTTURE DELL'ARCHITETTURA**

(ICAR 08 - ICAR 09 - ICAR 10 - ICAR 14 - ICAR17 - ICAR 18 - ICAR 19 – ICAR 20- MAT 02)

**Coordinatore:**

prof. Aldo De Poli

**Collegio docenti:**

prof. Bruno Adorni

prof. Carlo Blasi

prof. Eva Coisson

prof. Agnese Ghini

prof. Paolo Giandebiaggi

prof. Ivo Iori

prof. Marco Maretto

prof. Maria Evelina Melley

prof. Federica Ottoni

prof. Enrico Prandi

prof. Carlo Quintelli

prof. Paolo Ventura

prof. Chiara Vernizzi

prof. Michele Zazzi

prof. Andrea Zerbi

**Titolo della tesi:**

Seismic Response Assessment of RC Industrial Wall Structures.

Applications of Non-Linear Finite Element Modelling Techniques.

ICAR 09

**Dottorando:**

Alessandro Stocchi

**Tutor:**

prof. Ivo Iori

**Co-Tutor:**

prof.ssa Beatrice Belletti

**Chapter 7 supervisor:**

prof. Shyh-Jiann Hwang



*Cover image: crack opening contour from the time history analysis of the SMART2013 project shaking table test.*

**Seismic Response Assessment  
of RC Wall Structures.  
Applications of Non-Linear  
Finite Element Modelling Techniques.**







# Table of Contents

<b>INTRODUCTION</b> .....	<b>1</b>
<b>1 INTRODUCTION</b> .....	<b>2</b>
1.1 Definition of the research field .....	4
1.2 Aims of the research .....	6
1.3 Methodology .....	7
<b>PART I. CONCEPTS</b> .....	<b>9</b>
<b>CHAPTER II. THE PARC_CL REINFORCED CONCRETE MODEL</b> .....	<b>11</b>
<b>2 THE PARC_CL REINFORCED CONCRETE MODEL</b> .....	<b>12</b>
2.1 PARC fixed crack model .....	12
2.2 Adopted constitutive models .....	14
2.3 Aggregate interlock.....	16
2.4 Steel constitutive model .....	19
2.5 Tension stiffening .....	20
2.6 Dowel action.....	22
2.7 Stiffness matrix and numerical solution procedure .....	23
2.8 PARC_CL model.....	26
<b>CHAPTER III. A PROBABILISTIC APPROACH FOR STRUCTURAL ENGINEERING</b> .....	<b>29</b>
<b>3 A PROBABILISTIC APPROACH FOR STRUCTURAL ENGINEERING</b> .....	<b>30</b>
3.1 Probabilistic approach: a brief introduction.....	30
3.2 Probabilistic theory.....	31
3.2.1 Random Variables .....	31
3.2.2 Correlated Random Variables .....	34
3.3 Monte Carlo Simulations .....	36
3.3.1 Generation of normal random values.....	37
3.3.2 Generation of normal correlated random values .....	40
3.3.3 Generation of log-normal random values .....	43
3.3.4 Generation of log-normal correlated random values .....	45
3.4 Generation of fragility functions .....	45

<b>CHAPTER IV. ACCELEROGRAMS AND SPECTRA APPLICATIONS.....</b>	<b>51</b>
<b>4 ACCELEROGRAMS AND SPECTRA APPLICATIONS .....</b>	<b>52</b>
<b>4.1 Spectra calculation: the energy approach and its applications.....</b>	<b>52</b>
4.1.1 SDOF dynamic equation for Energy quantities .....	54
4.1.2 Energy based comparison with experimental data .....	67
4.1.3 Open issues and final remarks .....	80
<b>4.2 Input data for dynamic nonlinear analysis .....</b>	<b>81</b>
4.2.1 Analysis of fan input signal from SMART2013 shaking table model test .....	82
<b>4.3 A practical approach on the use of Fourier spectra .....</b>	<b>87</b>
<b>PART II. BACKGROUND .....</b>	<b>97</b>
<b>CHAPTER V. A REVIEW ON RC WALL STRUCTURES SHELL MODELLING .....</b>	<b>99</b>
<b>5 RC WALLS SEISMIC BEHAVIOUR: A BRIEF REVIEW .....</b>	<b>100</b>
<b>5.1 The Proposed Multi-Layered Shell Element And Parc_Cl Modelling .....</b>	<b>102</b>
5.1.1 PARC_CL crack model .....	103
<b>5.2 Three case studies .....</b>	<b>103</b>
5.2.1 Slender walls designed according to capacity design approach .....	103
5.2.2 Slender walls tested at the University of Brescia.....	108
5.2.3 Squat walls .....	109
<b>5.3 Final remarks .....</b>	<b>114</b>
<b>PART III. APPLICATIONS AND RESULTS .....</b>	<b>117</b>
<b>CHAPTER VI. CASE STUDY I: THE SMART2013 SHAKING TABLE TEST.....</b>	<b>119</b>
<b>6 CASE STUDY I: THE SMART2013 SHAKING TABLE TEST .....</b>	<b>120</b>
<b>6.1 Brief description of the SMART2013 project .....</b>	<b>121</b>
<b>6.2 Smart2013 shaking table test of a 1/4 electrical facility of CPY nuclear power plants .....</b>	<b>122</b>
<b>6.3 Modelling techniques .....</b>	<b>123</b>
6.3.1 The shaking table issue .....	126
6.3.2 Additional masses .....	128
<b>6.4 Frequency analysis: experimental vs. blind prediction vs. post diction .....</b>	<b>128</b>
<b>6.5 Time history analysis .....</b>	<b>131</b>
6.5.1 Absolute displacements.....	135
<b>6.6 Probabilistic analysis.....</b>	<b>140</b>
<b>6.7 Post-analysis: global results .....</b>	<b>151</b>

6.7.1	Model Updating .....	151
6.7.2	Mass distribution and foundation model .....	152
6.7.3	Seismic input.....	153
6.7.4	Spectral analysis of the acceleration response .....	156
<b>6.8</b>	<b>Remarks.....</b>	<b>161</b>

**CHAPTER VII. CASE STUDY II: THE 1/13 SCALED RCCV CYCLIC TEST..... 165**

<b>7</b>	<b>CASE STUDY II: THE 1/13SCALED RCCV CYCLIC TEST.....</b>	<b>166</b>
<b>7.1</b>	<b>Mock up and test description .....</b>	<b>166</b>
<b>7.2</b>	<b>Numerical model .....</b>	<b>168</b>
<b>7.3</b>	<b>Materials .....</b>	<b>171</b>
7.3.1	Material orientation .....	172
<b>7.4</b>	<b>Loading protocol.....</b>	<b>173</b>
<b>7.5</b>	<b>Preliminary elastic test .....</b>	<b>174</b>
7.5.1	Total base shear vs. top displacement.....	175
7.5.2	Fourth cycle .....	177
7.5.3	Complete preliminary cyclic test .....	178
<b>7.6</b>	<b>Full non linear test .....</b>	<b>179</b>
7.6.1	Total base shear vs. top displacement.....	179
7.6.2	Rebars and hoops strain .....	185
7.6.3	Horizontal hoops.....	195
7.6.4	Crack opening .....	203
7.6.5	Concrete in compression .....	204
<b>7.7</b>	<b>Vessel absolute displacements .....</b>	<b>206</b>
<b>7.8</b>	<b>Complete cycling test history .....</b>	<b>209</b>
7.8.1	NLFEA results .....	209
<b>7.9</b>	<b>Experimental results .....</b>	<b>212</b>
<b>7.10</b>	<b>Pushover analysis .....</b>	<b>213</b>
7.10.1	Total base shear vs. top displacement .....	213
<b>7.11</b>	<b>Damage analysis .....</b>	<b>215</b>
7.11.1	Damage in concrete.....	215
7.11.2	Damage in steel .....	217
7.11.3	Gobal damage in reinforced concrete .....	217
<b>7.12</b>	<b>Remarks.....</b>	<b>218</b>

**CHAPTER VIII. FURTHER APPLICATIONS AND FUTURE DEVELOPMENTS .....221**

<b>8</b>	<b>FURTHER APPLICATIONS AND FUTURE DEVELOPMENTS: THE RC INTERFACE PROBLEM .....</b>	<b>222</b>
<b>8.1</b>	<b>Contact behaviour .....</b>	<b>222</b>

8.1.1	Model description.....	223
8.1.2	Global model.....	224
8.1.3	Frictionless model.....	225
8.1.4	Friction model.....	228
8.1.5	Solid model (frictionless) .....	229
8.1.6	Global behaviour: total shear vs. top displacement .....	230
8.1.7	Cyclic behaviour .....	231
<b>8.2</b>	<b>Dowel action.....</b>	<b>232</b>
8.2.1	ABAQUS zero-length connectors elements .....	232
8.2.2	Implementation of a physical dowel action model in the user subroutine UEL.for: simplified elastic-plastic model .....	235
8.2.3	Implementation of a physical dowel action model in the user subroutine UEL.for: non linear BEF analogy .....	239
<b>CONCLUSIONS AND OPEN ISSUES .....</b>		<b>247</b>
<b>REFERENCES AND GLOSSARY .....</b>		<b>253</b>
Selected References .....		254
Technical Glossary.....		262
<b>ACKNOWLEDGEMENTS.....</b>		<b>269</b>

## **Abstract**

*(in Italian)*

Il problema del consumo di risorse energetiche è divenuto oggi di grandissima importanza in relazione anche al fenomeno del riscaldamento globale legato all'inquinamento provocato da centrali a combustibile fossile. Nel mondo, oltre alle centrali a combustibile tradizionale, gli impianti nucleari sono diffusi in trenta nazioni. In questo caso il problema energetico è correlato anche al più importante problema della sicurezza delle popolazioni nei confronti del rischio di fuoriuscita di radiazioni e quindi al problema dello sviluppo di metodi razionali e sicuri per il progetto di nuove strutture e per la valutazione della sicurezza di quelle esistenti. Infatti una considerevole quantità di energia viene prodotta ogni anno da centrali nucleari che necessitano di opere di rinnovamento a breve termine (Hsu et al. 2014) ed in particolare il 27% dell'energia elettrica europea viene prodotto in strutture nucleari. I componenti in calcestruzzo rinforzato delle centrali nucleari (come ad esempio vessel di contenimento e sistemi strutturali a pareti) sono di estrema importanza per la sicurezza e per l'operatività delle centrali stesse. Tali componenti in calcestruzzo armato devono essere verificati nei confronti di elevate sollecitazioni dovute all'azione di forti eventi sismici, impatti ed esplosioni. Le strutture, se sottoposte a tali azioni, mostrano un forte comportamento non lineare con conseguente apertura di fessure. È dunque di fondamentale importanza poter prevedere correttamente il comportamento tridimensionale di queste strutture in modo tale da poter valutarne sia la risposta globale (ad esempio in termini di spostamenti) sia locale (fessurazione multi - direzionale). Appare dunque chiara la necessità di sviluppare strumenti numerici adeguati ed affidabili modelli per i materiali al fine di descrivere con buona approssimazione tutti questi aspetti così complessi e difficili da cogliere con una modellazione semplificata equivalente. La validazione di tali procedure con prove sperimentali costituisce un aspetto chiave del problema.

La tesi affronta dunque il problema della modellazione in campo non lineare di strutture a pareti attraverso lo sviluppo di modelli calibrati su recenti ed innovative campagne sperimentali internazionali. Attualmente sono a

disposizione degli ingegneri civili numerosi strumenti numerici per la modellazione di strutture a pareti di impianti nucleari, (Richard et al. 2013). La tesi si concentra dunque sulla modellazione del comportamento dinamico non lineare di un provino in scala  $\frac{1}{4}$  di un edificio di servizio per l'alloggiamento di apparecchiature elettriche per reattori nucleari CPY testato nell'ambito della blind prediction organizzata all'interno del benchmark internazionale SMART2013, ([www.smart2013.eu](http://www.smart2013.eu)). Inoltre, è stato analizzato e modellato il comportamento ciclico di un vessel di contenimento in C.A. per l'alloggiamento di reattori nucleari testato in scala 1/13 presso il laboratorio NCREE di Taipei (Taiwan).

La modellazione effettuate con elementi shell multi-layered ed il modello fessurativo tipo "smeared" PARC\_CL. Nelle analisi il modello PARC\_CL è stato utilizzato per la valutazione delle matrici di rigidezza non lineare nei punti di integrazione degli elementi shell. Il modello è implementato nella user subroutine UMAT.for del software commerciale ABAQUS. Tale approccio è stato applicato in quanto è stato osservato che la modellazione con elementi shell e fessurazione diffusa può predire adeguatamente gli indicatori di danno. È possibile in particolare stimare gli EDP (Engineering Demand Parameter) sia locali (aperture di fessura, deformazione nelle barre) che globali (spostamenti di interpiano), parametri fondamentali per la progettazione sismica definita "performance-based". La modellazione con elementi shell e modello fessurativo PARC\_CL si è rivelata adatta per la valutazione del comportamento dinamico non lineare e di entrambe le strutture presentate nei casi studio.

Nel primo capitolo a carattere introduttivo sono descritte le principali problematiche che sono alla base dello studio e la metodologia utilizzate nel corso della ricerca. Obiettivo della ricerca è la valutazione delle performance sismiche di strutture a pareti (in particolare edifici nucleari) attraverso modellazione agli elementi finiti di veri test di laboratorio.

I capitoli da 2 a 4 sono raggruppati in una parte prima relativa agli strumenti di indagine di maggiore interesse utilizzati nel corso della ricerca. Il primo di tali aspetti è la modellazione del materiale calcestruzzo armato attraverso il modello non lineare a fessurazione diffusa sviluppato per carichi ciclici PARC\_CL. Il modello PARC (Physical Approach on Reinforced Concrete) è un



modello a fessurazione ad inclinazione fissa ed armatura “smeared” (diffusa). Il modello è particolarmente efficiente nella valutazione nella risposta di strutture a pareti in quanto calibrato su problemi dominati da comportamento a taglio. Tali problemi sono infatti tipici di strutture strategiche quali strutture off shore, nuclei di contenimento, sistemi di pareti sismo resistenti. Il modello inoltre è funzionale alla valutazione delle performance locali della struttura in quanto in grado di valutare importanti parametri quali l’apertura di fessure nel calcestruzzo (parametro particolarmente importante per strutture di contenimento, particolarmente impiegate nell’ambito della progettazione nucleare, in quanto in questo la struttura deve anche prevenire la fuoriuscita di radiazioni o altri agenti contaminanti in caso di sollecitazioni elevate, dovute non solo ad eventi sismici ma anche ad esempio impatti ed esplosioni). Inoltre è possibile valutare tensioni e deformazioni nel calcestruzzo e nelle armature. Il modello è applicato alla modellazione con elementi shell multistrato. Dal punto di vista globale è dunque in grado di cogliere anche il comportamento tridimensionale di strutture complesse, come dimostrato nel capitolo 6 della tesi. Grazie all’implementazione del comportamento ciclico dei legami costitutivi di calcestruzzo ed acciaio il modello è inoltre in grado di tenere conto in maniera realistica della dissipazione dell’energia per isteresi, aspetto particolarmente delicato nella valutazione della risposta dinamica della struttura.

Il capitolo 3 costituisce una sintesi dell’approccio probabilistico all’analisi strutturale. In particolare, è presentato e descritto attraverso esempi applicativi un metodo probabilistico utilizzato in ambito di progettazione di strutture nucleari per la valutazione di curve di capacità in funzione di diverse misure di intensità (*intensity measures*) e parametri di valutazione della domanda (*engineer demand parameters*), che costituiscono un importante aspetto dei moderni approcci di verifica e progettazione impiegati non solo in ambito accademico. Tale ricerca è particolarmente importante ai fini di valutare la robustezza e l’affidabilità degli strumenti numerici impiegati nell’ingegneria strutturale. Tale procedura è stata applicata al fine di valutare le curve di fragilità nel capitolo 6.

Il capitolo 4 costituisce una breve review di importanti aspetti relativi all’utilizzo di accelerogrammi e alla generazione di spettri di risposta affrontati durante la ricerca. In particolare, è affrontato nel dettaglio il tema dell’utilizzo del cosiddetto approccio energetico per la realizzazione di spettri di risposta ai

fini ad esempio per la progettazione di organi dissipativi ad attrito. Inoltre viene discussa la problematica dell'impiego di accelerogrammi reali in analisi dinamiche al passo e sono forniti esempi pratici relativi a campionamento, filtro di frequenze, correzione della base-line. Infine un paragrafo è dedicato alla generazione di spettri di Fourier di segnali sismici, aspetto fondamentale dell'identificazione strutturale.

In quella che costituisce la seconda parte della tesi è presentata una review relativa all'utilizzo del modello PARC per la modellazione di strutture a pareti e pareti singole, prove sperimentali su tali strutture disponibili in letteratura ed è posta attenzione anche sulle procedure di calcolo analitiche disponibili per la determinazione della resistenza degli elementi a parete nei confronti delle diverse modalità di rottura. La terza parte della tesi raggruppa in sé i capitoli 6, 7 ed 8 e costituisce il nucleo di maggiore interesse nel corso della trattazione. Nel capitolo 6 è descritta nel dettaglio la modellazione di una struttura a pareti con forte comportamento torsionale. Tale struttura è stata testata in scala  $\frac{1}{4}$  presso i laboratori di Saclay (Francia) su tavola vibrante con l'applicazione di una sequenza di accelerogrammi di intensità crescente fino a 1.6g. La risposta non lineare della struttura è stata prima analizzata "in cieco" ovvero senza conoscere i risultati della prova sperimentale ma avendo noti solo gli input in termini di spostamento e accelerazione e le caratteristiche dei materiali. Il modello sviluppato con elementi shell e PARC\_CL è stato in grado di cogliere correttamente il campo di spostamenti e i fenomeni locali di fessurazione, taglio, snervamento delle barre d'armatura. Un ulteriore modello è stato realizzato in fase di post-analisi per valutare l'influenza di alcune variabili (introduzione della tavola vibrante nel modello globale, modellazione delle masse addizionali, definizione dell'input sismico, calibrazione del damping alla Rayleigh). Tuttavia il modello non è stato in grado di cogliere la rottura per crushing del calcestruzzo osservata in corrispondenza dell'interfaccia tra fondazione ed una delle pareti che costituivano il sistema sismo resistente.

Nel capitolo 7 è invece descritta la modellazione di un vessel di contenimento per reattori nucleari testato per carico ciclico quasi - statico in scala 1/13 presso il laboratorio NCREC di Taipei (Taiwan). Il modello implementato è stato in grado di cogliere il comportamento sia in fase lineare che fessurata del vessel. Inoltre localmente sono state stimate tensioni e deformazioni nelle barre d'armatura. Fenomeni di fessurazione sono stati osservati sia

numericamente che sperimentalmente e globalmente è stato possibile stimare la forza di picco raggiunta in fase sperimentale. Durante il test è stata identificata una modalità di rottura per taglio scorrimento all'interfaccia tra vessel e fondazione. Tale osservazione ha portato alla conclusione della necessità di sviluppare un modello locale da implementare nel codice di calcolo per tenere in considerazione appunto dal comportamento tra interfacce in calcestruzzo armato. Nell'ottavo capitolo è dunque riportata come estensione dello studio lo sviluppo e la calibrazione preliminare di una tecnica di modellazione locale in grado di cogliere le rotture di tipo taglio scorrimento. La filosofia alla base di tale modellazione è la stessa alla base delle formulazioni analitiche utilizzate in fase di verifica che valutano la resistenza a scorrimento come somma di due contributi principali per la trasmissione del taglio. La trasmissione del taglio per attrito viene considerata attraverso opportuna modellazione e definizione delle proprietà delle superfici di contatto tra parete e fondazione (dunque considerando incidenze diverse per gli elementi di fondazione e gli elementi che definiscono la parete). Il contributo dato dalla dowel action viene introdotto invece attraverso lo sviluppo di un elemento multi-spring spaziale in grado di tenere conto anche della risposta ciclica delle barre d'armatura attraverso l'implementazione di un legame sperimentale taglio-scorrimento.

Per concludere, nella moderna pratica progettuale una delle principali problematiche è la valutazione degli "engineering demand parameters" in modo da stimare correttamente le performance della struttura allo stato limite di danno (soprattutto per garantire l'operatività degli impianti e degli elementi non strutturali) ed allo stato limite di collasso. Questo aspetto risulta molto importante se si tiene in considerazione il fatto che le pareti in C.A. costituiscono spesso il sistema resistente di edifici strategici. Recenti programmi sperimentali su strutture a parete, in particolare il programma SMART2013 (Saclay, Francia), [www.smart2013.eu](http://www.smart2013.eu), e la campagna di prove su una struttura cilindrica di contenimento presso il laboratorio NCREC di Taipei (Taiwan), hanno evidenziato che attualmente esistono ancora incertezze che dovrebbero essere considerate nella valutazione della sicurezza sismica delle strutture. In particolare entrambe le prove sono state condizionate da una modalità di rottura per taglio scorrimento. I modelli proposti nella presente tesi si sono dimostrati efficienti nella valutazione delle performance locali e

globali di strutture a parete in C.A. di edifici a pareti in calcestruzzo rinforzato ed in particolare di centrali nucleari. Tuttavia, ulteriori studi saranno portati avanti a partire dai risultati ottenuti per l'implementazione e la calibrazione di un modello numerico in grado di cogliere le rotture per taglio scorrimento negli elementi a pareti.

## **Abstract**

*(in English).*

The problem of energetic resources exploitation is nowadays of strong relevance because of the pollution correlated to CO<sub>2</sub> production by carbon fossil power plants. All over the world, beside traditional power plants, nuclear power plants (NPPs) are still used in 30 nations. In this case the energetic problem is also closely related to the issue of population safety towards radiation leakage. Therefore, rational methods must be developed and analyzed for the design and assessment of such structures. In fact, a large amount of energy is actually produced each year by NPPs which will need of a renewal process in a short term (Hsu et al, 2014). In particular, 27% of electric energy produced in Europe is actually produced by NPPs. The reinforced concrete (RC) members in NPPs structures (containment vessels, service buildings with structural walls systems) perform a strategic function for the safety and operation of the whole system itself. Such RC components must be verified towards strong seismic input, impacts and explosions (Labbé, 2013). When RC structures are subjected to these external actions, they show a strong non linear behaviour and crack openings. It is then of great interest to develop methods which are able to predict with adequate approximation the 3D behaviour of wall structures used in NPPs design. In this way, it would be possible to evaluate both the global (e.g. top displacements) and local (multi-cracking phenomena) behaviour. Thus, it is clear that reliable and adequate numerical tools are needed in order to catch such complex but relevant non linear behaviours. Moreover, it is remarked that many complex phenomena would be impossible to be caught with a simplified equivalent modelling. The validation of non linear numerical modelling tool is then a key point of the problem.

The current thesis faces the problem of non linear modelling of RC wall structures, which are of strong relevance for NPPs systems design and assessment. The case studies here presented are calibrated on international experimental benchmark. Nowadays many numerical tools are available for researchers and engineers for the evaluation of wall structures behaviour,

(Richard et al., 2013). The thesis focuses on the modelling of the dynamic behaviour of a  $\frac{1}{4}$  scaled mock up of a wall service building of a CPY reactor tested on a shaking table in Saclay (France) within the international workshop SMART2013 ([www.smart2013.eu](http://www.smart2013.eu)). Moreover, it was analyzed the cyclic behaviour of a  $\frac{1}{13}$  scaled specimen of a reinforced concrete containment vessel (RCCV) tested at the National Center for Research on earthquake Engineering, Taipei (Taiwan).

Numerical analyses were carried out by means of multi-layered shell elements and the fixed crack smeared RC model PARC\_CL (developed at the University of Parma). The PARC\_CL model was used in order to evaluate the non linear stiffness matrix at each integration point. This model is implemented in the user subroutine UMAT.for in Abaqus code. Such model was applied as it demonstrated to provide good results both in terms of local and global behaviour of other wall structures. In particular, local and global engineering demand parameters, which are at the core of modern “performance based” approach, were evaluated for both case studies. In fact, the multi layered shell modelling with PARC\_CL modelling is able to provide relevant results in terms of EDPs.

In [chapter 1](#), an introduction on the thesis content is provided. The main topics and issues at the research core are presented. The main aim of the research was to assess the seismic performance of wall structures (and in particular of NPPs structures) by means of finite element (FE) modelling and to validate it through lab tests comparison.

Chapters from 2 to 4 are grouped in part 1 which is mainly related to theoretical tools implemented and used during the research. The first tool is presented in [chapter 2](#) and it is the PARC\_CL model (Physical Approach on Reinforced Concrete applied to Cyclic Loads). This is a fixed crack and smeared reinforcement model applied to the case studies presented in the thesis. The model is tailored on the response of shear sensitive problems like off shore structures, vessels, walls systems. The model is also able to catch multi direction crack openings. This is of great interest for wall structures in NPPs as in this case the structural continuous RC elements should also prevent radiation leakage. Moreover, it is possible to evaluate stresses and strains in concrete and steel rebars. The model is applied to multi-layered shell

elements, so it is possible to catch the full 3D behaviour of wall elements. Cyclic materials constitutive models are implemented in the subroutine so it is possible to catch with good approximation (as the model here presented is with secant unloading) the hysteretic behaviour of the structures.

In chapter 3 the probabilistic approach used for the generation of fragility curves in chapter 6 is described. The method described, which is often used in NPPs design, is described beside basic probabilistic theory. The chapter may be considered as a “stand alone” guide line for the application of probabilistic concepts in civil engineering.

In chapter 4 it is reported a review on the accelerograms and spectra theory. Some aspects are discussed, in particular the implementation of energy quantities spectra for design and the manipulation of digital accelerograms in dynamic numerical analyses. Basic concepts are provided also for the evaluation of Fourier amplitude spectra use. Examples are provided, too. Chapter 4, similarly as chapter 3, can be used as a simpleguide line on dynamic concepts.

Part 2 of the thesis is about the background on shell modelling of wall structures with PARC\_CL. Chapter 5 is a brief review on examples available in literature is presented and discussed. In particular, it is analyzed the ability of shell modelling with PARC\_CL to catch rea failure modes in wall structures and advantages/disadvantages in comparison with other modelling techniques.

Chapters from 6 to 8 constitute the Part 3 and the core examples and concepts are presented. In chapter 6 the first case study is presented. The non linear shell modelling of a wall structure subjected to torsional behaviour is described. The structure mock up was tested in  $\frac{1}{4}$  scale at Saclay (France ) laboratory on a 6 degrees of freedom shaking table. A sequence of accelerograms up to 6g PGA was applied. The structural respose was first analyzed by means of a blind prediction in order to assess the reliability of the proposed model. The modelling was able to catch the displacement field, local cracking phenomena, rebars yielding. One more model was developed during post-analyses in order to evaluate the influence of the introduction of the shaking table model and of input accelerograms manipulation. In chapter 7 it is presented the quasi-static analysis of a 1/13 scaled RCCV tested at NCREE lab under cyclic loading. The numerical simulation provided good results and the global base shear vs. top displacement diagram could be calculated with good accuracy up to force peak. However, the model was not able to catch the

sliding shear failure mode detected during the test. This is why in chapter 8 a preliminary extension of the research is reported. Both from chapter 6 and 7, the interface problem emerged to be relevant for wall structures. A modelling technique able to consider the rebars cyclic dowel action behaviour via a UEL for subroutine and concrete friction via the definition of surface contact is then proposed. Further investigation are needed for the calibration of the model.

To conclude, in the modern design practice it is important to evaluate the proper structural performances through the definitions of EDPs. Recent laboratory tests stressed the importance of developing and calibrating non linear models able to predict the local and global response of wall structures.



# Introduction

## 1 Introduction

The problem of energy resources exploitation is becoming nowadays of strong importance, in particular because of the global warming effects and the pollution generated by oil and coal power plants. Beside carbon fossil power plants, NPP are used in 30 countries all over the world. The need for energy is in this case also correlated to the essential problem of population safeguard towards radiations leakage risk and then the need for rational design methods and safety assessment of existing structures. In fact, a considerable amount of energy is produced by reactors that need or will need in a short time of a renewal process (Hsu et al., 2014). RC components in NPP (e.g. containment vessels, structural walls systems) are of strong importance for the safety and for the operation of the plants themselves.

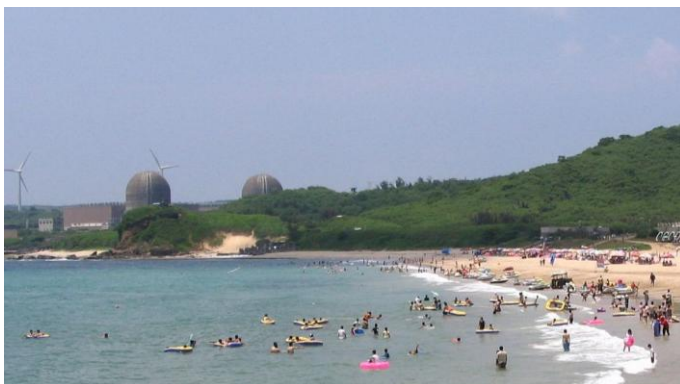
Such RC components should be analyzed under severe load conditions like strong earthquake motions, impacts, explosions, (Labbé, 2013). Under these conditions structures show strong non-linear material behaviour and consequent crack openings. It is essential to predict the 3D behaviour of these structures in order to evaluate global response (e.g. displacements) but also local phenomena (e.g. multi direction cracking). It is then clear the need of adequate and reliable numerical tools and material models able to catch with good approximation all these different aspects as analyses of complex three dimensional RC structures performed using simplified assumptions cannot capture the actual behaviour. The calibration of the models via experimental tests comparison is a key point for obtaining reliable solutions.

Structural wall systems are commonly used both in day to day and power plants design and their modelling is an actual problem. In fact, many uncertainties related to seismic behaviour and failure mechanisms concern this type of structural system. In civil building design it is common to find structural wall as they provide strength and stiffness towards seismic actions and then allow a better displacement control. Moreover, it is of interest to notice that nuclear power plants realised with many squat walls tend to be really stiff and with short fundamental mode vibration. In fact, regulatory standards recommend designing RC buildings devoted to nuclear activities as the assembly

of shear walls and frames. This design allows reducing the development of damage during high intensity extreme loadings. However, Bernoulli hypotheses may not be satisfied (this is particularly true for squat walls, often used in low rise structures), even in case of ductile elements, because of the geometrical features of RC walls themselves. In fact, walls are mostly constituted of discontinuity regions. Furthermore determination of the shear resistance (especially close to supports and floors), of the flexural bending resistance and of the curvature ductility (especially for composite wall cross sections) requires a-priori assumptions in order to be performed with equivalent beam modelling. The modelling of RC wall buildings under severe loading conditions is then a challenging problem.



**Figure 1.1** - In the upper left corner it is possible to notice the Lungmen power plant in northern Taiwan (credits: Stocchi).



**Figure 1.2** - On the background, the two domes of the Mintian power plant in southern Taiwan (credits: Wikicommons).

Nowadays many numerical tools are available for civil engineers for the modelling of wall structures, as documented for example in (Richard et al., 2014). These approaches can be summarized on the basis of the finite element type used for the modelling of the critical members of the structure. Lumped mass based models, discrete elements models and within finite elements method beam elements, shell elements and solid elements models are commonly used. One of the most common approaches however resulted to be the ones using shell elements. The modelling techniques also differentiated on the basis of the adopted material non-linear behaviour (e.g. concrete biaxial state of stresses, softening, hysteretic loops and permanent strain and steel cyclic and reverse loading and kinematic hardening). For shear-critical specimens, aggregate interlock, tension stiffening, multiaxial stress states and Poisson effects play all an important role in the structural response. Shell elements modelling with smeared crack models can be a useful tool to predict damage indicators: in particular it is possible to estimate local engineering demand parameters like concrete and rebar strains and crack opening values, and global engineering demand parameters like displacement values which are necessary for the application of performance-based earthquake engineering. The multi layer total strain fixed crack PARC\_CL model presented in chapter 2 with shell elements approach is particularly tailored for shear sensitive problems which demonstrated to be of great interest in engineering design. The shell modelling with multi layer PARC\_CL is then applied to shear dominant analyses problems (wall structures, containment vessel) under severe cyclic and dynamic loads.

## **1.1 Definition of the research field**

The presented thesis deals with the seismic assessment of wall structures and, in particular, of nuclear power plants by means of non linear finite element method analyses.

Mainly after recent earthquakes all over the world it is clear that modern and reliable modelling techniques are needed. Moreover, as already stated, the issue of the seismic safety of NPPs and containment structures is of great interest. The study of the causes of collapse is of strong importance in this case in order to preserve human lives and preserve national economies and energies.

The interest for these topics led to many international workshops and conferences. Since the '50s great efforts have been put for the definition of safe criteria for the design of RC structures. It must be stressed the fact that besides NPPs this problem involves a great amount of different existing structures, such as shear walls structures, containers, off shore and containment structures. Moreover, the comprehension of the behaviour of RC infrastructures for energy systems is a key point also for the future, e.g. for nuclear fusion power plants (like ITER project) which will need solid confinement vessel.

The thesis is organized in the following way. Chapters from 2 to 4 describe the tools and the theory used during the research. These sections may be used also as general guidelines as practical examples are provided besides the theory description.

The thesis is organized along three main parts. Part 1 (chapter 2 – 4) is mainly related to the analytical and numerical tools that were implemented and used throughout the research. Part 2 is related to only one chapter (chapter 5) and it is mainly a review and state of the art on the shell modelling of wall structures. Part 3 is the main corpus of the thesis, where two main case studies are presented (chapter 6 and 7). Finally, an extension of the studies is presented together and conclusions and further appendixes are provided.

In chapter 2 it is given the description of the model used for the evaluation of the non linear behaviour in the reinforced concrete elements, the PARC\_CL fixed crack model. The PARC\_CL (Physical Approach for Reinforced Concrete subjected to Cyclic Loading) is implemented in the user subroutine UMAT of Abaqus Code. It is then applied to multi layered shell modelling.

In chapter 3 it is reported and explained also with some examples the implementation of fragility curves. Some practical extensions to analytical calculation are presented by means of spreadsheets examples. The method will be then applied to a case study.

In chapter 4 the numerical issues and techniques investigated and used for the current research are discussed, in particular for what it is concerning dynamic problems. The generation of response spectra is also discussed. The chapter focuses also on the so called “energy approach” to dynamic problems, one example of application is also provided.

In chapter 5 a comprehensive review wall structures modelling techniques is presented and discussed. Moreover, references are provided for available

tests in literature.

In chapter 6 case study one is presented. The numerical analysis of a scaled nuclear structure is carried out by means of non linear time history. In chapter 7 the quasi static analysis of a scaled nuclear containment vessel will be presented.

In chapter 8 it is discussed the preliminary numerical implementation of the so called “contact problem” which emerged as one of the main issues both for experimental procedures and modelling techniques based on FEM. These results are an extension of the research topics that emerged during the analyses presented in chapter 6 and 7, and they will be extended in the future with further research.

## **1.2 Aims of the research**

As already stated, the evaluation of the seismic assessment of nuclear structures is of great interest both for the evaluation of design numerical techniques, for the safeguard of population and for the knowledge transfer.

The presented work will show numerical results for the description of the behaviour of NPP structures under the effect of strong earthquakes. It is demonstrated that it is very important the calibration of the numerical methods by means of experimental test data. The experimental data are from two campaigns, one run at the Saclay laboratories within the SMART2013 project and the other one run at NCREC lab in Taipei.

The research organization is reflected in the organization of the thesis itself (Part 1 to 3). In the first part of the research the main numerical, statistical and mathematical tools are described in order to clearly understand the meaning of the obtained results. In the second phase the numerical tools are then applied for the modelling of scaled structures which have been tested via both dynamic and quasi-static tests.

The topics discussed are of interest not only for design operative purposes but also for much wider field of the non linear analysis of structures which is fundamental for the research.

### 1.3 Methodology

Nowadays several numerical tools are available for the evaluation of seismic response of RC wall structures. However, research is needed in order to assess the reliability of numerical modelling. As many parameters need to be properly tuned, the blind prediction and post diction analysis of experimental tests is of strong relevance in this way. In the present work two main case studies were analyzed. In both cases non linear shell modelling with PARC\_CL model was evaluated in order to understand if the proposed modelling was able to properly describe the structural performances.

The shell modelling with PARC\_CL proved to be quite efficient in the past (chapter 5) as it is a model tailored on shell dominant problem. The adopted FEM code was Abaqus 6.12.1. The implicit method was adopted by the solver while the Newton-Rhapson method was used as convergence criterion. Analyses ran on a 3.20 GHz machine with 16 GB RAM. Non-linear analyses however ran on a single CPU as UMAT subroutine does not allow parallel calculation. In the analyses it was adopted the default Abaqus/Standard Hilber-Hughes-Taylor time integration. The Hilber-Hughes-Taylor operator is an extension of the Newmark method. Meshes have been firstly tailored on the reinforcement distribution, geometry and computing resources available.

Preliminary results have been obtained and then compared to final test data. Particularly attention was given to the estimation of local strains, especially to crushing phenomena in concrete which proved to have a significant impact on tests results, displacements field, base shear and cracking distribution. By results comparison then some remarks and final observation were made. It appeared that shell modelling with PARC\_CL may provide good results both in terms of local and global EDPs for different IMs levels. However, the research stressed also the importance of the development of numerical implementation of the so called interface problem which may be relevant especially for existing wall structures which are usually provided with poor detailing.





# Part I. Concepts



## **Chapter II.**

# **The PARC\_CL Reinforced Concrete Model**

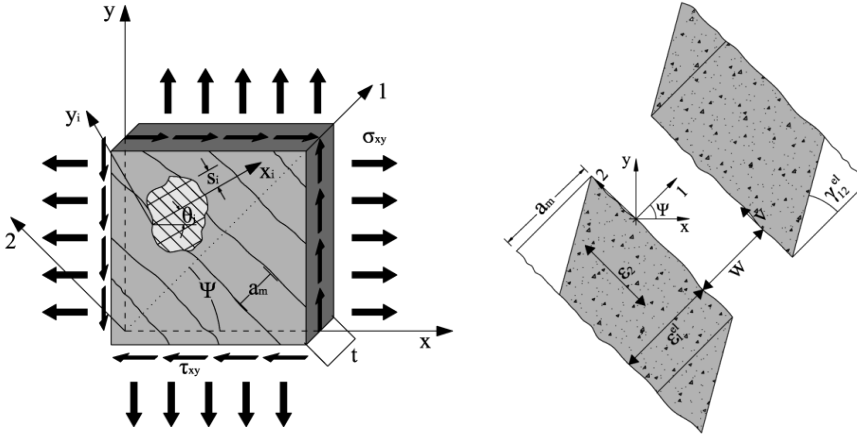
## 2 The PARC\_CL reinforced concrete model

In this section, the PARC\_CL model for the description of the reinforced concrete model implemented in the user subroutine UMAT.for of Abaqus code is briefly described.

### 2.1 PARC fixed crack model

A physical approach for reinforced concrete for the analysis of the nonlinear behaviour up to failure of reinforced-concrete membrane elements under monotonic loadings is a model proposed by Belletti et al. (2001). It is based on a set of works concerning the study of both reinforced concrete and prestressed elements under torsion (Iori and Dei Poli 1985; Cedolin et al. 1987, Carpinteri et al. 1996; Cerioni et al. 1998) and membrane elements (Cerioni and Iori 1995). By a local fixed-crack approach similar to those proposed in (Bazant and Gambarova, 1980), (Walraven and Reinhardt, 1981), and (Walraven, 1981), the phenomena such as aggregate interlock, tension stiffening, dowel action, and strain of concrete struts in compression have been taken into account. The obtained constitutive relationship can be used for analysis by a finite-element method of several structures (shear walls, deep beams, etc.), treated as an assembling of reinforced-concrete membrane elements.

The model is based on a fixed total strain crack approach, in which at each integration point two reference systems are defined: the local  $x,y$  coordinate system, parallel to the global  $X,Y$  coordinate system, and the  $1,2$  coordinate system along the principal stress directions. The angle between the  $1$ -direction and the  $x$ -direction is denoted as  $\psi$ , whereas  $\alpha_i = \theta_i - \psi$  is the angle between the direction of the  $i$ th order of the bar and the  $1$ -direction, where  $\theta_i$  is the angle between the direction of the  $i$ th order of the bar and the  $x$ -direction. When the maximum tensile principal stress reaches the concrete tensile strength  $f_{ct}$ , cracking starts to develop, and the  $1,2$  coordinate system is fixed. The concrete behaviour is assumed to be orthotropic, both before and after cracking; softening in tension and compression, a multiaxial state of stress and the effect of aggregate interlock are taken into account.



**Figure 2.1** - Energy spectra quantities in case of linear behaviour.

The reinforcement is modelled through a smeared approach; dowel action and tension stiffening phenomena are considered. The total strains at each integration point are calculated, in the  $1,2$  coordinate system, as the sum of the elastic (superscript  $el$ ) and the inelastic (superscript  $cr$ ) strains:

$$\varepsilon_1 = \varepsilon_1^{el} + \varepsilon_1^{cr} = \varepsilon_1^{el} + \frac{w}{a_m} \quad (2.1)$$

$$\varepsilon_2 = \varepsilon_2^{el} + \varepsilon_2^{cr} \quad (2.2)$$

$$\gamma_{12} = \gamma_{12}^{el} + \gamma_{12}^{cr} = \gamma_{12}^{el} + \frac{v}{a_m} \quad (2.3)$$

Where  $w$  = crack opening;  $v$  = crack sliding; and  $a_m$  = crack spacing calculated through an a priori method (Leonhardt and Schelling, 1974) based on the transmission length of bond between concrete and steel. The strains in the  $x,y$  coordinate system,  $\{\varepsilon^{(x,y)}\}$ , are obtained through the transformation matrix  $[T_\varepsilon]$ , which is a function of the fixed angle  $\psi$ . The overall stiffness matrix in the  $x,y$  coordinate system,  $[D^{(x,y)}]$ , is obtained by assuming that concrete and reinforcement behave like two springs placed in parallel:

$$\begin{aligned} [D^{(x,y)}] &= [T_\varepsilon]^T [D_c^{(1,2)}] [T_\varepsilon] + [T_{\theta_i}]^T [D_s^{(x_i,y_i)}] [T_{\theta_i}] \\ &= [T_\varepsilon]^T \begin{bmatrix} \bar{E}_{c1} & 0 & 0 \\ 0 & \bar{E}_{c2} & 0 \\ 0 & 0 & \beta G \end{bmatrix} [T_\varepsilon] + [T_{\theta_i}]^T \begin{bmatrix} \rho_i \bar{E}_{si} g_i & 0 \\ 0 & \rho_i d_i \end{bmatrix} [T_{\theta_i}] \end{aligned} \quad (2.4)$$

In Eq. (2.4), the concrete stiffness matrix  $[D_c^{(1,2)}]$  is defined, in the 1,2 coordinate system, as a function of the concrete contribution in tension and in compression ( $\bar{E}_{c1}$  and  $\bar{E}_{c2}$ ) and of the aggregate interlock effect ( $\beta G$ ). The steel stiffness matrix  $[D_s^{(x_i, y_i)}]$  is defined, in the  $x_i, y_i$  coordinate system, as a function of a reinforcement contribution ( $\bar{E}_{si}$ ), tension stiffening ( $g_i$ ), and dowel action ( $d_i$ ). The transformation matrixes  $[T_\varepsilon]$  and  $[T_{\theta_i}]$  are used to rotate the concrete matrix from the 1,2 to the  $x, y$  coordinate system and the steel matrix from the  $x_i, y_i$  to the  $x, y$  coordinate system, respectively. The stresses  $\{\sigma^{(x, y)}\}$ , in the  $x, y$  coordinate system are defined by

multiplying the stiffness matrix  $[D^{(x, y)}]$  and the strain vector  $\{\varepsilon^{(x, y)}\}$ . The constitutive model PARC\_CL allows secondary cracking perpendicular to primary cracking by imposing  $\bar{E}_{c2}$  equal to zero.

## 2.2 Adopted constitutive models

The concrete and steel behaviour as well as their interaction effects are modelled with constitutive relationships for loading - unloading - reloading conditions. The stress-strain relationship for concrete is described by Eq.(2.5) for concrete in tension and in Eq.(2.6) for concrete in compression.

$$\sigma = \begin{cases} E_c \varepsilon & 0 \leq \varepsilon \leq \varepsilon_f \\ f_{ct} \left[ 1 + 0.85 \left( \frac{\varepsilon - \varepsilon_f}{\varepsilon_f - \varepsilon_{t1}} \right) \right] & \varepsilon_{c0} \leq \varepsilon < 0 \\ 0.15 f_{ct} \left[ 1 + \left( \frac{\varepsilon - \varepsilon_{t1}}{\varepsilon_{t1} - \varepsilon_{tu}} \right) \right] & \varepsilon_{t1} \leq \varepsilon < \varepsilon_{tu} \end{cases} \quad (2.5)$$

$$\sigma = \begin{cases} f_c \left[ 1 - \left( \frac{\varepsilon - \varepsilon_{c0}}{\varepsilon_{cu} - \varepsilon_{c0}} \right)^2 \right] & \varepsilon_{cu} \leq \varepsilon < \varepsilon_{c0} \\ \frac{E_c}{E_{cs}} - \frac{\varepsilon}{\varepsilon_{c0}} E_{cs} \varepsilon_c & \varepsilon_{c0} \leq \varepsilon < 0 \\ 1 + \left( \frac{E_c}{E_{cs}} - 2 \right) \frac{\varepsilon}{\varepsilon_{c0}} & \end{cases} \quad (2.6)$$

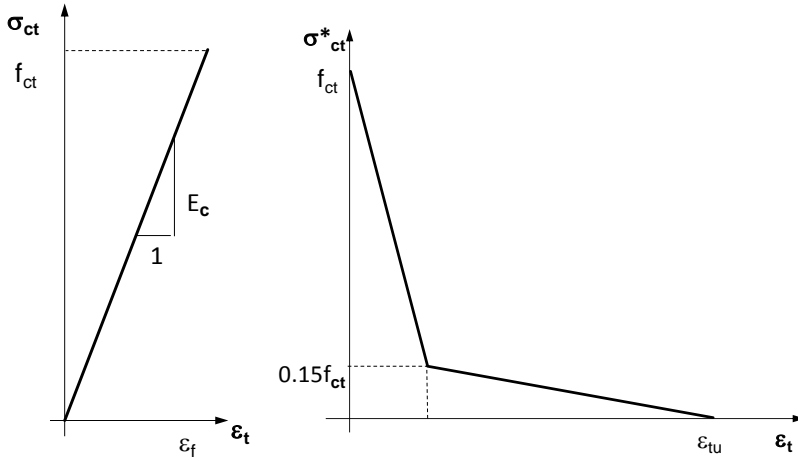
where  $E_c$  and  $E_{cs}$  are the initial modulus of elasticity and the secant stiffness corresponding to the peak strain  $\varepsilon_{c0}$ , respectively. The stress-strain relationship for concrete in tension is defined as a function of its tensile strength  $f_{ct}$ , the

concrete strain at cracking  $\varepsilon_f$ , and the strain  $\varepsilon_{t1}$  and  $\varepsilon_{tu}$  (corresponding to residual stress equal to  $0.15 f_{ct}$  and zero, respectively) :

$$\varepsilon_{t1} = \frac{G_f \cdot (2 - 0.15 \cdot \alpha_f)}{a_m \cdot f_{ct}} + 0.15 \cdot \varepsilon_f \quad (2.7)$$

$$\varepsilon_{tu} = \frac{\alpha_f \cdot G_f}{a_m \cdot f_{ct}} \quad (2.8)$$

Where  $G_f$  =fracture energy in tension; and  $\alpha_f$  is a coefficient (CEBFIP, 1993).



**Figure 2.2** - Tensile behaviour of concrete.

The compressive branch before reaching the peak is defined in agreement with Sargin's formulation (CEB-FIP, 1993) and after the peak with Feenstra's relationship (Feenstra, 1993), as a function of the concrete compressive strength  $f_c$  and concrete fracture energy in compression  $G_{fc}$ . Therefore, the ultimate concrete strain in compression is given by Eq.(2.9).

$$\varepsilon_{cu} = \varepsilon_{c0} + \frac{3 \cdot 250 \cdot G_f}{2 \cdot a_m \cdot f_c} \quad (2.9)$$

The ratio between the concrete fracture energy in compression and in tension is assumed equal to 250 (Nakamura and Higai in Shing and Tanabe, 2001). To model the multiaxial stress state, the concrete compressive strength

and the corresponding peak strain are reduced because of the presence of lateral cracking (Vecchio and Collins, 1993):

$$\zeta = \frac{1}{0.85 - 0.27 \cdot \frac{\varepsilon_t}{\varepsilon_{c0}}} \quad (2.10)$$

where  $\varepsilon_t$ =current tensile strain.

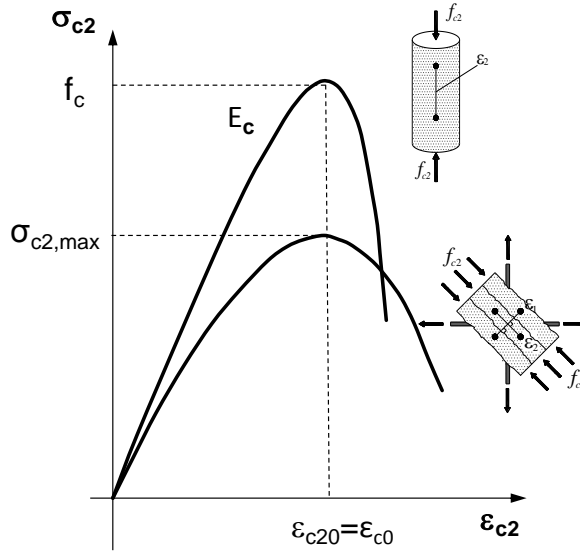


Figure 2.3 - Compressive behaviour of concrete.

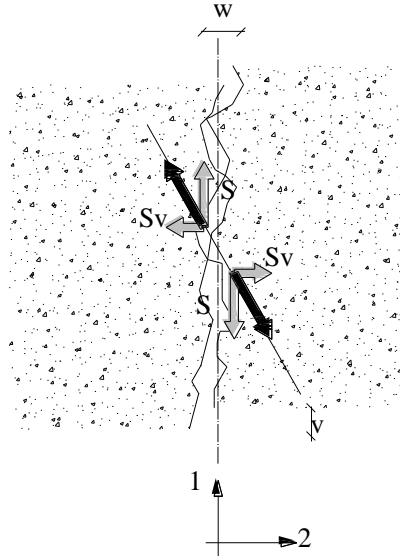
### 2.3 Aggregate interlock

The shear stress caused by the effect of aggregate interlock is evaluated on the basis of the crack opening,  $w$ , and the crack sliding, (Gambarova, 1983), Figure 2.4:

$$\tau_{12} = \bar{\tau} \cdot \left( 1 - \sqrt{\frac{2 \cdot w}{D_{max}}} \right) \cdot \frac{a_3 + a_4 \cdot \left| \frac{v}{w} \right|^3}{1 + a_4 \cdot \left( \frac{v}{w} \right)^4} \cdot \frac{1}{w} \cdot v \quad (2.11)$$

where  $\bar{\tau} = 0.27f_c$ ;  $a_3 = \frac{2.45}{\bar{\tau}}$ ;  $a_4 = 2.44 \cdot \left( 1 - \frac{4}{\bar{\tau}} \right)$ ; and  $D_{max}$  = maximum aggregate diameter.





**Figure 2.4** - Interaction between two cracks: aggregate interlock and confinement actions.

Gambarova's relation can be schematized with a bilinear curve (Figure 2.6) in which the endpoint of the elastic part  $A(v^*, \tau^*)$  has coordinates equal to:

$$v^* = \frac{f_c}{a_5} \cdot w + a_6 \quad (2.12)$$

$$\tau^* = \bar{\tau} \cdot \left( 1 - \sqrt{\frac{2 \cdot w}{D_{max}}} \right) \cdot \frac{a_3 + a_4 \cdot \left| \frac{v^*}{w} \right|^3}{1 + a_4 \cdot \left( \frac{v^*}{w} \right)^4} \cdot \frac{1}{w} \cdot v^* = c^* \cdot v^* \quad (2.13)$$

where  $a_5 = 0.366 \cdot f_c + 3.333$  and  $a_6 = f_c/110$ .

The proposed bilinear curve is used to define the stress-strain relationship between the shear stress  $\tau^{12}$  and the shear strain  $\gamma_{12}^{cr}$  in the cracked phase of the concrete. In this phase, the tangential elastic modulus,  $G_{cr}$ , is equal to:

$$G_{cr} = \begin{cases} G_{cr}^* = c^* a_m & \gamma_{cr}^{12} < \gamma_{cr}^* \\ \frac{\tau^*}{\gamma_{cr}^{12}}, & \gamma_{cr}^{12} \geq \gamma_{cr}^* \end{cases} \quad (2.14)$$

where  $c^*$  is defined by Eq. (12) and  $\gamma_{cr}^* = v^*/a_m$ .

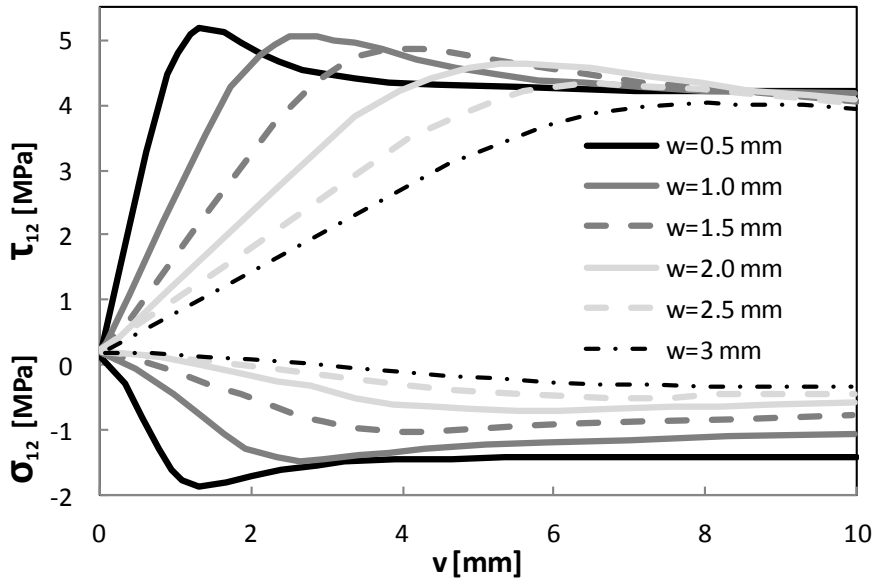


Figure 2.5 - Gambarova stress vs. crack sliding relationship.

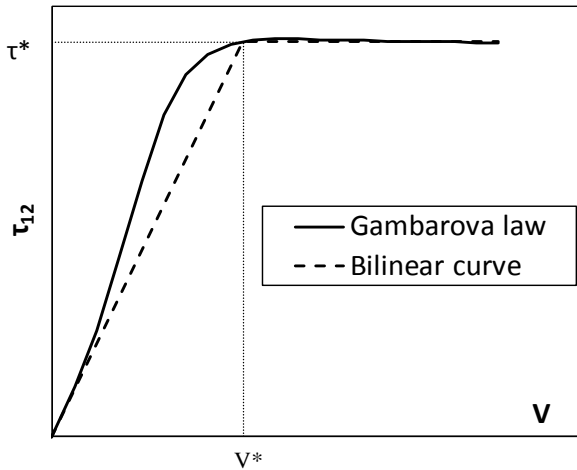


Figure 2.6 - Linearization of tangential stress vs. crack sliding for a given crack opening  $w$  value.

According to the total strain concept, it is assumed that the uncracked concrete, characterized by the elastic deformation  $\gamma_{12}^{el}$ , and the cracked concrete, characterized by the cracking deformation  $\gamma_{12}^{cr}$ , work as two springs

placed in series. Therefore, the overall shear modulus can be defined by multiplying its initial values for the shear retention factor  $b$ , equal to:

$$\beta = \begin{cases} 1 & \text{uncracked phase } \gamma_{12} \leq \gamma_f \\ \frac{G_{cr}}{G_{cr} + G} & \text{cracked phase } \gamma_{12} > \gamma_f \end{cases}$$

$$\beta = \begin{cases} 1 & \gamma_{12} \leq \gamma_f \\ \frac{G_{cr}^*}{G_{cr}^* + G} & \gamma_f < \gamma_{12} < \gamma_p \\ \frac{\tau^*}{G\gamma_{12}} & \gamma_{12} \geq \gamma_p \end{cases} \quad (2.15)$$

where  $G$  and  $G_{cr}$  are the initial and degraded values of the shear modulus, respectively. The strain  $\gamma_f$  corresponds to the shear strain at the onset of concrete cracking. The strain  $\gamma_p$  defines the point after which the shear stress remains constant for a given crack opening  $w$ , and is equal to

$$\gamma_p = \gamma_{cr}^* + \frac{\tau^*}{G} \quad (2.16)$$

The coefficient  $\beta$  is assumed to be constant when unloading occurs. The aggregate interlock phenomenon is neglected for crack opening values higher than half the maximum aggregate diameter.

## 2.4 Steel constitutive model

The stress-strain relationship for reinforcing steel is represented by an idealized elastic-hardening plastic bilinear curve, identical in tension and compression, Figure 2.7.

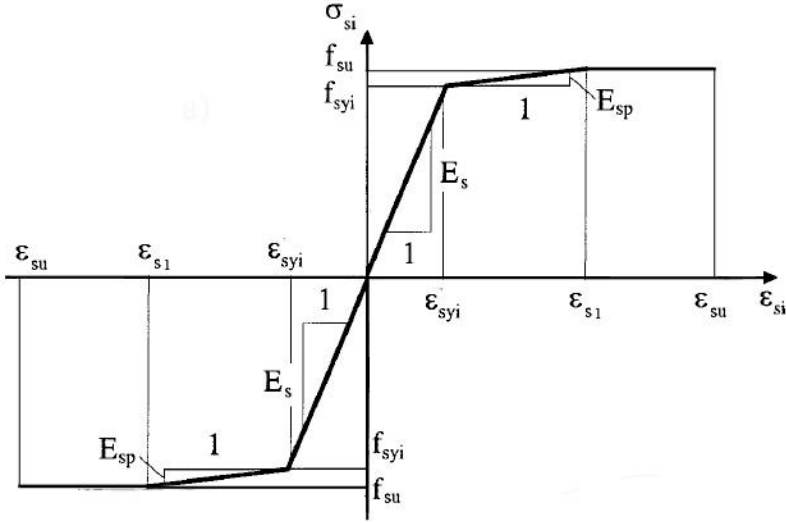


Figure 2.7 - Steel constitutive model.

The stress  $\sigma_{si}$  in the  $i$ -th steel bar is obtained by:

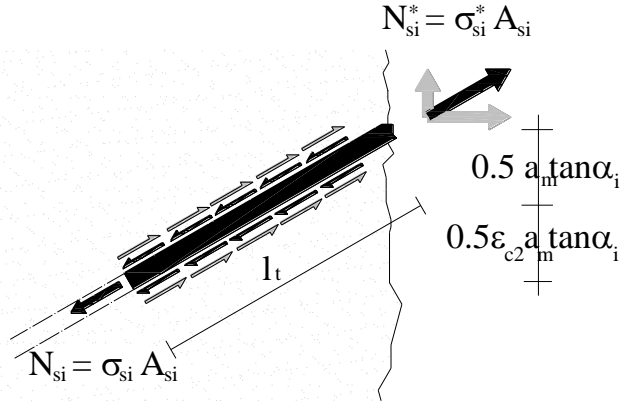
$$\sigma_{si} = \bar{E}_{si} \cdot \varepsilon_{si} \quad (2.17)$$

where the secant modulus assumes the following expression:

$$\bar{E}_{si} = \begin{cases} E_{si} & \varepsilon_{si} \leq \varepsilon_{syi} \\ \frac{f_{syi} + (\varepsilon_{si} - \varepsilon_{syi})E_{spi}}{\varepsilon_{si}} & \varepsilon_{syi} \leq \varepsilon_{si} \leq \varepsilon_{s1i} \\ \frac{f_{sui}}{\varepsilon_{si}} & \varepsilon_{s1i} < \varepsilon_{si} < \varepsilon_{ui} \end{cases} \quad (2.18)$$

## 2.5 Tension stiffening

In the model both the stress  $\sigma_{si}^*$  in the  $i$ th steel bar near the cracks and the stress  $\sigma_{si}$  far from the cracks are taken into account (Figure 2.8).



**Figure 2.8** - Effect of bond between concrete and steel on stress in bar.

The relationship between the two steel stresses defined above is governed by the tension stiffening effect that the concrete included between cracks produces on steel. The stress  $\sigma_{si}^*$  is evaluated by means of an appropriate increment of the steel bar average strain (Giuriani 1981) and is expressed by the following equations:

$$\sigma_{si}^* = \bar{E}_{si}^* (\varepsilon_{si} + \Delta\varepsilon_{si}) = \bar{E}_{si}^* \left( 1 + \frac{\Delta\varepsilon_{si}}{\varepsilon_{si}} \right) \varepsilon_{si} = \bar{E}_{si}^* g_i \varepsilon_{si} \quad (2.19)$$

Where:

$$\Delta\varepsilon_{si} = \varepsilon_i^* \cdot g_0 \quad (2.20)$$

$$\varepsilon_i^* = \frac{w}{a_m} \cos^2 \alpha_i + \frac{v}{a_m} \cos \alpha_i \sin \alpha_i \quad (2.21)$$

$$g_0 = g_{1i} + k_1 \cdot g_{2i} \cdot (\varepsilon_i^*)^{k_2 - 1} \quad (2.22)$$

With:

$$g_{1i} = \lambda_i \cdot \frac{\cosh \lambda_i}{\sinh \lambda_i} - 1; \quad g_{2i} = \frac{2 \cdot \tau_0}{\tau_1 \cdot a_m} \cdot \lambda_i \cdot \frac{\cosh \lambda_i - 1}{\sinh \lambda_i};$$

$$\lambda_i = \sqrt{\frac{\tau_1 \cdot a_m^2}{0.5 \cdot E_{si} \cdot \phi_i}}; \quad \tau_0 = 3 \text{ MPa}; \quad \tau_1 \cdot \phi_i = 75 \text{ MPa};$$

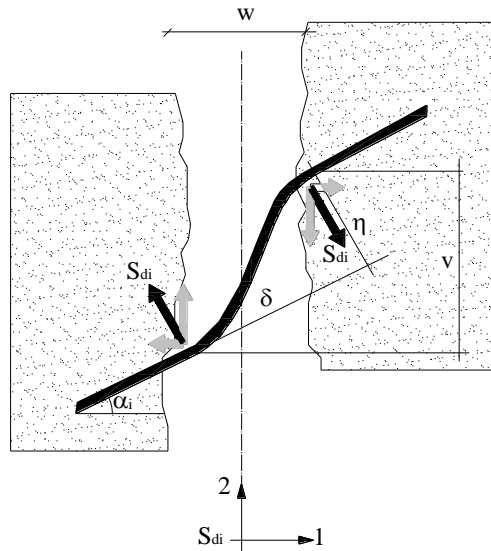
$$k_1 = 4.0; \quad k_2 = 0.2$$

## 2.6 Dowel action

For the dowel-action  $S_{di}$ , the following basic expression (Walraven and Reinhardt 1981) is adopted:

$$S_{di} = 10\eta^{0.36} \phi_i^{1.75} f_{cc}^{0.38} (\delta + 0.2) \quad (2.23)$$

where  $\delta$  and  $\eta$  = relative displacements parallel and perpendicular to the directions of the reinforcing bar, respectively. The values of  $\delta$  and  $\eta$  are calculated in the crack considering the displacements that the ends of the steel bars undergo while crack lips are opening and sliding, Figure 2.9.



**Figure 2.9** - Effect of bond between concrete and steel on stress in bar.

Hence,  $d$  and  $h$  are functions of crack opening  $w$  and sliding  $v$ , as follows:

$$\eta = |-w \sin\alpha_i + v \cos\alpha_i| \quad (2.24)$$

$$\delta = |w \cos\alpha_i + v \sin\alpha_i| \quad (2.25)$$

## 2.7 Stiffness matrix and numerical solution procedure

The material stiffness matrix  $[D']$  gives the following relationship between the stresses  $\{\sigma'\}$  and strains  $\{\varepsilon'\}$  in the 1,2-coordinate system:

$$\{\sigma'\} = [D'] \{\varepsilon'\} \quad (2.26)$$

Thus, generalizing to the case of  $n$  reinforcing layers, placed along  $\alpha_i$  directions and with  $\rho_i$  steel geometric percentage, the nine terms of the stiffness matrix result:

$$D'_{11} = \sum_{i=1}^n (\bar{E}_{si}^* \rho_i g_i \cos^4 \alpha_i + d_i^* \cos \alpha_i \sin^2 \alpha_i) + c_t a_m \quad (2.27)$$

$$D'_{21} = \sum_{i=1}^n (\bar{E}_{si} \rho_i \cos^2 \alpha_i \sin^2 \alpha_i) \quad (2.28)$$

$$D'_{31} = \sum_{i=1}^n (\bar{E}_{si}^* \rho_i g_i \cos^3 \alpha_i \sin \alpha_i - d_i^* \cos^2 \alpha_i \sin \alpha_i) \quad (2.29)$$

$$D'_{12} = \sum_{i=1}^n (\bar{E}_{si} \rho_i \cos^2 \alpha_i \sin^2 \alpha_i) \quad (2.30)$$

$$D'_{12} = \sum_{i=1}^n (\bar{E}_{si} \rho_i \cos^2 \alpha_i \sin^2 \alpha_i) \quad (2.31)$$

$$D'_{22} = \bar{E}_c + \sum_{i=1}^n (\bar{E}_{si} \rho_i \sin^4 \alpha_i) \quad (2.32)$$

$$D'_{32} = \sum_{i=1}^n (\bar{E}_{si} \rho_i \cos \alpha_i \sin^3 \alpha_i) \quad (2.33)$$

$$D'_{13} = \sum_{i=1}^n (\bar{E}_{si}^* \rho_i g_i \cos^3 \alpha_i \sin \alpha_i - d_i^* \cos^2 \alpha_i \sin \alpha_i) - c_v a_m \quad (2.34)$$

$$D'_{23} = \sum_{i=1}^n (\bar{E}_{si} \rho_i \cos \alpha_i \sin^3 \alpha_i) \quad (2.35)$$

$$D'_{33} = \sum_{i=1}^n (\bar{E}_{si}^* \rho_i g_i \cos^2 \alpha_i \sin^2 \alpha_i + d_i^* \cos^3 \alpha_i) + c_a a_m \quad (2.36)$$

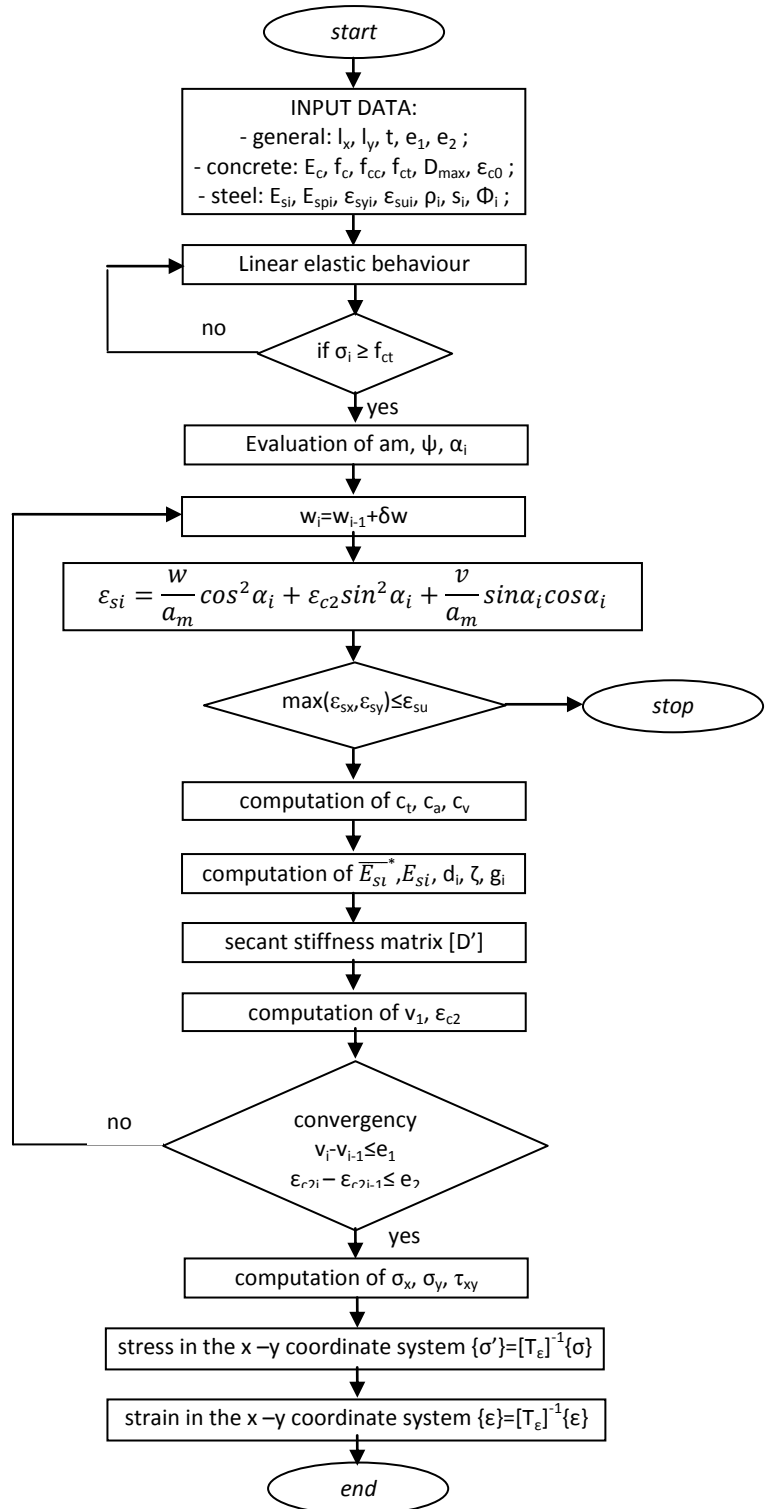
In the global x,y-coordinates, the relationship between the stresses  $\{ \sigma \}$  and strains  $\{ \varepsilon \}$  is:

$$\{ \sigma \} = [D]\{ \varepsilon \}$$

where  $[D] = [T_\varepsilon]^T [D'] [T_\varepsilon]$

In this model, the crack opening  $w$  is increased step by step: an iterative procedure is used for reaching the convergence in terms of values of crack sliding  $v$  and concrete strain  $\varepsilon_{c2}$ . The main steps of the implemented algorithm are shown in the flowchart.





## 2.8 PARC\_CL model

PARC\_CL model (Physical Approach for Reinforced Concrete subjected to Cyclic Loading) describes the behaviour up to failure of reinforced-concrete membrane elements under cyclic loadings.

The model was developed because in a structure under monotonic loadings, due to redistribution of internal stresses, the stress state could assume a cyclic behaviour. The previous PARC model could only move forward or backward on the envelope curve. The model is based on a secant approach, with unloading to the origin. This approach however does not allow considering plastic strain.

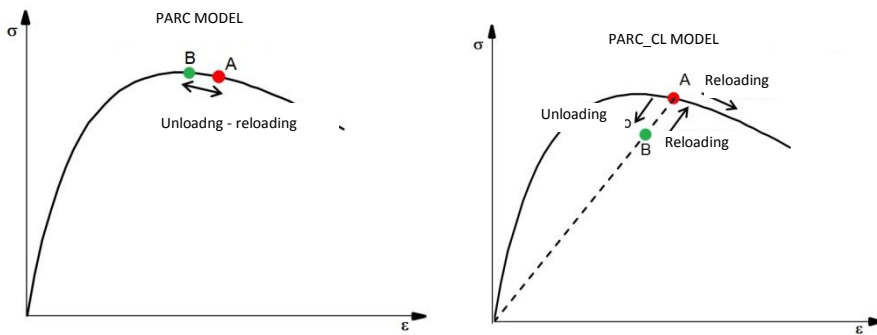


Figure 2.10 - Evolution of PARC to PARC\_CL.

The constitutive stress-strain relationships for concrete and steel are modified in order to take into account the cyclic behaviour, Figure 2.11 and Figure 2.12.

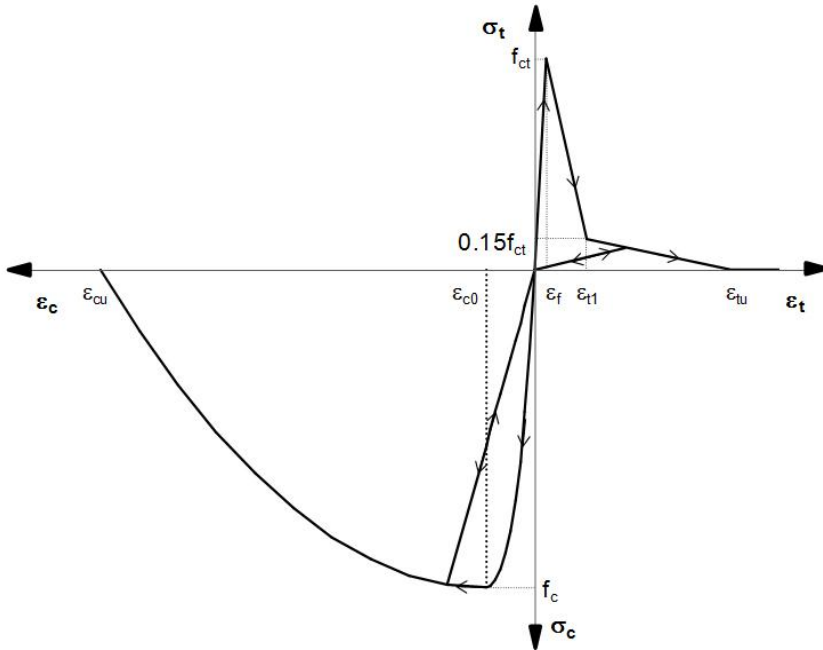


Figure 2.11 – Cyclic constitutive model for concrete in PARC\_CL.

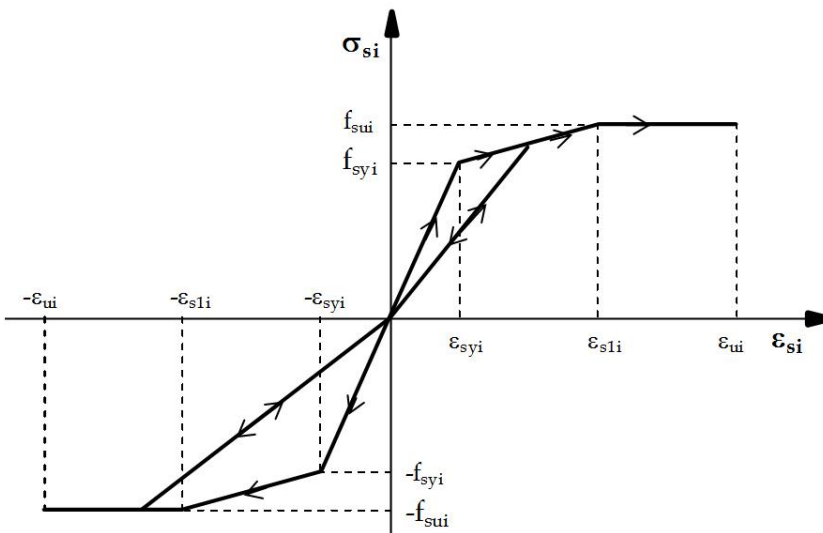


Figure 2.12 - Cyclic constitutive model for steel in PARC\_CL.



**Chapter III.**  
**A probabilistic approach**  
**for Structural Engineering**

### **3 A probabilistic approach for structural engineering**

In this chapter the main concepts and theory that will be applied in chapter VI are described. Some analytical examples are provided and illustrated for a spreadsheet calculation. Examples solved in Excel spreadsheet step by step are selected from (Nowak and Collins, 2000). Further information and applications can be found in (Pitilakis et al., 2014), in (FEMA, 2012) and (Huang et al., 2011).

#### **3.1 Probabilistic approach: a brief introduction**

The fragility functions are a fundamental component of a seismic risk loss assessment model and this is why they are so important. Fragility functions describe the probability of exceeding different limit states (such as damage levels) given a level of ground shaking. Fragility functions are usually derived by means of analytical methods. The vulnerable conditions of a building can be described using vulnerability functions or fragility functions). Vulnerability functions describe the probability of losses (e.g. social or economic losses) given a level of ground shaking. Fragility functions describe the probability of exceeding different limit state (e.g. damage or injury state) given a level of ground section. Vulnerability functions can be derived from fragility curves by means of consequence functions. In this guide this aspect will not be investigated. Analytical fragility curves are constructed starting from the statistical elaboration of damage distributions that are simulated from analyses of structural models under increasing earthquake intensity. It must be noticed that the application of analytical methods might be limited by the computational effort of the analyses. Simplified models are often implemented however the variability in the definition of the structural (and non-structural) elements may significantly affect the results. The similarity between the model and the actual structure, which strongly influences the reliability of the results, is dependent on the modelling capabilities. Analytical models can be divided into two classes of analysis: non-linear static or and dynamic analyses. In particular, the dynamic approach uses a detailed model that is subjected to ground motion recordings (accelerograms). This kind of analysis is time

consuming but it is closer to reality and allows the influence of the record-to-record variability of the structural response to be accounted for. However, this method can be sensitive to the number and characteristics of the selected accelerograms. The basic theory background, methods and examples for the estimation of fragility functions are reported in the following paragraphs.

## 3.2 Probabilistic theory

### 3.2.1 Random Variables

Any random variable is defined by its cumulative distribution function (CDF), or  $F_X(x)$ . The probability density function,  $f_X(x)$  of a continuous random variable is the first derivative of  $F_X(x)$ .

#### 3.2.1.1 Uniform random variable

All numbers are equally likely to appear. It corresponds to the function *random()* (in Italian *rand()*) of Microsoft Excel.

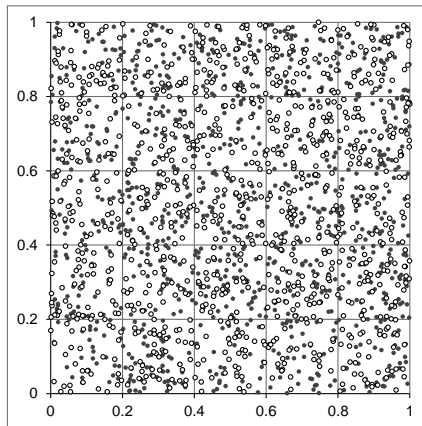


Figure 3.1 - Example of two uniformly distributed random series.

#### 3.2.1.2 Normal Random Variables

The *normal distribution* is widely used in structural reliability theory. The PDF for a normal random variable is reported in Eq. (3.1).

$$f_X(x) = \frac{1}{\sigma_X 2\pi} \exp \left[ -\frac{1}{2} \left( \frac{x - \mu_X}{\sigma_X} \right)^2 \right] \quad (3.1)$$

There is no closed-form solution for the CDF of a normal random variable. However it can be approximated as:

$$F_X(x) = \frac{1}{2} \left[ 1 + \operatorname{erf} \left( \frac{x - \mu_X}{\sigma_X \sqrt{2}} \right) \right] = \Phi \left( \frac{x - \mu}{\sigma} \right) \quad (3.2)$$

Where *erf* is the (Gauss) error function defined as the probability of a random variable with normal distribution of mean 0 and variance 1/2 falling in the range  $[-x, x]$ . An example of PDF and CDF is reported in Figure 3.2.

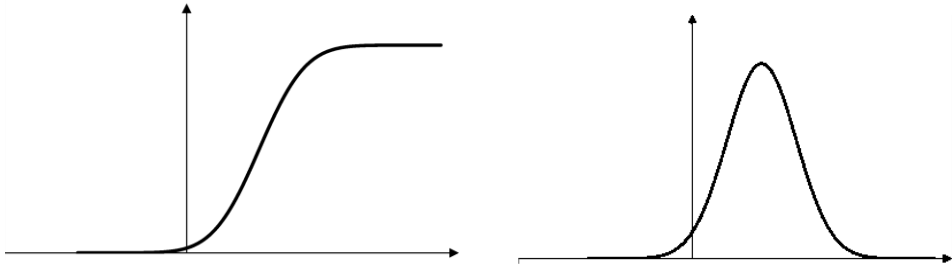


Figure 3.2 - PDF and CDF for a normal random variable.

The standard normal variable is defined as a PDF with mean equal to 0 and standard deviation equal to 1.

$$\phi(z) = \frac{1}{\sqrt{2\pi}} \exp \left[ -\frac{1}{2} (z)^2 \right] \quad (3.3)$$

The CDF of the standard normal variable is usually indicated as  $\Phi(z)$ .

It is possible to calculate normally distributed random variables with Microsoft Excel as follows.

1. Generation of  $i=1$  to  $N$  numbers  $u_i$  by means of the function *RAND()* (or *CASUALE()* for Italian users). N.B. These values are random values between 0 and 1: they represent the Y-axis of the CDF function.
2. Definition of *NORMSINV*( $u_i$ ) for each random value. The X-axis values of the corresponding *standard* normal distribution are obtained. These values are named as  $z_i$ .
3. For the random variable chosen of given mean  $\mu$  and standard deviation  $\sigma$  it is possible to define  $i=1$  to  $N$  random values  $x_i = \mu + z_i \sigma$ .



However, the PDF and CDF functions can be immediately calculated simply with the function NORMINV( $u_i$ ;  $\mu$ ;  $\sigma$ ; TRUE/FALSE) where the true statement gives the CDF (cumulative) function and the false statement gives the PDF function.

### 3.2.1.3 Log-Normal Random Variables

The random variable  $X$  is a lognormal random variable if  $Y=\ln(X)$  is normally distributed. It is important to notice that it can be defined for positive values only ( $x \geq 0$ ). The PDF and CDF can be calculated using the standard normal random variable.

$$F_X(x) = F_Y(y) = \Phi\left(\frac{y - \mu_Y}{\sigma_Y}\right) \quad (3.4)$$

It must be noted that in this case we must use the mean and the standard deviation of the logarithm of the variable.

$$F_X(x) = \Phi\left(\frac{\ln(x) - \mu_{\ln(x)}}{\sigma_{\ln(x)}}\right) \quad (3.5)$$

The logarithmic quantities may be expressed as a function of mean, standard deviation and coefficient of variation, Eq. (3.6).

$$\begin{aligned} \sigma_{\ln(x)}^2 &= \ln(V_X^2 + 1) \\ \mu_{\ln(x)} &= \ln\left(\mu_X - \frac{1}{2}\sigma_{\ln(x)}^2\right) \end{aligned} \quad (3.6)$$

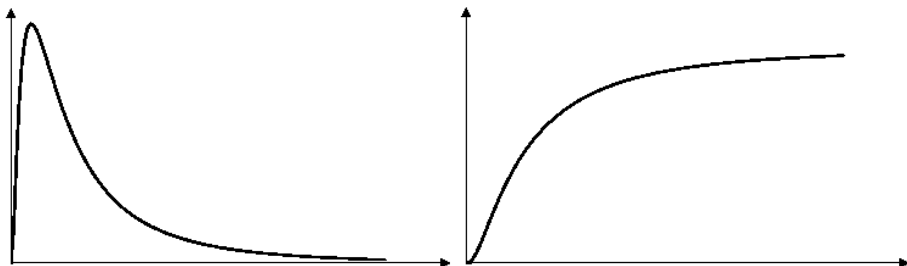


Figure 3.3 - PDF and CDF for a lognormal random variable.

It is possible to calculate lognormally distributed random variables with Microsoft Excel as follows.

1. See 3.2.1.2.
  2. Define LOGINV( $u_i$ ,  $\mu$ ;  $\sigma$ ; TRUE/FALSE).
  3. It is important to notice the following aspects of Microsoft Excel:
    - $\mu$  and  $\sigma$  are the mean and standard deviation of  $\ln(x)$ .
    - These functions give the same value (given  $\mu$   $\sigma$  mean and standard deviation of  $\ln(x)$ ):
- LOGNORMDIST( $x$ ;  $\mu$ ;  $\sigma$ ; TRUE/FALSE)=NORMDIST( $\ln(x)$ ;  $\mu$ ;  $\sigma$ ; TRUE/FALSE)

Microsoft Excel does not automatically calculate mean and standard deviation of the logarithm which must be manually calculated next to the arithmetical values.

### 3.2.2 Correlated Random Variables

It is possible to have two or more random values correlated by means of a *coefficient of correlation*. It indicates the degree of linear dependence between two random variables. If it is close to zero the two variables are not linearly related to each other.

The variance is defined as:

$$\text{Var}(X) = E[(X - \mu)^2] \quad (3.7)$$

Where  $E[ ]$  is the expected values.

$$E(X) = x_1 P(X = x_1) + \dots + x_n P(X = x_n) \quad (3.8)$$

Where  $P(X=x_j)=f(x_j)$  and  $E(X)=\sum x f(x)$ . Given  $X$  a continuous random variable with PDF  $f(x)$  the expected value  $E[ ]$  is equal to:

$$E(X) = \int_{-\infty}^{+\infty} x f(x) dx \quad (3.9)$$

If all the probabilities have the same value the expected value is the mean value. The positive square root of the variance is equal to the standard deviation. Let  $X$  and  $Y$  being two random variables with means  $\mu_x$  and  $\mu_y$  and standard deviations  $\sigma_x$  and  $\sigma_y$ . The covariance of  $X$  and  $Y$  is defined as:

$$\text{CoV}(X, Y) = E[(X - \mu_x)(Y - \mu_y)] = E[XY - X\mu_y - \mu_x Y + \mu_x \mu_y] \quad (3.10)$$

Where  $E[ ]$  is the expected value. It is possible to note that the variance is just a special case of covariance where  $X=Y$ . In case of continuous variables it is:

$$\text{CoV}(X, Y) = \int_{-\infty}^{+\infty} \int_{-\infty}^{+\infty} (x - \mu_X)(y - \mu_Y) f_{XY}(x, y) dx dy \quad (3.11)$$

The covariance matrix then for n-correlated variables  $X_n$  is reported in Eq. (3.15):

$$[C] = \begin{bmatrix} \text{CoV}(X_1, X_1) & \text{CoV}(X_1, X_2) & \dots & \text{CoV}(X_1, X_n) \\ \text{CoV}(X_2, X_1) & \text{CoV}(X_2, X_2) & \dots & \dots \\ \dots & \dots & \dots & \dots \\ \text{CoV}(X_n, X_1) & \text{CoV}(X_n, X_2) & \dots & \text{CoV}(X_n, X_n) \end{bmatrix} \quad (3.12)$$

By the definition, the coefficient of correlation between two random variables  $X$  and  $Y$  is equal to:

$$\rho_{XY} = \frac{\text{CoV}(X, Y)}{\sigma_X \sigma_Y} \quad (3.13)$$

In same case it is more convenient to introduce a correlation matrix as reported in Eq. (3.14):

$$[\rho] = \begin{bmatrix} \rho_{11} & \rho_{12} & \dots & \rho_{1n} \\ \rho_{21} & \rho_{22} & \dots & \dots \\ \dots & \dots & \dots & \dots \\ \rho_{n1} & \rho_{n2} & \dots & \rho_{nn} \end{bmatrix} \quad (3.14)$$

The covariance matrix then becomes:

$$[C] = \begin{bmatrix} \rho_{11} \sigma_{X_1}^2 & \rho_{12} \sigma_{X_1} \sigma_{X_2} & \dots & \rho_{1n} \sigma_{X_1} \sigma_{X_n} \\ \rho_{21} \sigma_{X_2} \sigma_{X_1} & \rho_{22} \sigma_{X_2}^2 & \dots & \dots \\ \dots & \dots & \dots & \dots \\ \rho_{n1} \sigma_{X_n} \sigma_{X_1} & \rho_{n2} \sigma_{X_n} \sigma_{X_2} & \dots & \rho_{nn} \sigma_{X_n}^2 \end{bmatrix} \quad (3.15)$$

Both  $[C]$  and  $[\rho]$  are symmetric. The diagonal terms of  $[\rho]$  are all equal to 1 by definition. Note that if the variables are all uncorrelated (3.15) and (3.14) become:

$$[\rho] = \begin{bmatrix} 1 & 0 & \dots & 0 \\ 0 & 1 & \dots & \dots \\ \dots & \dots & \dots & \dots \\ 0 & 0 & \dots & 1 \end{bmatrix} \quad (3.16)$$

$$[C] = \begin{bmatrix} \sigma_{X_1}^2 & 0 & \dots & 0 \\ 0 & \sigma_{X_2}^2 & \dots & \dots \\ \dots & \dots & \dots & \dots \\ 0 & 0 & \dots & \sigma_{X_n}^2 \end{bmatrix} \quad (3.17)$$

### 3.3 Monte Carlo Simulations

It is possible to generate series of random variables (both correlated and uncorrelated) for the evaluation of the input parameters for structural analyses. The response (evaluated through damage indicators or damage measure DM) then will depend on the variables variation (e.g. materials characteristic values, equivalent stiffness, damping ratio...) and on the accelerograms sets chosen (the so called Intensity Measure IM).

Usually, the input values set are random sets of log-normally distributed numbers. By means of the Monte Carlo method (which is not a unique method but a whole family of resolution techniques) it is possible to solve every kind of structural problems. However it is really useful to solve complex problems for which closed form solutions do not exist or are extremely difficult to be obtained.

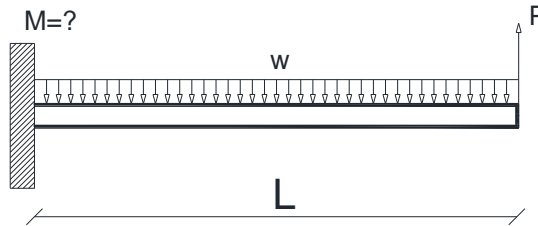
The Monte Carlo method is used also to avoid many simplifying assumption required for deterministic resolution techniques. Of course, the accuracy of the results obtained increases with the number of analyses performed; a robustness analysis is then required in order to evaluate the amount of simulations to be used.

At the core of all Monte Carlo simulation is the generation of random numbers that are uniformly distributed between 0 and 1.

### 3.3.1 Generation of normal random values

As shown in 3.2.1.2 it is easily possible to generate random numbers normally distributed with a particular mean and standard deviation. It is shown how to solve in Excel a simple linear problem by means of the Monte Carlo method.

	P [N]	W [N/m]	M [Nm] @ L
$\mu$	4000	50	23100
$\sigma$	400	5	2402



**Figure 3.4** - The simple problem of a cantilever beam.

Given  $L=6m$  the resulting moment is  $M=6P-18w$ . The mean and standard deviation of  $M$  have then the following exact values (as  $M$  is a linear function of  $P$  and  $w$ ):

$$\begin{aligned} \mu_M &= 6\mu_P - 18\mu_w = 23100 \text{ Nm} \\ \sigma_M &= \sqrt{(6\sigma_P)^2 + (18\sigma_w)^2} = 2402 \text{ Nm} \end{aligned} \tag{3.18}$$

Now we can calculate the resulting moment using a probabilistic approach. The flow chart is the following:

- Two series of random values are generated (e.g. 10 numbers each one).
- 10 values for  $P$  and ten values for  $w$  are generated according to their mean and standard deviation.
- 10 normal random values for  $M$  are calculated according to the linear relation  $M_i=6P_i-18w_i$ .

**Table 3.1** - Calculation of normal standard values for  $P$  and  $w$ .

	A	B	C	D	E	F	G
1	$u_{i,P}$	$u_{i,w}$	$z_{i,P}$	$z_{i,w}$	$P_i$	$W_i$	$M_i$
2	=rand()	=rand()	=NORMSINVT(A2)	=NORMSINV(B2)	$=\mu_P+C2*\sigma_P$	$=\mu_M+D2*\sigma_P$	$=6*E2-18*F2$
3	...	...	...	...	...	...	...
...	...	...	...	...	...	...	...
11	=rand()	=rand()	=NORMSINVT(A10)	=NORMSINV(B11)	$=\mu_P+B11*\sigma_P$	$=\mu_M+D11*\sigma_P$	$=6*E10-18*F11$

It is remarked that the calculation of the normal standard values can be avoided by means of the built-in function of Excel  $\text{NORMINV}(x; \mu; \sigma; \text{TRUE})$ . The resulting spreadsheet is reported in Table 3.2:

**Table 3.2** - Numerical example (10 extractions).

	A	B	C	D	E	F	G
1	$u_{i,p}$	$u_{i,w}$	$z_{i,p}$	$z_{i,w}$	$P_i$	$W_i$	$M_i$
2	0.897	0.962	1.264	1.770	4505.6	58.9	25974.1
3	0.538	0.242	0.096	-0.699	4038.5	46.5	23394.0
4	0.116	0.012	-1.196	-2.245	3521.7	38.8	20432.0
5	0.520	0.125	0.051	-1.149	4020.3	44.3	23325.3
6	0.541	0.920	0.102	1.403	4041.0	57.0	23219.5
7	0.361	0.237	-0.356	-0.717	3857.8	46.4	22311.3
8	0.665	0.498	0.426	-0.004	4170.3	50.0	24122.2
9	0.339	0.811	-0.415	0.880	3833.9	54.4	22024.3
10	0.460	0.108	-0.101	-1.235	3959.7	43.8	22969.5
11	0.478	0.436	-0.054	-0.160	3978.4	49.2	22984.7

	M (exact values)	M (M.C. method)
$\mu_M$	23100	23076
$\sigma_M$	2402	1356

The Monte Carlo method provides then a certain estimation of mean and standard deviation (which are mean and standard deviation of column G, Table 3.2). It is interesting to notice the variation of the results for a higher number of extractions. This time 30 instead of 10 numbers extraction.

**Table 3.3** - Numerical example (30 extractions).

	A	B	C	D	E	F	G
1	ui,P	ui,w	zi,P	zi,w	Pi	Wi	Mi
2	0.127	0.737	-1.142	0.634	3543.2	53.2	20302.4
3	0.059	0.444	-1.564	-0.141	3374.2	49.3	19358.2
4	0.358	0.654	-0.364	0.395	3854.4	52.0	22190.8
5	0.569	0.085	0.173	-1.373	4069.2	43.1	23638.7
6	0.640	0.849	0.359	1.033	4143.7	55.2	23869.3
7	0.354	0.898	-0.375	1.272	3850.1	56.4	22086.4
8	0.054	0.495	-1.607	-0.011	3357.4	49.9	19245.3
9	0.311	0.922	-0.492	1.421	3803.2	57.1	21791.2
10	0.024	0.144	-1.982	-1.063	3207.2	44.7	18438.8
11	0.460	0.317	-0.100	-0.477	3960.1	47.6	22903.5
12	0.907	0.165	1.323	-0.974	4529.3	45.1	26363.3
13	0.996	0.860	2.632	1.078	5052.9	55.4	29320.4
14	0.306	0.632	-0.506	0.337	3797.5	51.7	21854.4
15	0.415	0.423	-0.215	-0.194	3913.8	49.0	22600.4
16	0.980	0.265	2.051	-0.629	4820.3	46.9	28078.2
17	0.268	0.127	-0.618	-1.143	3752.9	44.3	21719.9
18	0.683	0.213	0.476	-0.796	4190.4	46.0	24314.2
19	0.945	0.626	1.596	0.321	4638.2	51.6	26900.3
20	0.025	0.543	-1.965	0.107	3214.2	50.5	18375.3
21	0.691	0.817	0.497	0.903	4198.9	54.5	24212.4
22	0.387	0.796	-0.288	0.828	3884.8	54.1	22334.3
23	0.516	0.473	0.040	-0.068	4016.2	49.7	23203.2
24	0.918	0.199	1.390	-0.844	4555.8	45.8	26510.9
25	0.539	0.202	0.098	-0.834	4039.0	45.8	23409.2
26	0.291	0.452	-0.551	-0.120	3779.6	49.4	21788.4
27	0.696	0.420	0.512	-0.202	4204.7	49.0	24346.5
28	0.413	0.330	-0.219	-0.441	3912.6	47.8	22615.1
29	0.750	0.115	0.675	-1.202	4270.2	44.0	24829.2
30	0.286	0.760	-0.566	0.706	3773.7	53.5	21678.5
31	0.604	0.765	0.265	0.724	4105.8	53.6	23669.9

	M (exact values)	M (M.C. method)
$\mu_M$	23100	23065
$\sigma_M$	2402	2591

It can be noticed that the estimation of the mean values does not change, however the estimation of the standard deviation is much better for the second case.

### 3.3.2 Generation of normal correlated random values

It is possible to generate correlated normal random values as follows:

- Calculation of the covariance matrix [C] according to the coefficient of correlation and standard deviation of each series.
- Generation of the eigenvectors matrix [T] and eigenvalues diagonal matrix [D] (for example in Matlab: [T,D]=eig(C), but also open source program like FreeMat or Maxima can be used to perform the same calculation). [D] is the covariance matrix of the corresponding uncorrelated series and so the square roots of its diagonal elements are the standard deviations  $\sigma_y$  of each uncorrelated series.
- Being  $\{\mu_x\}$  the vector containing the mean values of the correlated given series, the corresponding uncorrelated mean vector is given by  $\{\mu_y\}=[T]^t\{\mu_x\}$ .
- Generation of  $u_i$  series of uniformly distributed random values.
- Generation of uncorrelated series of normal values (as already described) with the calculated values of  $\mu_y$  and  $\sigma_y$ .
- If [Y] is the matrix containing the uncorrelated random vectors  $\{Y_i\}$ , the corresponding correlated matrix is given by  $[X]=[Y] [T]^t$ .

#### Example

Generate two normal random correlated values given mean, standard deviation and coefficient of correlation.

	X1	X2
$\mu$	10	15
$\nu$	0.1	0.2
$\sigma$	1	3
$\rho$	0.5	



$$[C] = \begin{bmatrix} 1 & 1.5 \\ 1.5 & 9 \end{bmatrix} \quad (3.19)$$

By solving the eigenvector problem we calculate the transformation matrix:

$$[T] = \begin{bmatrix} 0.984 & 0.178 \\ -0.178 & 0.984 \end{bmatrix} \quad (3.20)$$

$$[D] = \begin{bmatrix} \sigma_{Y1}^2 = 0.728 & 0 \\ 0 & \sigma_{Y2}^2 = 9.27 \end{bmatrix}$$

$$[T] = \begin{bmatrix} 0.984 & 0.178 \\ -0.178 & 0.984 \end{bmatrix} \quad (3.21)$$

$$\{\mu_x\} = \begin{Bmatrix} 10 \\ 15 \end{Bmatrix} \quad (3.22)$$

$$\{\mu_y\} = [T]^t \begin{Bmatrix} 10 \\ 15 \end{Bmatrix} = \begin{Bmatrix} 7.17 \\ 16.54 \end{Bmatrix} \quad (3.23)$$

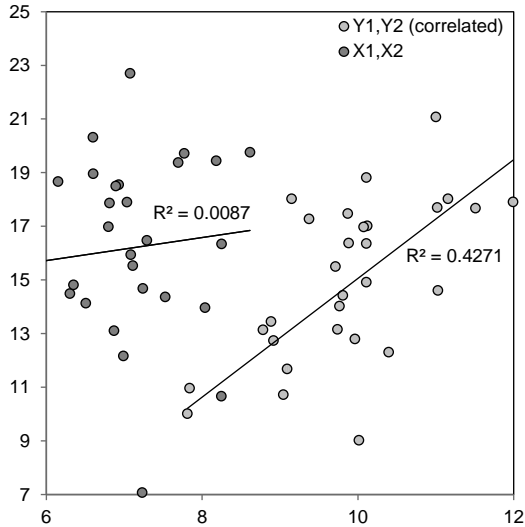
It is now possible to generate two uncorrelated normal series Y1 and Y2 with the following means and standard deviations.

	Y1	Y2
$\mu$	7.17	16.54
V	0.12	0.18
$\sigma$	0.85	3.04

The resultant values are reported in Table 3.4:

**Table 3.4-** Generated of random normal correlated values X1 and X2.

<b>u1</b>	<b>Y1</b>	<b>u2</b>	<b>Y2</b>	<b>X1</b>	<b>X2</b>
0.19	6.43	0.41	15.88	9.16	14.48
0.25	6.60	0.82	19.37	9.94	17.88
0.95	8.55	0.09	12.52	10.64	10.80
0.12	6.16	0.26	14.63	8.67	13.30
0.56	7.29	0.37	15.56	9.95	14.02
0.01	5.31	0.37	15.56	8.00	14.36
0.85	8.04	0.96	21.90	11.81	20.12
0.05	5.80	0.92	20.74	9.40	19.38
0.88	8.17	0.37	15.54	10.81	13.83
0.58	7.35	0.67	17.91	10.42	16.32
0.82	7.94	0.61	17.39	10.91	15.70
0.42	7.00	0.81	19.18	10.30	17.62
0.40	6.95	0.07	11.98	8.97	10.55
0.46	7.09	0.91	20.60	10.64	19.01
0.36	6.87	0.50	16.57	9.70	15.08
0.39	6.93	0.06	11.69	8.90	10.27
0.30	6.73	0.55	16.94	9.64	15.47
0.97	8.78	0.84	19.61	12.13	17.73
0.50	7.17	0.56	17.00	10.08	15.45
0.25	6.59	0.55	16.92	9.50	15.48
0.96	8.70	0.20	13.93	11.04	12.16
0.38	6.90	0.24	14.41	9.35	12.95
0.82	7.96	0.35	15.34	10.56	13.68
0.84	8.00	0.05	11.55	9.93	9.95
0.63	7.46	0.31	15.07	10.03	13.50
0.34	6.82	0.72	18.36	9.98	16.85
0.77	7.80	0.14	13.25	10.03	11.65
0.20	6.45	0.12	12.92	8.65	11.56
0.58	7.35	0.39	15.73	10.03	14.17
0.83	7.97	0.11	12.87	10.14	11.25



**Figure 3.5** - Uncorrelated and correlated generated random normal series (and corresponding linear regression).

### 3.3.3 Generation of log-normal random values

It is shown how to generate uncorrelated *i*-series (each series of *N*-values) of concrete tension strength  $f_{ct}$ , to be used for example in a time history analysis of a three story building.

**Table 3.5** - Statistical parameters for  $f_{ct}$ .

Parameter	Value	Log Parameter	Value
$\mu$	3 MPa	$\mu \ln X$	1.08
$V$	33%		
$\sigma$	1 MPa	$\sigma \ln X$	0.1897

**Table 3.6** - Log-normal random variables obtained by means of the Excel built-in function.

	A	B
1	ui	$f_{ct,i}$
2	rand()	=LOGINV(A2; $\mu \ln X$ ; $\sigma \ln X$ )
3	...	...
...	...	...
N	rand()	=LOGINV(AN; $\mu \ln X$ ; $\sigma \ln X$ )

It is important to note that the same values can be obtained as follows by using the standard normal distribution and the relationship between normal and lognormal variables:

**Table 3.7** - . Log-normal random variables obtained by means of the normal/lognormal relationship.

	A	B	C
1	ui	zi	fct,i
2	=rand()	=NORMSINV(A1)	=exp( $\mu \ln X + B2 * \sigma \ln X$ )
3	...	...	...
...	...	...	...
N	=rand()	=NORMSINV(A50)	=exp( $\mu \ln X + BN * \sigma \ln X$ )

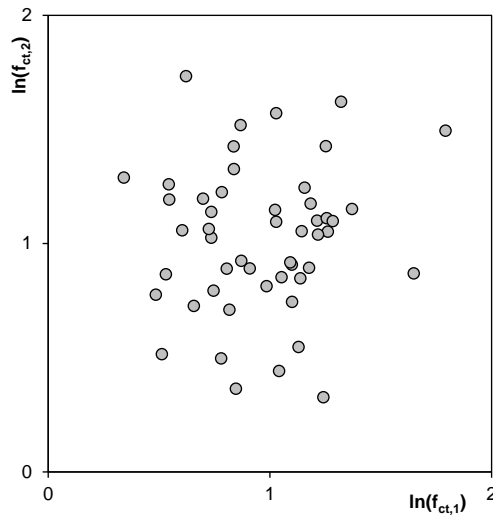
Values obtained in column B, Table 3.6, and in column C, Table 3.7, must be the same.

Instead of using the standard normal distribution it can be immediately used the normal distribution for given mean and standard deviation.

**Table 3.8** - Log-normal random variables obtained by means of the normal built-in inverse function of Excel.

	A	B
1	ui	fct,i
2	=rand()	=exp(NORMINV(A2; $\mu \ln X$ ; $\sigma \ln X$ ))
3	...	...
...	...	...
N	=rand()	=exp(NORMINV(AN; $\mu \ln X$ ; $\sigma \ln X$ ))

It is remarked that methods shown in Table 3.6, Table 3.7 and Table 3.8 give the same results. In Figure 3.6 are reported on the x-axis the 50 values of a random series  $f_{ct,1}$  and on the y-axis the 50 values of the random series  $f_{ct,2}$ . It can be noticed that the two series are uncorrelated and that values are reported in the bi-logarithmic axes.



**Figure 3.6** - Example of two uncorrelated log-normal distribution series.

It is remarked that this procedure is only valid for normal distribution, for other random variables it is just an *approximation*.

### 3.3.4 Generation of log-normal correlated random values

It is possible to imagine that some structural characteristics may be lognormally distributed uncertain quantities with a certain correlation  $\rho$ . The technique for the generation of log-normally correlated random values can be the same of section 3.3.2, however this constitute an approximation. Matlab<sup>®</sup> is provided with built in functions for the multivariate analysis.

## 3.4 Generation of fragility functions

It is finally possible to evaluate the response of the structure through the evaluation of EDP (engineering demand parameters) after the time history analyses has been performed. In the end a damage measure DM is provided.

The following algorithm may be adopted:

- The Monte Carlo simulation provide the data to be used in the generation of the fragility function
- First, the cloud table is created. The entries are: on the x-axis the intensity measure IM used in the simulation (e.g. PGA of the seismic

input), on the y-axis the corresponding EDP values (e.g. interstorey drift or eigenfrequency drop).

- A linear regression is performed on the data. Keep attention that the linear regression must be performed on the lognormal values of the data if the hypothesis of the problem is that data are log-normally distributed.
- The linear regression may be performed on the whole set of data or on the single set of damage measure. For example, the different simulation may fall in the range of a particular damage state (usually light, controlled, extended and collapse). A linear regression then may be performed on each interval cloud data.

Considering different possible damage states of buildings there could be a number of fragility functions for a given typology which can be used to estimate the damage level. Generally, for a given limit state a fragility function is derived considering a standard normal cumulative distribution function of the logarithmic difference of the seismic intensity and threshold capacity of limit states with certain level of standard deviation:

$$P[D \geq d_{LS}/SD = sd_{ls}] = \Phi \left[ \frac{1}{\beta} \ln \left( \frac{SD}{sd_{ls}} \right) \right] \quad (3.24)$$

At this point it is possible to notice that as the (logarithmic) linear regression is performed, each function can be described with only two parameters: the limit state capacity of the system  $sd_{ls}$  (usually the median value capacity indicated as  $A_m$ ) and  $\beta$  natural logarithmic standard deviation. Let's illustrate all the procedure with a step by step example.

The output values of a time history analysis are summed up. It is based on a small Monte Carlo simulation (N=22 analyses performed), Table 3.9.

**Table 3.9** - Output data (interstorey drift  $\Delta x$ ) and intensity measure (PGA) of an example simulation.

N	$\Delta x$ [mm]	PGA [g]
1	3.84	0.29
2	0.91	0.17
3	1.03	0.15
4	0.72	0.13
5	10.96	0.37
6	1.31	0.19
7	2.47	0.28
8	0.88	0.15
9	4.17	0.26
10	11.65	0.33
11	5.84	0.33
12	4.66	0.26
13	8.20	0.40
14	7.69	0.26
15	10.13	0.48
16	5.26	0.36
17	5.26	0.15
18	9.78	0.33
19	1.38	0.38
20	0.48	0.07
21	0.49	0.08
22	3.97	0.16

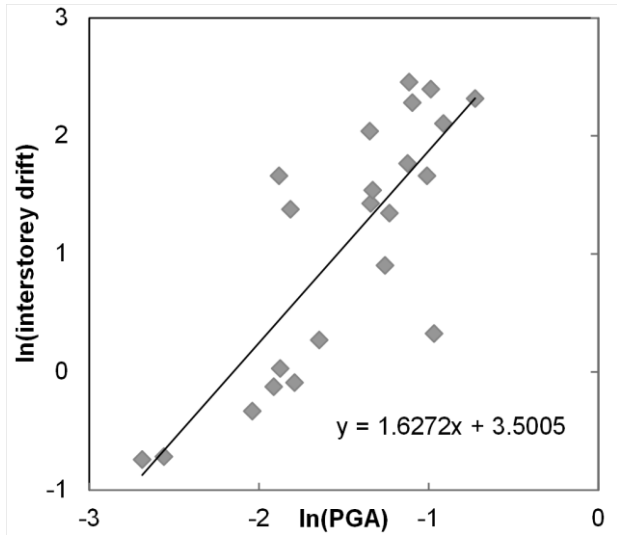


Figure 3.7 - Data cloud in the bi-logarithmic axes from Table 3.9 and linear regression.

In Figure 3.7 it is also reported the linear regression of the data cloud. The linear regression can be performed also by means of the built in Excel function LINEST (in Italian REGR.LIN). The parameters  $a$  and  $b$  are then known. The linear interpolation can be described by means of the general formulation  $\ln(Y)=a + b \ln(\Theta)$ , where  $Y$  is the generic EDP (in the example maximum interstorey in x-direction of the structure) while  $\Theta$  is the intensity measure (PGA). As already mentioned, it is necessary to evaluate the fragility function parameters  $A_m$  (median capacity) and  $\beta$  standard deviation:

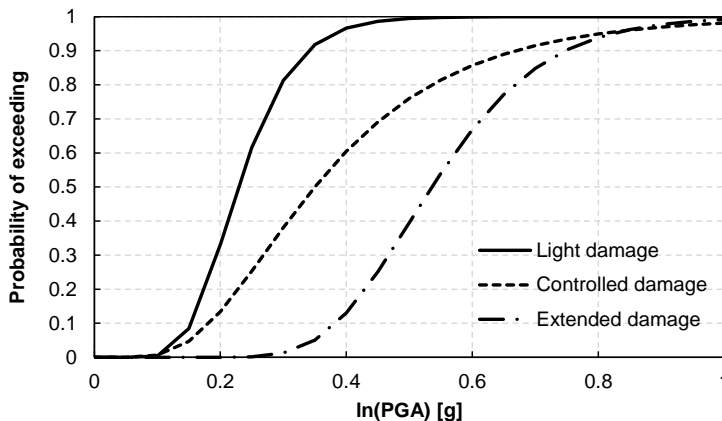
$$\ln(A_m) = \frac{\ln(s) - a}{b} \quad (3.25)$$

$$\beta^2 = \frac{1}{N} \sum_{i=1}^N (\ln(Y_i) - \mu_i)^2 \quad (3.26)$$

$$\mu_i = a + b \ln(\Theta_i) \quad (3.27)$$

Where  $s$  is the critical threshold of the damage measure (e.g.  $H \setminus 100$  where  $H$  is the interstorey height may be the extended damage level for the interstorey drift). It can be noticed that  $A_m$  represents the approximated demand value (in the example, the PGA) corresponding to the given  $s$  value on the fitting linear curve. The standard deviation estimates the difference between real values ( $Y_i$ ) and the approximated values ( $\mu_i$ ).

Once evaluated median capacity and log-standard deviation the fragility function can be plotted by means of the Excel function  $\text{NORMDIST}(x; A_m; \beta; \text{TRUE})$ , where  $x$  series is arbitrary defined by the operator. Please note that it is generated a function for each damage state (as it is possible to define three  $A_m$  values if the regression is operated on the whole population and also three different  $\beta$  is the regression is operated for each interval of damage).



**Figure 3.8** - Fragility functions for interstorey drift demand parameter.







# **Chapter IV.**

## **Accelerograms and Spectra Applications**

## 4 Accelerograms and Spectra Applications

In this chapter some aspects related to dynamic problems faced during simulation are analyzed. In particular, the use of energy spectra is further discussed. Moreover, it is discussed the use of accelerograms in time history analysis and some practical information are provided on the use of Fourier amplitude spectrum. Examples of calculations by means of commonly available software are also provided (Excel© spreadsheets, Seismosignal©). Part of the chapter was developed during a traineeship period at the European Laboratory for Structural Assessment, Joint Research Centre, Ispra (VA), Italy.

### 4.1 Spectra calculation: the energy approach and its applications

One of the greatest uncertainties in earthquake engineering is the earthquake load itself. It is then of strong relevance to select and investigate appropriate accelerograms when dynamic analyses are involved. This assumption is very important both for experimental applications (dynamic and pseudo-dynamic structural tests) and numerical simulations. In order to provide a correct prediction of the structural response and therefore of the structural damage, it is first necessary to define and characterize the input signal. Since the structural response is due not only to the maximum response (e.g. lateral displacement) but also to cumulative cyclic damage, it would be useful to characterize the input from an energetic point of view. In fact, the seismic performance may be evaluated in terms of local and global maximum deformations, however an energy based approach may be a useful tool as it is able to take into account the balance between absorption and dissipation of energy. In fact, it is interesting to notice that the structural failure can be seen as the inability of the structure to dissipate the input energy through hysteretic phenomena (or other dissipative mechanisms) and not only as in terms of maximum ductility or global displacement. It is then clear the importance of a proper characterization of the seismic input.

It is general accepted in modern displacement based design that damage is measured in terms of maximum displacements or maximum ductility. On the

other hand, failure can occur when the total demand to dissipate energy is higher than the energy dissipation capacity of the structure. However, it is not trivial to evaluate at which ratio damage is related to maximum response or to energy dissipation. Since the mid-50s, (Housner, 1956), it is recognized the need to provide adequate energy dissipation capacity to structural components. The fundamental premise behind energy-based approaches is that the energy dissipation capacity can be calculated based on the predicted energy demand from the seismic input.

It is now clear then that these concepts are particularly relevant for the definition of the characteristics of the accelerograms that are used in time history analyses. One of the main parameters considered is usually the peak ground acceleration. It was demonstrated that damage may be due also to inelastic excursions below the maximum response and so to energy dissipated through hysteretic cyclic behaviour. As the maximum ground acceleration may not be the best parameter to indicate damage potential of an earthquake, other parameters should be used like energy based measures. The energy parameters of the accelerogram are then relevant and they should be taken into account. Moreover, it is interesting to notice that energy based parameters are related to cyclic response of the structure and they can implicitly capture the effect of ground motion duration. The seismic input energy, paragraph 4.1.1, is also generally considered a stable parameter of the structural response.

Nowadays the so-called energy methods based on the definition of relative and absolute input energy are of growing interest, especially for design and retrofitting purposes. Though, it is remarked that the damage is caused not only by maximum response but also for accumulation of plastic deformation. It is well known that failure criteria in earthquake resistant structures should take into account energy dissipation as well as maximum ductility. Energy based approaches may be a useful and valuable tool for taking into account in a rational way the effects of low cycle fatigue and cyclic damageability. The damage resulting from recent earthquakes proved that the safety of the structure is affected also by the amount of dissipated energy and not only by the maximum ductility capacity. In order to investigate the use of accelerogram and corresponding energy spectra, an application for the design of a dissipation system will be described in paragraph 4.1.2.1. Actually, passive controls devices are of strong importance for many structural applications, such as base

isolation, dissipation and damping control. It might be of interest the investigation of rational approaches for the definition of an analytical procedure able to optimize the structural performances in terms of force and displacements by means of an energy methods. It is also pointed out that energy based methods are of growing interest for researchers in terms of design application, development of spectra, evaluation of structural response (Akbas et al., 2001, Benavent-Climent et al., 2002, Decanini and Mollaioli, 2001., Manfredi, 2001, Ordaz et al. 2003).

To sum up, the evaluation of the seismic input, resultant effects on the structural response and consequent damage could be carried out by means of an energy approach. An application is also presented in order to investigate this particular technique and also to provide further information on the definition of useful seismic intensity measures and demand parameters.

#### 4.1.1 SDOF dynamic equation for Energy quantities

The well-known dynamic equation for a generic SDOF system can be written as Eq. (4.1):

$$m\ddot{u} + c\dot{u} + f_s = -m\ddot{u}_g \quad (4.1)$$

Where  $m$  is the SDOF mass,  $c$  is the damping coefficient,  $f_s$  is the restoring force and  $u$  is the relative displacement of the oscillator. Subscript  $g$  refers to ground quantities, subscript  $t$  to total quantities and if nothing is specified it is a relative quantity. By integration of each equation term with respect to total displacements it is possible to obtain the energy formulation of the dynamic equation.

$$\int m\ddot{u}_t du + \int c\dot{u}du + \int f_s du = 0 \quad (4.2)$$

According to the integrator chosen for the mass proportional term, two formulations are available.

##### 1. Absolute formulation

The mass term integrator can be written as  $du=du_t-du_g$ , this leads to the energy formulation reported in Eq. (4.4):

$$\frac{m(\dot{u}_t)^2}{2} + \int c \dot{u} du + \int f_s du = \int m \ddot{u}_t du_g = m \int \ddot{u}_t \dot{u}_g dt \quad (4.3)$$

$$E_k + E_c + E_a = E_i \quad (4.4)$$

Where:

$E_k$  = absolute kinetic energy

$E_c$  = damped energy

$E_a$  = adsorbed energy (which is the sum of an elastic and an hysteretic contribution)

$E_i$  = absolute input energy

The absolute formulation is physically meaningful as it represents the work done by the total base shear at the foundation times the ground displacement itself.

## 2. Relative formulation

The mass term integrator can be written as integrating on  $du$  the relative formulation of the equation of motion, this leads to the energy formulation reported in Eq. (4.5) and Eq. (4.6):

$$\frac{m(\dot{u})^2}{2} + \int c \dot{u} du + \int f_s du = - \int m \ddot{u}_g du = -m \int \ddot{u}_g \dot{u} dt \quad (4.5)$$

$$E_k' + E_c + E_a = E_i' \quad (4.6)$$

Where:

$E_k'$  = relative kinetic energy

$E_c$  = damped energy

$E_a$  = adsorbed energy (which is the sum of an elastic and an hysteretic contribution)

$E_i'$  = relative input energy

The relative formulation describes the input energy as the work done by the static equivalent force (mass times ground acceleration) through the relative displacement. The difference between absolute and relative energy is then equal to the difference between absolute and relative kinetic energy. Therefore the difference between the two formulations can be expressed as:

$$E_i - E_i' = \frac{1}{2} m (\dot{u}_g^2 + 2\dot{u}_g \dot{u}) \quad (4.7)$$

For a very long period structure  $T \rightarrow \infty$  it will be  $u \approx -u_g$  and then  $u_t = u_g + u \approx 0$ . This leads to the fact that absolute input energy is equal to zero while the relative energy is equal to  $E_i' = 0.5m\dot{u}_g^2$ . On the other hand, if  $T \rightarrow 0$  then  $u_t \approx u_g$  and so  $u \approx 0$ . For a very stiff structure the relative energy is then equal to zero while the absolute energy converges to the value of  $E_i' = 0.5m\dot{u}_g^2$ . Some authors, e.g. (Akiyama, 1999), demonstrated that relative energy formulation is more significant in seismic design. However for the purpose of the current example this difference is not of strong relevance.

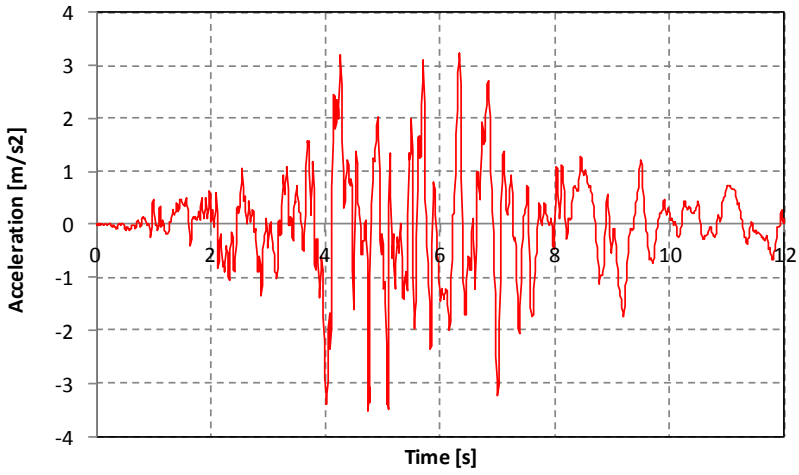
#### 4.1.1.1 Input energy: elastic SDOF

As already stated, the adsorbed Energy is basically given by the sum of two main contributions. The first one is the elastic strain energy. For an elastic SDOF the only contribution available is obviously given by:

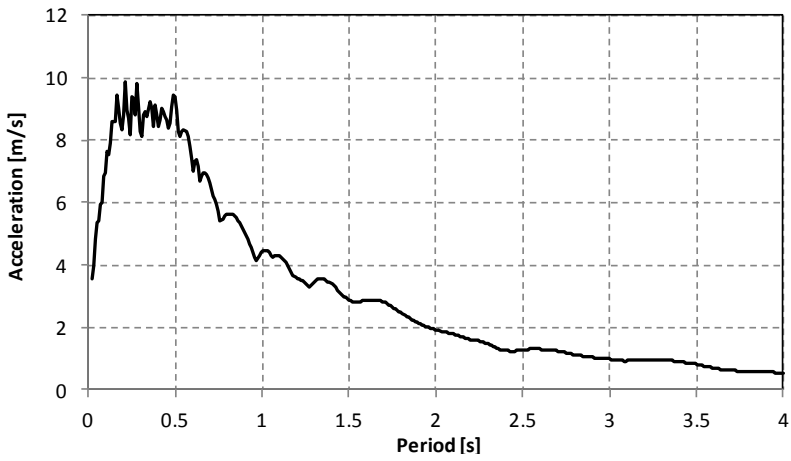
$$E_a = \int f_s du = \int kudu = \frac{1}{2} ku^2 \quad (4.8)$$

It can be noticed that for an elastic SDOF great part of the input energy is dissipated through the damped energy. In Figure 4.3 it is reported the time history for a SDOF elastic oscillator of frequency equal to 1Hz and damping ratio equal to 5%, absolute formulation and mass equal to 1kg. The sum of the three contributions is equal to the absolute input energy, Figure 4.4. For an elastic system the input energy is mainly dissipated through the structural damping. The accelerogram used is 0.36g and is a spectrum compatible input with duration equal to 12s, Figure 4.1. The SDOF response is calculated with the exact method implemented in a VBA subroutine.





**Figure 4.1** – Spectrum compatible accelerogram used for the time history SDOF analyses.



**Figure 4.2** - Spectral acceleration.

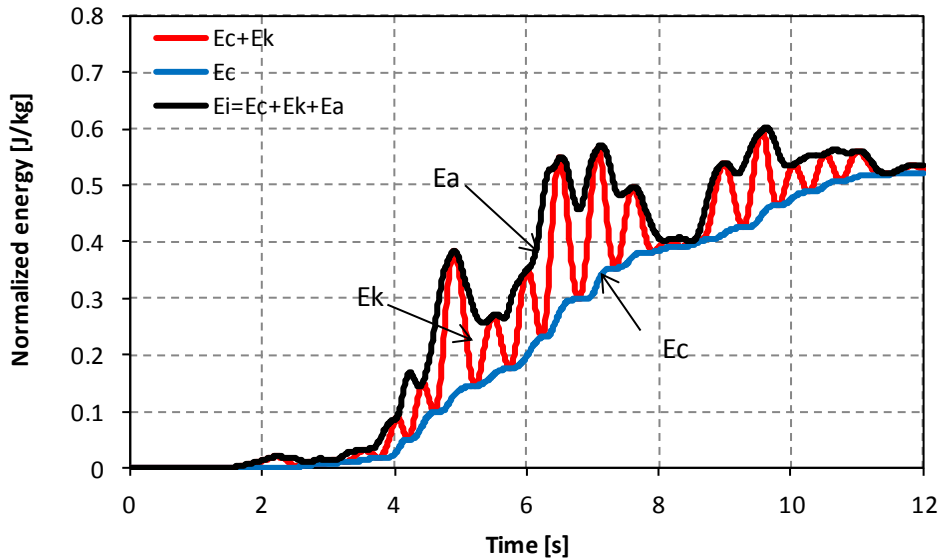


Figure 4.3 - Time history for a 1Hz SDOF subjected to a 0.36g 12s seismic input.

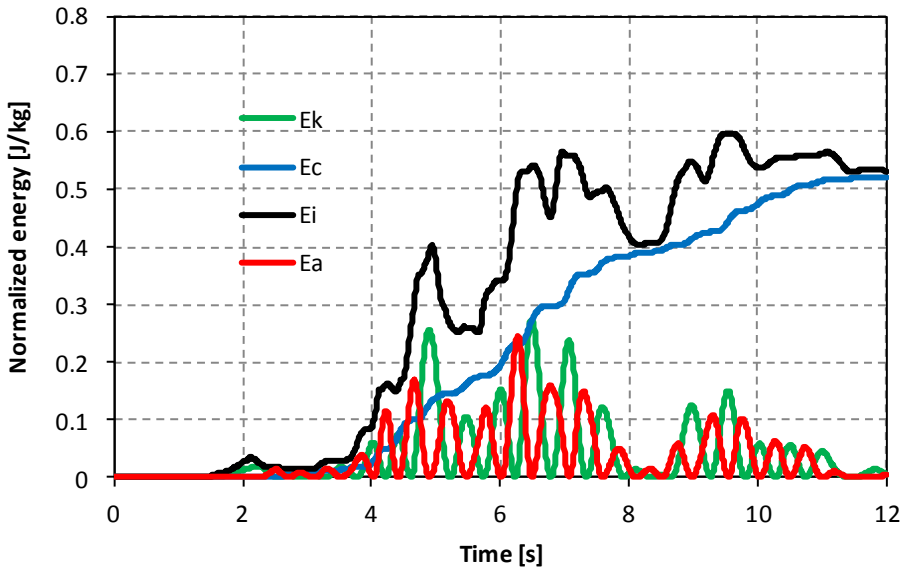


Figure 4.4 - Time history of each energy term.

In Figure 4.5 the relative quantities are compared to the absolute ones. It can be noticed that the final value is approximately the same for both the formulations while there are some differences around local peaks.

The difference between the two formulations is very small. However it may be of interest to observe the time history results for a SDOF in case of a long period structure and of a short period structure.

If it is considered an- elastic SDOF,  $T = 2$  s the time histories reported in Figure 4.6 and Figure 4.7 can be obtained.

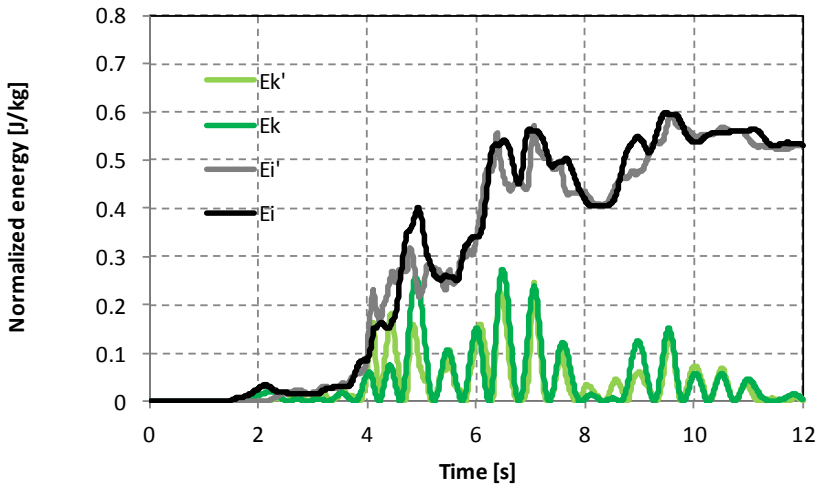


Figure 4.5 - Absolute and relative quantities comparison.

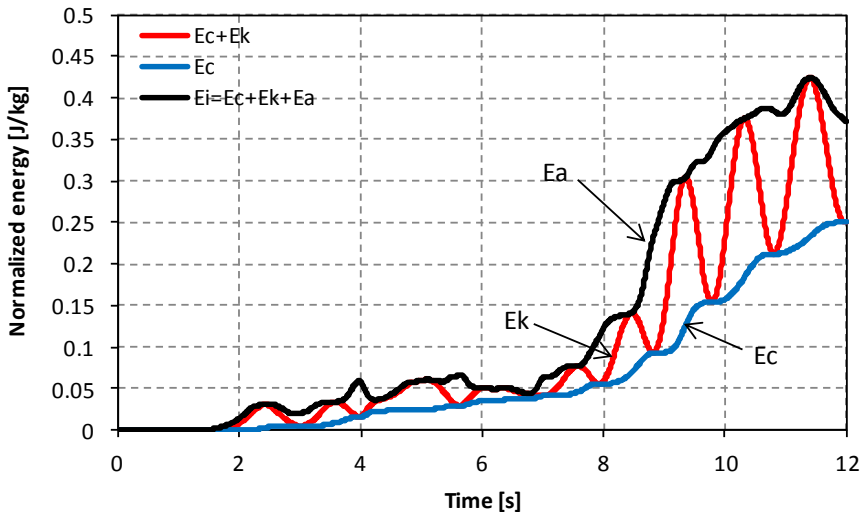
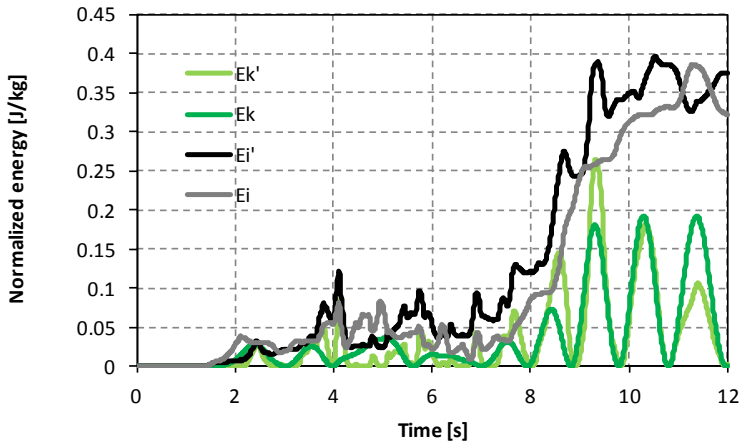


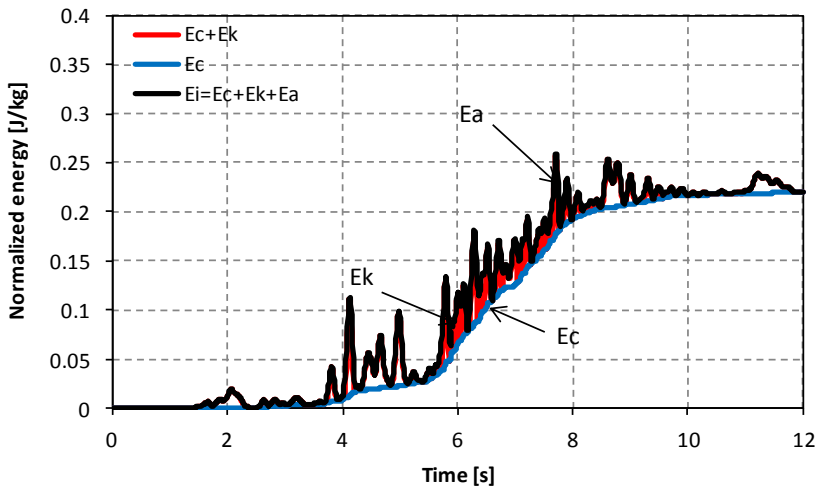
Figure 4.6 - Time history results for an elastic SDOF, damping 5%,  $T=2$ s, absolute formulation.



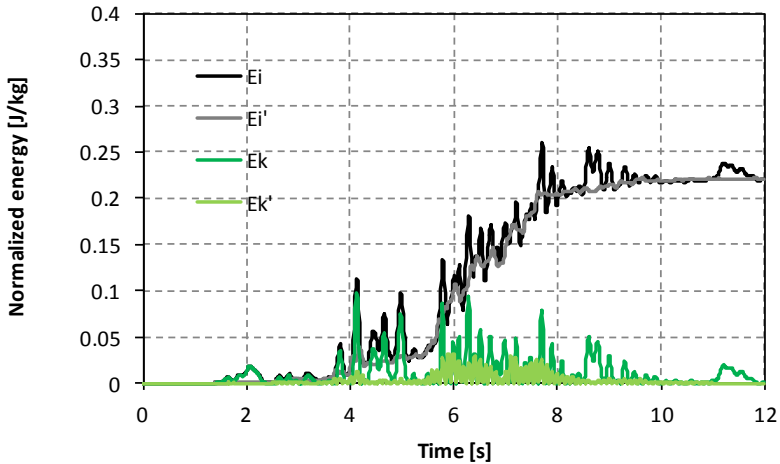
**Figure 4.7** - Time history results for an elastic SDOF, damping 5%,  $T=2s$ , absolute vs. relative quantities.

For a longer period structure (in this case 2s) the energy dissipated by damping is much less than in the previous case, especially near the end of the motion. However, even with some significant differences at some peaks, the final energy values are similar both for  $E_i$  and  $E_i'$ . The amount of input energy is less when compared to the case of the 1Hz oscillator.

On the other hand, if it is considered an- elastic SDOF,  $T = 0.2 s$  the following time histories can be obtained.

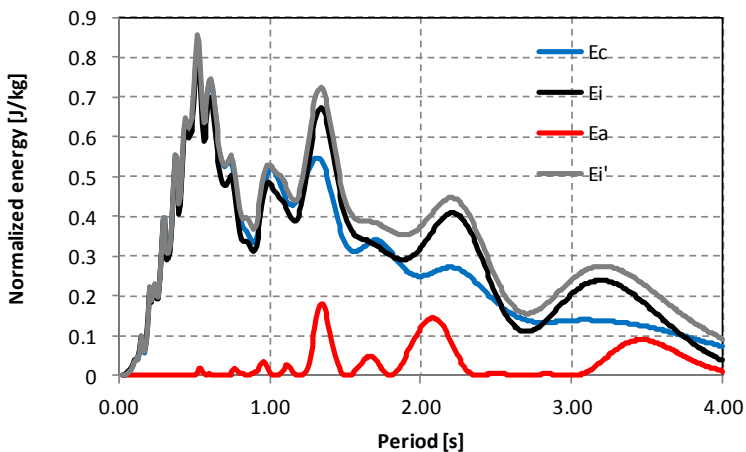


**Figure 4.8** - Time history results for an elastic SDOF, damping 5%,  $T=0.2s$ , absolute formulation.



**Figure 4.9** - Time history results for an elastic SDOF, damping 5%,  $T=0.2s$ , absolute vs. relative quantities.

Again, the input energy is slightly less than the case for the 1Hz oscillator. The differences between the two formulations are stronger in the transient region; however, final values are similar. It can be noticed that almost all of the energy is dissipated through damping. It has been demonstrated from the energetic point of view that structures cannot absorb (and then dissipate) a large amount of energy through elastic deformation. However, it is possible to evaluate spectra for the energy terms. The quantities considered are in this case the final values for each SDOF time history.



**Figure 4.10** - Energy spectra quantities in case of linear behaviour.

The final values of each time history analysis (the higher value for each time history could be different from the last one, however the latter is chosen as representative value of earthquake energy) are reported in Figure 4.10. Some differences between the two formulations arise in the field of high periods. For the elastic case, it is clear that all the input energy is dissipated through damping and, for longer period structures, also through some strain and kinetic energy. It is also clear the importance of energy for the design of long period structures (e.g. with base isolation) provided with additional dampers or viscous-dampers. As these kinds of structure are designed to show an elastic behaviour in structural members, it must be ensured that the input energy is dissipated through damping systems.

#### 4.1.1.2 Input energy: non linear SDOF

It is well known that the response of structures subjected to a strong motion input is usually characterized by non linear behaviour. In this case, some energy may be dissipated through hysteresis behaviour of structural members (typically columns and walls) or of friction devices adequately designed.

In this case if the structure gets into the plastic field the total absorbed energy is given by the contribution of elastic and a plastic part.

The same examples analyzed for the elastic case are reported in the following. It is important to notice that the structural behaviour in this case is described by the elastic stiffness and the yielding force (post yielding stiffness is supposed to zero). In the calculation the yielding force is set equal to the peak acceleration times the mass of the oscillator (which is equal to 1kg). The SDOF response is calculated with the Newmark-beta method in a VBA subroutine based on the work of (Negro, 1997).

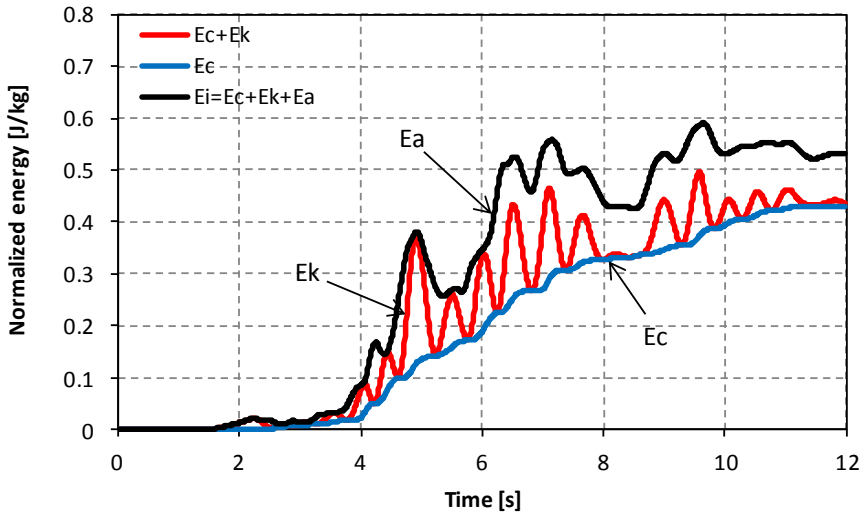


Figure 4.11 - Time history for a 1Hz non linear SDOF.

In this case some input energy was dissipated through the hysteretic contribution of the non linear oscillator. In fact, once the structure reaches the yielding point, it is possible to observe a plastic residual drift in the energy time history.

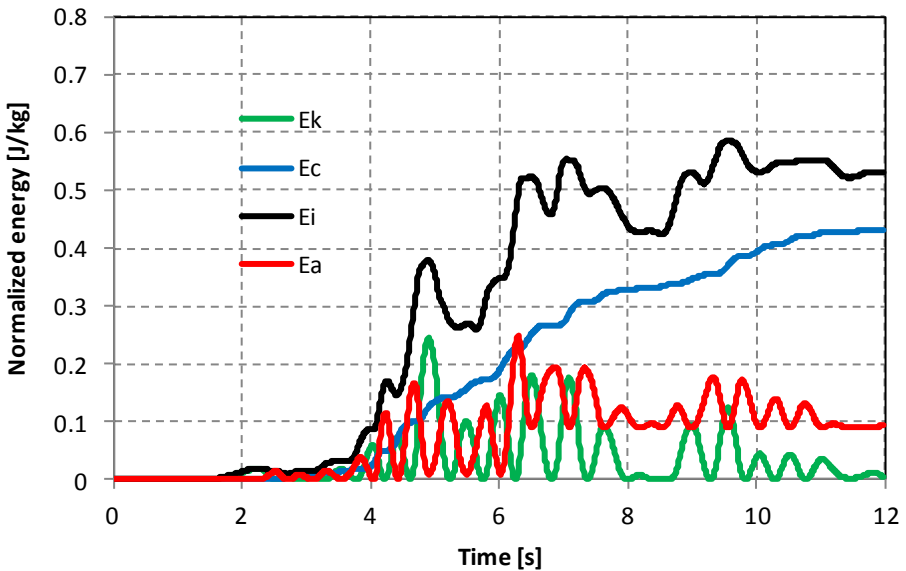
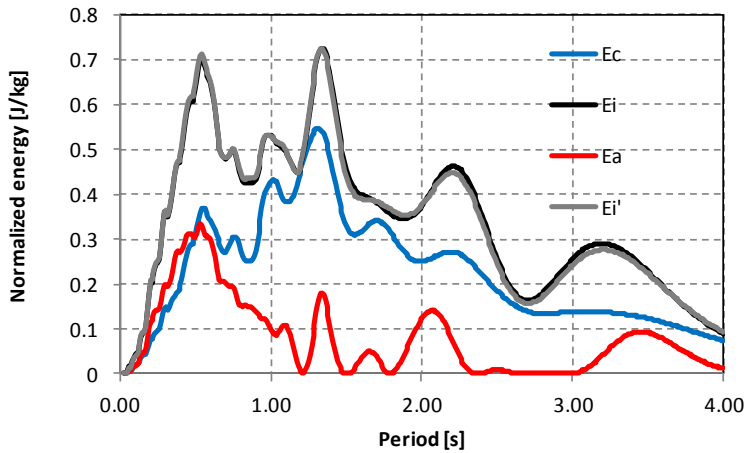
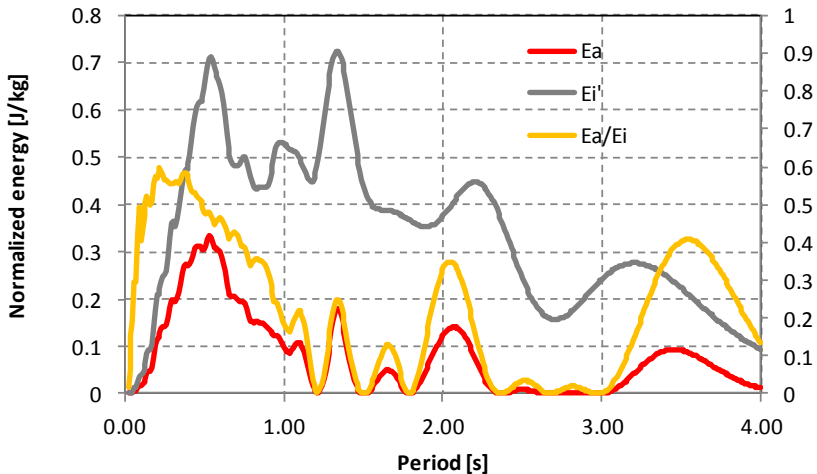


Figure 4.12 - Time history absolute results for an elastic plastic SDOF, damping 5%,  $T=1s$ .



**Figure 4.13** - Energy spectra quantities in case of non linear behaviour and damping 5%.

As stated by some authors, the energy quantities can be good and stable estimators of the structural performance. In particular, it would be interesting to evaluate if it possible to maximize the absorbed energy vs. input energy ratio. In fact, this would be very interesting in order to evaluate and to predict structural damage and moreover for the retrofiting of structures by means of dissipative devices. In Figure 4.13 it can be noticed that in the region of low periods ( $<1s$ ) it is possible to evaluate a region where the  $E_a/E_i$  rises to a top value (approximately 60%) at around  $T=0.4s$ .



**Figure 4.14** - Absorbed and input energy (left axis) and  $E_a/E_i$  ratio (right axis) for an elastic - plastic oscillator.



The energy approach will be used in paragraph 4.1.2.1 for the development of an analytical method for precast single storey industrial buildings analysis and retrofitting.

#### 4.1.1.3 Input energy: Fourier amplitude Spectra calculation

As suggested in (Ordaz et al., 2003) the relative energy input linear spectra can be calculated from the Fourier amplitude spectrum. This may lead, in general, to a fastest calculation time. However, the whole procedure may provide further information on the energy content of the seismic signal. The relative input integral can be solved in the frequency domain using the following equations.

$$\frac{E_i'}{m} = - \int_{-\infty}^{+\infty} \ddot{u}_g du = - \int_{-\infty}^{+\infty} \ddot{u}_g \dot{u} dt \quad (4.9)$$

$$\dot{U}(v) = A(v)H_V(v, \Omega, \xi) \quad (4.10)$$

where the Fourier transform of the velocity is expressed as a function of  $\Omega$ , the natural frequency of the oscillator,  $H_V$ , the complex transfer function (from ground acceleration to relative velocity), and  $A(v)$ , the Fourier transform of the ground acceleration

$$H_V(v, \Omega, \xi) = - \frac{iv}{\Omega^2 - v^2 + 2i\xi\omega\Omega} \quad (4.11)$$

By definition the velocity time history can be written as:

$$\dot{u}(t) = \frac{1}{2\pi} \int_{-\infty}^{+\infty} A(v)H_V e^{ivt} dv \quad (4.12)$$

by substituting the relative velocity expressed in the frequency domain in Eq. (4.9) an equivalent expression of the input energy can be written as:

$$\frac{E_i'}{m} = \frac{1}{2} \int_0^{+\infty} |A(v)|^2 f(v, \Omega, \xi) dv \quad (4.13)$$

where:

$$f(v, \Omega, \xi) = \frac{1}{\pi} \frac{4\xi\Omega v^2}{(\Omega^2 - \omega^2)^2 + (2\xi v \Omega)^2} \quad (4.14)$$

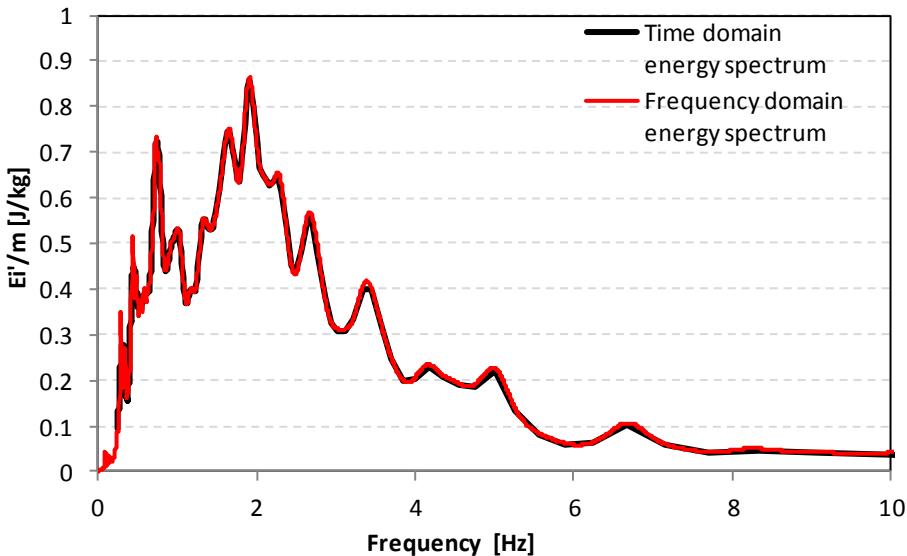
From the operative point of view it is possible to create the input energy spectrum with a spreadsheet with the following algorithm:

- A FFT is performed on the input ground motion acceleration and  $A(v)$  is then available. In Microsoft Excel™ the FFT is performed on a data set with  $N=2^n$  recordings as discussed in the following. Then  $\Delta v$  is equal to  $1/T$ , where  $T$  is the duration of the accelerogram.

- The target frequency  $\Omega$  and damping ratio  $\xi$  are fixed. The function  $f(v, \Omega, \xi)$  can be evaluated and the integral is solved and the final value is stored.

- The  $f(v, \Omega, \xi)$  function and the integral are recalculated for all the  $\Omega$  values of the final spectrum.

One example of time vs. frequency domain calculation of the energy spectrum is provided in Figure 4.4.



**Figure 4.15** - Relative energy input spectra calculation: Time vs. frequency domain. Some differences can be seen in the high periods field due to numerical and sampling issues, 5% damping.

It is interesting to notice that for the zero damping case we have:

$$\frac{E_i'}{m} = \frac{1}{2} \int_0^{+\infty} |A(v)|^2 f(v, \Omega, \xi) dv = \frac{1}{2} \int_0^{+\infty} |A(v)|^2 \cdot 1 dv = \frac{1}{2} |A(\Omega)|^2 \quad (4.15)$$

In this case, as the Fourier transform of the input acceleration can be enveloped by the zero damping velocity spectrum, the relative input energy spectrum can be evaluated also from the velocity spectrum itself.

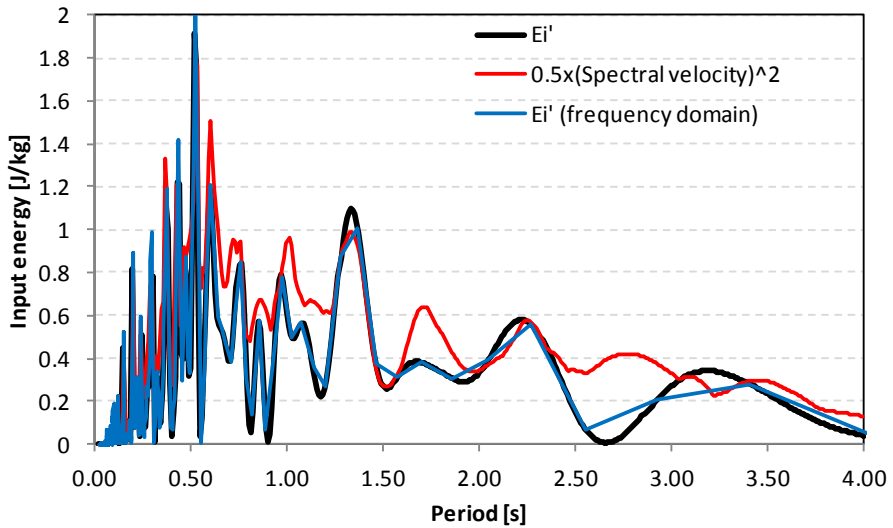


Figure 4.16 - Relative energy input spectra calculation: Time vs. frequency domain, 0% damping.

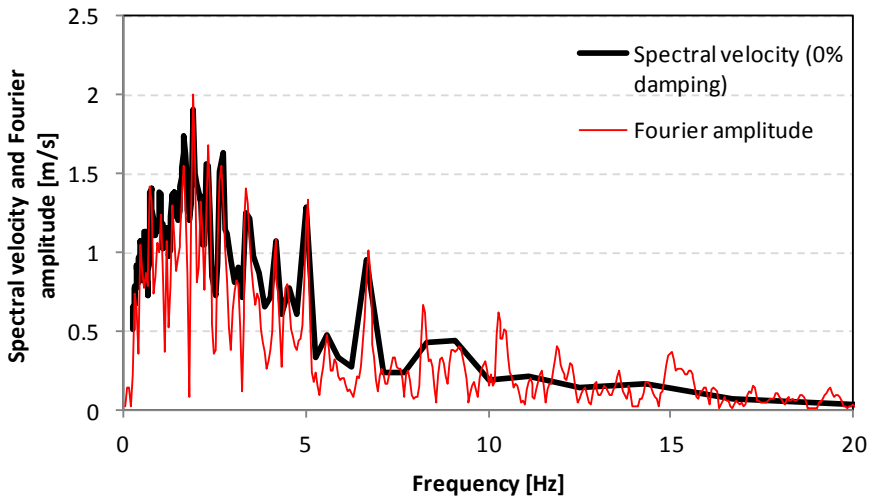


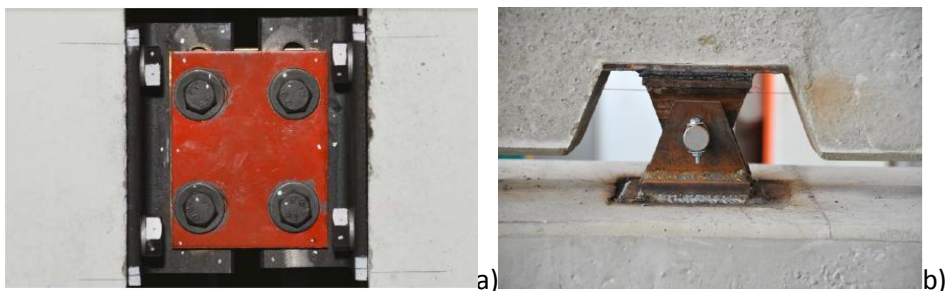
Figure 4.17 – Velocity spectrum Vs. Fourier amplitude.

#### 4.1.2 Energy based comparison with experimental data

In the previous paragraph some energy concepts have been discussed, especially with respect to the creation of energy quantities spectra.

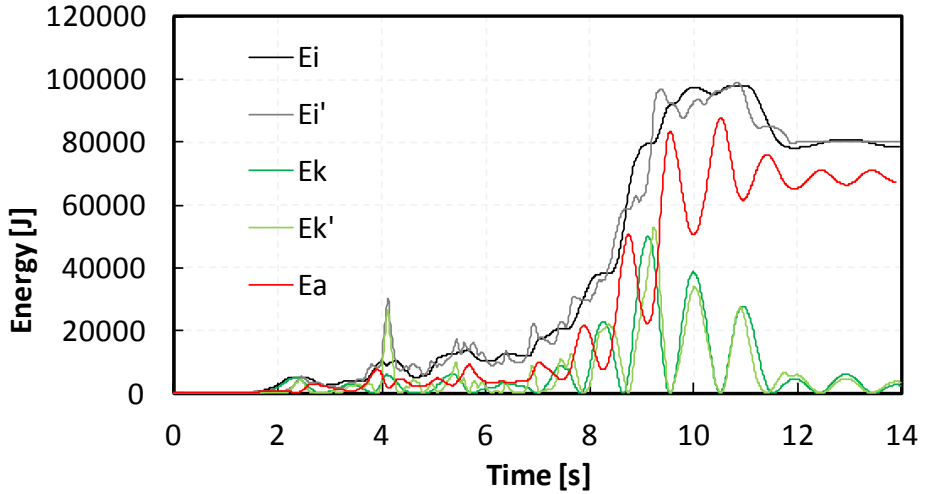
These concepts will be applied to the analysis of available experimental data from the Safeccladding project.

In the industrial precast structures design practice, cladding panels are usually considered as additional masses attached to columns and beams which do not contribute to the overall structural stiffness. Although this modelling technique is commonly used by engineers, it does not work properly, as demonstrated by the damages detected in precast structures after recent earthquake (L'Aquila IT, Christchurch NZ, Emilia-Lombardia IT), where many cladding systems collapsed and therefore constituted one of the main sources of risk. This was mainly due to the high force level on panel-structures fasteners. These devices, although properly manufactured and installed, had to undergo a force level much higher than the one they had been designed for. The panels and their fasteners should then be considered as an integral part in numerical simulations. To understand the behaviour of cladding system, the experimental SAFECLADDING campaign was carried out at ELSA lab (JRC). A typical full scale, 6 columns, 8m height and 170t weight representative precast structures unit was tested by means of pseudo-dynamic technique. Three main panels configurations for vertical and horizontal panels were considered: isostatic (with sliding frame, double pendulum and rocking panels), integrated (hyperstatic connections configuration) and dissipative (with friction or plasticity dissipative devices for panel connections). The data analysis will focus on the behaviour and seismic assessment of the precast specimen provided with friction brass dissipative devices (FBD), Figure 4.18 a) and vertical cladding panels with top and bottom hinge connections, Figure 4.18 b). Results are compared with the performance of an equivalent structure without FBDs.

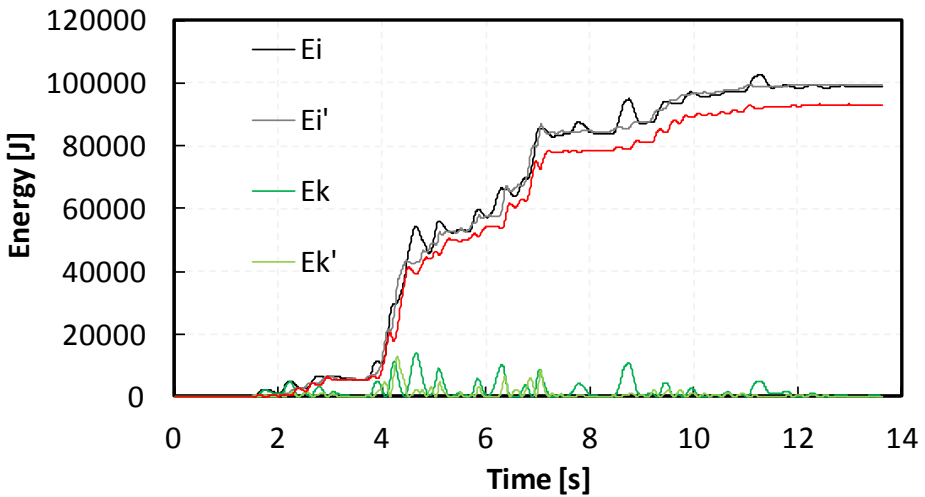


**Figure 4.18** – a) Friction based device at panels interface and b) connections hinges at the top and at the bottom of panels, isostatic arrangement. (Negro et al., 2015, courtesy of ELSA, JRC).

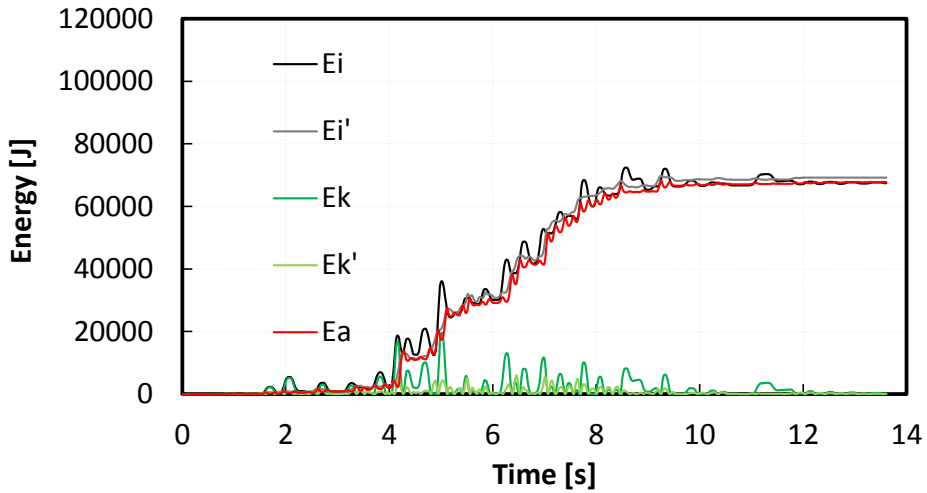
The structures were experimentally subjected to the accelerogram shown in Figure 4.1 which is expected to correspond to a ultimate limit state of the structure. In figures Figure 4.19 - Figure 4.22 the time history graphs for each structures, based on experimental data, are reported.



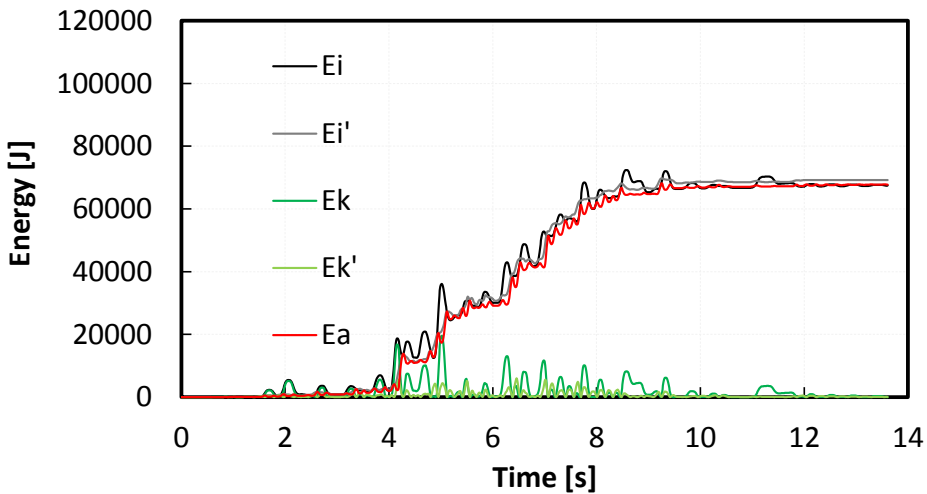
**Figure 4.19** – Time history of energy quantities for the structure not provided with any FBD at ULS.



**Figure 4.20** – Time history of energy quantities for the structure provided with 1 FBD at each panel to panel connection at ULS.



**Figure 4.21** – Time history of energy quantities for the structure provided with 2 FBDs at each panel to panel connection at ULS.



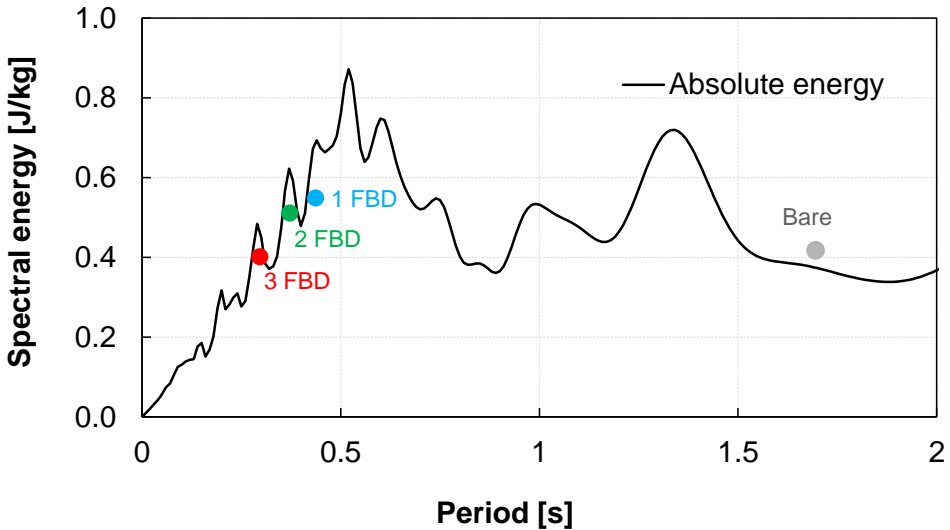
**Figure 4.22** – Time history of energy quantities for the structure provided with 3 FBD at each panel to panel connection at ULS.

It is remarked that during pseudo-dynamic test, the damping matrix  $[C]$  is not taken into account in the resolution of the dynamic equation. This means that  $E_c$  contribution is an unknown part of the adsorbed energies. It can be noticed that the kinetic quantities are much stronger for the 0 FBD structure. This can be explained by checking the natural periods of each specimen.

**Table 2.** Materials and geometrical parameters.

Structure	Period [s]	Adsorbed energy $E_a$ [J/kg]
Bare frame	1.7	0.41
1 FBD	0.52	0.55
2 FBD	0.36	0.51
3 FBD	0.30	0.40

It is remarked that the spectral values considered are the final energy values at  $t=12s$ , so measured at the end of the input acceleration. This value may slightly differ from the peak value, especially in the long period field. However, the final value was considered as the most representative one for the purposes of the research.

**Figure 4.23** – Input energy spectra and adsorbed energy experimental values

It can be noted that the elastic input energy is usually very similar to the final value of the experimental adsorbed energy (the only expected difference is in the kinetic energy content). However, at ULS the structure will exhibit some non linear behaviour. In this case the input energy will be dissipated partly in damping and partly in elastic and hysteretic energy. One key observation is that the introduction of FBDs makes the structure stiffer. Moreover, as shown in Figure 4.13 and Figure 4.14, for the input acceleration used, stiffer oscillators (at

about 0.5s) are subjected to higher input energy values, however the ratio  $E_a/E_i$  is also the highest. Given that the connections are properly designed or retrofitted according also to capacity design criteria, this means that all the energy is dissipated through the FBDs and through the damping. Longer period structures, like for example the 0 FBD test specimen, will dissipate energy only through structural damping and column elastic and plastic deformation (especially during input energy peaks).

#### 4.1.2.1 Application: simple design analytical method for precast structures retrofitting

The observations on the energy behaviour of SDOF led to the following conclusions:

1. The input energy (both relative and absolute) is made by three main contributions. The ratio between adsorbed energy (which is the sum of plastic and elastic strain energy) and input energy can be used as a performance index of the structure.
2. Friction metal devices used as panel to panel connections make the global behaviour stiffer with lower natural periods. However, the energy is efficiently dissipated by the devices themselves. The energy dissipation does not rely only on damping or plastic hinges.

A simple design procedure can be evaluated based only on the definition of the FBD stiffness and yielding force.

The procedure is dependent on some basic hypotheses:

1. The maximum global displacement is calculated as the maximum displacement allowed by dissipative connection. Above this threshold the FBDs cease to be operational.
2. The method is applied to a cladding system of isostatic vertical panels provided with panel to beam and panel to foundation hinged connections (pendulum behaviour).
3. The “bare frame” and the FBD system behaves like two parallel systems.
4. The bare frame system is designed according to vertical loads and it is supposed to remain in the elastic field during any ground motion. This means that yielding force of the bare frame must be



higher than the one provided by FBDs. For lower seismic both bare frame and FBDs systems display an elastic behaviour.

5. The FBDs hysteretic cycles are stable and they are able to dissipate all the adsorbed energy through their plastic deformation. It must be remarked that the global behaviour of the structure is not subjected to cyclic degradation and all the adsorbed energy (the  $E_a$  contribution to absolute or relative input energy) is dissipated through the FBD system. It is then not necessary to evaluate with a-priori method the number of cycles that must be accomplished by dissipators themselves.

A simplified procedure for the design of FBDs under the hypothesis reported is described in the following.

#### *Bare frame design*

The bare frame is designed according to vertical loads. It is assumed that all the connections are able to transfer the horizontal loads to each member of the structures. The natural period of the structure is dependant only on the columns stiffness. For the experimental test,  $T_1$  is equal to 1.6s. The ultimate displacement of the experimental frame and here used for comparison is equal to 420mm. The yielding displacement is measured at plastic hinge formation in columns and it is equal to 100mm. Plastic force is equal to 270 kN and therefore elastic stiffness is equal to 2.7 kN/mm.

#### *FBD system design*

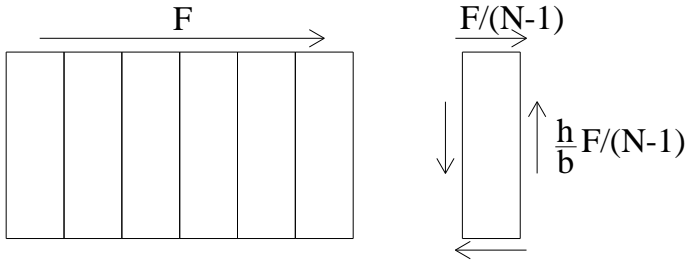
By hypothesis, the global structure behaviour is given by two parallel systems. One is the bare frame, whose stiffness  $K_b$  is given by the columns stiffness designed according to vertical loads. The second one is the panels connected one to each other with FBDs. The bare structure stiffness depends only on the vertical loads design or from original design in case of retrofitting. The FBD system stiffness can be simply calculated by means of geometric considerations.

The relative displacement between two points of the vertical panels

interface is given by the simple Eq. (4.16).

$$d' = d \frac{b}{h} = d \frac{2.49}{7.78} = 0.32d \quad (4.16)$$

where  $d$  is the top displacement,  $h$  is the top hinge height and  $b$  is the base length of the panel. Moreover, it is possible to calculate the distribution of the global force on each panel to panel interface according to Figure 4.24 ( $N$ =number of panels).



**Figure 4.24** – Global force distribution on single panels.

If  $n$  = number of dissipative connections at the panel interface, then the force  $f$  on each connection is given by:

$$f = \frac{h}{b} \frac{F}{n(N-1)} \quad (4.17)$$

The elastic stiffness of a single FBD can be written as a function of top displacement and global force:

$$k_{\text{fbd}} = \frac{f}{d'} = \frac{h^2}{b^2} \cdot \frac{F}{d} \cdot \frac{1}{n(N-1)} \quad (4.18)$$

The global stiffness  $K_{\text{fbd}}$  of the panels/FBDs system can then be written as:

$$K_{\text{fbd}} = \frac{b^2}{h^2} \cdot k_{\text{fbd}} \cdot n \cdot (N-1) \quad (4.19)$$

It is then possible to estimate the total stiffness of the structure and then its natural period once the elastic stiffness of the FBDs is chosen.

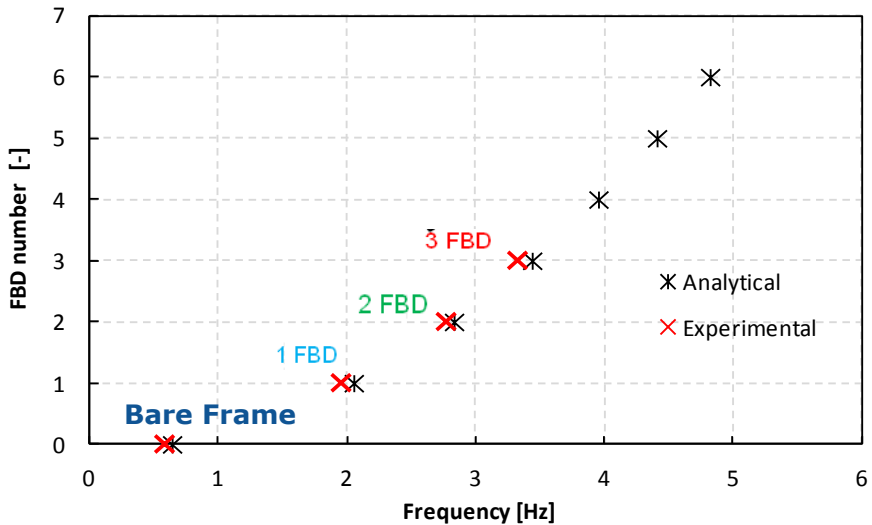
$$K_{\text{tot}} = K_b + K_{\text{fbd}} \quad (4.20)$$

$$v = \frac{1}{2\pi} \sqrt{\frac{m}{K_{\text{tot}}}} \quad (4.21)$$

Once the elastic stiffness of the global system is known, it is possible to evaluate the natural frequency of the structure and check it on the energy

spectrum. It must be remarked that there is an upper limit due to the maximum relative displacement allowed for the FBD. For the FBDs considered the maximum displacement allowed is equal to 50 mm. The consequent maximum global displacement is then equal to 155 mm. It is remarked that this value has to be checked by the end of the design procedure.

It is possible to evaluate a function able to correlate the design frequency of the structure to the number of panel to panel connections at each interface. It can be seen from Figure 4.25 that the analytical estimation of the structure frequency can be made with good accuracy with Eq. (4.20) and (4.21).



**Figure 4.25** – Number of FBDs for each panel to panel connection vs. frequency relationship.

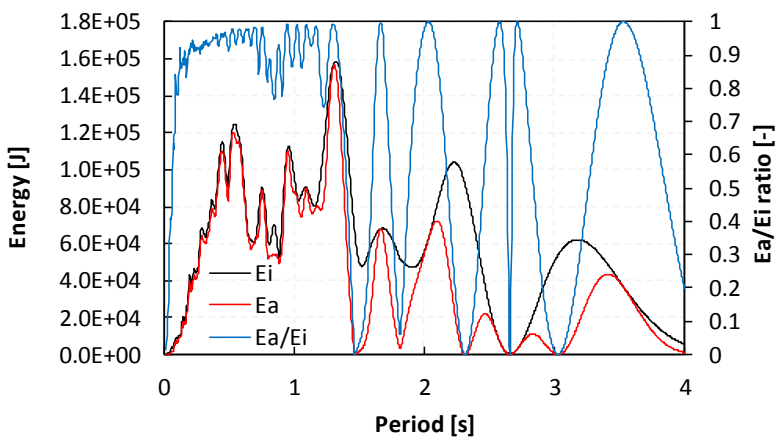
Structure	Experimental frequency [Hz]	Predicted frequency [Hz]
Bare frame	0.59	0.64
1 FBD	1.92	2.06
2 FBD	2.78	2.84
3 FBD	3.33	3.44

Thanks to the procedure described, the designer can choose the number of FBDs, as a first attempt, only on the base of the FBD elastic stiffness. From Figure 4.14 it can be assumed that a frequency of approximately 5 Hz (or a period of 0.2s) can be assumed as upper bound not only because of the high force rate but also because the  $E_a/E_i$  ratio for high frequency structure quickly drop to lower values.

#### *Evaluation of the seismic performances of the dissipative structure*

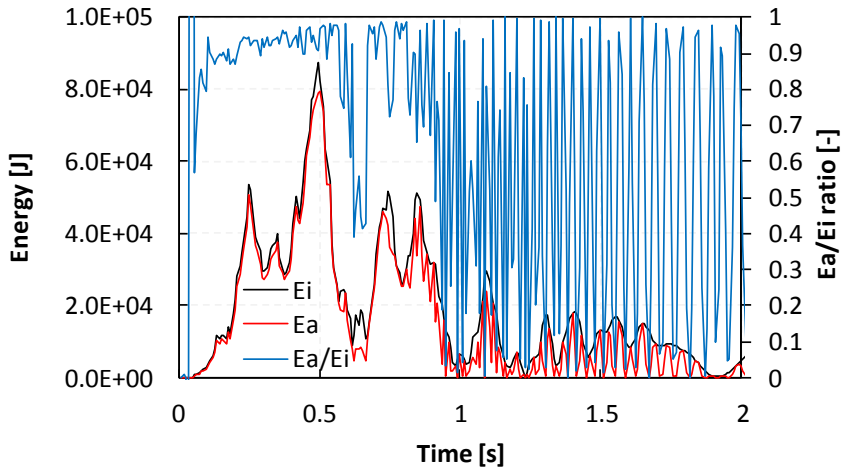
The best design choice from an energetic and economic point of view seems to be the one which considers one FBD at each panel to panel interface. In order to demonstrate this statement the procedure is applied also to real strong motion accelerograms and to spectrum compatible accelerogram used for pseudo-static testing. Global performances in terms of maximum displacement and base shear are compared. Therefore the non linear spectra of input and adsorbed energy are generated by means of a Newmark algorithm implemented in VBA. It is assumed that all the energy is dissipated through the devices so 0% damping is considered. Moreover, the yielding force of the equivalent SDOF oscillator is reported in Eq. (4.22). It is remarked that at this stage it is considered that the structure displays plastic behaviour at the peak acceleration level. The real plastic behaviour will also be discussed.

$$F_y = a_{g,max} \cdot m = 0.36g \cdot 170000kg \approx 600kN \quad (4.22)$$

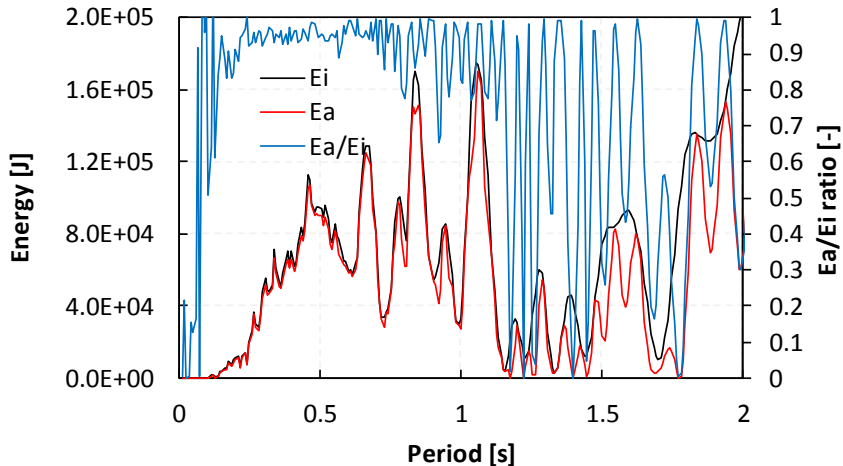


**Figure 4.26** – Input energy, adsorbed energy spectra and their ration (right axis) for  $F_y=600$  kN and no damping for the spectrum compatible accelerogram used for test.

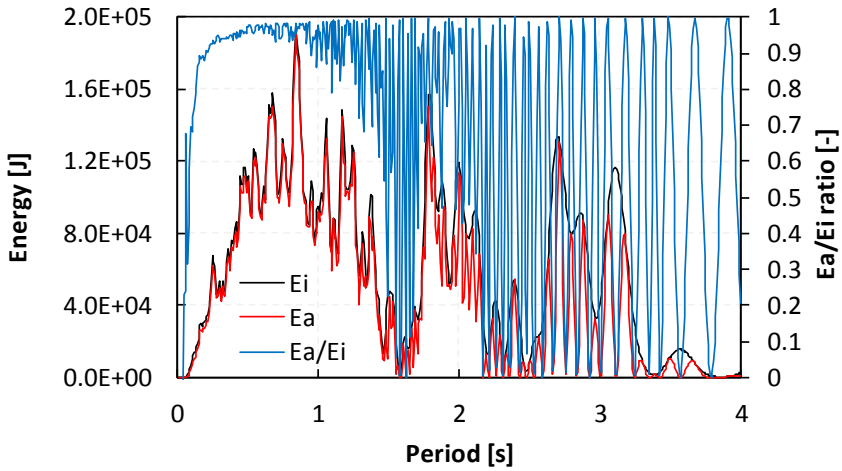
It is quite obvious that without damping all the input energy is divided into two contributions (kinetic and adsorbed) so the  $E_a/E_i$  ratio is always close to 1 in the low periods field. However, if damping is taken into account, it is effective only in the high period field ( $>1s$ ) so outside of the design period usually considered. More results are provided for a real Tolmezzo, El Centro and Izmir ground motion.



**Figure 4.27** – Input energy, adsorbed energy spectra and their ration (right axis) for  $F_y=595$  kN and no damping for real Tolmezzo input (0.35g).

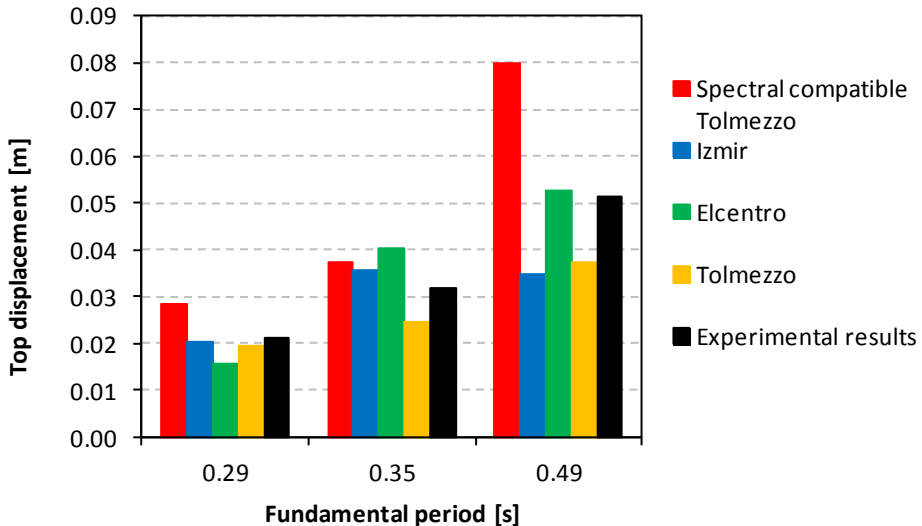


**Figure 4.28** – Input energy, adsorbed energy spectra and their ration (right axis) for  $F_y=595$  kN and no damping, real Izmir input (0.30g).



**Figure 4.29** – Input energy, adsorbed energy spectra and their ratio (right axis) for  $F_y=470$  kN and no damping, real El Centro input (0.28g).

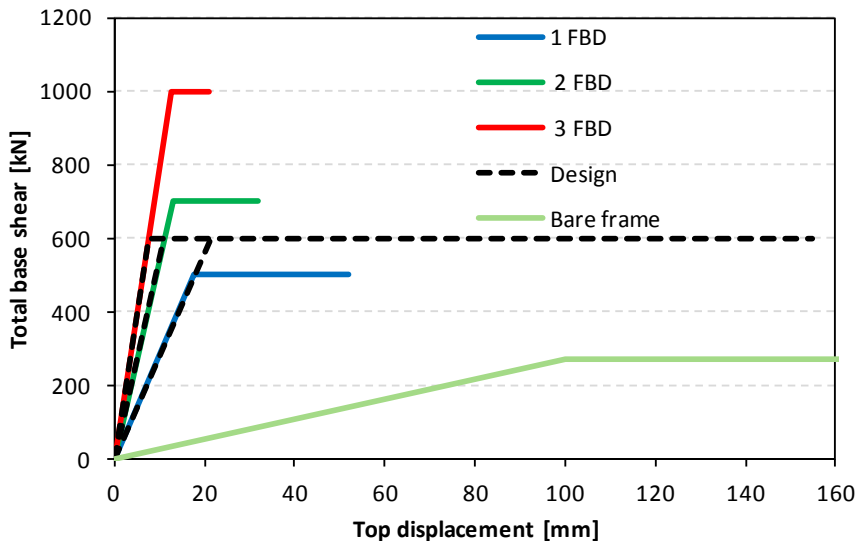
It is shown that for zero damping,  $E_a$  measured as final value of each time history analysis,  $E_a/E_i$  ratio assumes a stable value in the 0.2 to 1.5s period interval. The results are reported in Figure 4.30.



**Figure 4.30** – Maximum displacement for three different design solutions and experimental results test comparison.

It must be remarked that it is used an elastic plastic SDOF. The displacement is always below the maximum displacement allowed by FBDs which is equal to 0.155m. The energetic approach assures that if the structure is correctly provided with FBDs it is possible to obtain the lowest displacement given a maximum acceptable load.

The best solution is the one that is able to approximate the design values of the global elastic plastic response. In this way the elastic plastic behaviour is assured and moreover the system is able to dissipate energy. According to Figure 4.31 the design total base shear vs. top displacement bilinear diagrams are presented for the experimental structures and for the design structure.



**Figure 4.31** – Elastic plastic global behaviour: comparison between design behaviour and real behaviour.

The solution with one FBD fully exploits the dissipative behaviour and it could be immediately adopted and verified through a non linear time history analysis. However, it is also slightly over-reinforced and it displays the maximum displacement (which is in any case below the maximum displacement allowed by FBD deformation). The solution with two FBDs solution leads to lower displacements, however it must be verified that the force level is not excessive. The solution with three FBDs at each interface may be too onerous both in terms of maximum forces and cost of intervention. It must be remarked that the

selected design may be tuned with the modification of the tightening torque of the bolts that are keeping the FBD plates in contact. By doing this it is possible to lower or to raise the sliding force between the metal plates without changing the elastic stiffness.

### *Conclusions to the presented method*

The energetic approach is used in order to evaluate the performance of a structure. It was noticed that for the design or retrofitting of a precast structure provided with vertical panels with isostatic pendulum behaviour the introduction of dissipative device can optimize the dissipation of energy. This is proved by comparing the energy spectra from different input ground motions. The bare frame constitutes the soft part of the structure while the FBD-panels system is the stiff part. The two systems behave like parallel springs. The global stiffness can be evaluated with simple geometric considerations and it is possible to calculate the main frequency of the structure. The number and displacement threshold of FBDs are assumed as main design parameters. The target plastic force is fixed according to the maximum acceleration of the input accelerogram and the connections can be consequently designed according to capacity design rules. In the end, the designer is able to rationally choose the FBD configuration which can automatically provide the lowest displacements at the maximum accepted loads.

### **4.1.3 Open issues and final remarks**

In paragraph 4.1 some concepts and applications about the energy approach in seismic engineering have been presented. It is remarked the importance of a rational approach to the definition of the seismic load, with respect not only to maximum amplitude but also to energy content of the signal. Further investigation is needed for the evaluation of the relationship between seismic input energy as intensity measure and demand parameters. Moreover, it would be of great interest the extension of the study to multi degrees of freedom systems. Further applications may be found for the assessment of non-linear modelling technique (damping vs. hysteretic dissipation) and for the prediction of dissipated energy in structural systems.



## 4.2 Input data for dynamic nonlinear analysis

It is not trivial how to manage with real input data when dealing with time history analyses. The analyses are in general run by applying accelerograms at the base of foundations. The accelerograms can be real ones but building codes require spectra compatible accelerograms which can be artificially generated with software (but these artificial accelerograms have unrealistic energy content). However, it is obviously possible to solve the dynamic problem also applying displacements.

It must be remarked that in theory acceleration and displacement at one point are always correlated by double integration (or derivative). However, further considerations must be taken into account.

1. Raw recorded accelerograms may be affected by errors. These records usually have unrealistic high frequency content.
2. The “zero acceleration level” of a recorded accelerogram is unknown; this fact leads to the so-called baseline correction.
3. Time integration (or derivative) is a numerical procedure, not analytical. Each adopted numerical technique (e.g. Hilber Huges algorithm) may reduce or amplify some frequencies of the record.

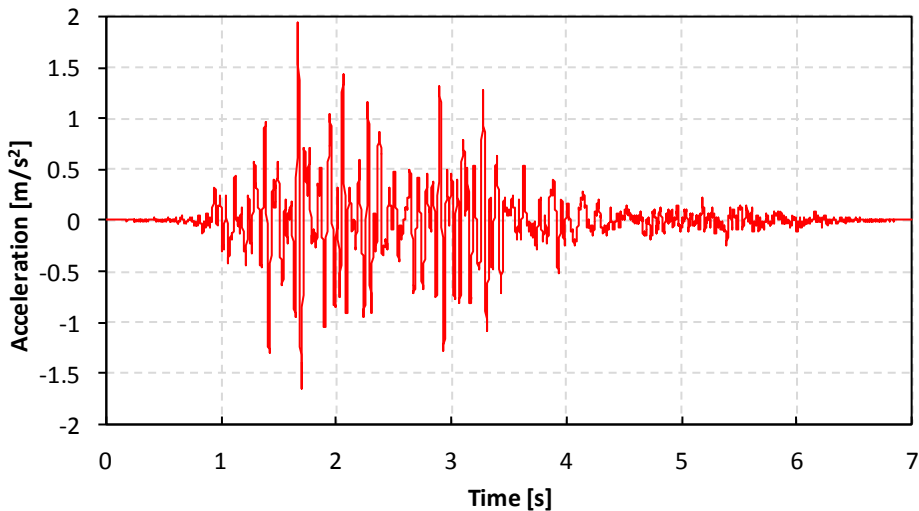
For all these reasons, a record displacement and a record acceleration are not precisely correlated by numerical integration/derivative. On the other hand, in a FE program if we apply acceleration in a point the displacement response is equal to the derivative of the acceleration (at least, with the approximation introduced by the numerical algorithm used). In general, a displacement input is “smooth” so relatively “poor” of information. A double derivative will introduce unrealistic spikes in the acceleration response. The acceleration input is very rich of information; a double integration will smooth all this data. However, unrealistic frequency content can strongly affect the displacement response.

To sum up, each time it must be paid attention on what we are using as each choice we make has aftermaths. The Internet-Site for European Strong-Motion Data is a reliable source of data for the model calibration. For more details and useful definition please refer to (Thunell, 2014). Data are provided in two forms: uncorrected (raw) data and corrected data.

#### 4.2.1 Analysis of fan input signal from SMART2013 shaking table model test

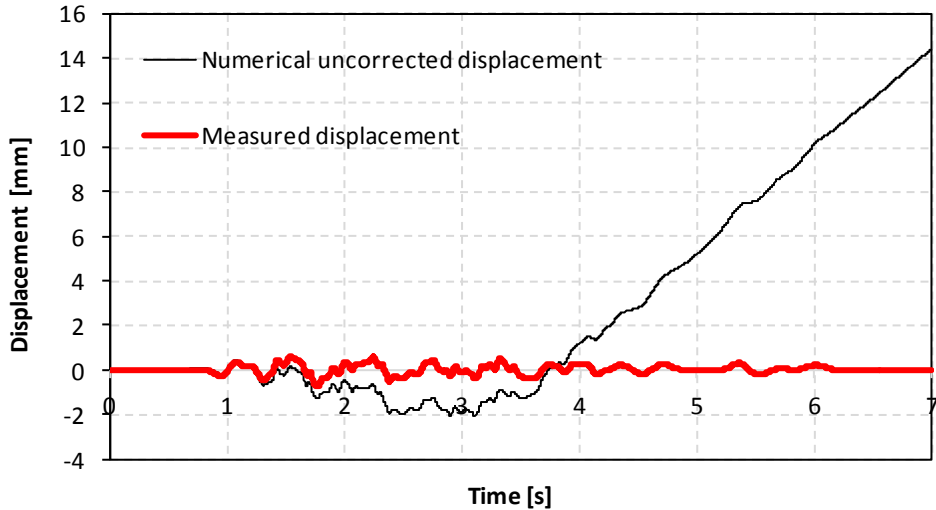
In order to correctly assess the non linear dynamic behaviour of a structure some post processing of the signal data may be necessary. One of the most important parameter to be considered is in fact the input applied. In fact, small variations for a time history input can strongly affect the structural response. In the following it is described as example the manipulation on an input signal from the SMART2013 shaking table test described in chapter 6.

In this case the acceleration signal and displacement signal at one actuator level are analyzed. The given acceleration signal is reported in Figure 4.32.



**Figure 4.32** – Acceleration input signal for Run #07, SMART2013 shaking table test, x-direction, actuator 1., 1024 Hz.

For the same signal the given measured displacement is compared with the numerically integrated displacement of the acceleration signal (trapezoidal rule is applied for numerical integration).



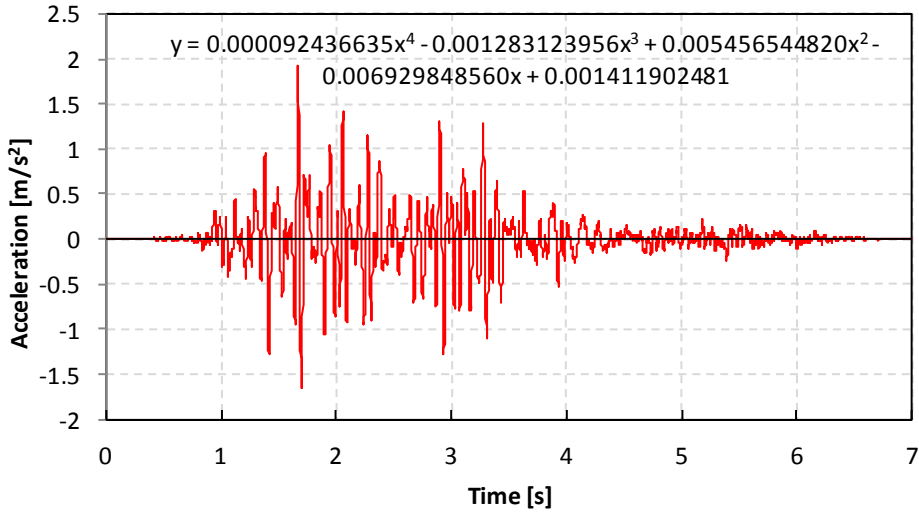
**Figure 4.33** – Measured displacement vs. numerically integrated displacement from acceleration signal.

It can be noted that the direct application of acceleration at actuator level would lead to a totally different displacement field. This is due to the so called base line correction issue. This phenomenon, which consists of a shift of integrated velocities and displacements, should be prevented. In fact, this non physical shift is due in general to the deterioration of recorded signal because of the system of acquisition, filter of the seismograph (for accelerograms) or truncation of part of the signal. The input signal then can be corrected according to different techniques.

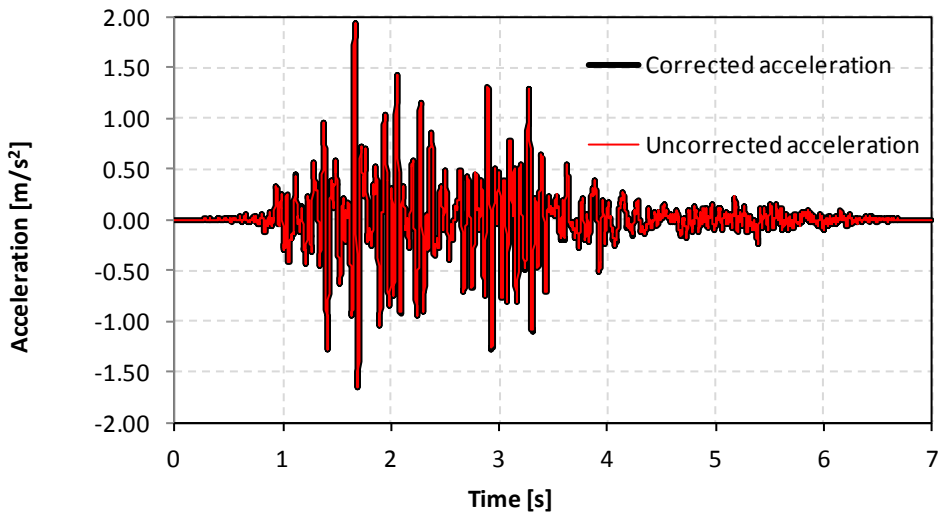
The base line correction method consists on the determination of a polynomial form of the shift (the base line) which is calculated and then removed from the signal.

In order to explain the problem one example is provided. The signal is corrected in a simplified way just by means of Excel spreadsheet tools.

A regression analysis is carried out on the acceleration signal interpolated by means of a 4<sup>th</sup> grade polynomial trend line, which is equal to the base line shift. The parabolic base line is then subtracted from the original signal. The corrected and uncorrected signals are equal at the naked eye.

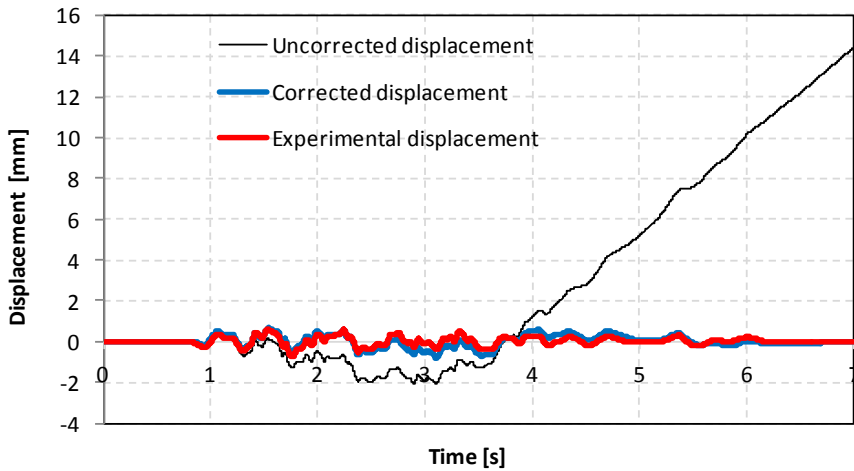


**Figure 4.34** – Baseline evaluation of by means of the trend line tool of Excel. The parabolic equation of the trend line is also reported.



**Figure 4.35** – Corrected vs. uncorrected accelerogram.

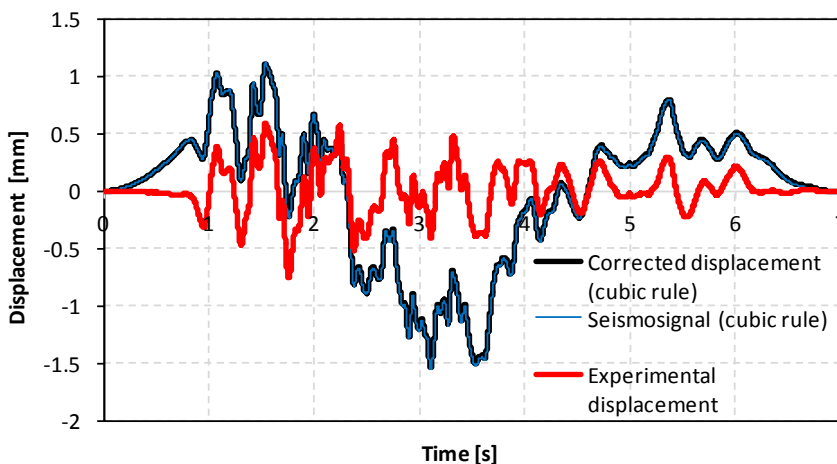
Although acceleration time series are very similar, the uncorrected and corrected displacements are very different. The corrected displacement is calculated with a trapezoidal rule from the corrected acceleration.



**Figure 4.36** – Corrected vs. uncorrected displacement and comparison with experimental measure.

Although acceleration time series are very similar, the shift correction is evident in the displacement graph.

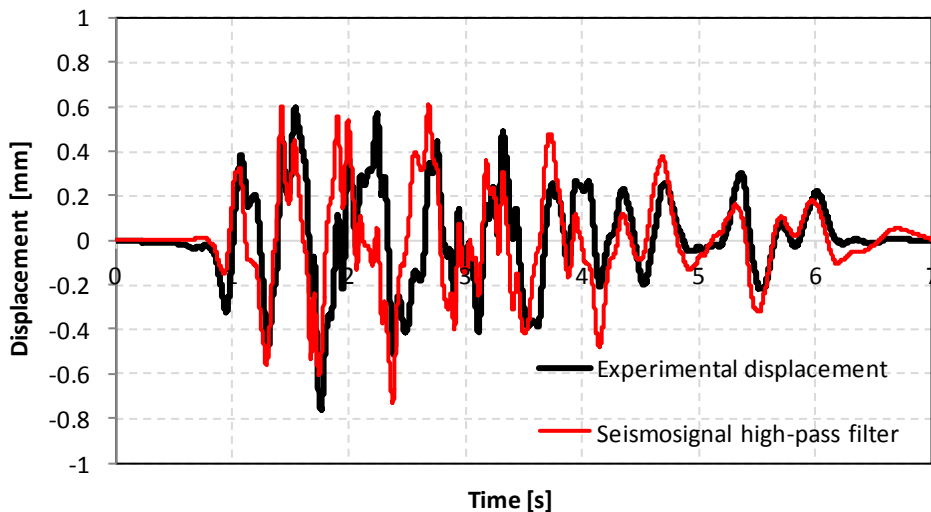
Moreover, the same procedure may be obtained by means of the base line correction tool available in Seismosignal software ([www.seismosoft.com](http://www.seismosoft.com)). Seismosignal can evaluate the base line correction by means of constant, linear, quadratic, and cubic rules. In figure, baseline correction carried out with a cubic rule by means of Seismosignal and Excel is compared with experimental results.



**Figure 4.37** – Corrected vs. uncorrected displacement carried out with cubic rule on Seismosignal software and Excel spreadsheet.

It can be noted that the application of a cubic correction on the input signal may be not sufficient for a proper evaluation of the base line. However, results given by manual calculation and the software are exactly the same.

On the other hand, Seismosignal is a powerful tool for signal filtering. By means of high pass filtering it is possible to remove spurious low frequency noise from the signals. The cut-off frequencies can be derived by a trial-and-error procedure, where cut-off frequencies producing the best matching displacements compared to experimentally measured displacements. By means of a 5<sup>th</sup> order Butterworth high-pass filter set on 0.7 Hz frequency cut-off it is possible to obtain a base line corrected displacement field.



**Figure 4.38** – Experimental displacement vs. displacement obtained by filtering the input acceleration.

The resulting displacement field is corrected however it is slightly distorted with respect to the experimental result. To conclude, the modified acceleration signals are believed to be a fairly close match to the real event. However there will always be the possibility of deviances in the processed signals, in which case the structural responses predicted by the numerical simulations, using these signals as input, will include errors due to a misfit in input. This is why, if available, displacements records may be simpler to be applied. However, higher frequency components not preserved when differentiating the experimentally measured displacement signals twice may not be included in the analysis.

### 4.3 A practical approach on the use of Fourier spectra

For some civil engineering applications Fourier spectra may be a useful tool. Thanks to the mathematical theory we can associate to a random signal (e.g. an earthquake oscillation) a series of harmonic functions. Each harmonic function has a frequency and amplitude associated. Intuitively the Fourier transform can describe the frequency content of a signal and can give an idea of the energy correlated to each frequency. In spectral analysis the goal is to determine the frequency content of a signal. It is important to that in case of an **analog** (continuous) signal the *Fourier series* are used, while when a **digital** (discrete) signal is available *discrete Fourier transform* might be used. Many references are available for the study of Fourier series so a brief practical example of a digital signal will be discussed.

In fact, nowadays signal are provided mainly in digital form. Moreover, if the sampling time is adequate, the Nyquist-Shannon theorem states that it is possible to obtain a complete description of the waveform. Given a sampled waveform, it is immediately possible to calculate the Discrete Fourier Transform (DFT), which is much easier to handle than the Fourier series (and it's also more general). If the sampling time of the waveform is correct, also the DFT will be correct (and also vice versa if we want to run an inverse discrete Fourier transform, but this is not the case). One efficient procedure for the calculation of the DFT is called Fast Fourier Transform (please note that this is a numerical procedure that can be efficiently implemented on a calculator, the FFT is NOT the same thing of a DFT). The DFT  $F$  is defined as follows:

$$F(k\Delta f) = \sum_{n=0}^{N-1} f(n\Delta t) e^{-i(2\pi k\Delta f)(n\Delta t)} \quad \text{for } k=0, 1, 2, \dots, N-1.$$

It is interesting to notice that:

- $f$  is the signal
- $F$  is a complex function (the DFT output)
- $F$  is defined with a sum (not an integral as for the Fourier Transform)
- The time domain quantities are:
  - $N$ =total number of discrete points taken
  - $T$ =total sampling time
  - $\Delta T=T/N$ =time interval between data points

- $f_s = 1/\Delta T = N/T =$  sampling frequency

The frequency domain quantities are:

- $\Delta f = 1/T =$  frequency increment or frequency resolution of the DFT output
- $F(k \Delta f) =$  DFT output, a complex number for each frequency that provides information about the relative contribution to the signal by each discrete frequency

The problem is that the resolution  $\Delta f$  has nothing to do with the frequency content of the signal, it is just an arbitrary value correlated to the total sample time  $T$  and number of samples  $N$ . Moreover, information are provided only for harmonics of  $\Delta f$  and as already said this is an arbitrary value, so this may lead to some errors. Another important thing to remember is that the Nyquist criterion says that if the sampling frequency is  $f_s$ , then the reliable information are only at  $f_s/2$  (aliasing problem: the same sampling points can describe different function at the same times, the correct one and the fake ones, called alias). This means globally that only the first halves of DFT results are reliable, the highest frequencies are of no use.

The Nyquist criterion states:

*“If a function  $x(t)$  contains no frequencies higher than  $B$  Hz, it is completely determined by giving its ordinates at a series of points spaced  $1/(2B)$  seconds apart.*

*A sufficient sample-rate is therefore  $2B$  samples/second, or anything larger. Equivalently, for a given sample rate  $f_s$ , perfect reconstruction is guaranteed possible for a bandlimit  $B \leq f_s/2$ .”*

So for example if it is considered a 0.001s time step history, the sampling rate is 1000 Hz. This means that it is possible to obtain no aliased information on frequency up to 500 Hz, higher frequency are of no use. However, for civil engineering application 500 Hz is quite a high frequency (very low period,  $T=0.002s$ ) and probably the frequencies that are missing are out of the range of interest (generally structures have a response at much higher frequencies, for example 1 Hz). Moreover, it is important to remark that for example, in case of time history analysis, re-sampling is not “for free”. Each time a signal is resample, there is a loss of information as in fact the highest frequencies are

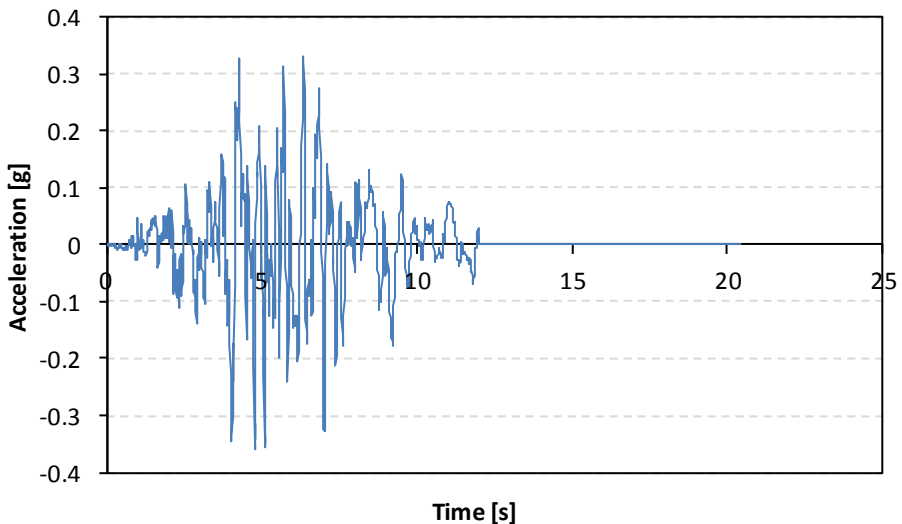


being filtered.

This paragraph is intended to provide a practical guideline for the use of Fourier analysis with analytical tool so a procedure is briefly analyzed. The analysis gives two values in correspondence of each frequency: the real and the imaginary part of the complex solution. What we need is the modulus of this complex number (square roots of the sum of the squares). What it is called “spectrum” is the plot of the magnitude (modulus) vs. frequency. Please note that the spectrum has not the same dimension of input signal by definition.

#### *Analysis of a seismic acceleration signal*

In order to perform a Fourier analysis of a signal the “Data analysis” tool of Data module must be activated. An acceleration signal will be analyzed (Tolmezzo earthquake spectral compatible signal, PGA=0.36g).



**Figure 4.39** – Acceleration signal, frequency sampling 100Hz.

A zero sequence value is added to the signal as the number of digital samples in order to perform a Fourier analysis with Excel should be  $n_{\text{samples}}=2^x$ . In this case  $x=11$  and  $n_{\text{samples}}=2048$ , and total duration is  $T=20.48\text{s}$ .

The Fourier analysis of the 2048 samples (that must be specified as input range) run by Excel provides 2048 complex number. Each number refers to a frequency. The output frequency resolution is equal to  $1/T=0.0488\text{Hz}$ . As the sample frequency is equal to 100Hz, the maximum useful frequency value is

equal to 50Hz, so only the first half of the output should be considered (the last part is symmetrical and must be discarded). In order to generate a Fourier spectrum of the input acceleration equal to the one provided for example by Seismosignal tool, further manipulations are needed.

- The module must be corrected by dividing each value for the frequency sample rate so that the amplitude of the transform corresponds to the amplitude of the signal.
- Attention must be paid to units. Seismosignal spectra are consistent with an accelerogram expressed in [g].

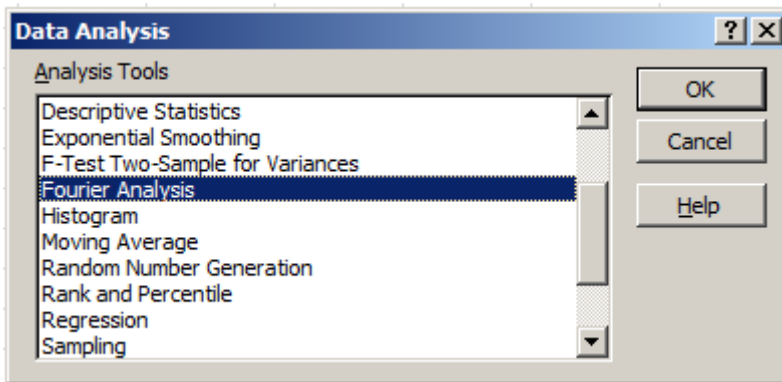


Figure 4.40 – Excel Data Analysis toolbox.

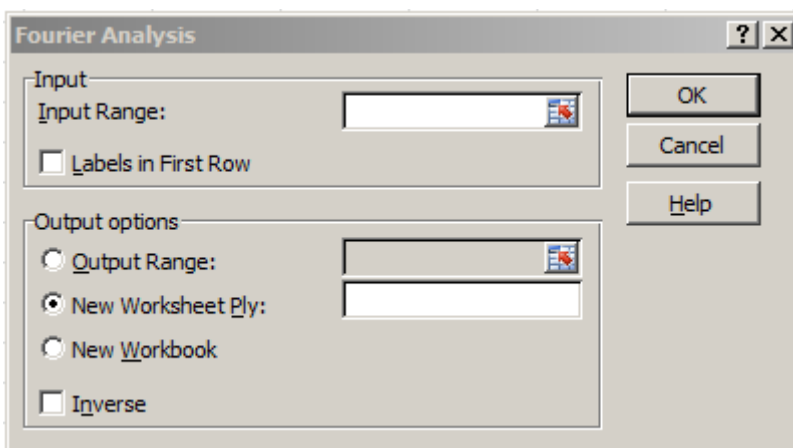
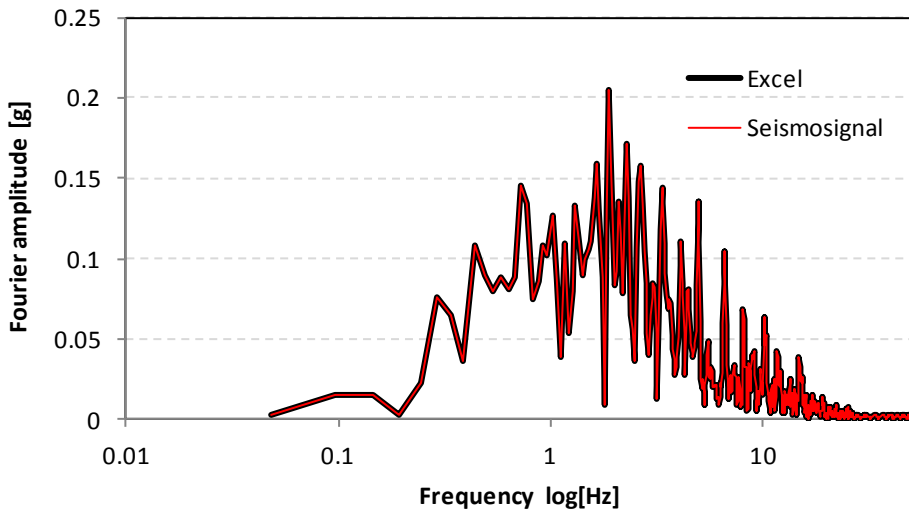


Figure 4.41 – Excel Fourier analysis interface.

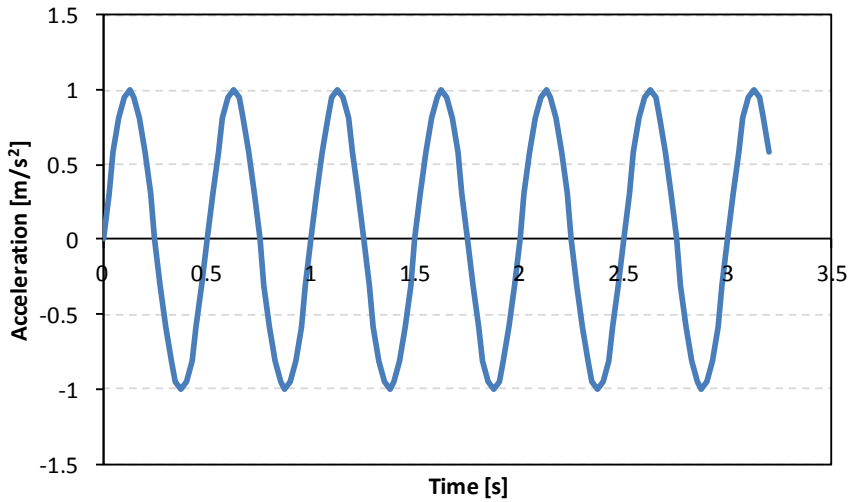


**Figure 4.42** – Fourier amplitude, Excel results vs. Seismosignal results.

It can be noticed that the amplitude calculation is exactly the same for both the spreadsheet and Seismosignal software calculation. The Fourier amplitude spectrum calculated according to this definition is approximately enveloped by the elastic velocity spectrum for zero damping.

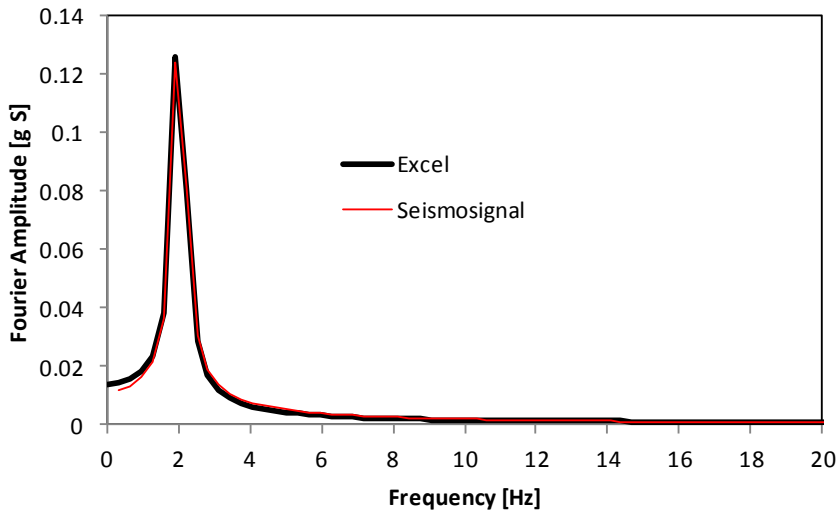
*Example: analysis of a sinusoidal signal*

In order to understand the information provided by the Fourier amplitude spectrum it might be useful to analyze a simplified input signal, amplitude equal to  $1\text{m/s}^2$ , frequency equal to 2 Hz, sample rate equal to 0.025s (40Hz), 128 samples.



**Figure 4.43** – Simplified sinusoidal input.

The resulting spectrum (normalized according to Seismosignal software technique) is reported.

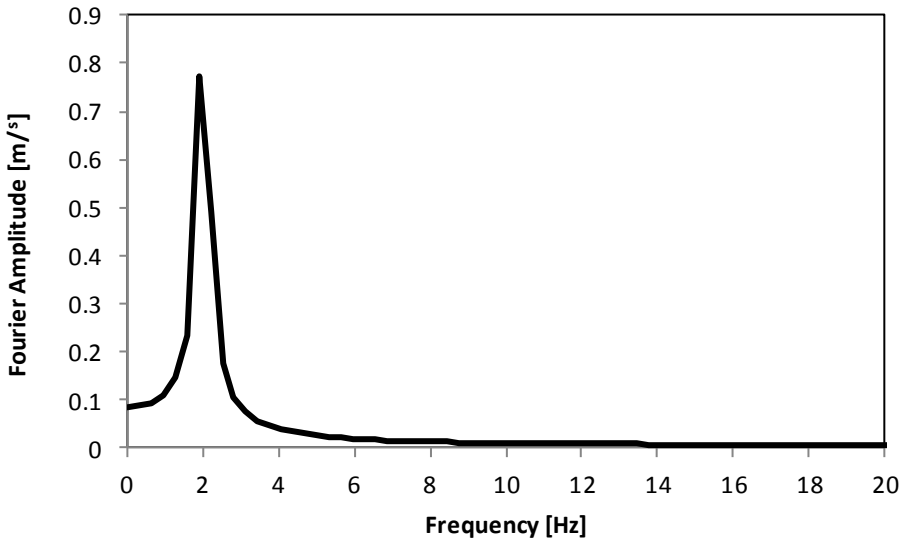


**Figure 4.44** – Fourier amplitude spectrum of a sinusoidal waveform.

As expected, the spectrum detects a single spike at about 2 Hz. However, due to frequency sample limitations, this spike is identified at 1.875 Hz. In fact, output values are calculated at  $40/128 \text{ Hz} = 0.3125 \text{ Hz}$ . In order to improve the

accuracy, the time sampling should be reduced or the number of samples should be greater.

Some comments have to be made for the amplitude definition. In general, the Fourier spectrum is used to identify the frequency content of a signal. Anyway, it is possible also to correct the amplitude output by dividing the results by  $N_{\text{samples}}/2$ . In this way the corrected amplitude corresponds directly to the amplitude of the signal, Figure 4.45.



**Figure 4.45** – Fourier amplitude corrected spectrum of a sinusoidal waveform.

It is possible to note that the spike amplitude is slightly lower than the amplitude of the signal (in this case equal to  $1 \text{ m/s}^2$ ). This is due to the leakage phenomenon. In fact, leakage appears when the discrete data acquisition does not stop at exactly the same phase as it started. If an infinite number of sample points are taken, leakage would not be a problem. In any case a real data acquisition system performing FFTs uses always a finite number of discrete data points, and there will be some leakage.

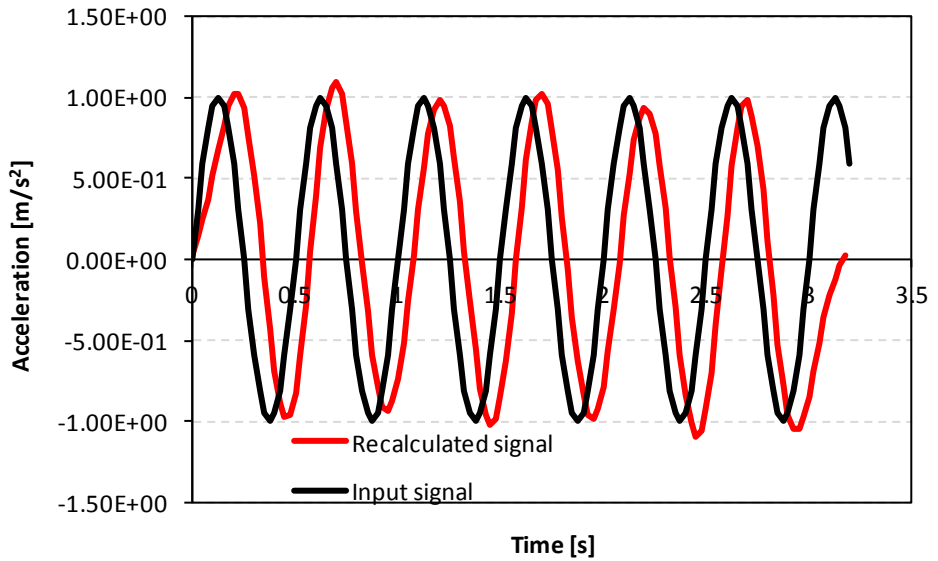
In order to verify the results and to have a better understanding of the Fourier analysis tool available in Excel, the input signal is recalculated from the Fourier spectrum.

Sample	Time t	Signal a(t)	Fourier analysis Output		Module	Frequency $\xi$
-	s	m/s <sup>2</sup>	Real part	Imaginary part		Hz
1	0	0	8.46E-02	0.00E+00	0.08464	0
2	0.025	0.309017	8.69E-02	-4.72E-03	0.087019	0.3125
3	0.05	0.587785	9.44E-02	-1.02E-02	0.094926	0.625
4	0.075	0.809017	1.10E-01	-1.77E-02	0.111387	0.9375
5	0.1	0.951057	1.42E-01	-3.01E-02	0.145469	1.25
6	0.125	1	2.26E-01	-5.88E-02	0.233112	1.5625
7	0.15	0.951057	7.38E-01	-2.27E-01	0.771674	1.875
8	0.175	0.809017	-4.64E-01	1.63E-01	0.4914	2.1875
9	0.2	0.587785	-1.65E-01	6.47E-02	0.177489	2.5
10	0.225	0.309017	-9.74E-02	4.17E-02	0.105939	2.8125
11	0.25	5.67E-16	-6.78E-02	3.13E-02	0.074647	3.125
12	0.275	-0.30902	-5.14E-02	2.53E-02	0.057276	3.4375
13	0.3	-0.58779	-4.11E-02	2.13E-02	0.046318	3.75
14	0.325	-0.80902	-3.41E-02	1.85E-02	0.038823	4.0625
15	0.35	-0.95106	-2.91E-02	1.64E-02	0.033403	4.375

The input signal in the time domain can be calculated at each time step with Eq. (4.23).

$$a(t) \approx \sum_{i=1}^n \text{Re}_i \sin(2\pi\xi_i t) - \text{Im}_i \cos(2\pi\xi_i t) \quad (4.23)$$

Obviously, there will be some differences in the time domain results as a consequence of the several parameters involved in the signal description (e.g. windowing, phase of initial and final signal). The shift in frequencies is due to the fact that the peak frequency is identified at 1.875 Hz instead of 2 Hz (real input value).



**Figure 4.46** – Input signal vs. signal obtained from the Fourier analysis coefficients.





## **Part II. Background**



**Chapter V.**  
**A Review on RC Wall Structures**  
**Shell Modelling**

## 5 RC Walls Seismic Behaviour: a brief review

Structural wall systems are commonly used both in day to day and industrial power plant design. In civil buildings design it is common to find structural walls since they provide strength and stiffness towards seismic actions and then allow a better displacement control (Riva et al., 2003). Rectangular slender walls are also common since they proved to generate a good seismic behaviour if brittle failures are adequately prevented. Squat walls and low rise walls are widespread in power plant facilities as main horizontal resisting structures (Whyte and Stojadinovic, 2013).

From 1976 to 1984 Oesterle et al. (1976) tested many slender walls subjected both to monotonic and cycling loading in order to evaluate their inelastic behaviour. In these tests flanged, barbell and rectangular sections were analysed. Many other studies have been carried out to test the behaviour of slender walls towards lateral seismic forces. Some studies concerning slender walls are for example CAMUS (1995-1998), UCSD: NEES benchmark (2005-2006), LNEC Ecoleader (2003-2005).

Many experimental studies have been carried out in order to assess the behaviour of RC shear and squat walls. Such experimental campaign have been reviewed and summarized throughout the years by some authors and in PhD theses (Wood 1990, Martinelli 2007, Grifenhagen 2006 and Gulec 2009). Experimental tests, as reviewed by Wood and Martinelli, have been run mainly considering monotonic, repeated and alternating loading. Regarding low rise walls or squat and large walls many experimental tests have been run from the '70s (Barda et al. 1977, Maier and Thurlimann, 1985, Lefas and Kotsovos, 1990). Recently, tests have been run by (Pilakoutas and Elnashai, 1993) on specimen with aspect ratio equal to 2 subjected to severe cyclic loading, by (Gupta and Rangan, 1998) on high strength concrete HSC shear wall subjected to monotonic lateral loads, by (Kabeyasawa and Hiraishi, 1998) on flanged HSC walls with aspect ratio approximately equal to 2, by (Palermo and Vecchio, 2002) on squat flanged shear walls under cyclic displacement, by (Farvashany, 2004) on HSC shear wall with aspect ratio 1.25 subjected to monotonic loading. It can be noted that only few pseudo-dynamic tests are available in literature. In (Naze

and Sidaner,2001), within the SAFE project, the dynamic behaviour of very squat walls (with aspect ratio 0.4) was analyzed. Also (Mazars et al.,2002) conducted significant studies, starting from the results of the aforementioned SAFE project tests.

In the design practice, the structural analysis of RC walls systems, especially when software aided, is carried out as RC wall systems themselves were RC frames. Indeed, the traditional structural analysis of frame systems is well known in engineering practice and it is also used to carry out safety verifications of ductile wall systems (coupled or uncoupled) and dual systems (frame or wall equivalent), by transforming the walls behaviour to equivalent columns behaviour. Sometimes, due to the geometrical features of RC walls, the Bernoulli hypotheses are not suitable for the description of the real walls behaviour, even in case of ductile walls, because walls are principally constituted of discontinuity regions. Furthermore the shear resistance (especially near supports and floors), the flexural bending resistance and the curvature ductility determination (especially for composite wall cross sections like “U”, “L” and “C” shapes) requires a-priori assumptions to be performed with beam modelling. Standard codes recommend the use of variable inclination truss models or the use of a strut and tie model only for the evaluation of the shear resistance of shear walls. The structural analysis of RC walls with plate or shell elements modelling is currently adopted to carry out linear and non-linear dynamic or equivalent static analyses of wall systems or dual systems (Palermo and Vecchio, 2007).

The chapter focuses on the prediction of the non-linear behaviour of RC walls systems with multi-layered shell elements and total strain smeared crack models. Numerical results obtained with DIANA Code and ABAQUS Code will be presented; in particular a multi-layered shell element model, developed at the University of Parma using the finite element code ABAQUS will be illustrated. The latter procedure adopts PARC\_CL model, implemented in the user subroutine UMAT.for of ABAQUS Code, to evaluate the non-linear stiffness matrix at each integration point.

In the chapter a multi-story building will be adopted as case study to demonstrate that for ductile walls the structural response at collapse can be predicted with similar level of accuracy by adopting shell element models, distributed plasticity models or lumped plasticity models. However, the

modelling with shell elements and smeared crack models can be more powerful, if compared to other approaches, for the structural assessment of shear walls and walls building characterized by both brittle shear or torsional failure and ductile bending failure. Thus in the chapter the case studies of the Concrack 4 shear wall (Damoni et al. 2013, Belletti et al., 2013) and of a ductile wall tested at the University of Brescia will be presented to illustrate that the shell elements modelling with smeared crack models can properly predict the indicators of damage, as strains in concrete and rebars, crack opening values, displacements, which are fundamental for the application of performance-based earthquake engineering,

In the chapter analytical provisions and definitions provided by EC8 for the resistance evaluation of RC walls are reported and finally, for each case study, analytical resistance values are compared to NLFEA results.

## **5.1 The Proposed Multi-Layered Shell Element And Parc\_Cl Modelling**

It is well known that NLFE analyses allow for more realistic modelling of material and structural behaviour and, in this manner, can account for additional bearing capacity of the structure. Nevertheless, the results obtained from NLFE analyses strongly depend on the assumptions made in the modelling steps (Damoni et al., 2013). The presented procedure adopts a multi-layered shell modelling; each layer behaves as an element subjected to plain state of stresses. A total strain fixed crack model called PARC\_CL (Belletti et al. 2013b), implemented at the University of Parma in the user subroutine UMAT.for for ABAQUS code, has been used to evaluate the mechanical non-linearity of RC layers. PARC\_CL model is an evolution of the PARC model (Belletti et al. 2001). PARC\_CL model describes the behaviour up to failure of reinforced concrete structures subjected to loading-unloading-reloading conditions. The adopted crack model is tailored to analyse structures failing in shear. Strain penetration effects are not incorporated in the actual version of the model.

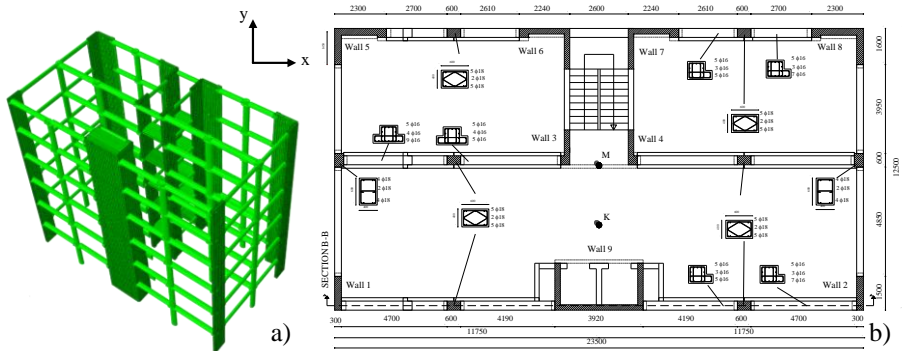
### 5.1.1 PARC\_CL crack model

The PARC\_CL model is based on a total strain fixed crack approach, in which at each integration point two reference systems are defined: the local  $x,y$  coordinate system and the 1,2 coordinate system along the principal stress conditions. The model is described in chapter 2.

## 5.2 Three case studies

### 5.2.1 Slender walls designed according to capacity design approach

The first case study presented in the chapter concerns the analysis of a regular multi-story building, Figure 5.1 (Belletti et al., 2013a). Three different models were adopted for the pushover analyses. The first and simplest one was a lumped plasticity model implemented by the authors in Excel VBa at the University of Parma, denoted “LPA”, the second one was a fibre-element model (implemented in Seismostruct software) and the third one the multi-layered shell element model described previously (Belletti et al., 2013b).



**Figure 5.1-** a) Global model of a building with U-shaped, L-shaped and rectangular walls and b) building ground floor section.

#### 5.2.1.1 Lumped plasticity model

For the lumped plasticity model the position of the resultant of the distribution of lateral forces has been evaluated as given in Eq. (5.1).

$$H_e = \frac{\sum_{i=1,n} F_i \cdot z_i}{\sum_{i=1,n} F_i} \quad (5.1)$$

The moment – curvature relation is evaluated by referring to the cross section and the reinforcement at the base of the walls subjected to the axial force derived from masses applied in frequency analyses. For each wall the moment versus curvature relation has been evaluated with the software Biaxial 1.3 by assuming an elastic-plastic behaviour for longitudinal rebars and a parabolic stress-strain relation for concrete in compression. The resulting moment versus curvature relation is transformed into a base shear versus top displacement bi-linear relation, Figure 5. The ultimate displacement  $\Delta = \Delta_y + \Delta_p$  is calculated on the basis of a yielding displacement  $\Delta_y$  and plastic displacement  $\Delta_p$  respectively given by Eq.(5.2) and Eq. (5.3).

$$\Delta_y = \frac{\chi_y}{3} H_e^2 \quad (5.2)$$

$$\Delta_p = (\chi_u - \chi_y) \cdot L_{pl} \cdot (H_e - 0.5 \cdot L_{pl}) \quad (5.3)$$

where  $\chi_y$  is the yield curvature and  $H_e$  the equivalent height of the wall. The plastic hinge length is evaluated with Eq. (5.4):

$$L_{pl} = k \cdot H_e + 0.1 \cdot l_w + L_{sp} \quad (5.4)$$

being  $k = 0.2 \cdot (f_u / f_y - 1) < 0.8$ ;  $L_{sp} = 0.022 \cdot f_y \cdot d_{bl}$ ;  $d_{bl}$  the equivalent longitudinal rebar's diameter.

Finally the force – displacement relation can be drawn in Figure 5.2 by assuming that  $V_y = M_y / H_e$  and  $V_u = M_u / H_e$ . The capacity of the entire building can be obtained by applying the same procedure for all the walls, adding the contribution of single walls, in terms of shear base versus displacement, for each direction of the building, Figure 5.3. In case of walls characterized by composite sections, the base shear versus displacement relations have been obtained for each principal axis of the transversal cross section and later combined through linear interaction diagrams in order to take into account for biaxial action effects.



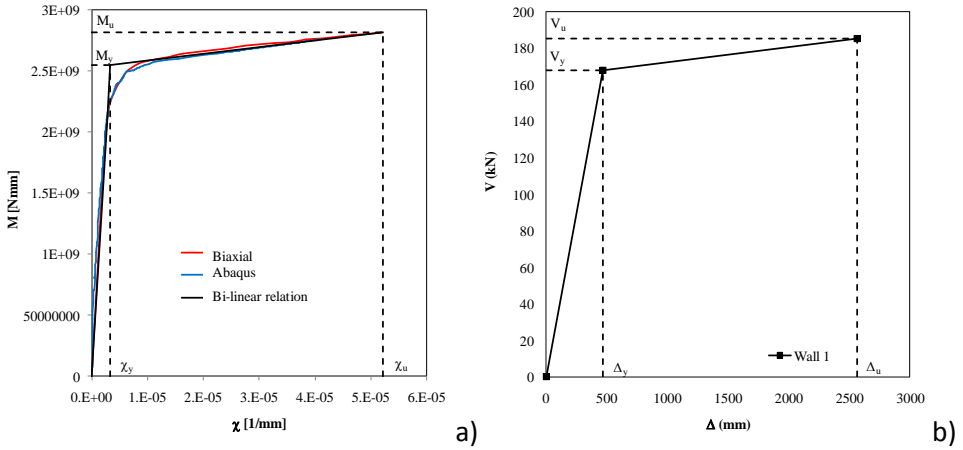


Figure 5.2- a) Moment versus curvature and b) base shear versus displacement relationships.

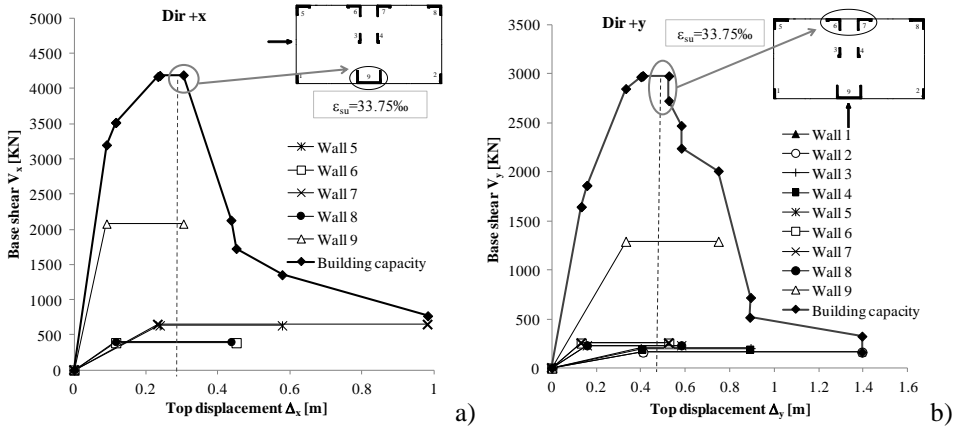


Figure 5.3- Capacity curves of the building obtained with LPA considering only the rigid translation for seismic forces acting along a) +x direction, b) +y direction.

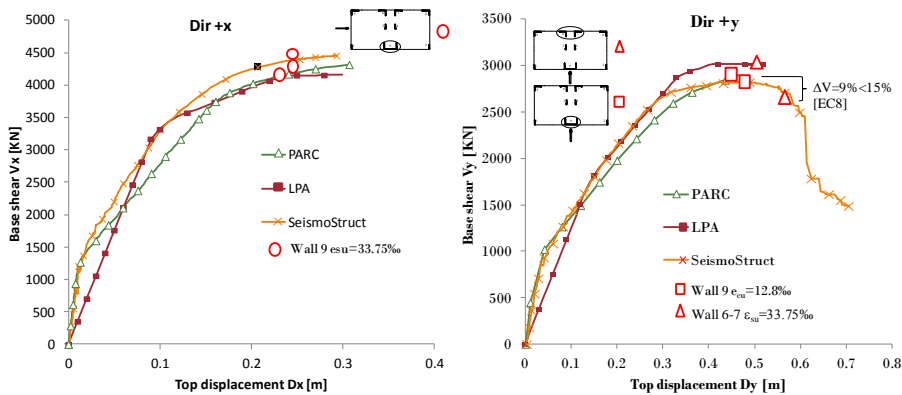
### 5.2.1.2 Distributed plasticity model

For the analyses carried out with Seismostruct software a uniaxial steel model based on stress-strain relationship proposed by (Menegotto and Pinto, 1973), coupled with the isotropic hardening rules proposed by (Filippou et al., 1983) is used for longitudinal rebars. An uniaxial nonlinear constant confinement model (Mander et al., 1988) is used for concrete. Two integration Gauss points per element are used for the numerical integration of the cubic formulation; each wall is subdivided in four elements per interstorey; the number of section fibres used in section equilibrium computations has been

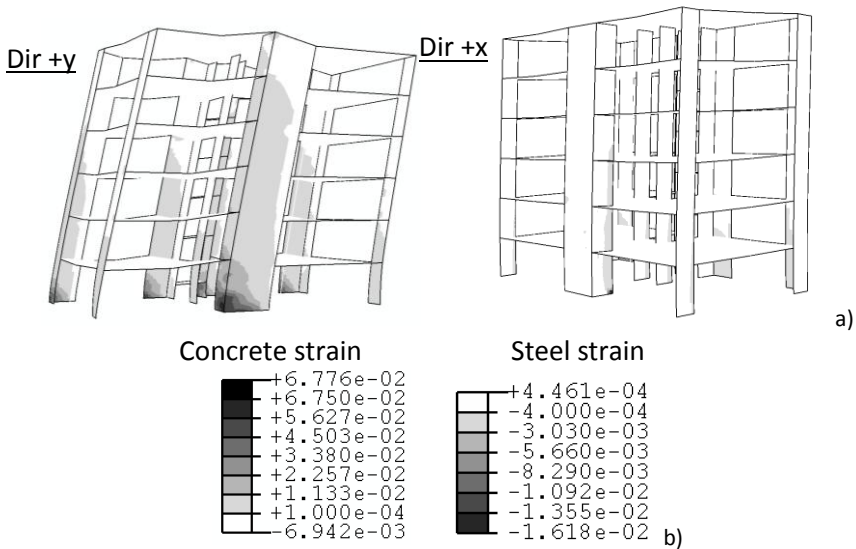
defined equal to 400. Lumped mass elements have been applied at each storey level and connected to wall. Masses and self-weight are automatically transformed to gravity loads for pushover analyses. The diaphragm behaviour is modelled by imposing (with “EqualDOF” option) the same translations along  $x$  and  $y$  axes and rotation along  $z$  axis of the mass centroid to all nodes placed at the storey level. The response control option has been chosen as loading/solution scheme by controlling the response of the node at the mass centroid of the top of the building.

### 5.2.1.3 Discussion of the results obtained with the three procedure

In Figure 5.4 the capacity of the building, in terms of base shear vs total displacement curves, obtained with the three methods previously described, is reported. Figure 5.4 a) shows that when the seismic force acts along  $+x$  direction the first wall that collapses is wall 9 due to the reaching of the ultimate strain in reinforcing bars ( $\epsilon_{su}=33.75\%$ ), while when the seismic force acts along  $+y$  direction, Figure 7b), the first walls that collapse are walls 6 and 7 due to the reaching of the ultimate strain in the reinforcing bars ( $\epsilon_{su}=33.75\%$ ). The limit of  $33.75\%$  for the ultimate strain value in reinforcing bars has been chosen in order to take into account for buckling phenomena that could occur during cyclic loading. The contour plots illustrated in Figure 5.5 are in agreement with the failure mode obtained with the lumped plasticity model and with the distributed plasticity model.



**Figure 5.4-** Shear-displacement diagrams for C-shaped and L-shaped walls according to different modelling techniques.



**Figure 5.5-** Steel and concrete strain at collapse detected in PARC model.

It can be noted that the shell modelling leads to a lower cracked stiffness than the one obtained with distributed plasticity approach. This is due to the fact that the shell modelling is able to evaluate the effects of multiple state of stresses in concrete and shear interaction, which are neglected if an equivalent beam modelling of the wall is adopted.

In general, the results of the analyses carried out with the three models, even if they are based on different assumptions, demonstrates that the structural response at collapse can be predicted with similar level of accuracy in case of ductile wall systems of regular building designed according to capacity design approach. It is important to remember that only when the modelling of RC walls with equivalent beams can be properly adopted (that is only in case of slender walls with beams that can be considered simply supported to walls), the structural behaviour can be predicted with the same level of accuracy by the three previously described modelling. In that case the lumped plasticity modelling configures as a relatively simple model, applicable even for hand calculations in the daily design procedure. On the other hand, it should be remarked that in case of composite sections the shear capacity depends on the interaction between axial forces, bending moments and shear forces acting on flanges and webs, which can be properly evaluated with shell modelling (Ile and

Reynouard, 2005). The interaction effects become more and more important in case of irregular buildings and in case of failure modes governed by shear.

### 5.2.2 Slender walls tested at the University of Brescia

A full scale wall, tested at the University of Brescia, Riva et al.(2003), Figure 5.6, has been modelled with the proposed multi-layered shell element approach (Belletti and Riva, 2008).

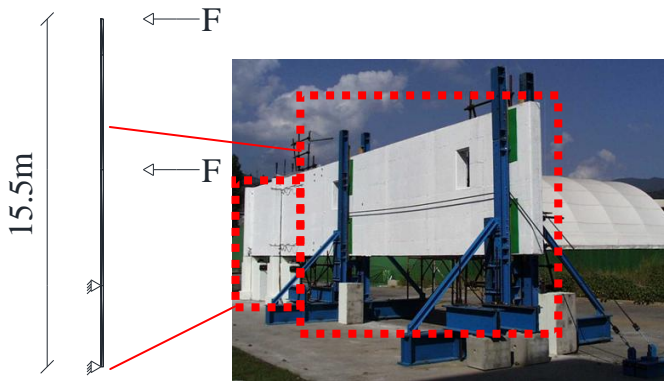


Figure 5.6- Test geometry and setup.

Table 5.1 - Materials and geometrical parameters.

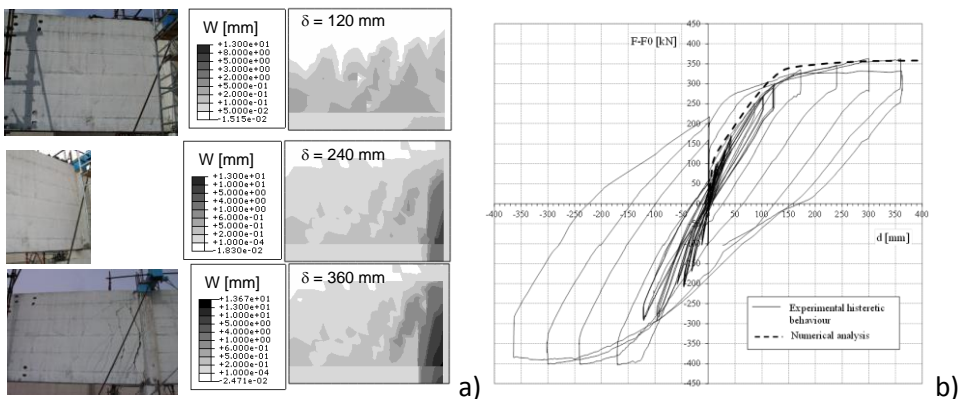
Parameters	Values
$R_{cm}$	40.7 MPa
$h_w$	11.5 m
$l_w$	2.8 m
$t_w$	0.4 m

The web of the specimen was reinforced with  $\Phi 8/200$  net corresponding to a reinforcement ratio  $\rho_h = 0.17\%$  lower than the minimum prescribed by EC8, equal to  $\rho_{min} = 0.2\%$ .

The specimen was modelled with the fixed crack model PARC\_CL and shell elements. The NLFE analysis demonstrated that the collapse occurred for a shear failure of the web reinforcement with the formation of a large crack nearby the base section, due to low reinforcement ratio of the web. Figure 5.7 shows that the model is in good accordance with the experimental test both in terms of crack patterns and failure load. This example demonstrates that shell

model is particularly adequate for the evaluation and influence of the detailing of the wall when analytical calculation could lead to a misinterpretation of the real failure mechanism.

Indeed the wall capacity evaluated according to EC8 provisions for medium ductility class structures (DCM), by adopting mean mechanical properties values, should lead to a bending failure in correspondence of a shear force equal to 708 kN, being the web shear and sliding strength equal to 1742 kN and 924 kN, respectively. The same evaluation carried out according to EC8 provisions for high ductility class structures (DCH) leads to a diagonal tension failure of the web reinforcement in correspondence of a shear force equal to 631 kN, being the sliding strength equal to 1930 kN. Experimentally the collapse mechanism, which occurred at a total applied force equal to 764 kN, was governed by shear with the formation of a large crack near the base section, leading to a failure of the longitudinal web reinforcement.

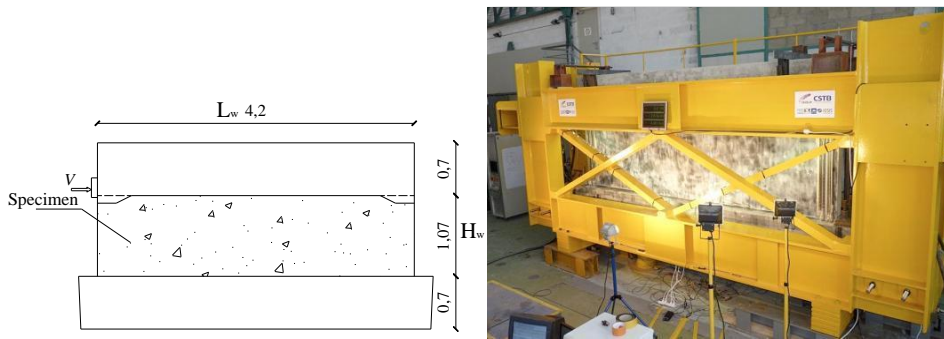


**Figure 5.7-** a) Comparison between experimental and numerical crack pattern of the tested wall; b) net force  $F-F_0$  at one actuator (where  $F_0$  is the force needed to equilibrate the self weight) vs top displacement curve, (Belletti and Riva, 2008).

### 5.2.3 Squat walls

For shear-critical specimens, aggregate interlock, tension stiffening, multiaxial stress states and Poisson effects play all an important role in the structural response. This is particularly true for squat walls, often used in low rise structures. It is common that aspect ratio is equal to 0.5 or even lower. Many uncertainties related to seismic behaviour and failure mechanisms concern this type of structural system because for these structures the performance requirements and compliance criteria for damage limit state (DLS)

verification can be more severe than the ones for ultimate limit state (ULS). For this reason it is fundamental the use of a model that can properly evaluate the actual crack pattern, like a shell element modelling. A case study of a squat wall which refers to the Concrack International Benchmark (2011), Figure 5.8, has been analyzed with strut and tie model, variable inclination truss model and NLFE analyses carried out by applying the constitutive model PARC\_CL implemented in ABAQUS Code and the software DIANA.



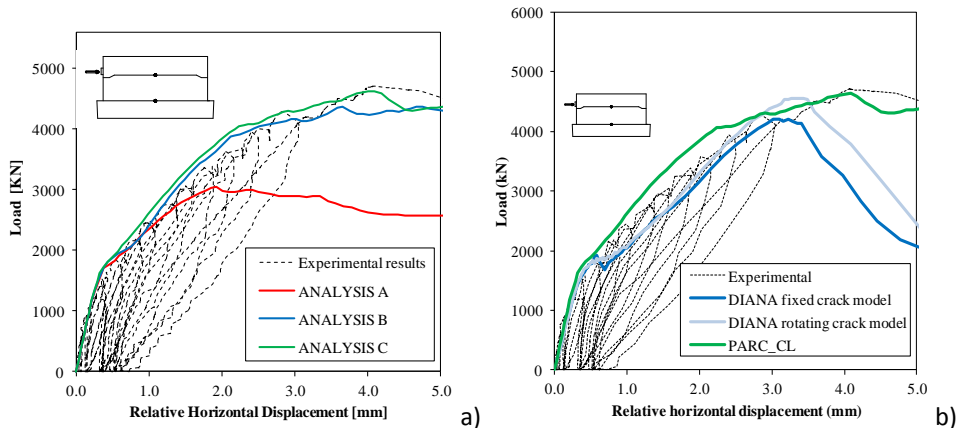
**Figure 5.8-** Specimen geometry and experimental setup.

**Table 5.2 -** Materials and geometrical parameters.

Parameters	Values
$f_{cm}$	42.5 MPa
$f_{ck}$	34.5 MPa
$h_w$	1.07 m
$l_w$	4.20 m
$t_w$	0.15 m

For the analyses performed with DIANA both a total strain fixed and rotating crack models have been adopted. A variable Poisson's coefficient that linearly decreases from 0.19, in the elastic phase, up to 0.0 as the residual tensile stress is 0.0 has been used. The biaxial state of stresses has been considered by adopting a maximum reduction of the compressive strength due to lateral cracking of 40% ( $f_{c,red}/f_c=0.6$ ). The tensile fracture energy  $G_f$  has been evaluated according to Model Code 2010, while in case of fixed crack model, a variable shear retention factor decreasing from 1, in the elastic phase, up to 0.0 has been adopted.

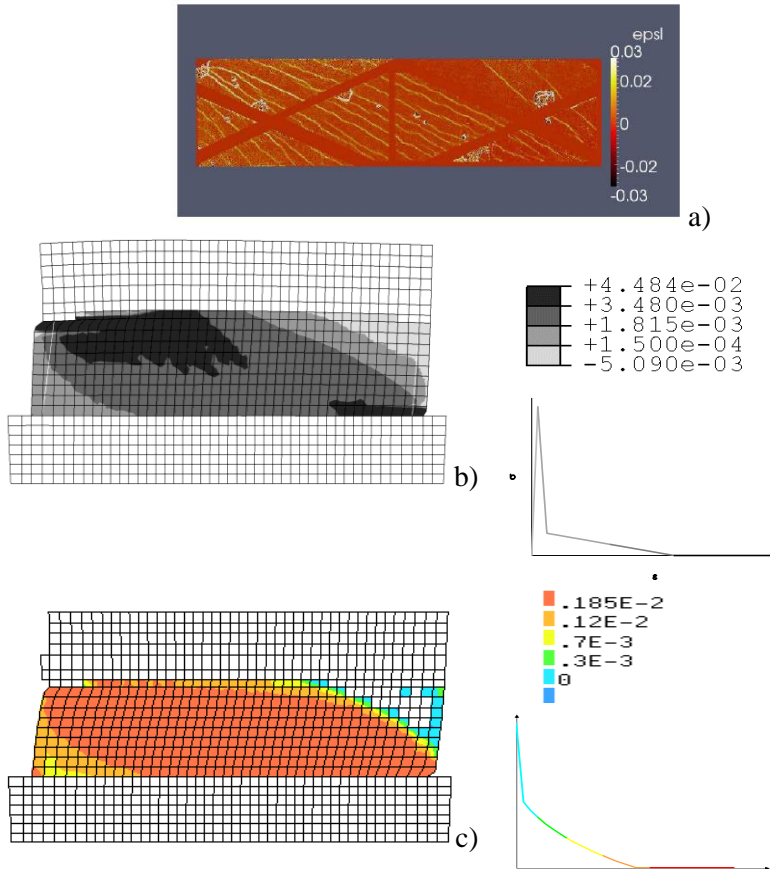
In order to underline the effects of phenomena that occur after cracking, a preliminary set of analyses have been carried out with the PARC\_CL model. First, only the mechanical contributions given by concrete and steel was taken into account (Analysis A), secondly the contribution of aggregate interlock (Analysis B) has been added and finally tension stiffening (Analysis C) has been considered. The three analyses are compared in terms of load versus displacement curve in Figure 5.9 a).



**Figure 5.9-** a) Comparison of the preliminary set of analyses carried out with PARC\_CL model, b) Load-displacement curves: comparison between PARC\_CL and DIANA models

By comparing analyses A and B, it is possible to note the large influence of the aggregate interlock, while by comparing analysis B to analysis C, it can be noted that the contribution due to the tension stiffening is not relevant in this case. The dowel action effect has been neglected in the study, in order to be in the same conditions as DIANA model, in which the dowel action effect is not taken into account. Figure 5.10 b) shows that both ABAQUS model and DIANA models adequately describe the wall behaviour in terms of load vs displacement curves. Due to the different basic hypotheses, in Figure 5.10 b) it is possible to observe a little difference in terms of peak load and stiffness of the structure in the cracked phase for the NLFEA curves obtained with fixed crack model and the rotating crack model implemented in DIANA code.

The ultimate load evaluated with NLFE analysis corresponds to crushing of concrete near the loading steel plate, as experimentally observed, Figure 13.



**Figure 5.10-** Comparison among a) experimental, b) PARC\_CL and c) DIANA tensile strain (and consequently crack distribution) in concrete at maximum base shear level (equal to 4800 kN).

The peak load is well predicted both with PARC\_CL model and with the rotating crack model of DIANA. The greatest difference between the two models is in the stiffness of the structure in the cracked phase and in the peak deformation. Indeed the different modelling of the biaxial state of stresses and the aggregate interlock effect in PARC\_CL model and in DIANA model leads to some differences in the structural prediction.

The results obtained with NLFEA are compared with the results obtained with strut and tie methods. All the analytical calculations refer to mean mechanical properties of materials, Table 2. The tested specimen has an aspect ratio equal to 0.25, then according to EC8 can be defined as a large wall. EC8 provisions simply give a suitable value for the evaluation of the strut width



which should not exceed  $0.25l_w$  or  $4b_w$ . In this case the strut width is equal to  $a_s = \min\{0.25l_w; 4b_w\} = 4b_w = 600\text{mm}$  where  $l_w$  is the wall length and  $b_w$  is its width. According to Model Code 2010 formulation the reduced concrete compression strength is equal to:

$$f_{c, \text{strut}} = \frac{k_c f_{ck}}{\gamma_c} = 20.8 \text{MPa} \text{ with } k_c = 0.55 \eta_{fc} = 0.49 \quad \eta_{fc} = \left( \frac{30}{f_{ck}} \right)^{1/3} = 0.89 \leq 1.0 \quad (5.5)$$

Finally, the shear force  $V$  correspondent to the compressive failure of the strut is equal to 1676 kN. In (Paulay and Priestly, 1992) it is suggested another formulation for the evaluation of the strut width, given by Eq. (5.6):

$$a_s = \left( 0.25 + 0.85 \frac{N_c}{A_c f_c} \right) \cdot l_w \quad (5.6)$$

If Eq.(5.6) is adopted and considering that the axial force  $N_c$  on the specimen is approximately equal to 0, the strut width is then equal to  $0.25l_w = 1050$  mm. The correspondent maximum shear force compression strength is equal to 2931 kN.

The shear capacity can also be evaluated in accordance to EC8 with a variable inclination truss model. Squat wall cannot rely on energy dissipation and consequently must be designed as DCM structures. Hence the shear strength can be evaluated according to the formula used for the calculation of shear strength in columns. According to the provisions of EC8 the shear strength is then equal to 4734 kN (for  $\cot\theta = 1.45$ ). Moreover, the failure mode prediction is related to sliding because the sliding shear strength results equal to 3315 kN, lower than the web shear stress.

### 5.3 Final remarks

In the chapter a brief review of the state of the art on squat walls and slender walls design has been presented together with NLFE method approaches. The main remarks are listed in the following:

- Alternative procedures to satisfy performance requirements and compliance criteria for RC walls resisting systems (modelled with shell elements) that circumvent the use of generalized stresses (N, M, V) could be proposed for NLFE software users.
- The proposed verifications can be performed in terms of displacements, material stresses and crack opening values limitations for damage limit state verifications and in terms of displacements, strain verifications for confined, un-confined concrete and for steel in tension and compression (considering also rebars buckling phenomena and second order effects in general) for ultimate limit state verifications.

Non linear shell modelling demonstrates to be a useful tool to predict indicators of damage fundamental for the application of performance-based earthquake engineering in wall structures.





## **Part III. Applications and Results**



**Chapter VI.**  
**Case Study I: the SMART2013**  
**Shaking Table Test**

## 6 Case Study I: the SMART2013 shaking table test

As stated in the introduction chapter, the exploitation of natural resources is nowadays of great importance, both for economical and environmental issues. The environmental issues are often correlated to the production of great amount of CO<sub>2</sub> in coal power plants. Moreover, besides carbon fossil plants, nuclear power plants are widespread in 30 nations all over the world. It is well known that in this case the need for energy is also correlated to the safeguard of population towards radiation leakage and dangerous aftermaths. It is then clear the need for a rational method for the evaluation of the safety of existing structures (several of these structures will need in a short time a renewal process) but also for the development of a methodology for a correct design. The RC members of NPPs like for example shear walls (either slender or squat) are of fundamental importance for the safety and for the operation of the power plant itself. Due to the strategic function of these power plants, the structures must be verified towards strong input forces, such as earthquakes, impacts and explosions. When subjected to strong forces structures exhibit a non linear behaviour with consequent crack opening. It is then of fundamental importance to try to predict the 3D behaviour of such structures in order to evaluate both the global and the local (e.g. multi direction cracking) response. It is then necessary to develop a research able to estimate the capacity of numerical models to predict such complex behaviour. Data validation through blind prediction and comparison of experimental tests is then a key point.

Actually several numerical instruments are used in the current practice and are available for engineers. The chapter is based on the analysis of the results produced for the blind prediction and post analyses of the results produced within the SMART2013 project. The SMART 2013 project consisted on the dynamic modelling of a service nuclear wall structure for CPY type reactors (second series of 900MWe pressurized water reactor, PWR). The  $\frac{1}{4}$  scaled model was built and tested at Saclay laboratories by SEISM institute, ([www.smart2013.eu](http://www.smart2013.eu)).

The model used is multi layer PARC\_CL model described in chapter 2. It is here remarked that this approach applied in (Belletti et al. 2013a), (Damoni et

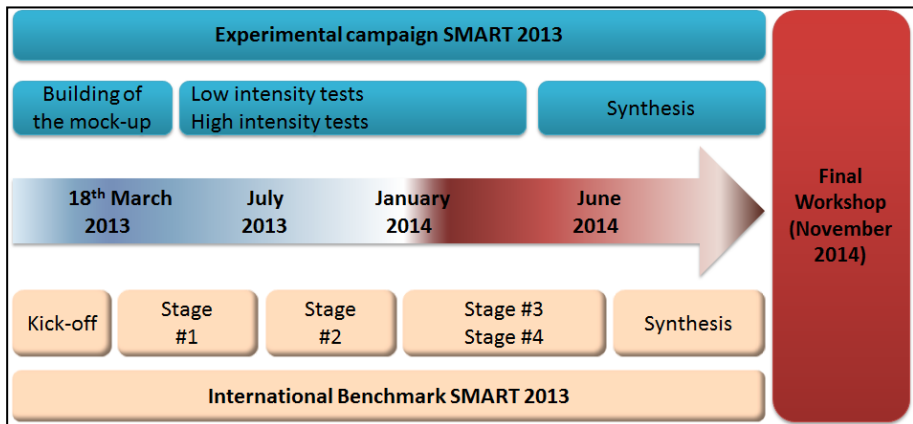


al. 2013) demonstrated to be a useful tool for the evaluation of the both local and global engineering demand parameters, EDPs, as also described in chapter 5. This is of fundamental importance for a modern performance based design. The chapter will focus on some aspects of the 4 main project stages and further details relative to post analyses will be presented.

## 6.1 Brief description of the SMART2013 project

Smart mock up: RC mock-up representing a 1:4 scaled part of a CPY type nuclear electrical building.

- The behaviour of irregular wall building characterized by coupled torsion/bending effects are investigated.
- Investigate the predictive capabilities of NLFE approaches when an irregular building is subjected to a highly damaging seismic scenario.
- Estimation of the seismic fragility.



**Figure 6.1** - SMART2013 international benchmark schedule (Richard et al., 2014).

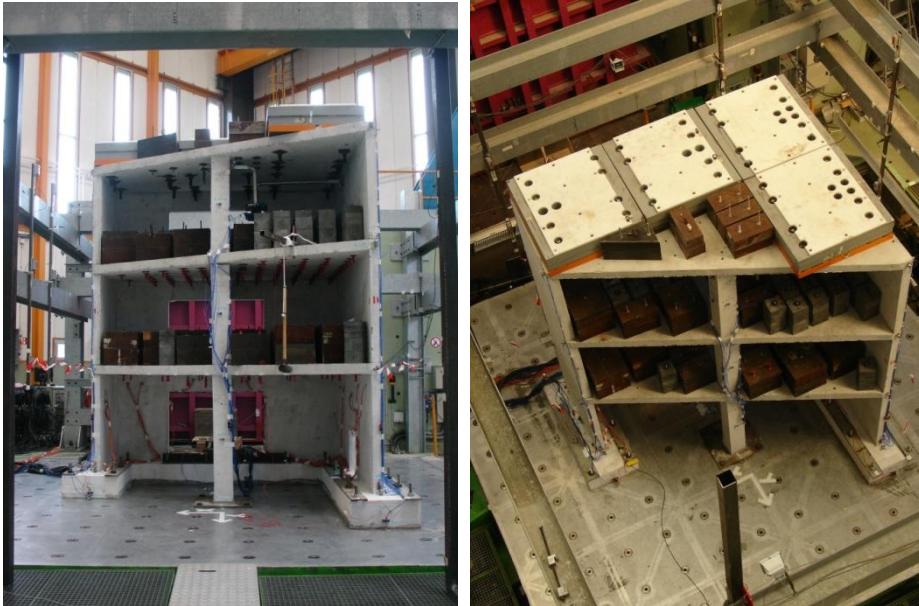
The organization committee asked the teams to complete four main stages:

- stage 1: numerical test on elementary elements,
- stage 2: dynamic linear analyses of the building,
- stage 3: nonlinear dynamic analysis under strong motion inputs,
- stage 4: generation of fragility curves.

72 teams from all over the world registered to the benchmark, 36 of them completed stage 1. Only 8 teams, including the authors that participate to the benchmark adopting the shell element model PARC\_CL, completed stage 4 (7 over 8 of them used shell elements in their nonlinear models).

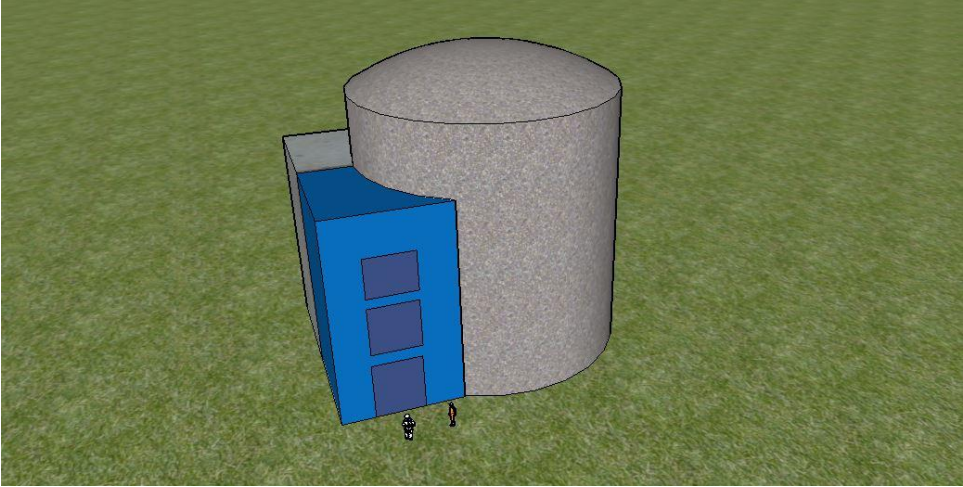
## 6.2 Smart2013 shaking table test of a 1/4 electrical facility of CPY nuclear power plants

In Figure 6.4 pictures of the specimen tested at CEA laboratory in Saclay (Paris, FR) within the SMART2013 international benchmark blind prediction are reported.

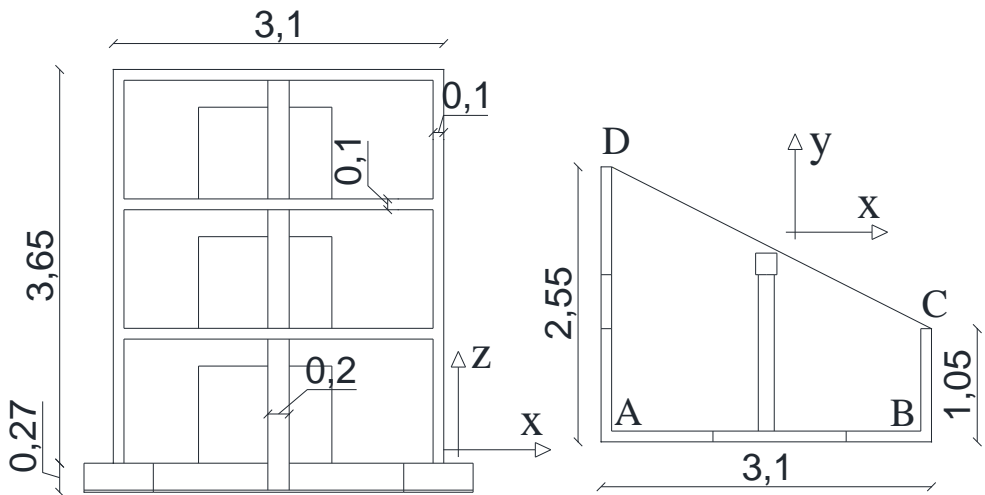


**Figure 6.2** - Mock up of the test, B. Richard, M. Fontan, J. Mazars. SMART 2013: overview, synthesis and lessons learnt from the International Benchmark. CEA/DEN Technical Report. CEA/DEN/DANS/DM2S/SEMT/EMSI/NT/14-037/A. 2014

The specimen is a simplified version of the half of a typical nuclear electrical auxiliary building, Figure 6.3. In Figure 6.4 the geometry of the mock up is reported (values are expressed in [m]).



**Figure 6.3** - Simplified 3D view of an auxiliary building (in blue) and the containment vessel.



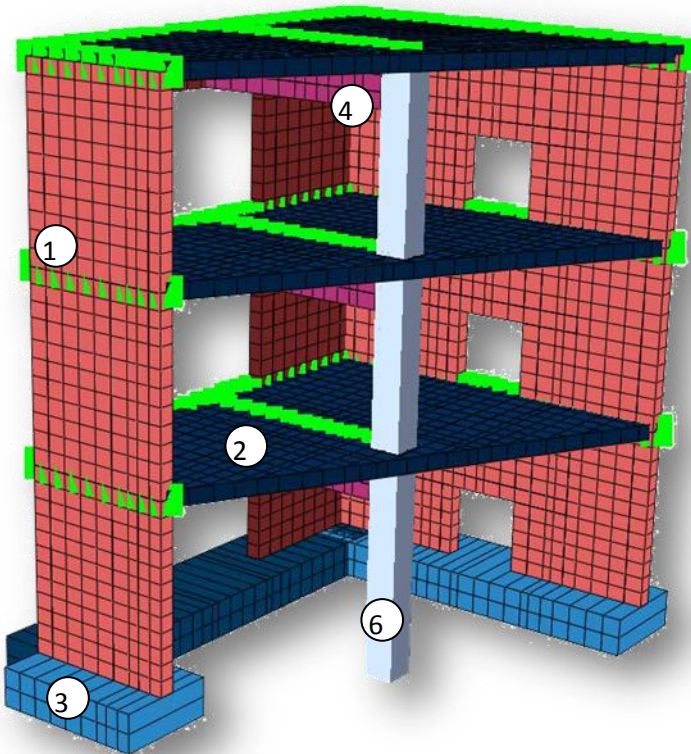
**Figure 6.4** - Specimen dimensions (measures in [m]).

### 6.3 Modelling techniques

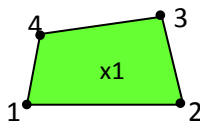
The numerical model characteristics are summarized and illustrated in Figure 6.5 and Table 6.1.

**Table 6.1** – Numerical model description.

Element	Description
[1] Walls	- Shell 4 nodes, reduced integration - Non-linear material - 3 integration points in the layer thickness
[2] Slabs	- Shell 4 nodes, reduced integration - Non-linear material - 3 integration points in the layer thickness
[3] Foundation	- Shell 4 nodes, reduced integration - Elastic material
[4] Beams	- Shell 4 nodes, reduced integration - Non linear material -3 integration points in the layer thickness
[5] Column	-3 nodes beam elements - Elastic material

**Figure 6.5** - Numerical model description.

Additional masses are considered as mass elements distributed along structural elements nodes (walls, beams, columns) which are supporting the slabs. This modelling technique may not be realistic however it can avoid convergence issues during non linear dynamic analysis. The seismic input ground motion was introduced as absolute displacements at the foundation base as no shaking table model was introduced during the blind prediction analyses. The whole specimen is 3.92m height and it is 46t weight (considering additional mass, too). The structural damping calibration is one of the main issues of the model. Only classical Rayleigh damping was considered. Moreover, for non linear elements only the mass proportional damping can be considered as the stiffness proportional damping should be introduced in the UMAT subroutine PARC\_CL. Moreover, the PARC\_CL is a secant model so it cannot properly take into consideration the correct hysteretic energy dissipation. For all these reasons the damping ratio was forced to a 10% value and the alpha Rayleigh coefficient was calculated on the first mode. The 10% value was calibrated on low intensity time history analyses with known response. Further references on this topic may be found in (Paulay and Priestley, 1992) and (ASCE, 2000). The implicit method was adopted by the Abaqus/Standard solver while the Newton-Rhapson method was used as convergence criterion. Analyses ran on a 3.20 GHz machine with 16 GB RAM. Non-linear analyses however ran on a single CPU as UMAT subroutine does not allow parallel calculation. In the analyses it was adopted the default Abaqus/Standard Hilber-Hughes-Taylor time integration. The Hilber-Hughes-Taylor operator is an extension of the Newmark method (ABAQUS, 2012). The adopted time interval is equal to 0.014s. This value was judged as a good compromise between calculation time, available memory and correct description of a seismic input sampled at 1024 Hz (0.00097s). Shell elements with 4 integration points and reduced integration (S4R elements) have been chosen in order to save memory usage and calculation time. Further studies will be conducted in order to understand the influence of upper grade shell elements, Figure 6.6.



**Figure 6.6** - S4R element (4 nodes, reduced integration).

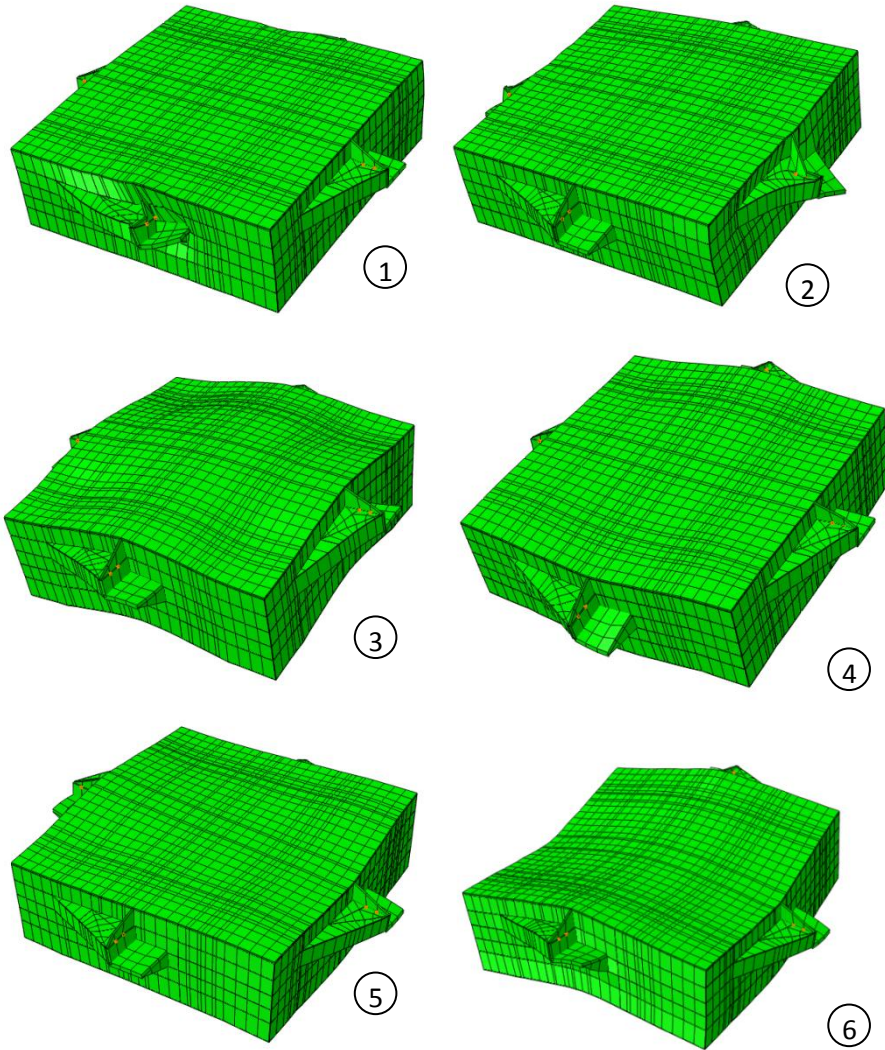
### 6.3.1 The shaking table issue

The shaking table has been modelled only as an early attempt and for the Stage #2 frequency analysis. In the linear and non-linear time history analyses the shaking table model has been removed in order to reduce the number of DOF and elements. However, it is described in the following the calibration of the shaking table model as it will be introduced in the results of RUN#19 as well.

**Table 6.2** – Frequency analysis results for shaking table model calibration.

<b>Frequency analysis: 8 rigid actuators boundary conditions</b>					
<u>Abaqus</u>					
Mode n.	Eigenvalue	Frequency		Error%	
		(RAD/TIME)	(CYCLES/TIME)		
1	1.14E+05	337.99	53.742	-1.03	
2	1.15E+05	338.88	53.884	-0.77	
3	1.75E+05	418.64	66.62	1.40	
4	2.21E+05	469.7	74.316	1.11	
5	2.22E+05	470.76	74.482	1.34	
6	3.99E+05	631.75	100.06	1.07	
				<b>Mean error</b>	<b>1.12</b>
<u>Given values</u>					
Mode n.	Eigenvalue	Frequency			
		(RAD/TIME)	(CYCLES/TIME)		
1	1.16E+05	341.2	54.3	-	
2	1.16E+05	341.2	54.3	-	
3	1.70E+05	412.8	65.7	-	
4	2.13E+05	461.8	73.5	-	
5	2.13E+05	461.8	73.5	-	
6	3.87E+05	622.0	99	-	

It is possible to notice that the shaking table is an extremely stiff element.



**Figure 6.7** - Shaking table modal shape.

### 6.3.2 Additional masses

As already stated, in the blind prediction model additional masses are considered as mass elements distributed along structural elements nodes (walls, beams, columns) which are supporting the slabs.

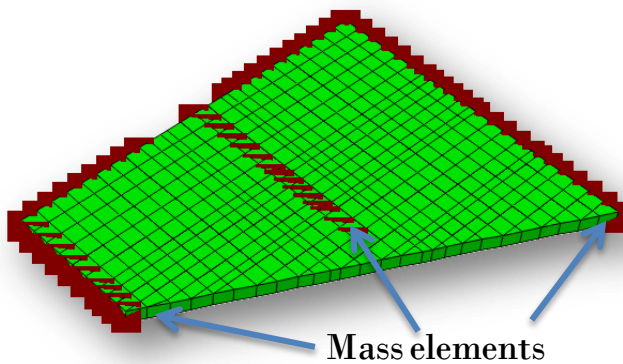
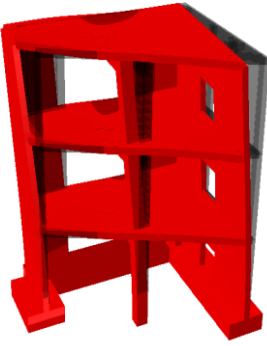
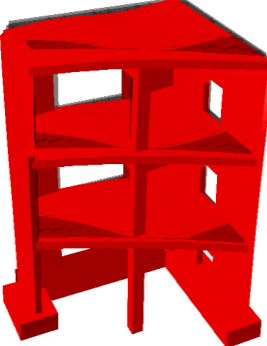
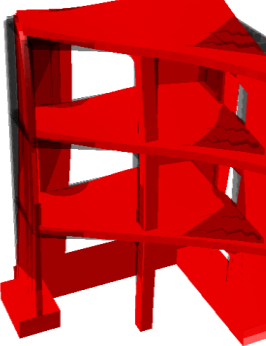
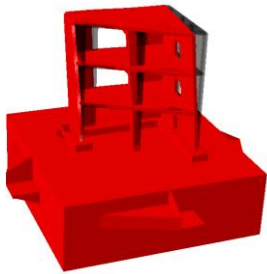

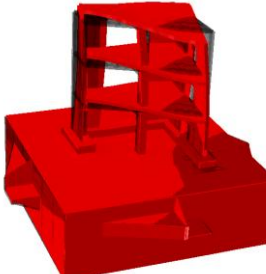


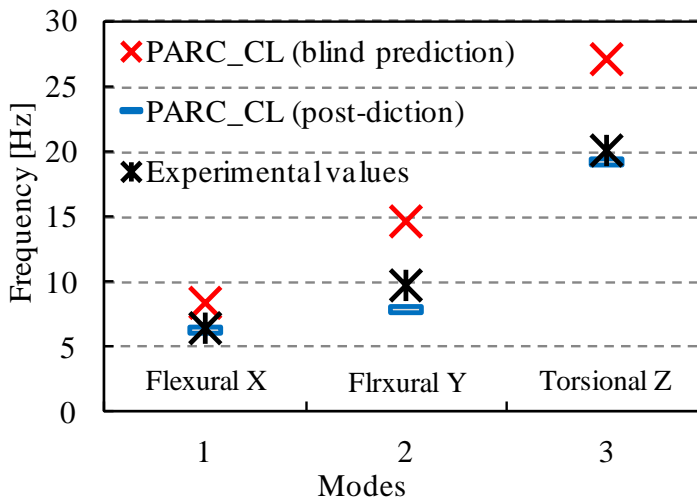
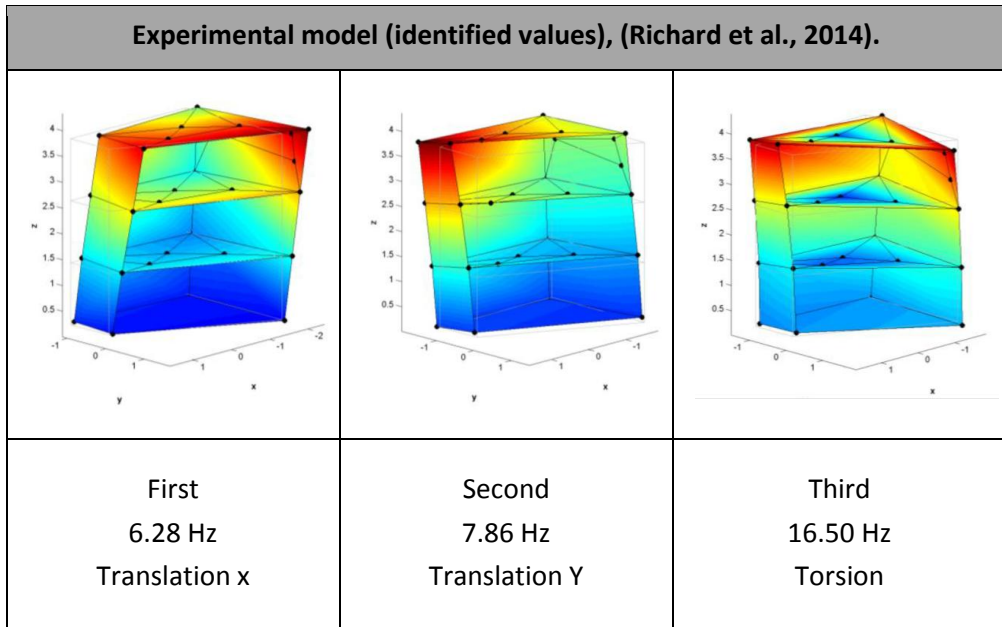
Figure 6.8 - Mass elements.

## 6.4 Frequency analysis: experimental vs. blind prediction vs. post diction

The non linear model was calibrated with frequency analysis on the first three modes which had been experimentally identified and provided during the benchmark. In Figure 6.9 a) the experimental results are compared with the numerical results given by the model described in 3.1 and with the results given by a “post diction” model. In the “post-diction” the shaking table is introduced, Figure 6.9 b), (further details are given in 6.7).



Non-linear model with additional masses (numerical values)		
		
<p>First 8.38 Hz Translation x</p>	<p>Second 14.64 Hz Translation Y</p>	<p>Third 27.11 Hz Torsion</p>
Non-linear model with additional masses and shaking table (numerical values)		
		
<p>First 6.43 Hz Translation x</p>	<p>Second 9.72 Hz Translation Y</p>	<p>Third 20.09 Hz Torsion</p>



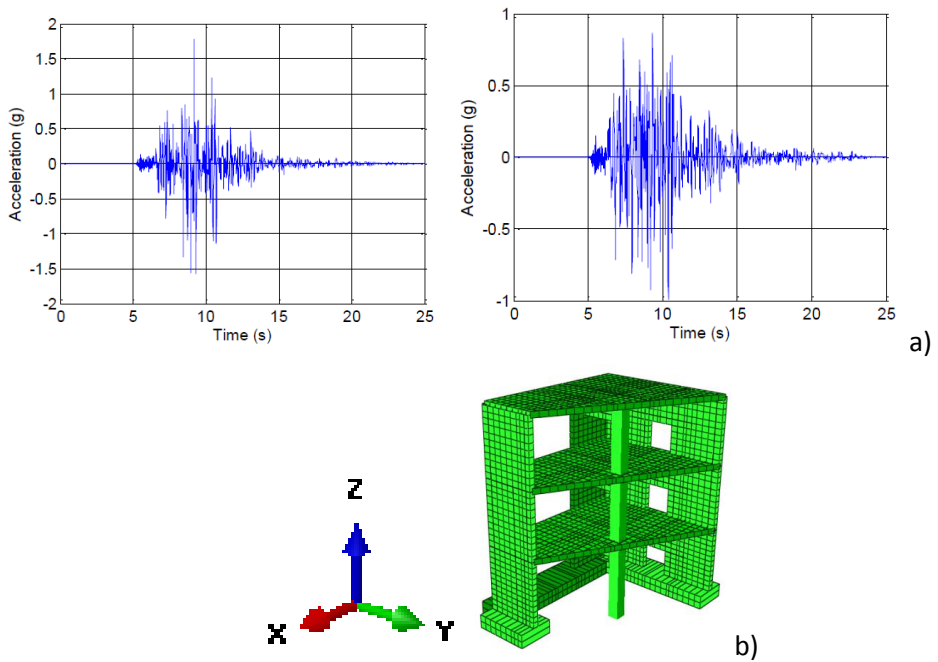
**Figure 6.9 - a)** Comparison between experimental and numerical frequency analyses.

The blind prediction model (without shaking table modelling) presented in the chapter can give a good estimation only of the first mode. The model implemented during the “post diction” analysis (with shaking table modelling) gives a better estimation of all the three modes. However, the introduction of

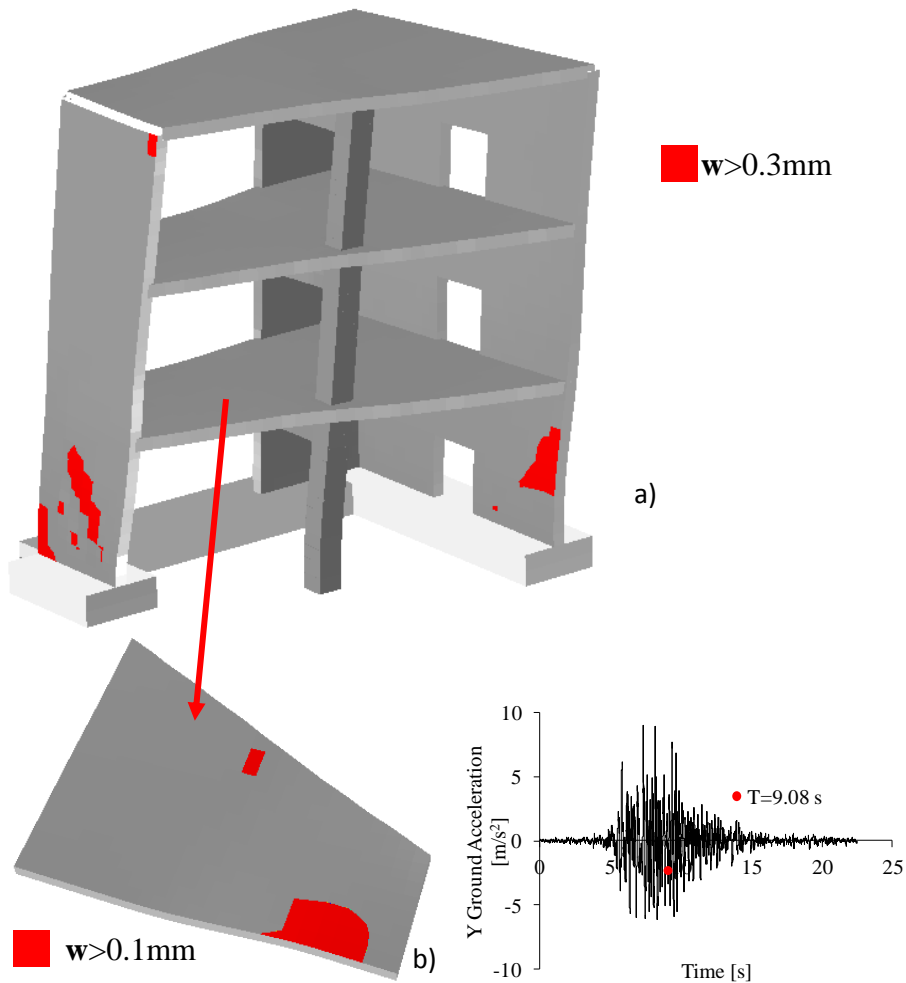
the shaking table model is paid with high computational costs during time history analyses. Further studies are required in order to assess the influence of the shaking table model on the global dynamic response.

## 6.5 Time history analysis

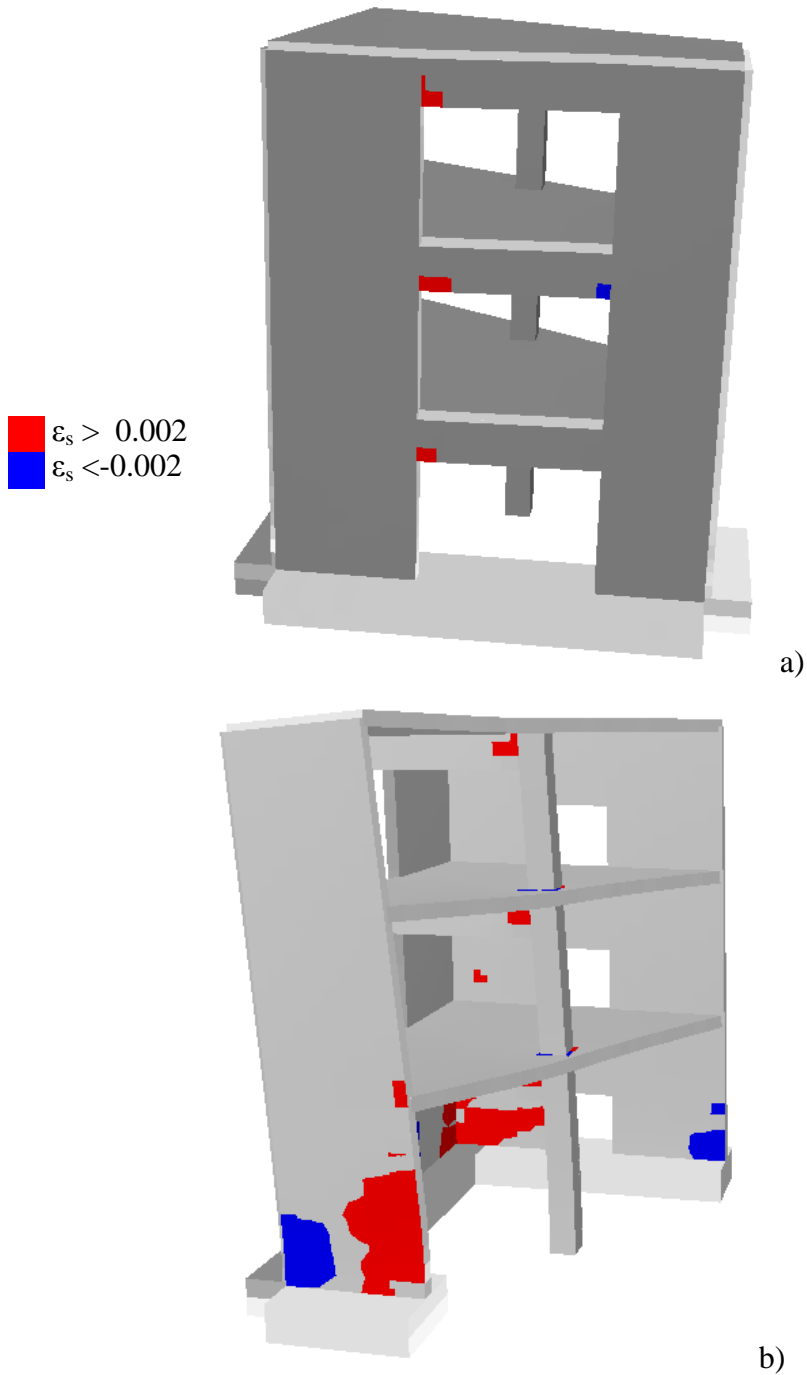
The most significant results related to the strongest seismic input adopted during the test (Run#19 of the benchmark, target PGA=1.6g, seismic input duration 22s, Figure 6.10). Results are reported in terms of crack opening and concrete and steel strains, Figure 6.11 to Figure 6.13.



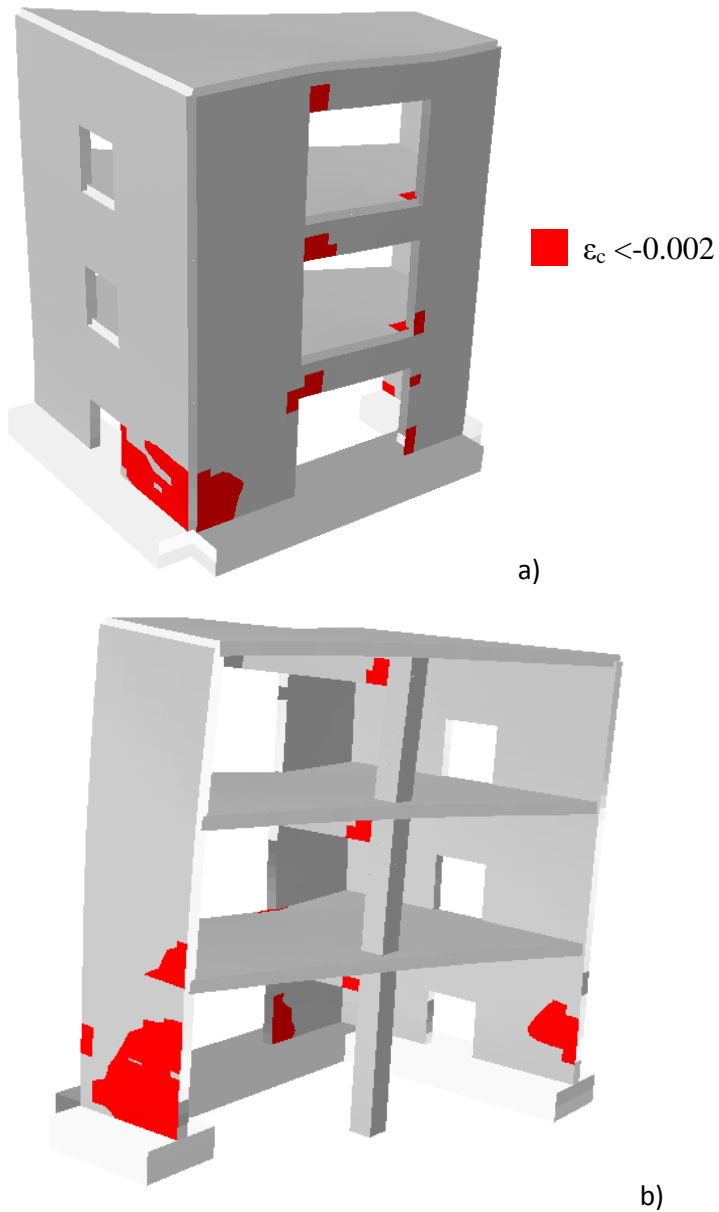
**Figure 6.10** - a) Ground motion input (for X and Y dimension, real Northridge), b) adopted reference system.



**Figure 6.11** -. a) Crack pattern, Run#19 @ 9.08s. The area where cracks are completely opened ( $w > 0.3\text{mm}$ ) is in black; b) cracking phenomena at first floor slab,  $w > 0.1\text{ mm}$ , Run#19 @ 8.76s. The corresponding acceleration is reported with respect to the total accelerogram.



**Figure 6.12** - a) Yielding of horizontal rebar in beams, Run#19 @ 6.33s; b) yielding of vertical rebar on the shortest wall, Run#19 @ 7.47s.



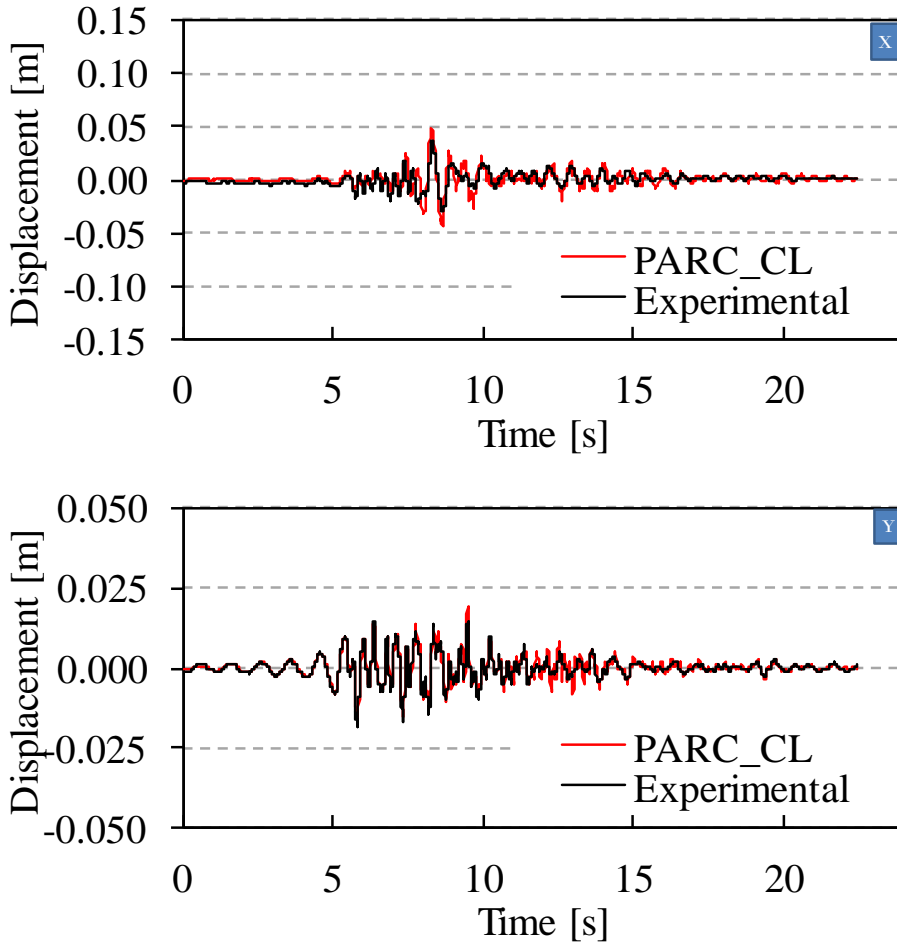
**Figure 6.13** - a) Areas where the compressive strains  $\epsilon_c$  are lower than the strain at peak compression stress are in white, Run#19 @ 8.07s; b) as the response direction changes, Run#19 @ 8.22s, it is possible to see a strong compression field at the base of the shortest wall where it was observed the experimental failure of the specimen for concrete crushing.

The model is able to catch in plane shear phenomena, as shown by crack opening in Figure 6.11 a) and b). Moreover, it is possible to notice that cracks develop also in concrete slabs and therefore the hypothesis of rigid floor, commonly adopted in the design practice, is not fulfilled. Rebars yield both in beams and at the walls basis. It is interesting to notice that the model shows a strong strain state at the base of the shortest wall, Figure 6.13 b), where during the experimental tests it was observed concrete crushing at wall/foundation interface. Further studies are needed in order to properly implement the interface modelling as this aspect may significantly affect the analysis especially in case of existing structures which are often provided with poor detailing.

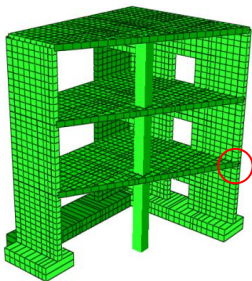
### **6.5.1 Absolute displacements**

In Figure 6.14 to Figure 6.16 the comparison between experimental and numerical data have been reported for point D (point D is indicated in Figure 6.4) both in X and Y direction. The blind prediction model overestimates the peak displacement of about 30%. Some frequencies tend to be under-damped in the post peak phase. In Y direction displacements are much smaller as the structure is stiffer in that direction. Also in this case the model overestimates the maximum displacement of about 30%. Some undamped frequencies are visible especially for the response of the 3rd floor, however the post peak absolute displacements are very small (< 1mm). In both directions the frequency response is evaluated with good accuracy.

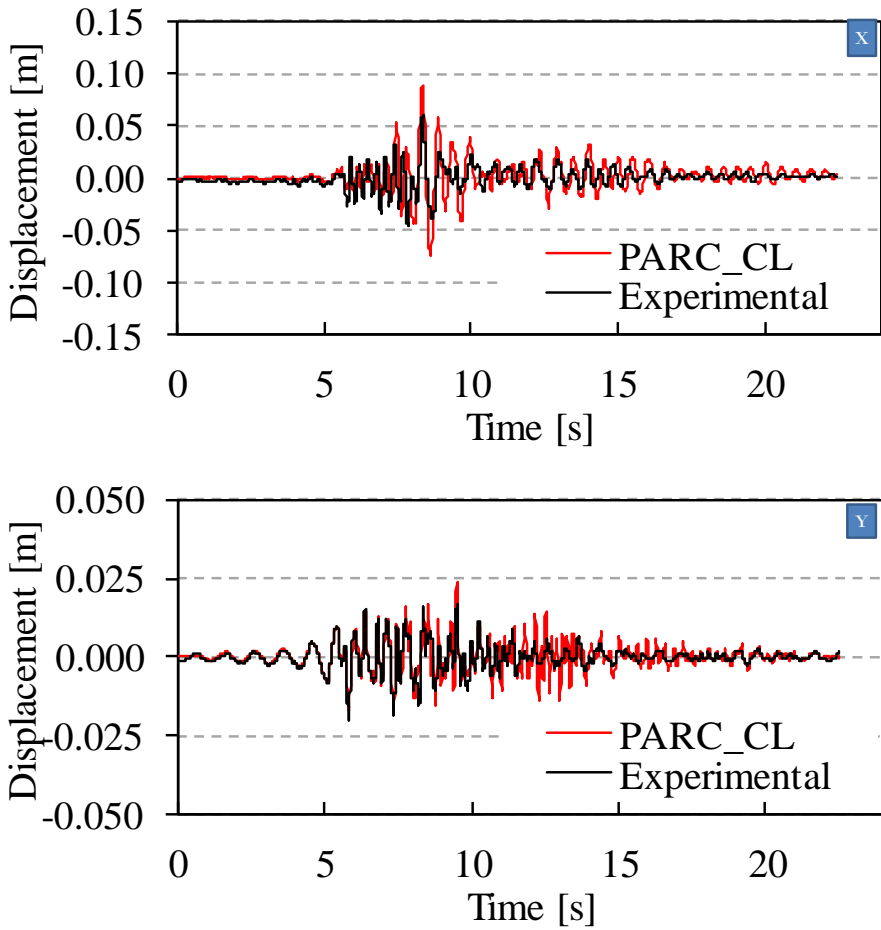
Results are compared also at each floor corner, Figure 6.17, Figure 6.19 (numerical results are in light blue and experimental outputs are in orange, scale factor equal to 10). It is remarked that the specimen failed at wall/foundation interface, point C: this failure mode was not caught in the model and led to some inconsistencies.



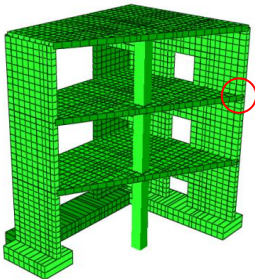
**Figure 6.14** - Comparison between numerical and experimental results for X and Y displacements measured at point D at floor #1.

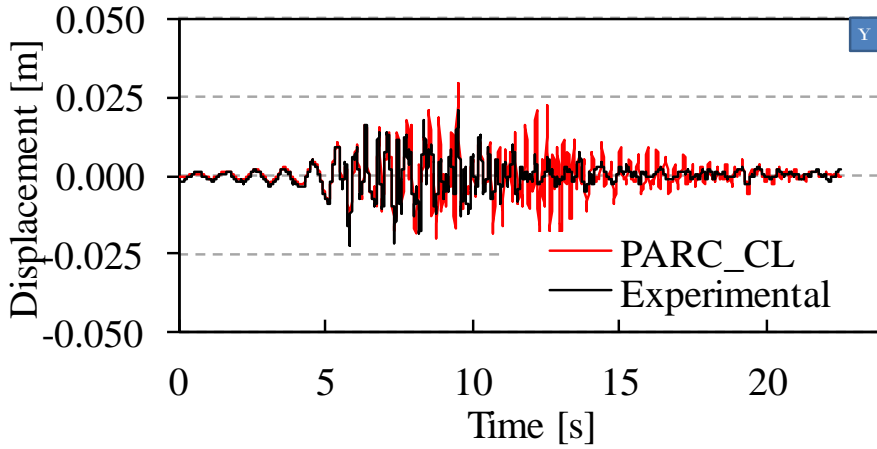
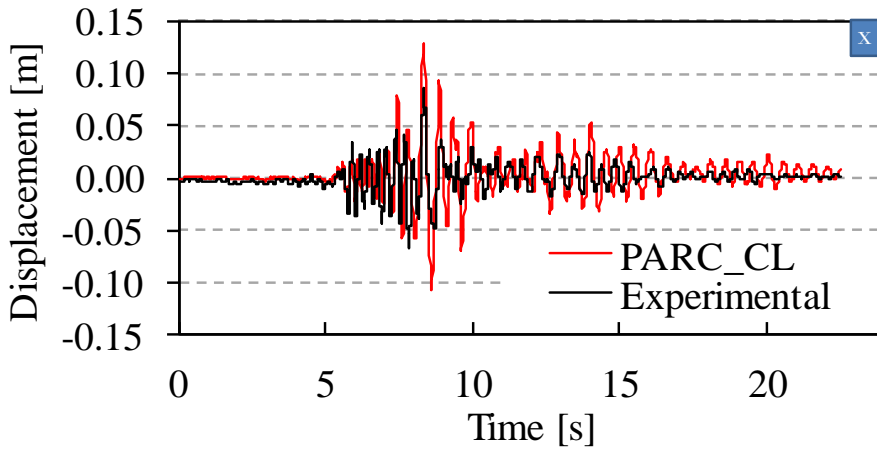




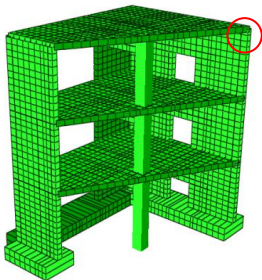


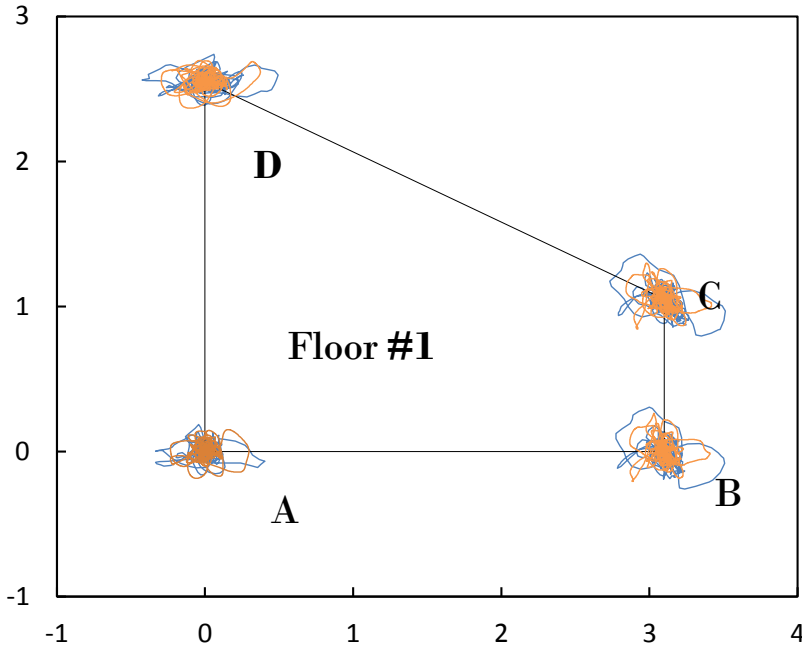
**Figure 6.15** - Comparison between numerical and experimental results for X and Y displacements measured at point D at floor #2.



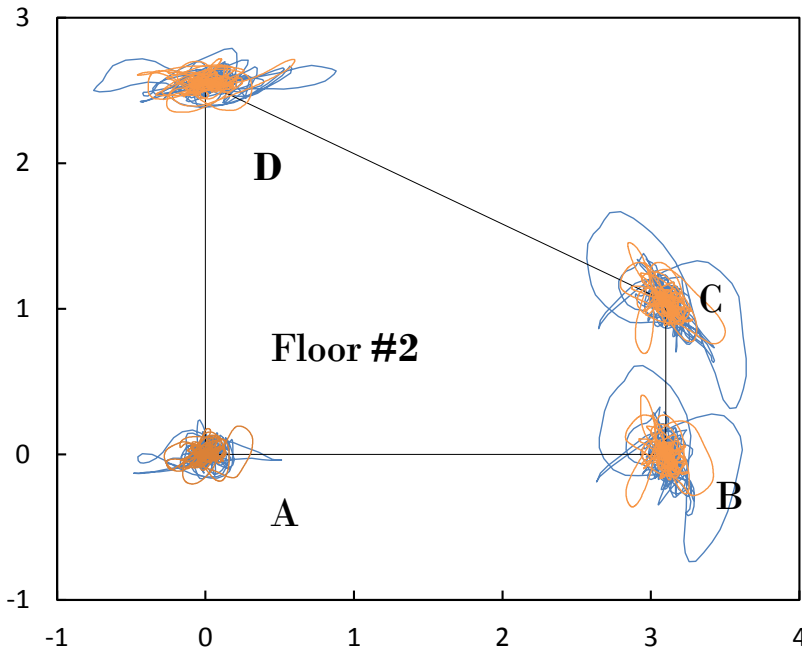


**Figure 6.16** - Comparison between numerical and experimental results for X and Y displacements measured at point D at floor #3.

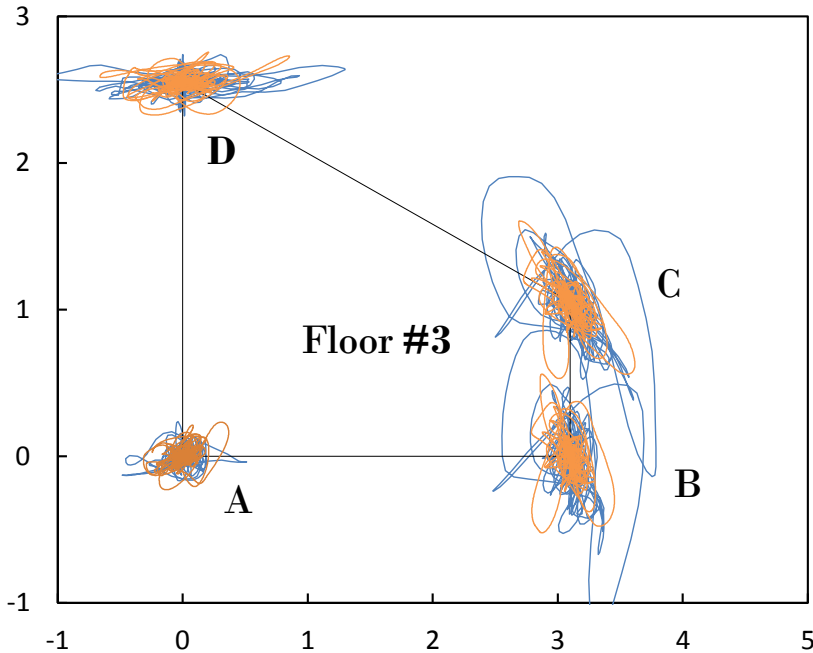




**Figure 6.17** - Comparison between numerical and experimental results, Floor #1 global displacements.



**Figure 6.18** - Comparison between numerical and experimental results, Floor #2 global displacements.



**Figure 6.19** - Comparison between numerical and experimental results, Floor #3 global displacements.

## 6.6 Probabilistic analysis

Fragility curves have been defined using 50 synthetic input accelerograms (provided by the test organizer) for a total of 50 non linear runs and 50 linear runs. The model used was modified with the introduction of a 6 DOFs connector at foundation level for the description of the soil structure interaction by setting proper values of equivalent damping and stiffness. For each run some parameters were changed according to a Monte Carlo simulation in the hypothesis of log normal distribution of random variables (concrete tensile strength  $f_{ct,i}$  at each  $i$  storey, additional structural damping  $\xi$ , equivalent damping  $\gamma$  and stiffness  $k$  of soil structure interaction). Analyses were run by applying acceleration at the foundation level.

**Table 6.3** - Random input variables used for each run.

RUN#	Seismic input	$f_{cti}$	Equivalent damping	Equivalent stiffness	Additional damping
1	+X <sub>1</sub>	$f_{ct1,1}$	$\gamma_{1,1}$	$k_{1,1}$	$\xi_1$
	+Y <sub>1</sub>	$f_{ct2,1}$	$\gamma_{2,1}$	$k_{2,1}$	
		$f_{ct3,1}$	$\gamma_{3,1}$	$k_{3,1}$	
...	...	...	...	...	...
50	+X <sub>50</sub>	$f_{ct1,50}$	$\gamma_{1,50}$	$k_{1,50}$	$\xi_{50}$
	+Y <sub>50</sub>	$f_{ct2,50}$	$\gamma_{2,50}$	$k_{2,50}$	
		$f_{ct3,50}$	$\gamma_{3,50}$	$k_{3,50}$	

**Table 6.4** - Statistical parameters of the random variables used in the analysis.

Variable	Mean value	Coefficient of variation	Probabilistic distribution
$f_{ct,i}$	3 MPa	33%	Lognormal
Additional damping	3%	20%	Lognormal
Equivalent stiffness			
X,Y	$3.50 \cdot 10^8 \text{ Nm}^{-1}$	1%	Lognormal
Z	$4.60 \cdot 10^8 \text{ Nm}^{-1}$	1%	Lognormal
rX	$6.47 \cdot 10^8 \text{ Nm}$	1%	Lognormal
rY	$11.3 \cdot 10^8 \text{ Nm}$	1%	Lognormal
Equivalent damping			
X,Y	$3.53 \cdot 10^6 \text{ Nsm}^{-1}$	2%	Lognormal
Z	$2.63 \cdot 10^6 \text{ Nsm}^{-1}$	2%	Lognormal
rX	$1.56 \cdot 10^6 \text{ Nsm}$	2%	Lognormal
rY	$3.18 \cdot 10^6 \text{ Nsm}$	2%	Lognormal

The Intensity measure, IM, parameters used for the generation of fragility curves with the corresponding mathematical formulation are (Eq. 7 – Eq. 9):

- **PGA**: peak ground acceleration.

$$PGA = \text{MAX}_{t \in [t_0, t_f]} |\Gamma(t)| \quad (7)$$

- **CAV**: Cumulative Absolute Velocity, (Campbell e Bozorgnia 2010).

$$CAV = \int_{t_0}^{t_f} |\Gamma(t)| dt \quad (8)$$

- **ASA:** Average Spectral Acceleration, (De Blasio et al. 2014).

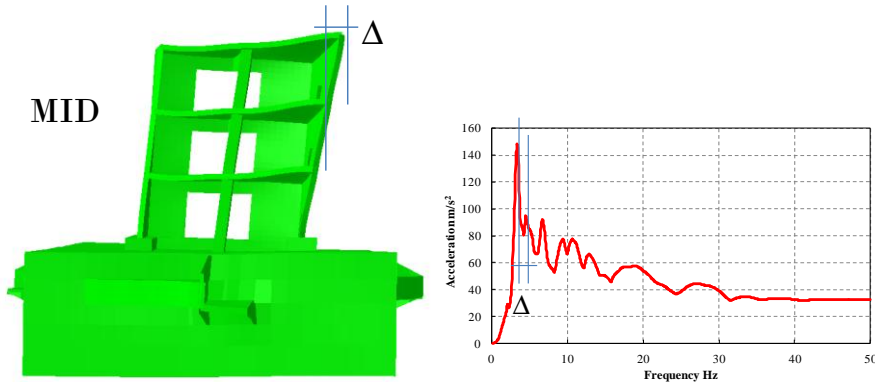
$$ASA = \int_{0.5f_0}^{f_0} Sa(f)df \quad (9)$$

where  $t_0$  e  $t_f$  are respectively the first and last time step of the accelerogram  $\Gamma(t)$ ,  $f_0$  is the fundamental frequency and  $Sa(f)$  is the spectral acceleration. It can be noted that the ASA value is dependant not only on the input characteristics but also on the structural ones (via the frequency value).

Two main engineering demand parameters were considered:

- Maximum Interstorey Drift, MID, in both direction
- Eigen Frequency Drop Off, EFDO, of the undamaged vs. damaged model

The two adopted EDPs are graphically described in Figure 6.20.



**Figure 6.20** – MID and EDFO examples.

The fragility curves parameters were calculated as described in Chapter 2 of the current thesis via linear regression of  $Y_i$  values of EDPs derived from the 50 runs in the bi-logarithmic graph and the correspondent  $\Theta_i$  values of the IMs, Eq 10.

$$\ln(Y) = a + b \cdot \ln(\Theta) \quad (10)$$

Once coefficients  $a$  and  $b$  are known it is possible to calculate the median capacity according to Eq.11:

$$\ln(A_m) = \frac{\ln(s) - a}{b} \quad (11)$$

where  $s$  is the threshold damage value, Table 6.5 ( $h$  = interstorey height).

**Table 6.5.** Damage levels.

	Light damage	Controlled damage	Extended damage
MID	$h/400=3\text{mm}$	$h/200=6\text{mm}$	$h/100=12\text{mm}$
EFDO	15%	30%	50%

Standard deviation may be defined as:

$$\beta^2 = \frac{1}{N} \sum_{i=1}^N (\ln(Y_i) - \mu_i)^2 \quad (12)$$

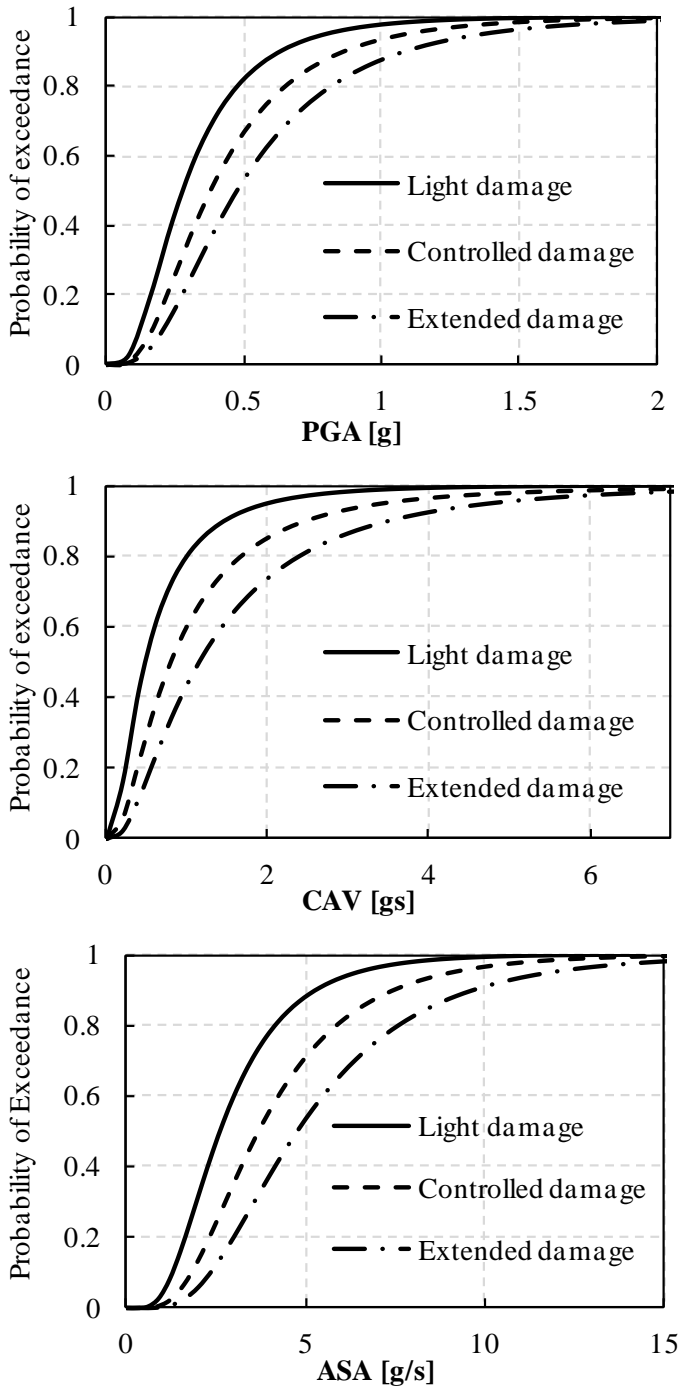
where  $N$  is the samples number,  $Y_i$  is the EDP output value for run  $i$  and  $\mu_i$  is calculated according to Eq. 13:

$$\mu_i = a + b \ln(\Theta_i) \quad (13)$$

where  $\Theta_i$  is the IM value of the  $i$  run. Finally, the fragility curve for a particular damage state is given by Eq. 14:

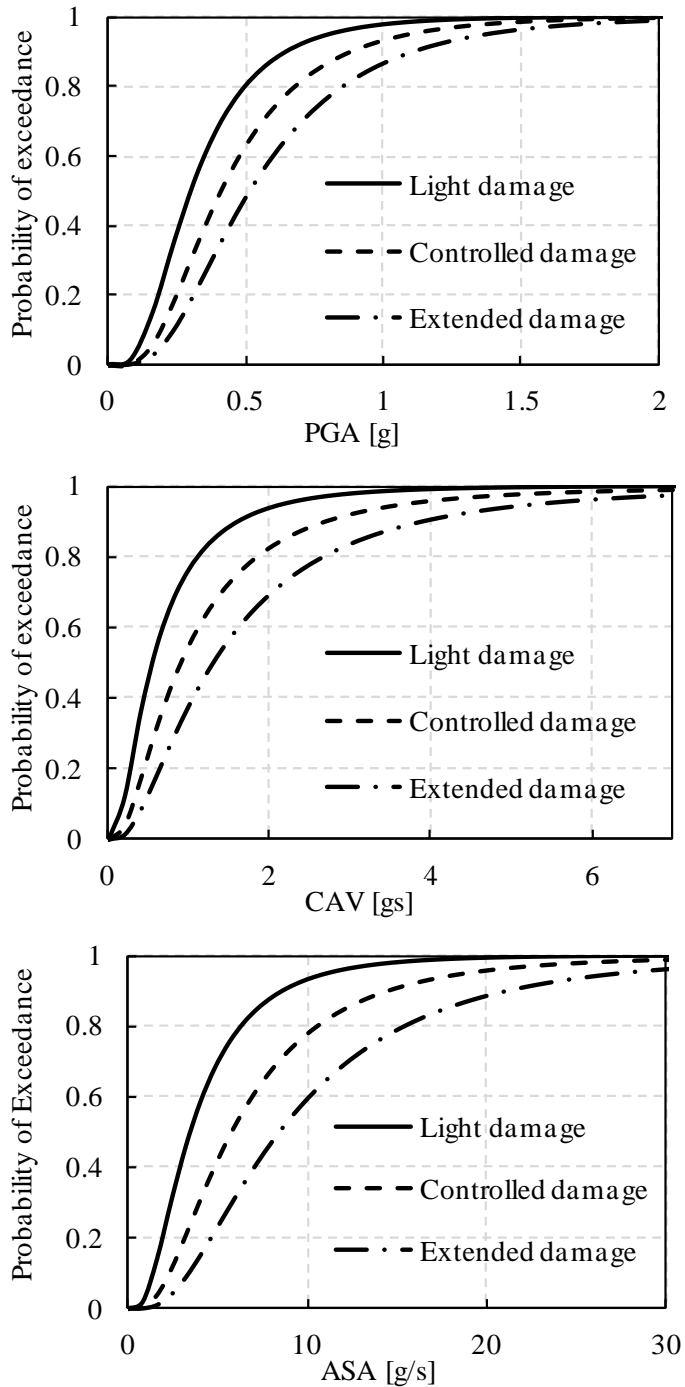
$$P_f(\theta) = \Phi\left(\frac{\ln(\theta / A_m)}{\beta}\right) \quad (14)$$

where  $\theta$  is the IM considered while  $\Phi(x)$  is the standard repartition function. The results of the probabilistic study are reported in the following. Two sets of non linear fragility curves are reported in the following. The first set is relative to MID for x-direction (Figure 6.21) while the second one is relative to EFDO of the first mode, Figure 6.23. IMs are calculated for the seismic input in the x-direction. It is observed that in particular the structure has an extended damage probability equal to 90% for a PGA equal to 1.2g. Moreover, the ASA40 IM resulted to be the best one in terms of mean squared error. This is quite rational as this indicator is able to take into account the structure response both in the damaged and undamaged state.

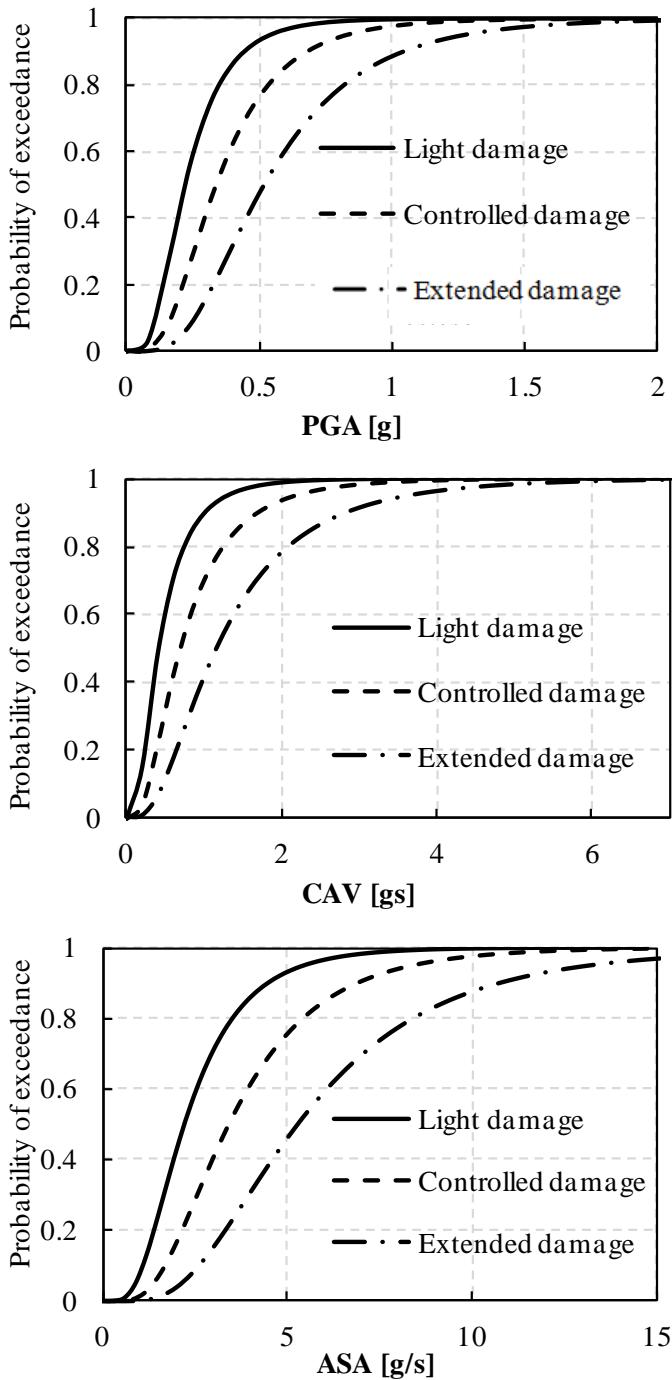


**Figure 6.21** –Eigen Frequency Drop Off (1st mode). IMs are calculated on the x-direction earthquake.

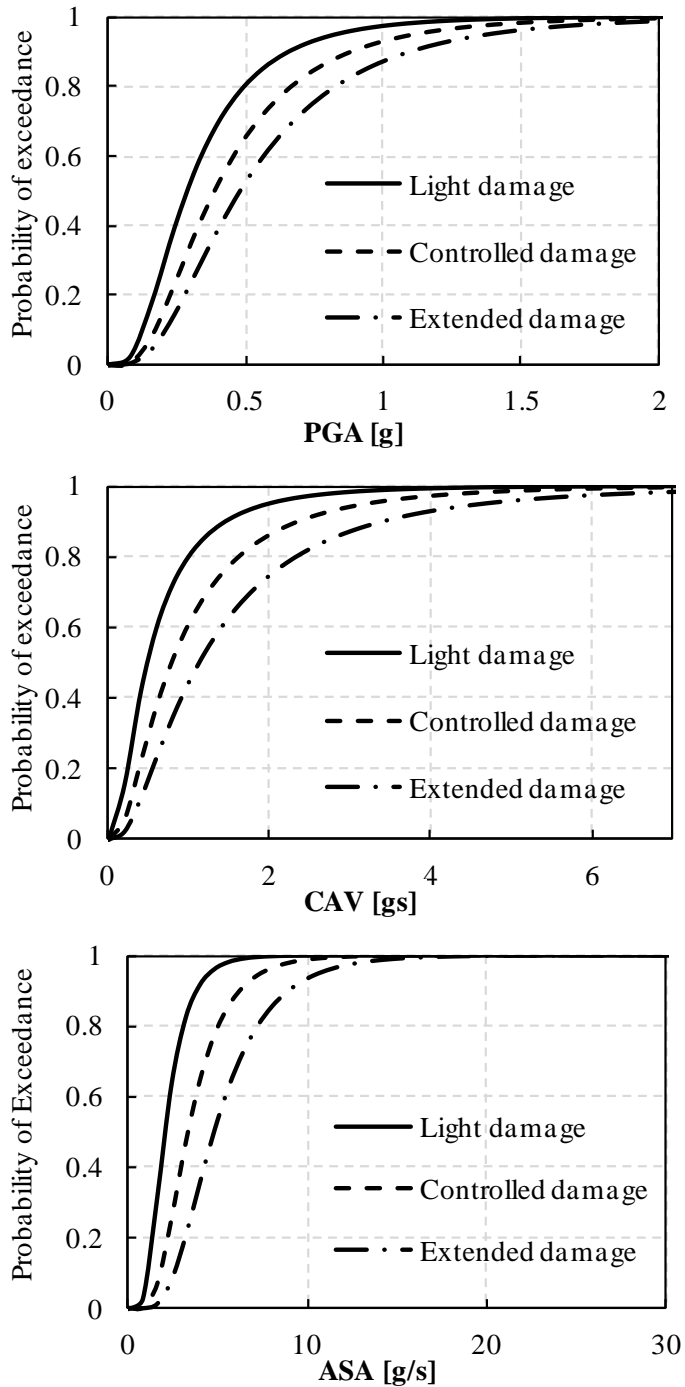




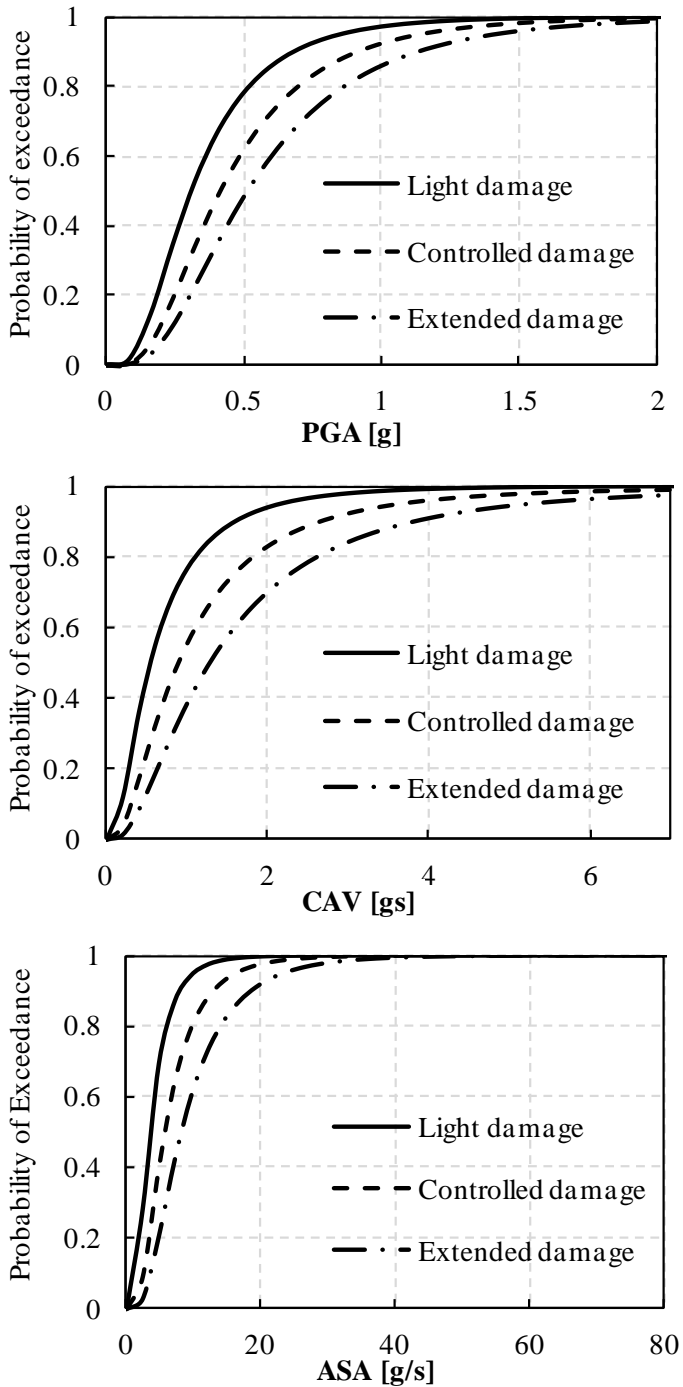
**Figure 6.22** –Eigen Frequency Drop Off (2nd mode). IMs are calculated on the x-direction earthquake.



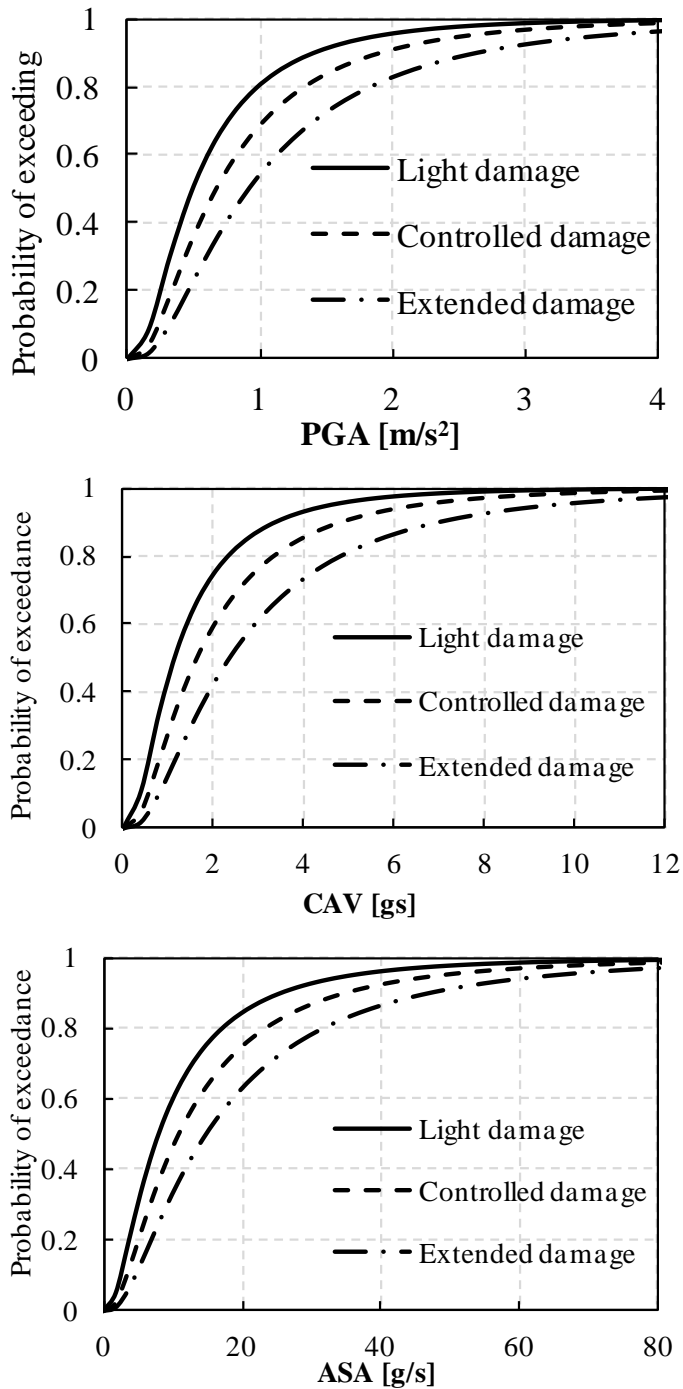
**Figure 6.23** – Maximum Interstorey Drift (x-direction). IMs are calculated on the x-direction earthquake and ASA is calculated on the first mode.



**Figure 6.24** –Eigen Frequency Drop Off (1st mode). IMs are calculated on the y-direction earthquake.



**Figure 6.25** –Eigen Frequency Drop Off (2nd mode). IMs are calculated on the y-direction earthquake.



**Figure 6.26** – Maximum Interstorey Drift ( $y$ -direction). IMs are calculated on the  $y$ -direction earthquake and ASA is calculated on the second mode.

In Table 6.6 and Table 6.7 the  $\beta$  values for each IM and EDF are reported. The ASA parameter seems to be the IM able to give significant values especially in correlation with EFDO.

**Table 6.6 –  $\beta$  values (IMs x-direction).**

	<b>PGA</b>	<b>CAV</b>	<b>ASA</b>
<b>MID</b>	0.55	0.70	0.55
<b>EFDO 1</b>	0.65	0.88	0.54
<b>EFDO 2</b>	0.64	0.85	0.72

**Table 6.7 –  $\beta$  values (IMs y-direction).**

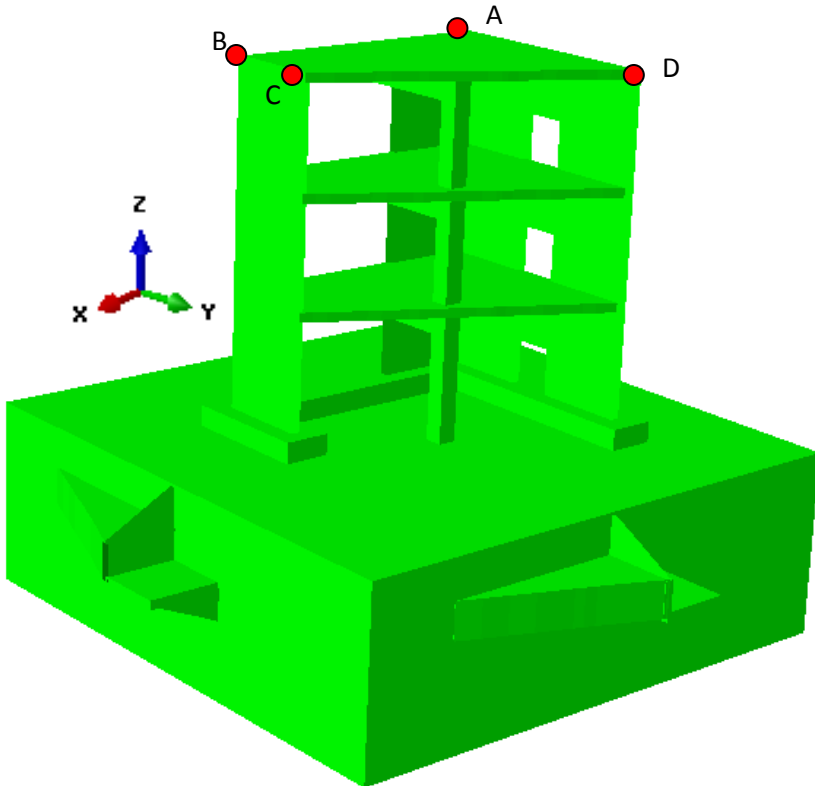
	<b>PGA</b>	<b>CAV</b>	<b>ASA</b>
<b>MID</b>	0.83	0.85	0.91
<b>EFDO 1</b>	0.65	0.87	0.49
<b>EFDO 2</b>	0.62	0.84	0.64

## 6.7 Post-analysis: global results

### 6.7.1 Model Updating

As mentioned before, one post analysis was run in order to improve the results.

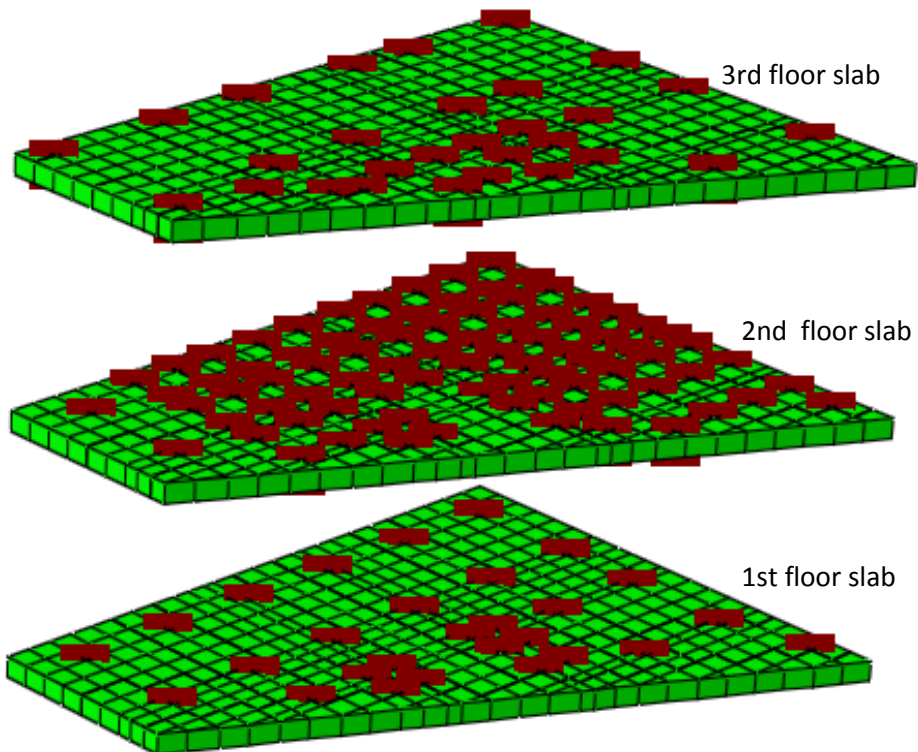
- shaking table was introduced in the model for a correct description of the modal shapes.
- signal resampling and base line correction accelerations were applied at actuator level.
- elastic brick elements were used for the foundation model.
- concentrated masses were redistributed on the non linear slabs elements.



**Figure 6.27** – Global model provided with shaking table. Important points are reported in order to better understand results.

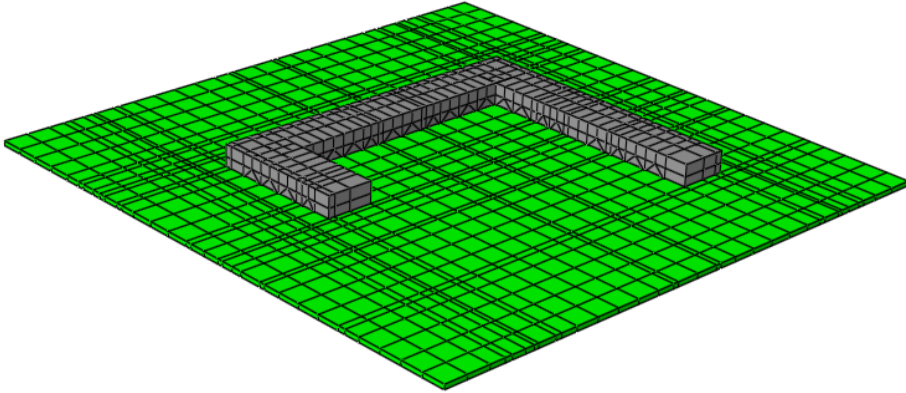
### 6.7.2 Mass distribution and foundation model

The concentrated mass elements have been distributed on points corresponding to steel plates and masses dowel connections, Figure 6.28. The updated foundation model is made by C3D8R and C3D6 elastic brick elements. The nodes geometry of the shaking table slab was left unchanged. Walls shell elements are embedded in foundation elements. Embedded shell elements have zero density and are used in order to consider stress penetration of wall reinforcement continuous to foundation, Figure 6.29.

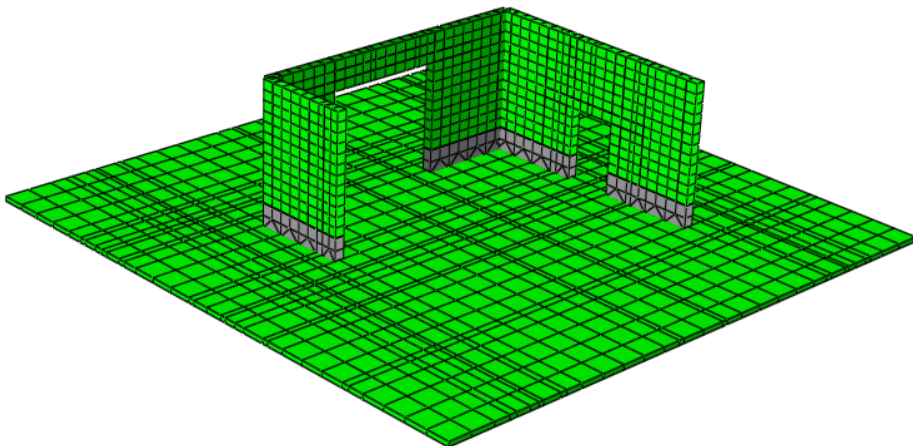


**Figure 6.28** – Concentrated masses on slabs of the updated model.





**Figure 6.29** – Foundation model with brick elements.



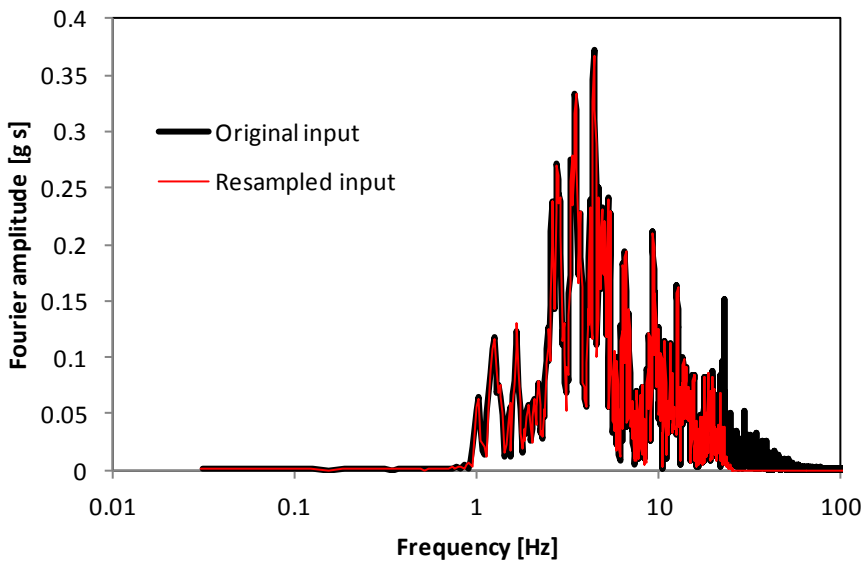
**Figure 6.30** – First storey walls: shell elements embedded in foundation in grey colour.

### 6.7.3 Seismic input

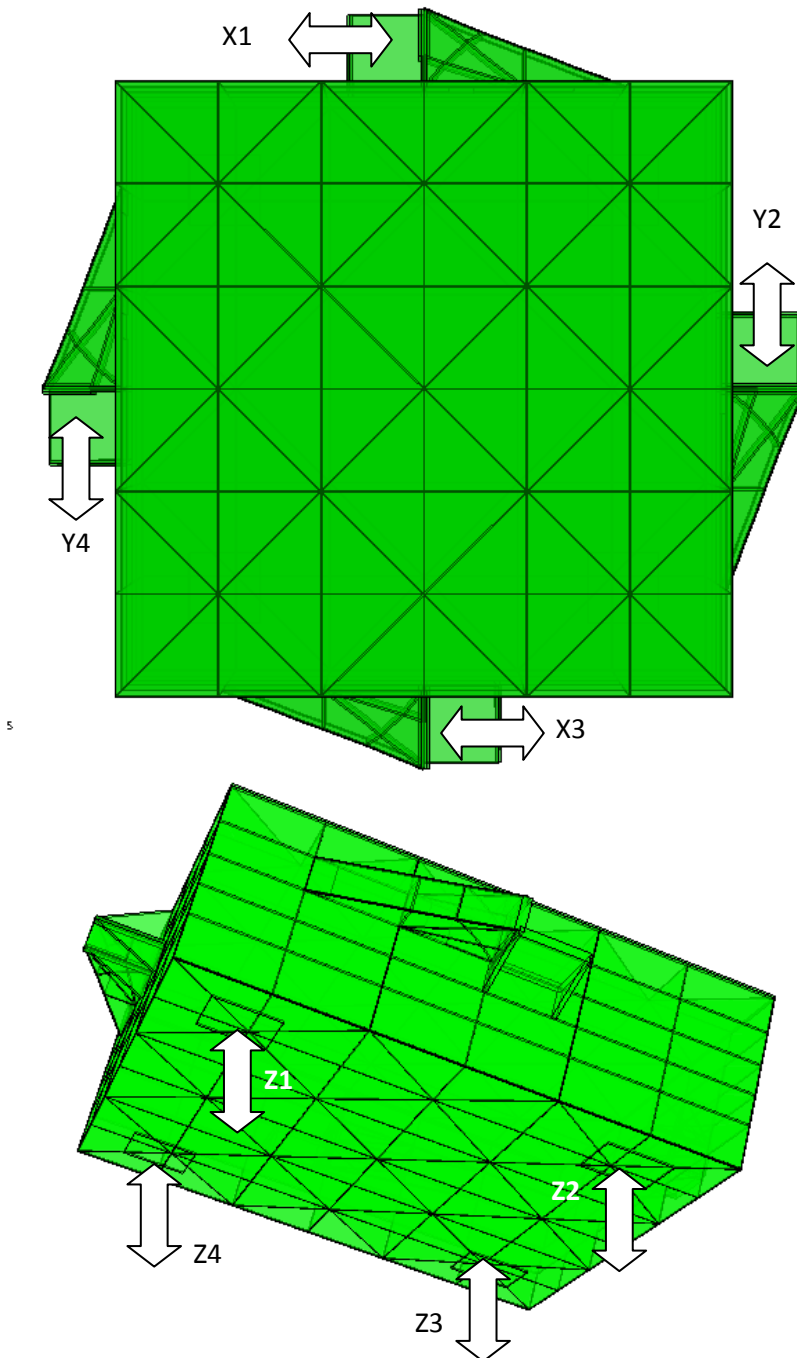
As mentioned before, the seismic input was applied as acceleration at actuators level. The eight actuators position is reported in figure. According to what said in chapter 4, the input accelerograms were modified according to the following procedure.

### *Resampling and filtering of the signal*

The signal was resampled according to (Thunell, 2014) from 1024 Hz to 45 Hz by means of the Matlab command `resample`, which follows the syntax `{a(t)resampled}=resample({a(t)},new_frequency,old_frequency)`. The resampling procedure works like a lowpass filter. Higher noise frequencies are filtered away while the 30Hz frequency (3rd vibration mode) is kept reasonably unchanged. The new signal is then sampled back to 1000Hz (1 kHz) in order to obtain a numerical simulation base motion input for time history simulations with an adequate representation of the event, and to correctly compute response spectrum having small errors, due to time signal temporal discretization, below frequencies of around 100 Hz. The effect of the resampling procedure are summarized in Figure 6.31 for the acceleration input at actuator X1.



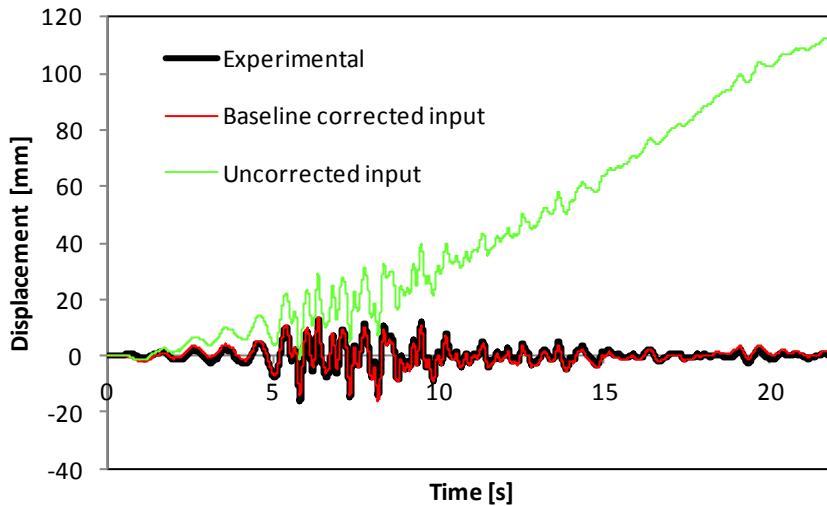
**Figure 6.31** – Effect of resampling on the original input. Frequency above 50 Hz are filtered.



**Figure 6.32** – Acceleration on the shaking table are applied at aactuators level (4 actuators in the plane, 4 vertical acutators).

### Baseline correction of the signal

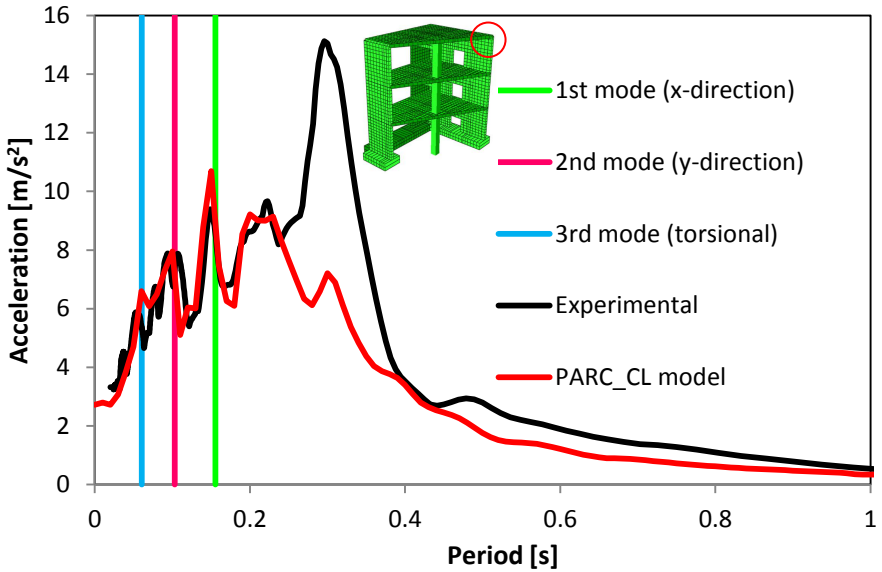
The resulting signal was corrected by means of a 3rd order baseline correction by means of Seismosignal input. It can be shown that in this case a cubic correction is sufficient to obtain a reasonable displacement field (but also avoiding distortions of the acceleration input).



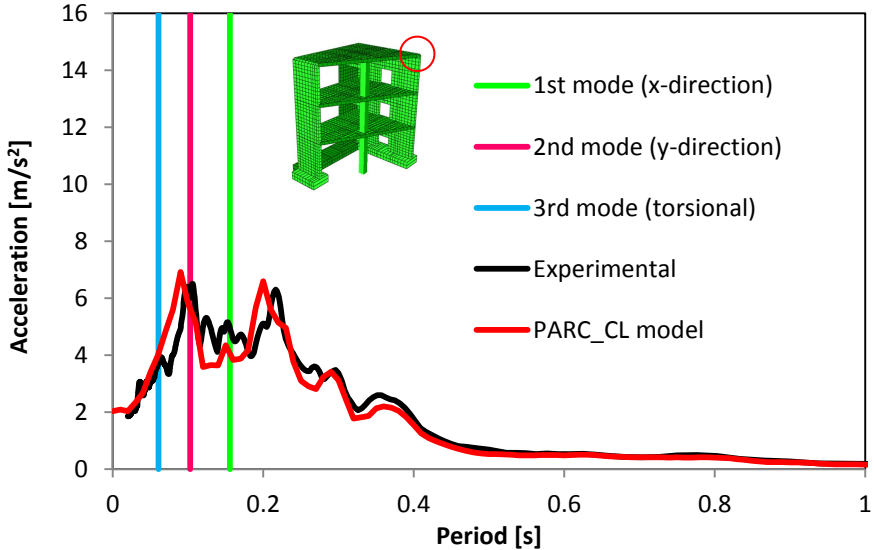
**Figure 6.33** – Effect of base line correction on the input. The displacement calculated from integration of corrected signal is equal to the experimental one.

#### 6.7.4 Spectral analysis of the acceleration response

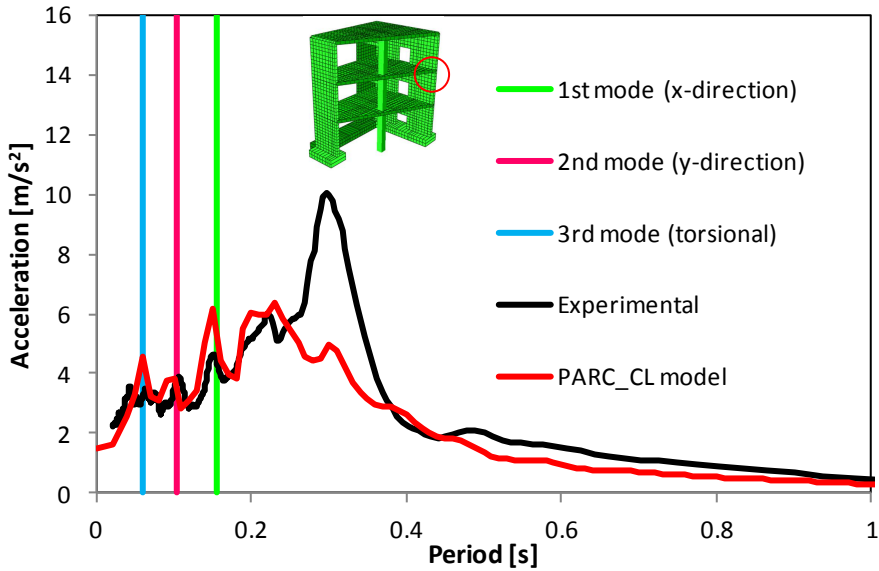
In order to assess the global response of the structure experimental and numerical acceleration spectra are compared for different point at different floors. It can be noticed that the new model is able to catch with good accuracy both the first and second elastic model. Moreover it is able to detect the damaged frequency in both direction. However, it underestimates the peak level for the damaged structures in X-direction (for example at point D). This is probably due to the fact that the failure mode at the interface of the shortest wall strongly influenced the global behaviour. Further comments about the interface problem are provided in chapter 8. Acceleration response spectra are given at significant points.



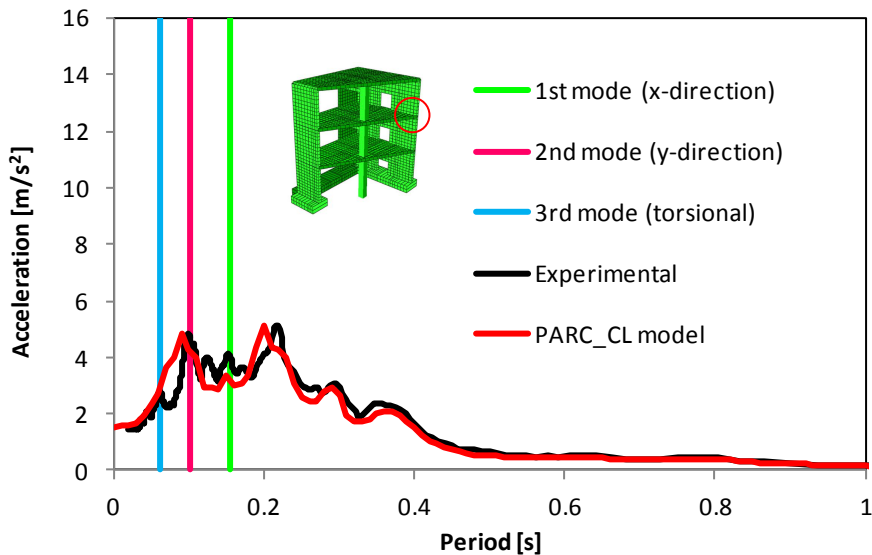
**Figure 6.34** – Spectral response for acceleration in X-direction, point D, third floor.



**Figure 6.35** – Spectral response for acceleration in Y-direction, point D, third floor.



**Figure 6.36** – Spectral response for acceleration in X-direction, point D, second floor.



**Figure 6.37** – Spectral response for acceleration in Y-direction, point D, second floor.

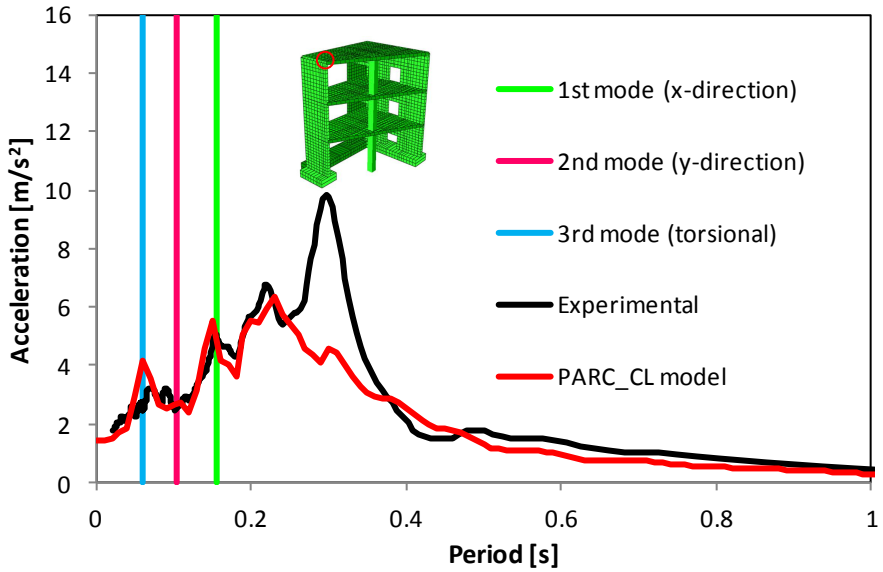


Figure 6.38 – Spectral response for acceleration in X-direction, point C, third floor.

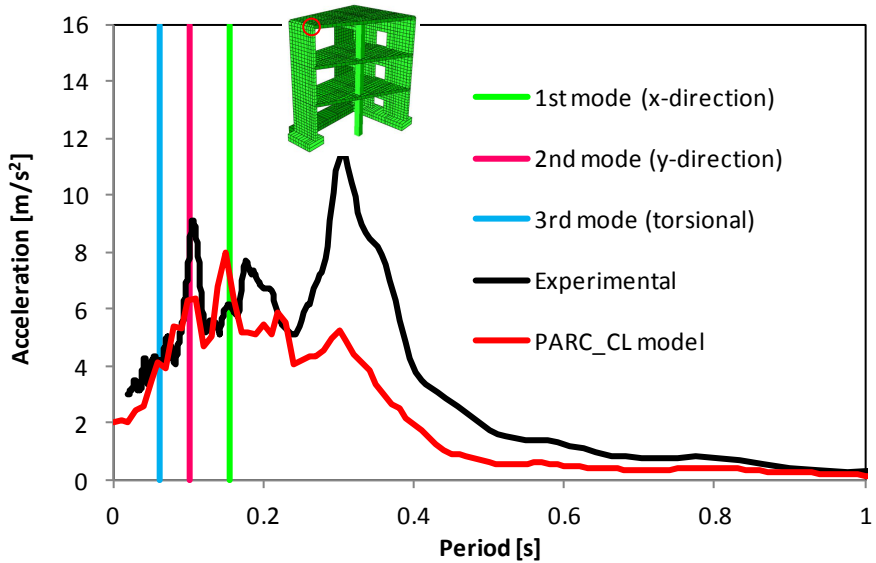
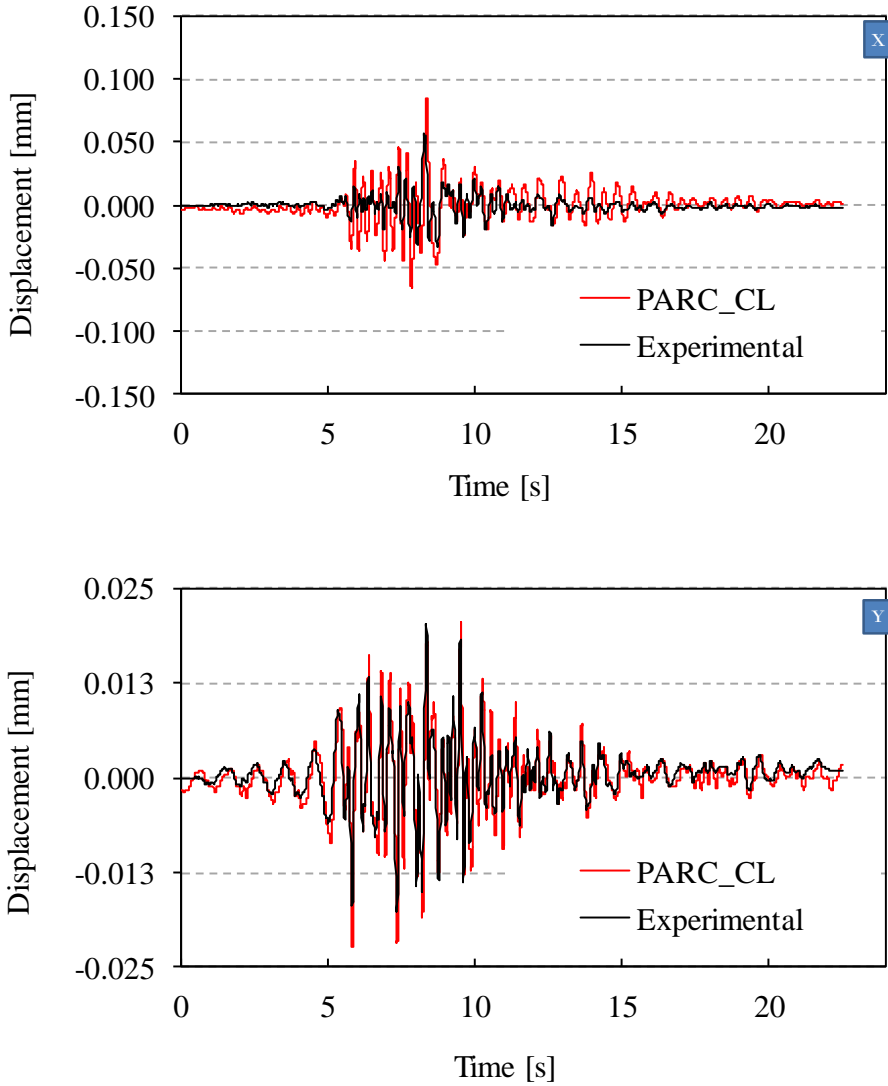
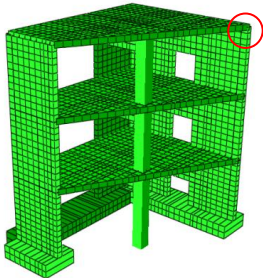


Figure 6.39 – Spectral response for acceleration in y-direction, point C, third floor.



**Figure 6.40** - Comparison between numerical and experimental results for X and Y displacements measured at point D at floor #3.

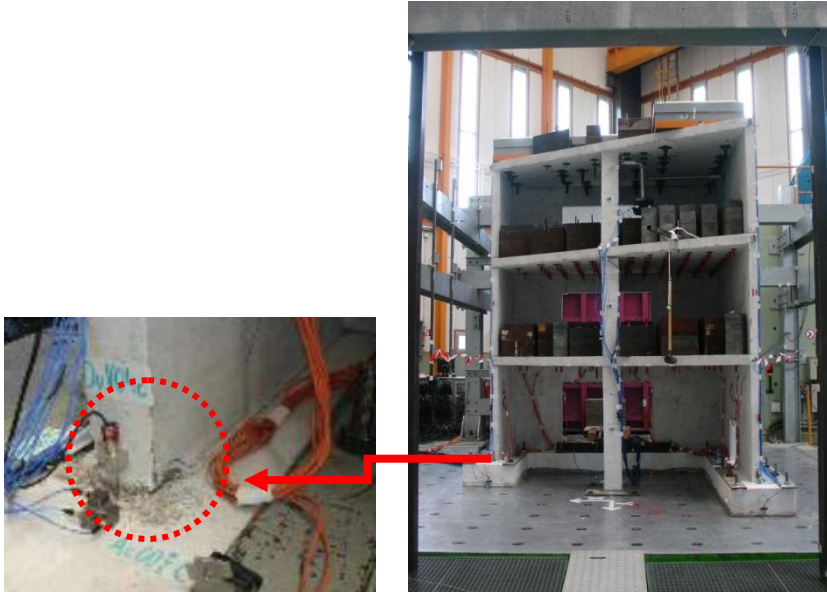




It is possible to notice that the model catches with good accuracy the frequency of the system both in the linear and non linear (damaged) field. However, both acceleration and displacement response seem to be slightly underestimated in the damaged phase. This is correlated to the aforementioned fact that the damage at wall/foundation interface could not be detected and to the fact that viscous damping proportional to stiffness matrix could not be implemented in the subroutine UMAT.for. This fact means that energy is dissipated only through mass proportional damping and to non linear materials hysteresis loops. However, it is remarked that Rayleigh classical damping is a numerical approximation of the phenomenon. The presented modelling is able then to catch the maximum peak response with sufficient accuracy in terms of displacement and frequency shift while the post peak displacement dynamic response require further research in order to be improved.

## **6.8 Remarks**

During the SMART2013 international benchmark project a simplified  $\frac{1}{4}$  scaled electrical auxiliary building of a nuclear power plant was tested. The structure, subjected to an ultimate limit state acceleration, resulted to be damaged at the interface between the shortest wall and the foundation. Concrete crushing at this interface was observed. It is interesting to notice that the participants to the blind prediction international workshop were not able to catch such damage as well. However, the numerical simulation was able to detect a strong compression field at this interface, as shown in Figure 6.13. In chapter 8 an extension for the interface problem with non linear shell modelling will be presented and discussed. In Figure 6.41 it is shown the main damage observed during the experimental test.



**Figure 6.41** – Concrete crushing at foundation to wall interface (Richard et al., 2014).





## **Chapter VII. Case Study II: the 1/13 Scaled RCCV Cyclic Test**

## 7 Case study II: the 1/13scaled RCCV cyclic test

The shell modelling with PARC\_CL was applied to the blind prediction of a cyclic analysis of a 1/13 reinforced concrete containment vessel (Hsu, 2015) held at National Centre for Research on Earthquake Engineering, Taipei (2015), Figure 7.1, in collaboration with the university of Houston, Texas. The research presented in the current chapter was successfully completed thanks to the Ministry of Science and Technology (MOST) of Taiwan and to the Research Exchange Program provided by the National Taiwan University.



Figure 7.1 –The NCREE lab in Taipei main entrance (credits: Stocchi, courtesy of NCREE).

### 7.1 Mock up and test description

The aim of the test was to evaluate the shear resistance of an existing nuclear vessel. The test was in displacements control. The vessel had a weight equal to 47t weight. Additional weight equal to 70t was added in order to reach realistically compression levels and was applied by means of 4 vertical actuators. Top displacements were applied by means of five horizontal hydraulic actuators. The global set up of the test is reported in Figure 7.2. Dimensions of the specimen are also reported in Figure 7.3 and Figure 7.4.



Figure 7.2 –The test set up (Credits: Stocchi, courtesy of NCREE).

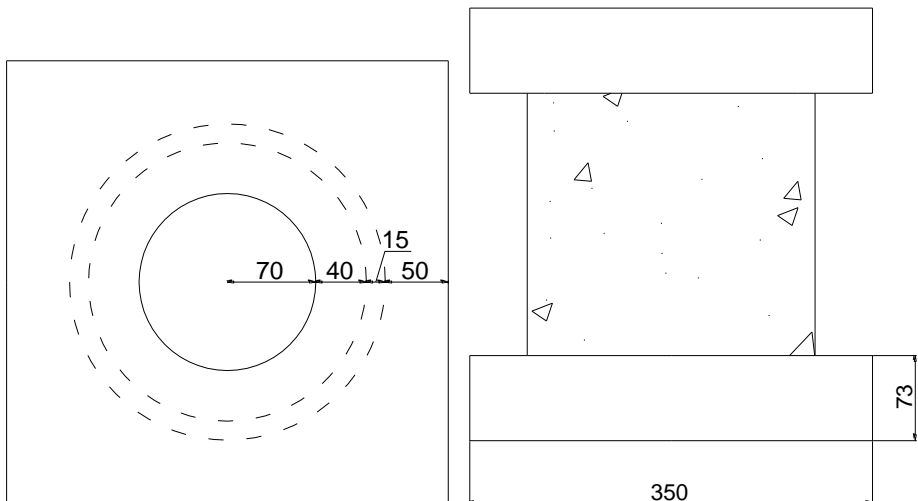
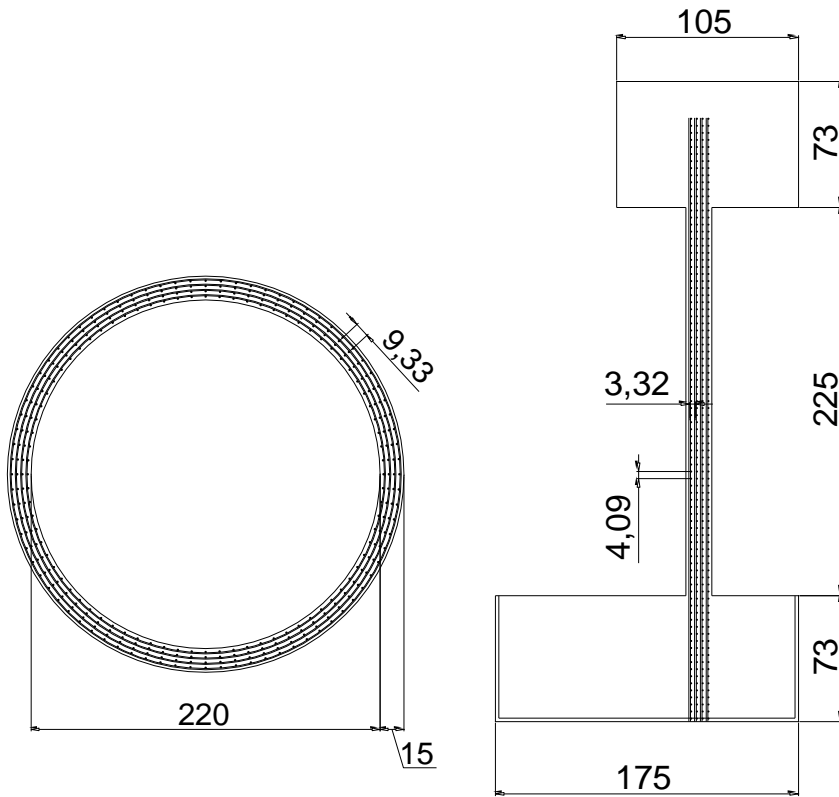


Figure 7.3 – Top and lateral view of the specimen.



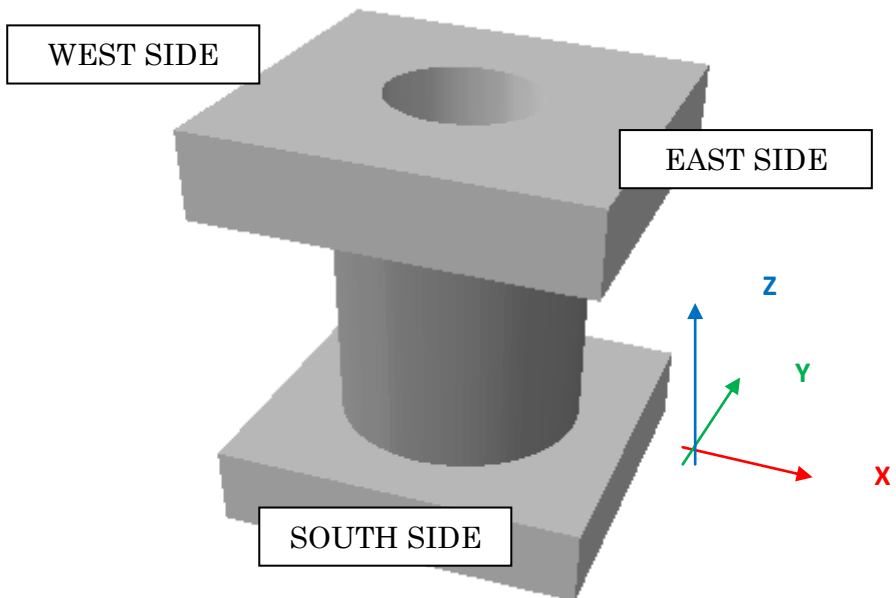
**Figure 7.4** – Horizontal and vertical sections of the mock up (not to scale).

## 7.2 Numerical model

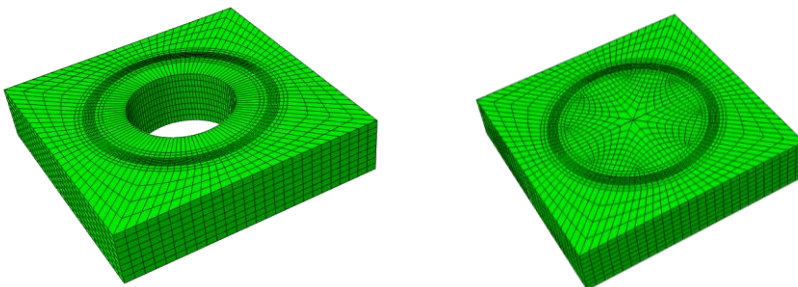
The numerical model is composed by three main parts: two thick slabs (for the application of the boundary condition) and the cylindrical vessel. Elastic bricks elements were adopted for the slabs while the vessel was modelled with four nodes, 2 layers shell elements. The vessel embedded parts are connected to bricks nodes of the slabs in order to consider the penetration of the vessel reinforcement for a better description of stresses distribution in the rebars. Thanks to the symmetry of the problem, only one half of the specimen was modelled and proper boundary conditions were introduced.



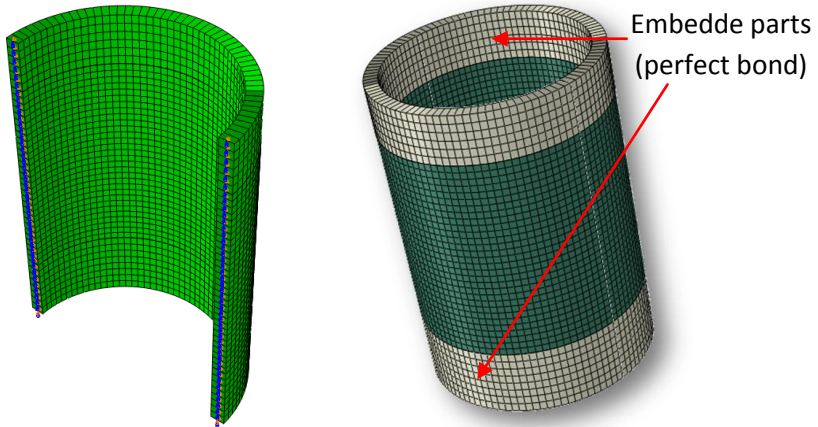
Structural Element	FE model description
Vessel	<ul style="list-style-type: none"> <li>- Shell 4 nodes</li> <li>- Non-linear material</li> <li>- 2 Layers</li> <li>- 3 integration points in each layer thickness</li> </ul>
Slabs	<ul style="list-style-type: none"> <li>- Solid 6 nodes elements</li> <li>- Elastic material</li> </ul>



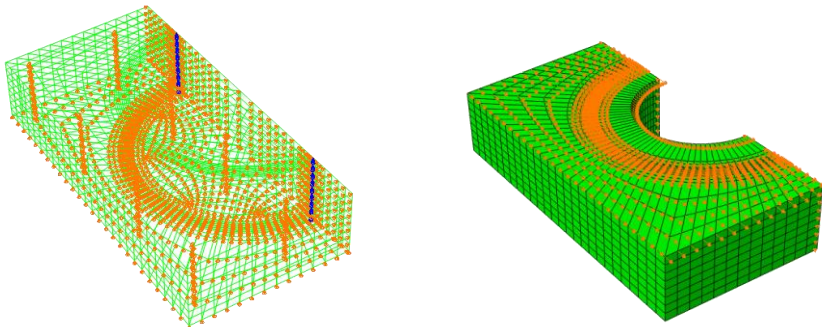
**Figure 7.5** - Reference system used in the experimental test and NLFEA.



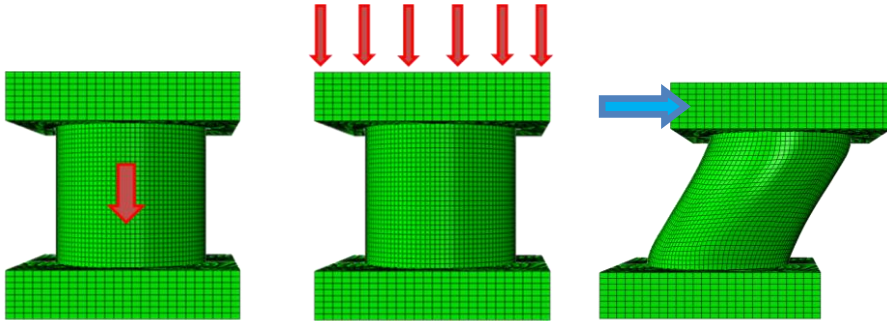
**Figure 7.6** – Top and bottom slabs modelling with 3d elastic brick elements.



**Figure 7.7** – Vessel modelling by means of non linear shell elements. Only half vessel is modelled and symmetry constraints are added on the nodes of the symmetry plane itself. Embedded shell elements have density equal to zero and are used to consider stress penetration.



**Figure 7.8** – Boundary conditions of top and bottom slabs. Horizontal displacements are restrained in the bottom slab nodes corresponding to dowels positions, vertical displacements are restrained at the bottom nodes and symmetry constraints are added on the symmetry plane. Displacements are applied at the top nodes of the top slab. The top slab is held horizontal by means of the \*EQUATION command in Abaqus so all the nodes have same vertical displacement.



**Figure 7.9** – Loading steps: 1) self weight; 2) additional weight (equal to 70t); 3) horizontal displacement.

### 7.3 Materials

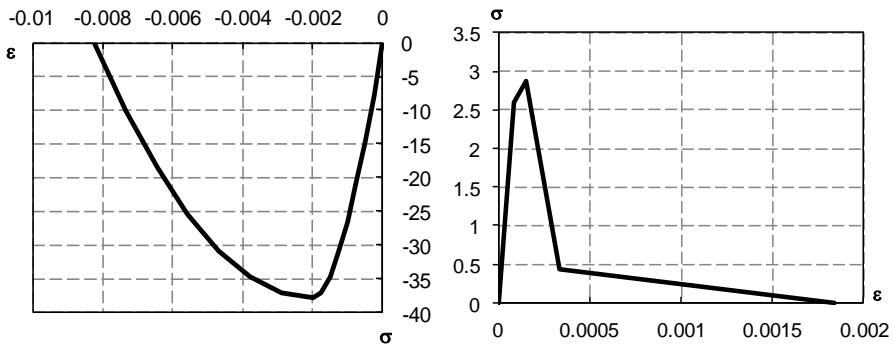
The complete set of values used in the subroutine for the constitutive laws definition is reported in Table 7.1 and Table 7.2. The concrete constitutive laws in compression and in tension are reported in Figure 7.10.

**Table 7.1** - Steel material properties.

#3 REBARS (VERTICAL)			#2 REBARS (HOOPS)		
$f_y$	386.3	N/mm <sup>2</sup>	$f_y$	383.3	N/mm <sup>2</sup>
$f_u$	583.6	N/mm <sup>2</sup>	$f_u$	576.5	N/mm <sup>2</sup>
$E$	209132	N/mm <sup>2</sup>	$E$	193397	N/mm <sup>2</sup>
$\epsilon_y$	0.001847	-	$\epsilon_y$	0.001982	-
$\epsilon_{su2}$	0.03	-	$\epsilon_{su2}$	0.03	-
$E_{sp1}$	7008	N/mm <sup>2</sup>	$E_{sp1}$	6896	N/mm <sup>2</sup>

**Table 7.2.** - Concrete material properties.

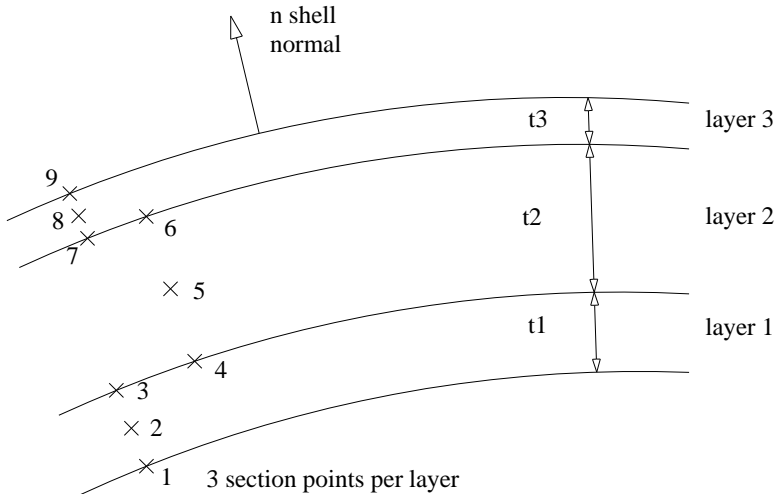
CONCRETE		
$f'_c$	37.76	N/mm <sup>2</sup>
$E_c$	21412	N/mm <sup>2</sup>
$f_{cc}$	45.5	N/mm <sup>2</sup>
$f_{ct}$	2.88	N/mm <sup>2</sup>
$\epsilon_{rc0}$	-0.002	-
$\epsilon_{rcu}$	-0.00838	-



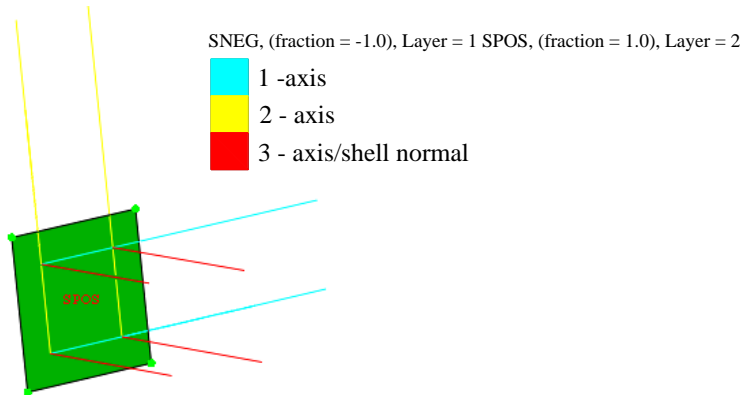
**Figure 7.10** - Concrete constitutive laws in compression and in tension.

### 7.3.1 Material orientation

The material orientation, layers material numbering and section points position are reported in Figure 7.11 and Figure 7.12. Numerical values are read in correspondence of the external section point of the layer. As the vessel was modelled with two layers elements with three integration points per layer and normal directed outside the vessel the considered section point is SP6 (an example of section points numbering is reported in Figure 7.11). Elements are four nodes shells with four integration points.



**Figure 7.11** - Example of layers and section points scheme used in Abaqus code for 3 layers and 3 section points per layer.



**Figure 7.12** - Local axes of a single shell elements and positive surface (defined as SPOS, corresponding to the top of layer 2).

As there are no significant differences between integration points of the same element, numerical results refer to integration point number 1. It is important to remind that strain gages results are reliable only in the elastic field until yielding point.

#### 7.4 Loading protocol

The cyclic test was split into two load sequences. The first one, called “preliminary elastic test” (cycles 1 to 6), aimed to investigate the setup calibration and the specimen response in the elastic field. The second series, called “full non linear test (cycles 7 to 15)” aimed to investigate the specimen behaviour in the non-linear field up to collapse. The complete load protocol is illustrated in Figure 7.13.

Displacements are applied along X direction, on the west-east axis. The preliminary elastic test is applied in order to verify the calibration of the test setup, paragraph 7.5. The full cyclic loading protocol (cycles 6 to 14) is applied in order to evaluate the non-linear behaviour of the vessel element under strong seismic input, paragraph 7.6.

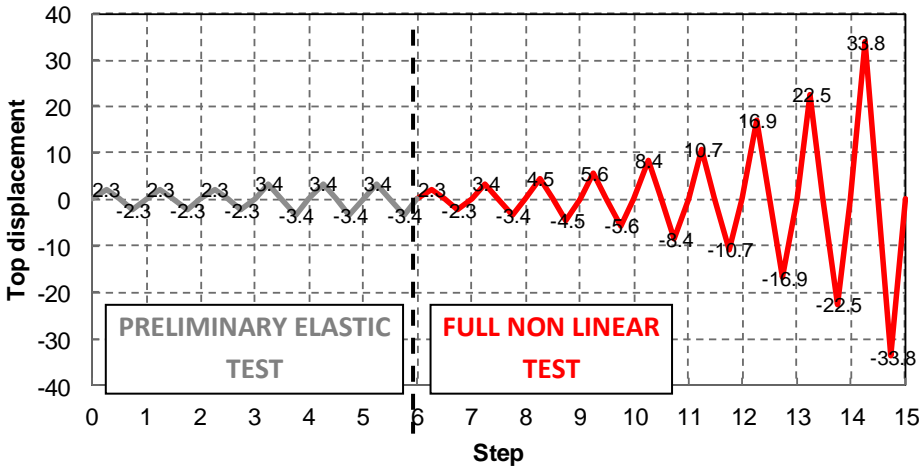


Figure 7.13 . Complete load protocol.

### 7.5 Preliminary elastic test

The scaled specimen was firstly subjected to a preliminary test. The test consisted of three cycles of low displacement in order to verify the test setup calibration and proper operative. The loading protocol of the preliminary run is reported in Figure 7.14. The first three cycles reach 2.25 mm of top displacement, the remaining three reach 3.75 mm. The preliminary test objective is to investigate also the elastic behaviour of the specimen before a stronger non linear phase.

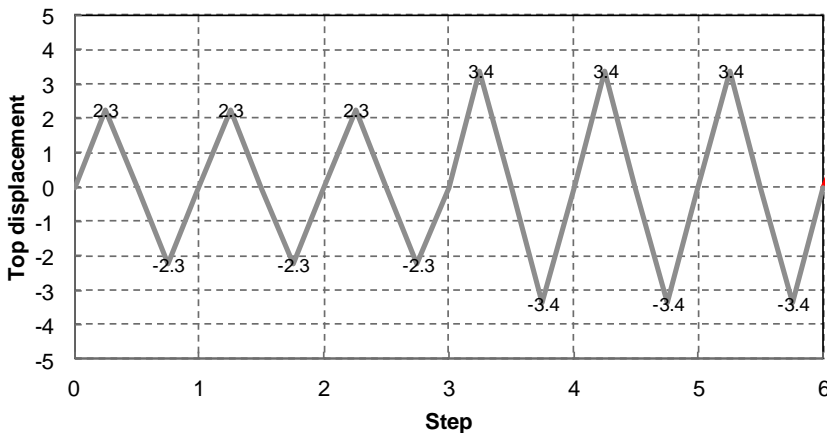


Figure 7.14. Elastic calibration experimental loading protocol close up.

## 7.5.1 Total base shear vs. top displacement

### 7.5.1.1 First cycle

The first cycle results are compared with the FEM analysis results in Figure 7.15. It can be noticed that a good estimation of the specimen behaviour is given on both loading direction. The elastic calibration of the model can be generally considered adequate. The curves on the positive quadrant are linearized for graphic purposes in order to compare the elastic initial stiffness of the specimen to the stiffness of the numerical model, Figure 7.16. The elastic stiffness of the FEM model is equal to 1648 kN/mm while the specimen stiffness is approximately equal to 1241 kN/mm (however it is unclear how to univocally define the end of the elastic field as it is of interest to notice that at this stage no cracks were seen on the specimen surface). The FE model overestimates the elastic stiffness of about 33%. Many factors may affect the evaluation of the global stiffness of the structure. In particular in the model the upper and the lower slabs elements are considered elastic and their stiffness may be higher than the real one. Moreover, no slip is allowed between the lower slab and the ground. The numerical model estimates the first concrete cracking at 1mm while the test data show an elastic behaviour until 1.5mm top displacement is reached. However, the final total base shear for top displacement of 2.25 mm (1% relative drift) is almost the same both for the experimental test and the numerical simulation (respectively 1886 kN and 2042 kN, with an overestimation equal to 7.6%).

Generally speaking, a top displacement from 1 to 1.5 mm can be considered a “critical” value for the global behaviour of the structure. Moreover, it is quite a small value (approximately 0.06% of drift ratio). The drift is an important global engineer demand parameter and can be efficiently used for the definition of structural damage (especially for static tests where dynamic quantities like frequency shift are not available) but it is important to pay attention when very stiff structures are involved as very small displacements may be critical for the damage definition. Therefore, a proper calibration of the non linear model is a fundamental passage in structural analysis.

It is of interest to notice that the global weight of the setup is equal about to  $W=117\text{ t}=1170\text{ kN}$  (top additional mass is equal to 70t). If  $F_h=1800\text{ kN}$  is the horizontal force corresponding to the maximum elastic displacement, then

roughly  $a_g = F_h/W = 1.5g$  is the theoretical base acceleration that could generate such force. This means that the structure is supposed to undergo quite short displacements under strong seismic input.

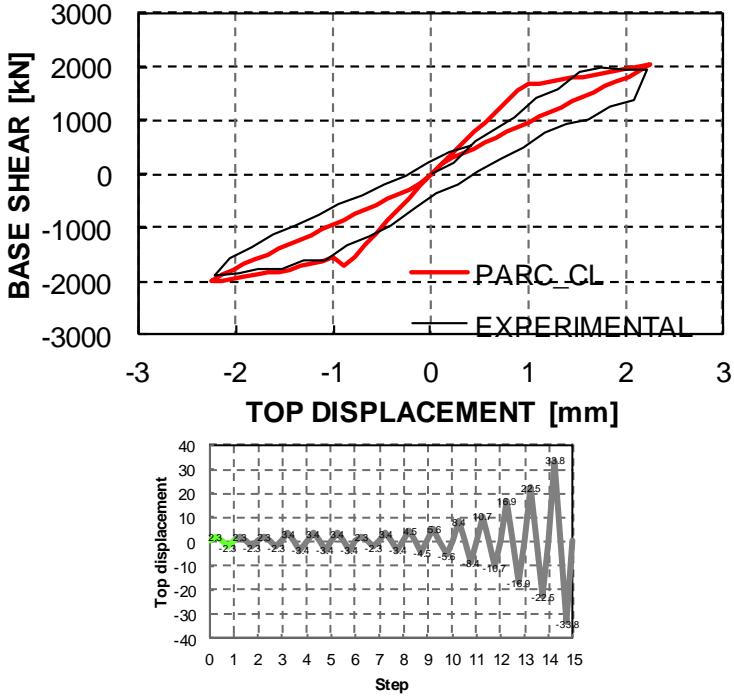


Figure 7.15 - FEM analysis vs. experimental results: base shear vs. top displacement.

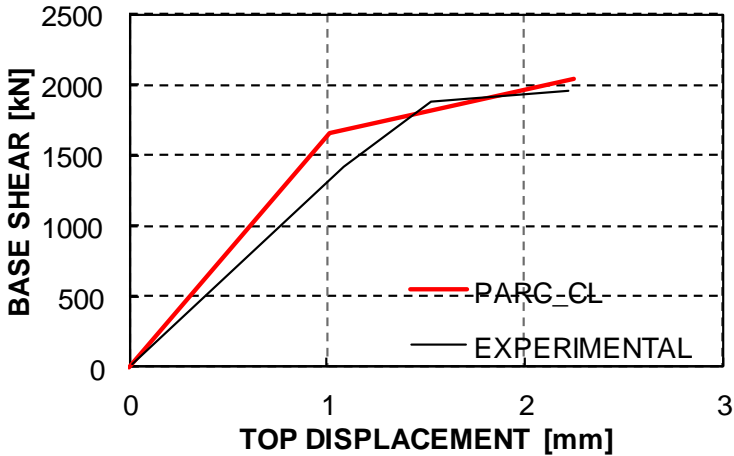


Figure 7.16 - FEM analysis vs. experimental results: base shear vs. top displacement.



### 7.5.1.2 Second cycle

In order to better understand the elastic preliminary test the second cycle results are reported both for experimental and numerical analysis.

It can be noticed that the loading protocol prescribes a maximum displacement equal to the one of the first cycle. The PARC\_CL curve as expected by the secant model behaviour follows the unloading curve of the first cycle (loops cannot be observed). The experimental curve describes a small hysteretic loop. It is worthy to notice that the new cracked stiffness is described with good approximation by the PARC\_CL model and that the maximum base shear is overestimated of about 10%.

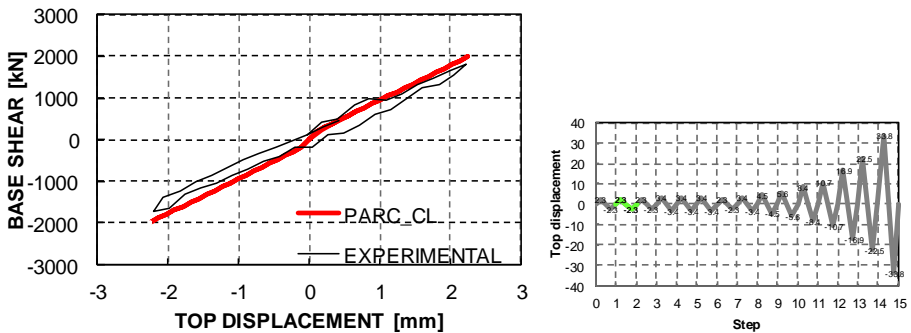


Figure 7.17 - Second cycle results for the preliminary elastic test.

### 7.5.2 Fourth cycle

During the fourth cycle the top displacement reached 3.4mm. Results are reported in Figure 7.18. Again, the stiffness is estimated with good accuracy. The maximum applied force is overestimated in both directions of about 9%.

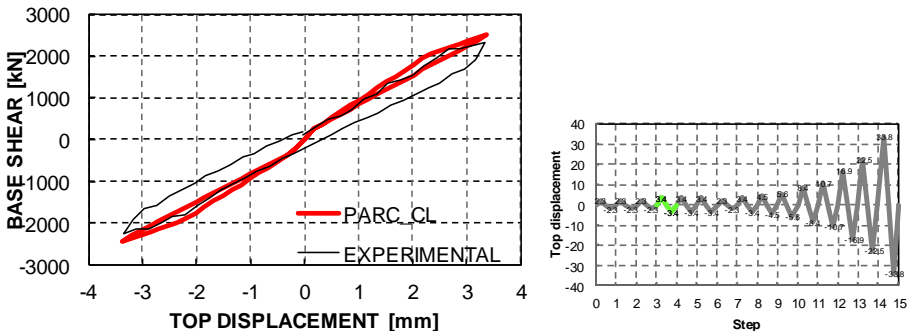


Figure 7.18. Fourth cycle results for the preliminary elastic test.

### 7.5.3 Complete preliminary cyclic test

The complete preliminary test is reported in Figure 7.19.

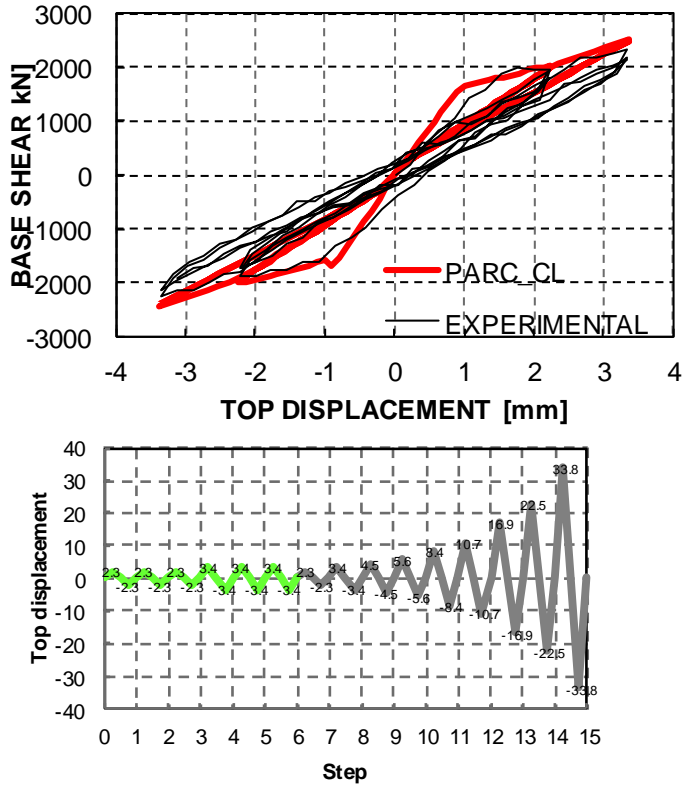
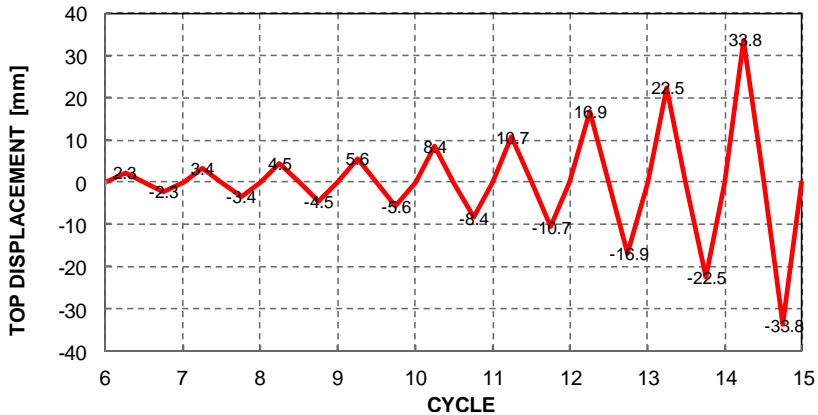


Figure 7.19 - Complete preliminary loading test.

The global behaviour of the vessel subjected to low input loading condition is in general adequately described in terms of total base shear. The maximum base shear (both negative and positive) during each cycle is overestimated from 7% to 10%. The envelope of the experimental cycles is then described with good accuracy. Strain gages data were not available during the preliminary run; this is why results are displayed only in terms of total base shear vs. top displacement. It can be noted that the secant experimental stiffness evaluated at the 6<sup>th</sup> cycle is equal to 650 kN/mm. This value is about the half of the initial elastic stiffness (approximately equal to 1240 kN/mm) then the specimen already exhibited some damage although not visible.

## 7.6 Full non linear test

The specimen was then tested in order to investigate the non-linear behaviour of the structure. Cycles from 10 to 15 aimed to bring the structure to rupture, while cycles 7 to 9 were low intensity cycles which were not supposed to bring the specimen into the strong non linear field. The loading protocol of this full non-linear test is displayed in Figure 7.20.



**Figure 7.20** - Full non linear test loading protocol (cycles 7 to 15 of the total load history).

It was demonstrated that the structure experienced non negligible stiffness degradation during the 6 preliminary cycles and so the initial step of the non linear test is not properly at undamaged state. However, the main cracking phenomena occurred during this phase of the loading protocol.

### 7.6.1 Total base shear vs. top displacement

In this section it is analysed the global behaviour of the specimen compared to FEA results in terms of top displacement vs. total base shear. Further details on local parameters will be discussed in following paragraphs.

#### 7.6.1.1 Low intensity cycles

It has been discussed that the main test started from a slightly damaged configuration. This is why the 7<sup>th</sup> cycle leads to different results although it is nominally equal to the first cycle (discussed in 7.5.1.1). Results are displayed in Figure 7.21.

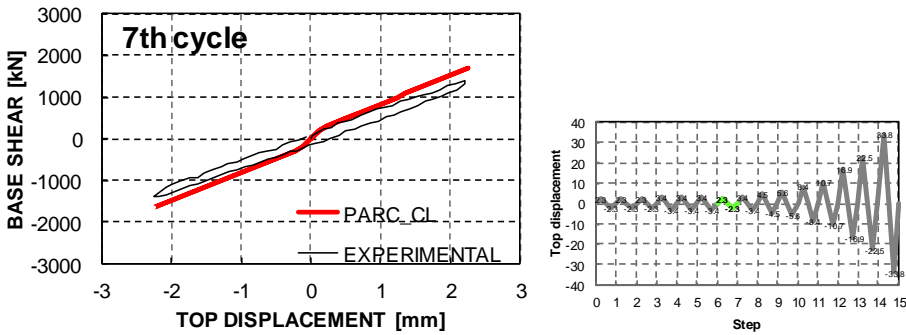


Figure 7.21 - 7<sup>th</sup> cycle results.

In this case the PARC\_CL model overestimates the maximum shear force of 20% (1702 kN vs. 1302 kN). However, the model seems still to catch pretty well the experimental data. The same error is detected during the 8<sup>th</sup> cycle. The numerical model is always slightly stiffer than the numerical one. The same trend can be observed also during the 9<sup>th</sup> cycle. The 7, 8 and 9<sup>th</sup> cycle are supposed to be low intensity input as slightly above the elastic behaviour of the structure.

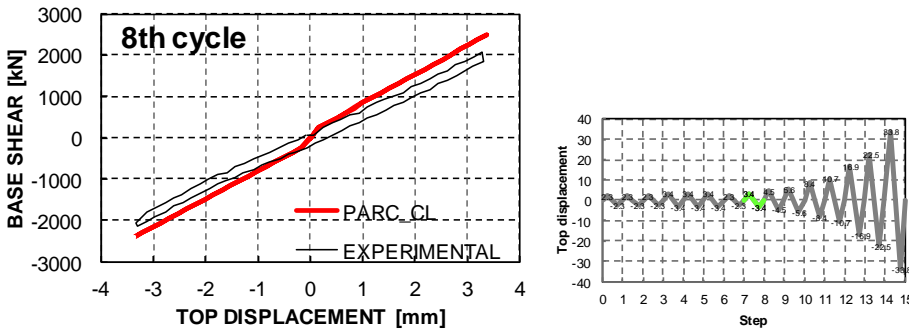


Figure 7.22 - 8<sup>th</sup> cycle results.

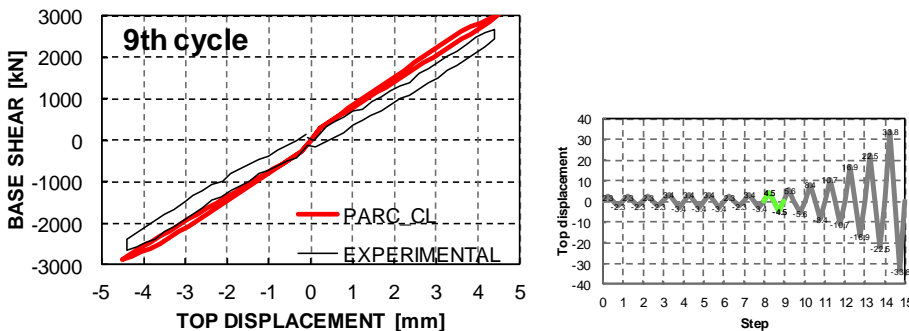


Figure 7.23 - 9<sup>th</sup> cycle results.

Finally, the comparison between FEA and experimental results for cycles 7, 8 and 9 is reported.

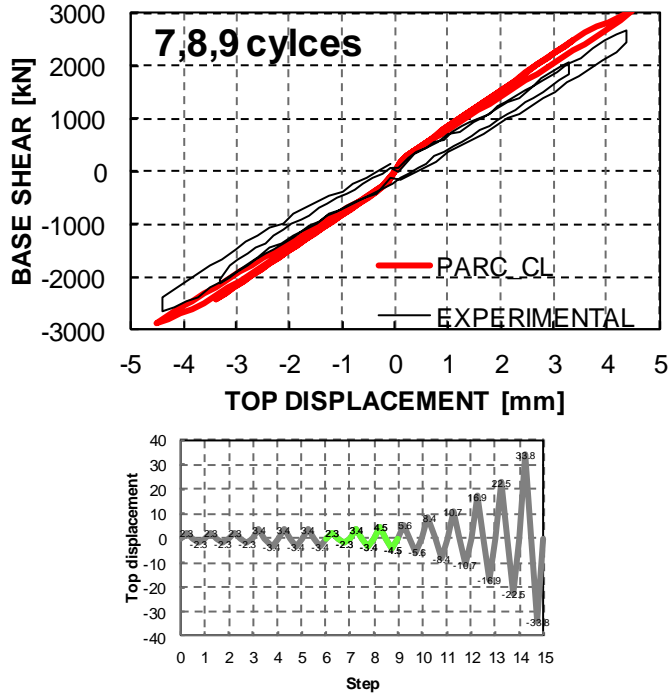


Figure 7.24 - 7, 8 and 9<sup>th</sup> cycles results.

It can be noticed from Figure 7.24 that the stiffness of the specimen does not significantly changes from one cycle to the next one.

#### 7.6.1.2 High intensity cycles

“High intensity” cycles are supposed to cause stronger damage up to rupture. Cycles 12, 11 and 12 comparisons are reported in Figure 7.25.

As damage increases, the FEA prediction gives slightly higher values in terms of total base shear. At the end of 12<sup>th</sup> cycle the maximum base shear is overestimated of 28% (5837 kN, while the experimental value is equal to 4540 kN). It is possible to notice slight stiffness degradation in the experimental loops. On the other hand, the numerical curve is still able to approximate the experimental envelope

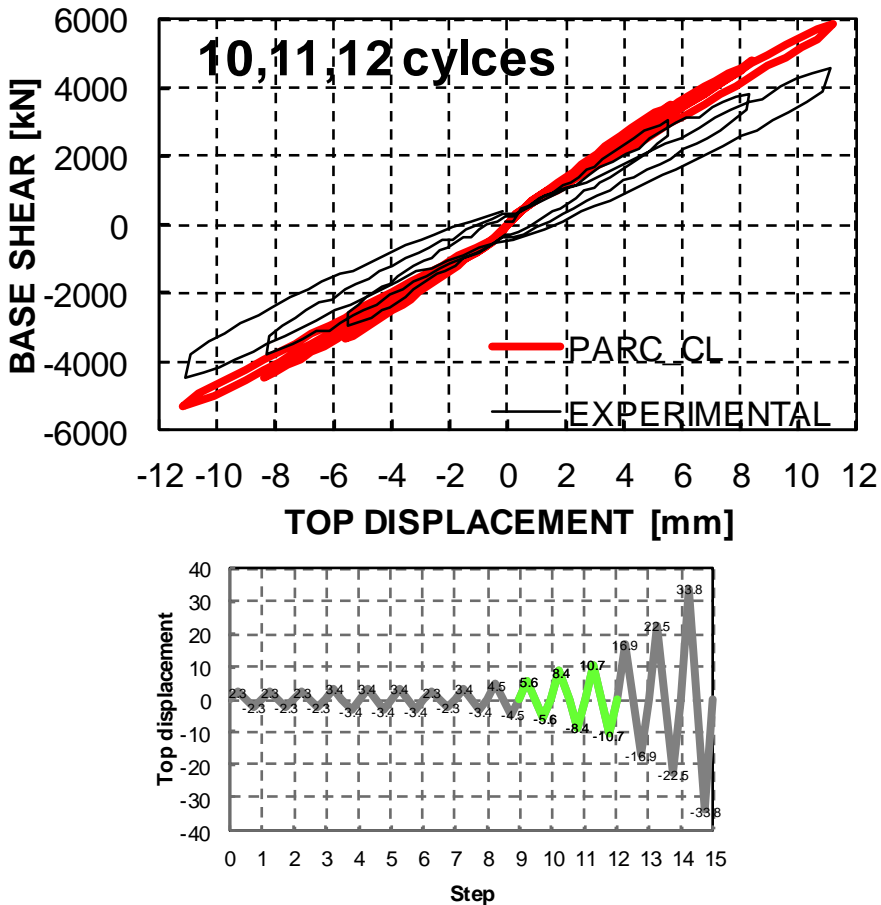


Figure 7.25 - 10, 11 and 12<sup>th</sup> cycles results.

The remaining cycles (number 13 and 14) revealed to be determinant for the global behaviour assessment, Figure 7.26. In fact, at the end of the 13<sup>th</sup> cycle both the FEA curve and the experimental curve reach the maximum total base shear in correspondence of a top displacement equal to 17 mm. However, the failure mode resulted to be different. The FE model failed because of crushing of the concrete in compressed strut while the specimen failed in sliding shear. This is why the curves differ so much (about 50%) in the 14<sup>th</sup> cycle. The experimental curve suffers a quick drop in terms of base shear as no more resistance is available after sliding shear at top slab to vessel interface occurred. Finally, the whole non linear test results are reported both in terms of complete loops and envelope curves.

It is remarked that the concrete crushing observed during cycle 13 is considered as ultimate value for the numerical analysis, as also explained in 7.8.1.

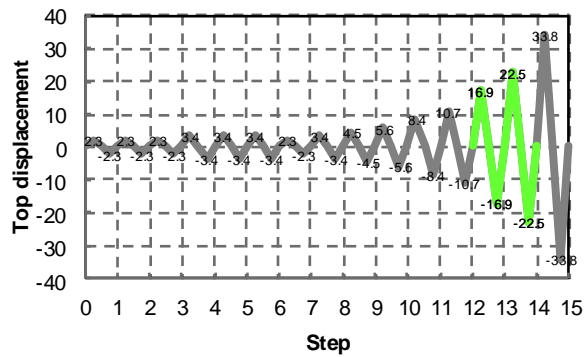
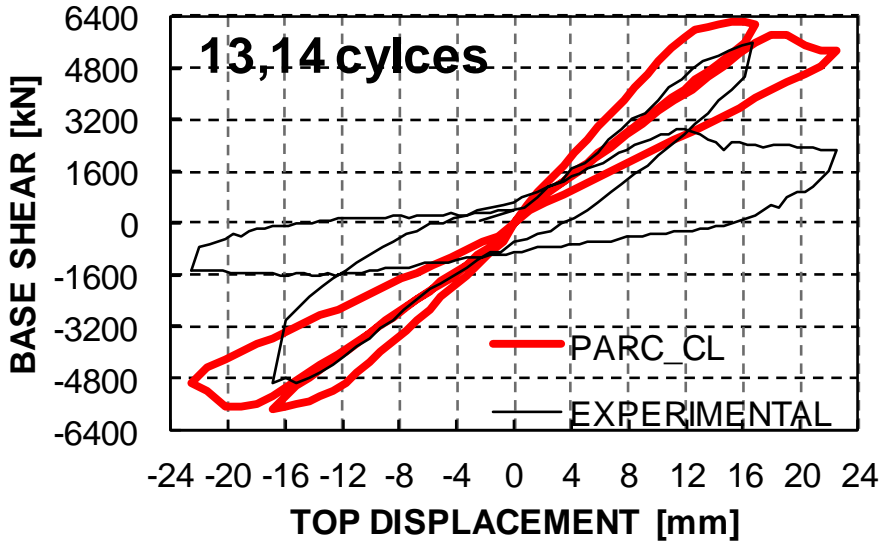


Figure 7.26 - 13 and 11 and 14<sup>th</sup> cycles results.

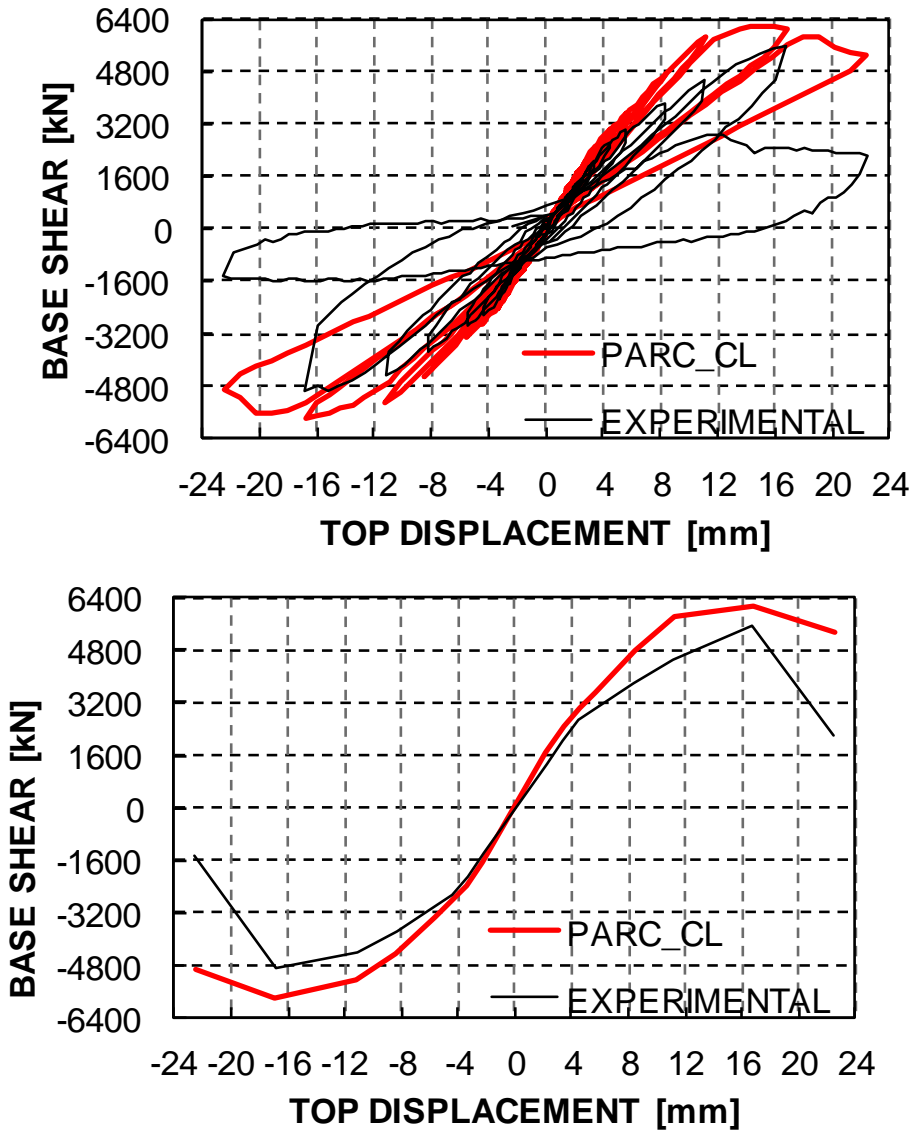


Figure 7.27 - Full non linear test results and curves envelopes.



## 7.6.2 Rebars and hoops strain

Strain gages measurements for steel strain during are available for the full non linear test. Vertical bars and horizontal hoops strains are then compared in correspondence of some significant points

### 7.6.2.1 Vertical rebars

For the steel characteristics of vertical rebars please refer to paragraph 7. For each figure the element analysed is reported together with the strain gage identification code. Results are reported for the south and east side of the vessel, at the top and central parts. Other regions are supposed to behave symmetrically.

Figure 7.28 is focused on the behaviour of the vertical rebars in the central area of the vessel in the direction perpendicular to applied load. Shear behaviour is mainly expected in this area. It can be noted that the steel strain is adequately described both before and after steel yielding. Quite good results are obtained.

In Figure 7.29 it is taken a closer look on the lower area of the vessel. Here as expected both the numerical and the experimental rebars strain values are quite low. As this area was strongly damaged when failure occurred, during the 13<sup>th</sup> cycle results start to differ consistently.

In Figure 7.30, Figure 7.31 and Figure 7.32 the behaviour of rebars on the east side of the specimen is analysed. Here mainly flexural behaviour is expected. The model can catch the strain pattern although nearby yielding point tensile strains are underestimated. Again, during cycle 13 results start to differ because of strong damage.

From Figure 7.33 to Figure 7.35 results are reported for the west side part of the specimen.

It can be observed that the ultimate strain equal to 0.03 (both in tension and in compression) is never observed during FEA. As strain gages are not reliable above yielding level it is not possible to verify if this happens also during the experimental test. Numerical results in Figure 7.35 show some inconsistency as they should have a formal trend equal or at least similar to the one showed in Figure 7.30.

The contour in correspondence of first yielding point for vertical rebars is reported in Figure 7.36. Rebars yielding is related to flexural behaviour.

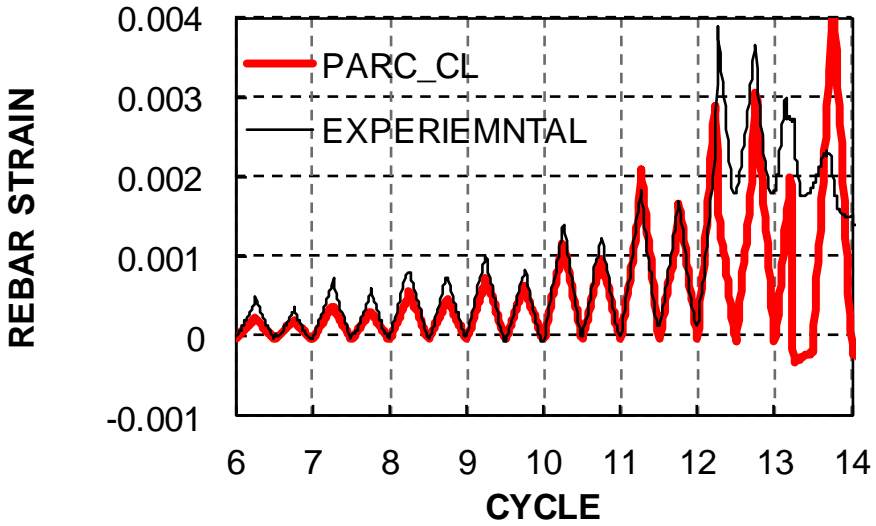
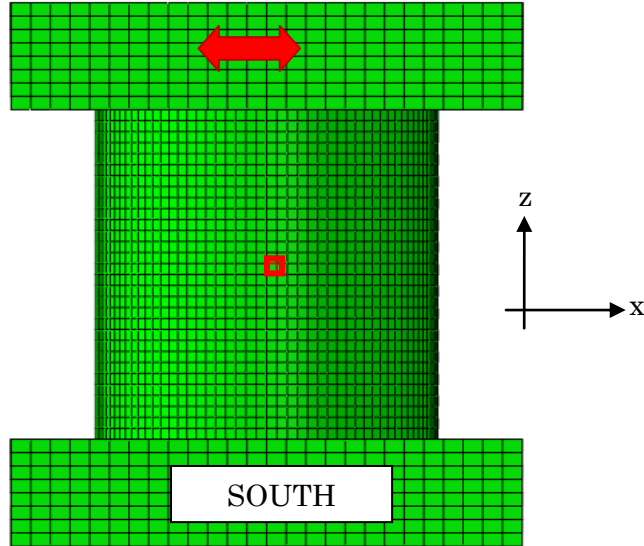


Figure 7.28 - Element 754, strain gage MCS000E results comparison.

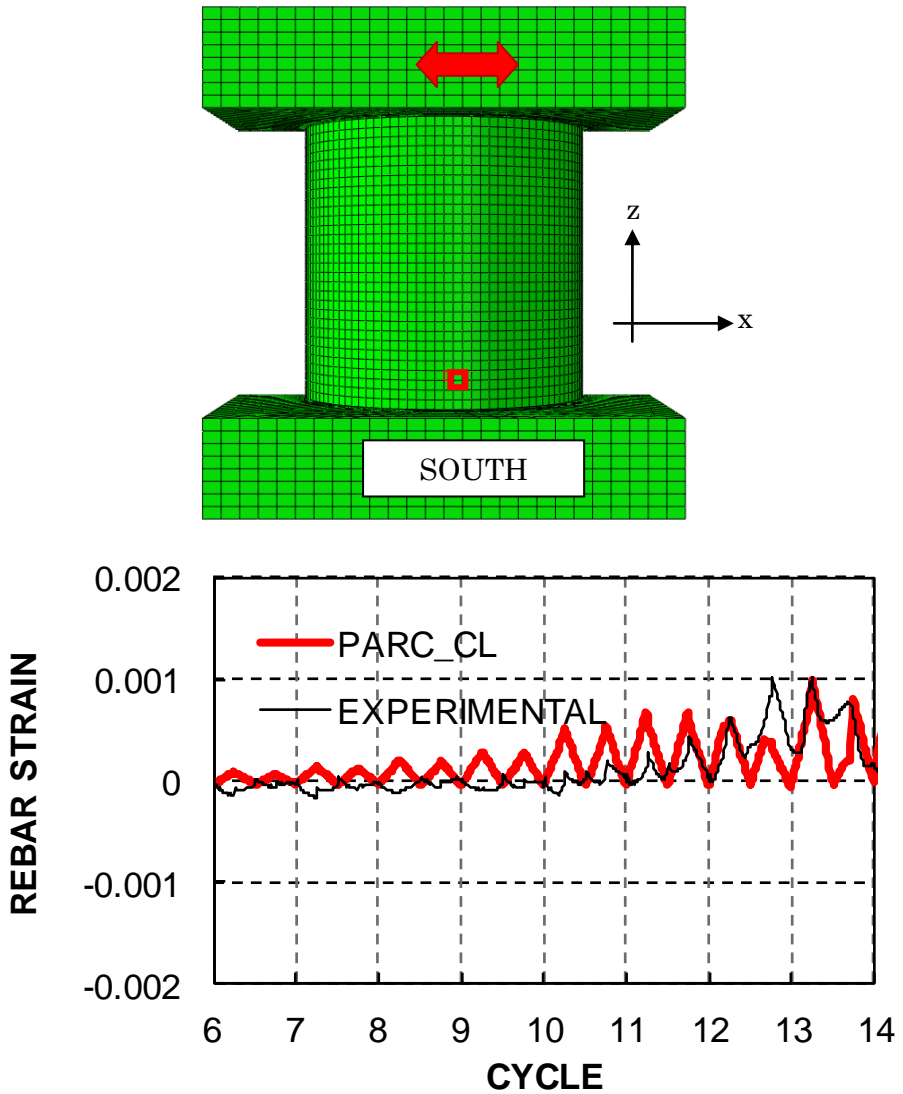


Figure 7.29 - Element 1378, strain gage MES000E results comparison.

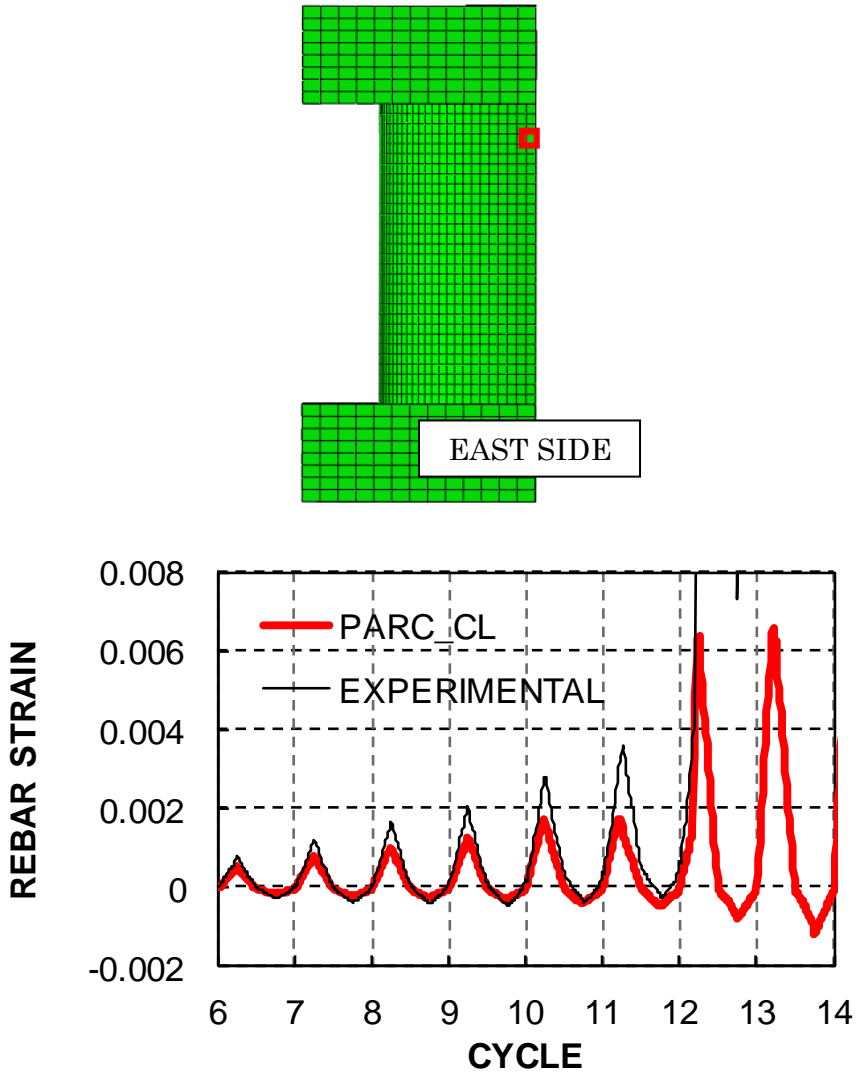


Figure 7.30 - Element 157, strain gage MAE000N results comparison.

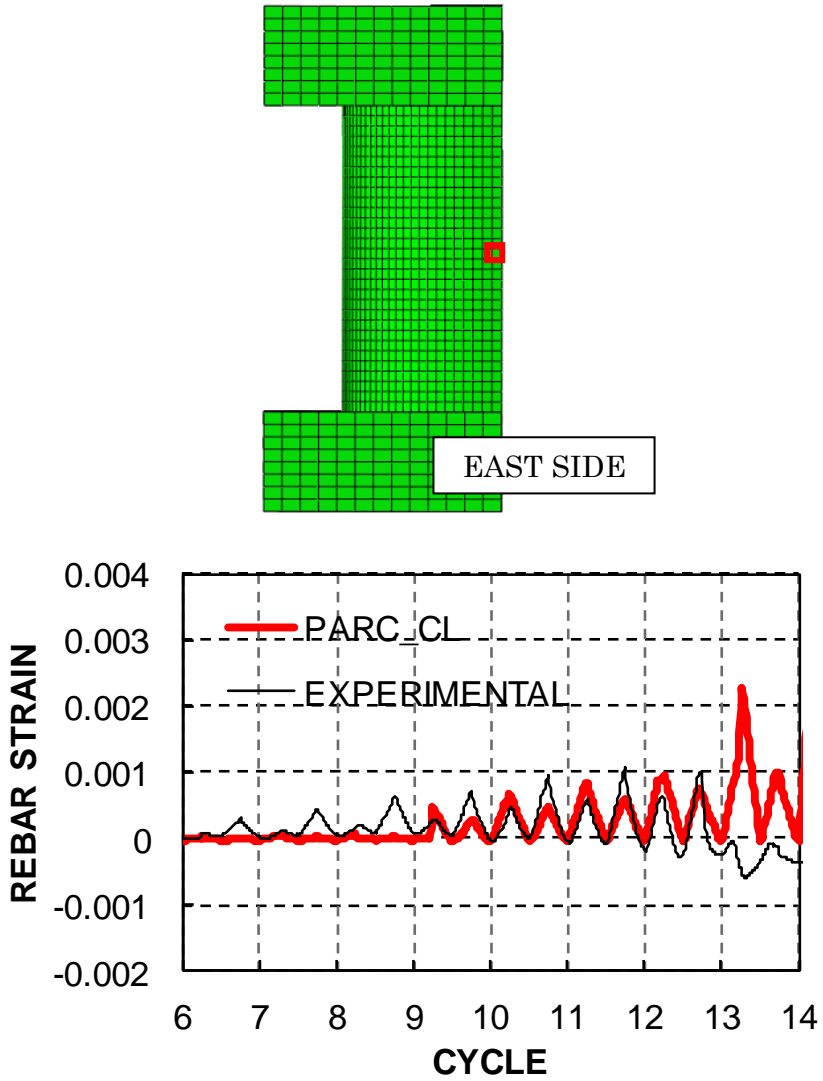


Figure 7.31. Element 729, strain gage MCE000N results comparison.

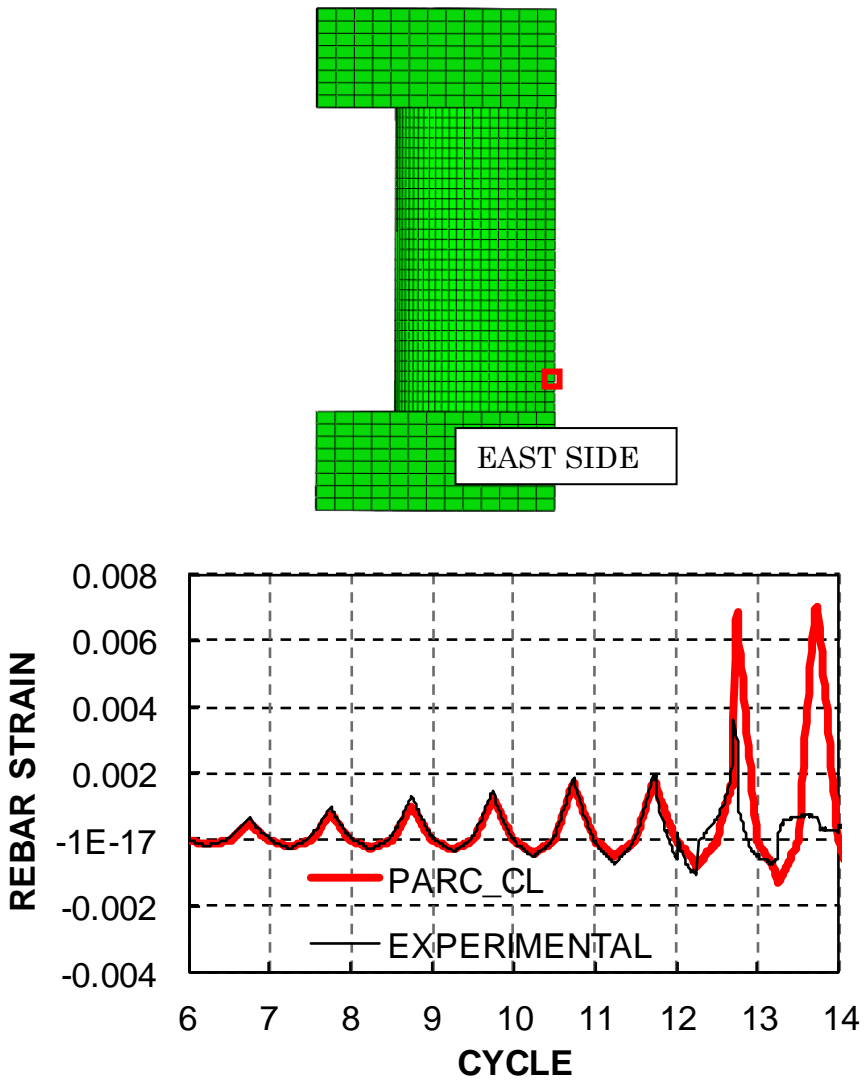


Figure 7.32 - Element 1353, strain gage MEE000N results comparison.

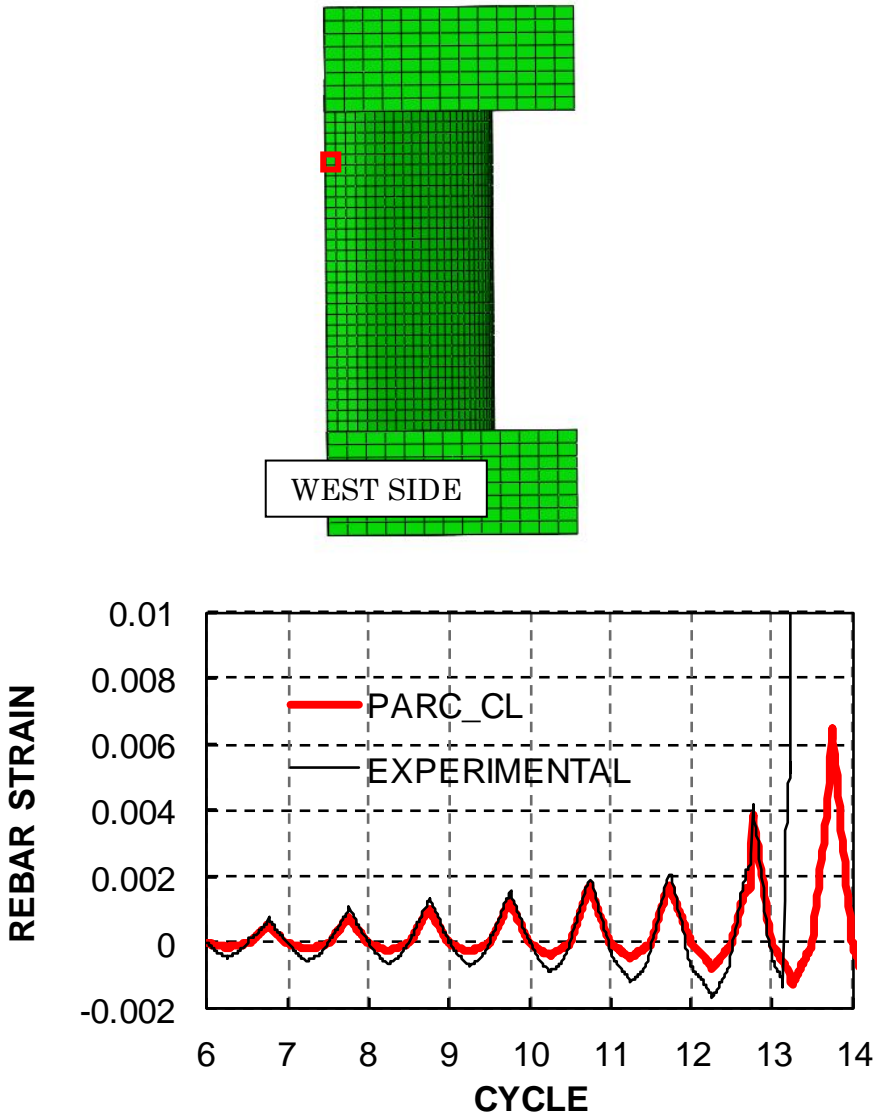


Figure 7.33 - Element 208, strain gage MAW000S results comparison.

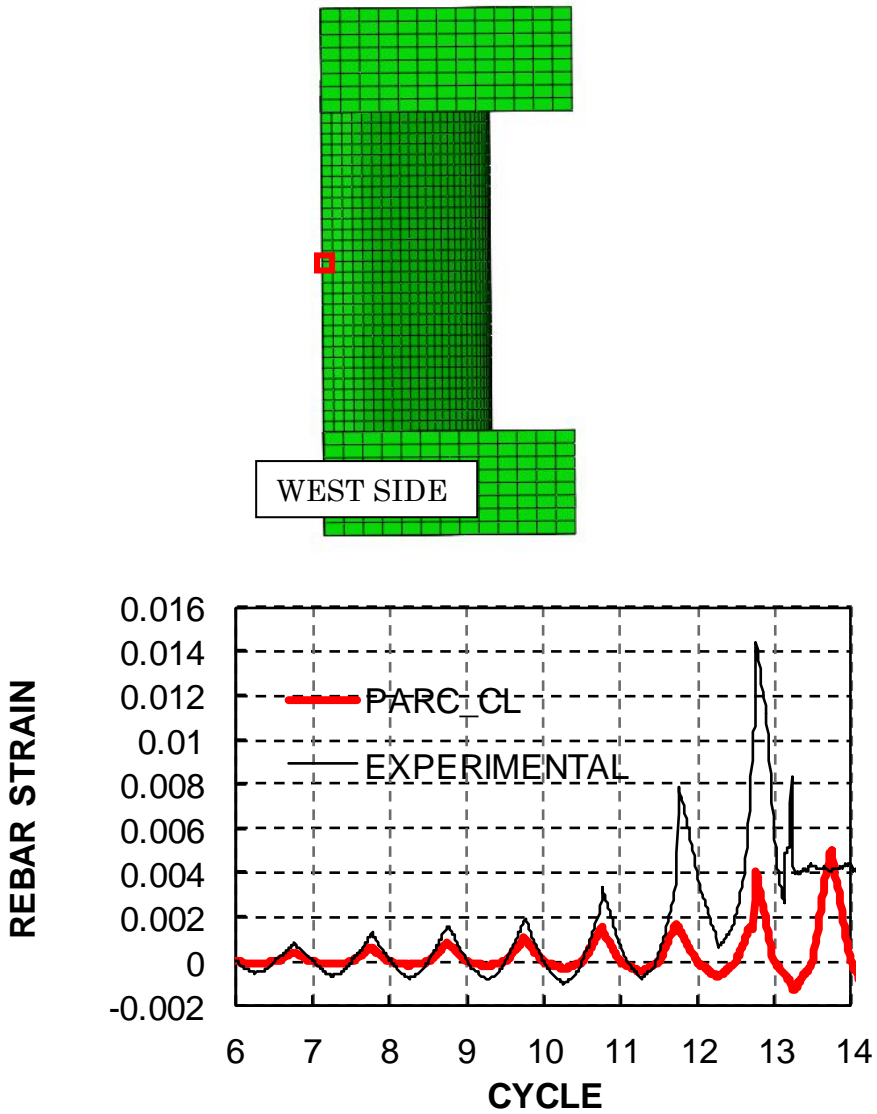


Figure 7.34 - Element 202, strain gage MAW225S results comparison.



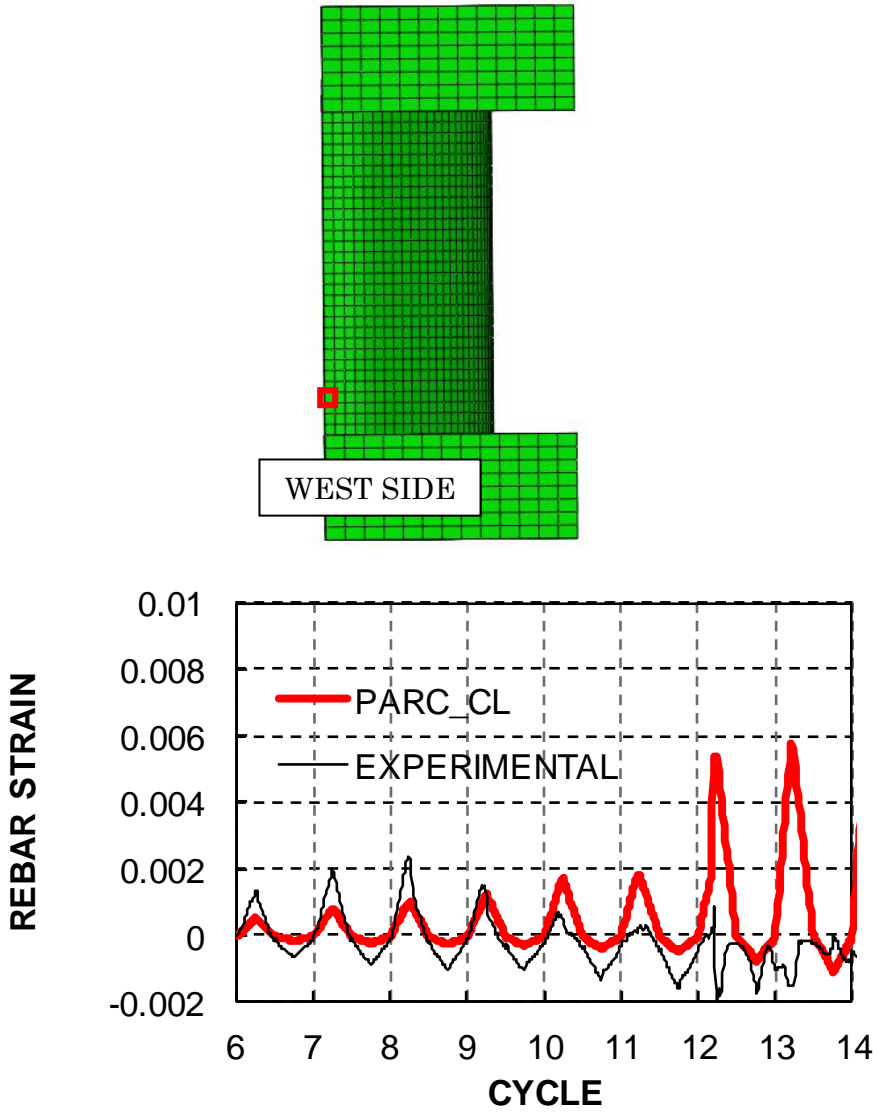
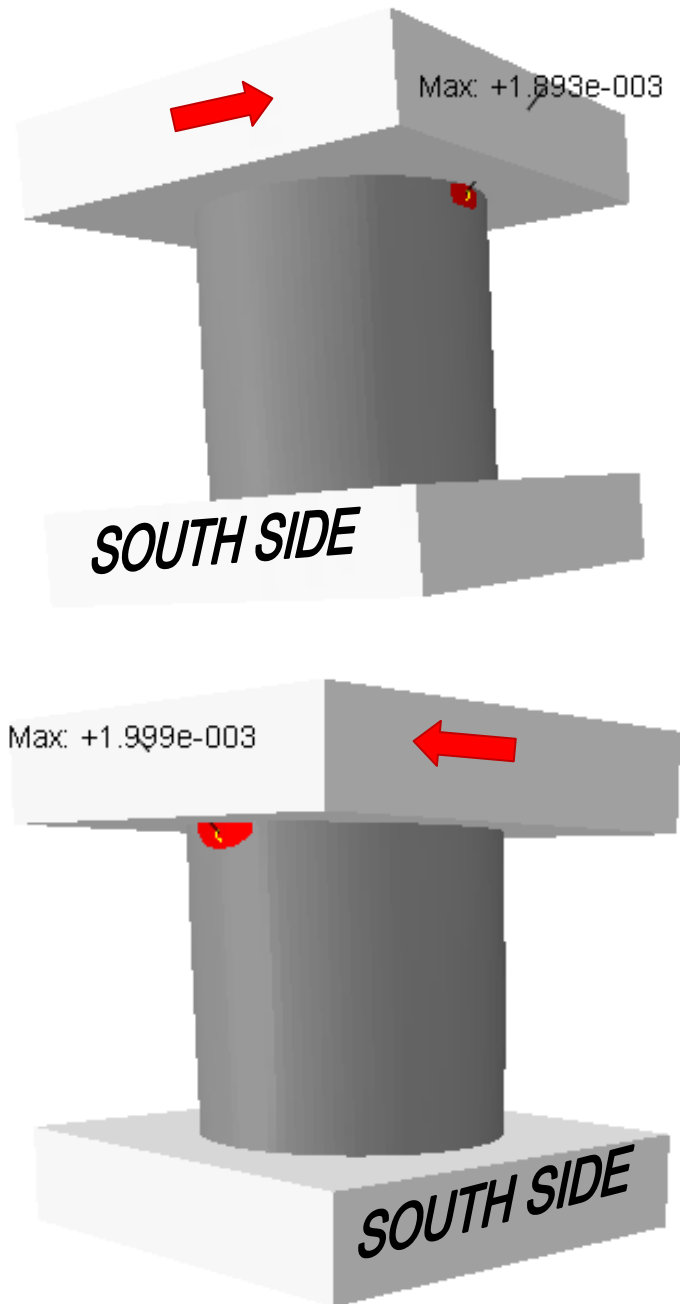


Figure 7.35 - Element 1404, strain gage MEW0005 results comparison.



**Figure 7.36** - Vertical rebars first yielding during cycle 11 in both direction (the area where  $\epsilon_s > \epsilon_y = 0.0018$  is displayed in red).

### 7.6.3 Horizontal hoops

For the material and characteristics of hoops please refer to 7. In the following the behaviour of the hoops around the central area of the south side of the specimen is showed as the main strains both in the experimental and numerical results are displayed in that area. From Figure 7.37 to Figure 7.40 it can be noted that the model catches with good accuracy the hoops strain but from cycle 13 values start to be different because of the different failure mode.

It is of interest to notice that closer to the top slab interface the model catches correctly also the low strain level. When rupture occurs, then experimental values suddenly go out of scale, Figure 7.41.

In Figure 7.42 it is showed the behaviour of a hoop point located halfway from the top slab and the central area (which is mainly subjected to shear phenomena). At failure (cycle 13) results start to diverge.

Finally, the contours graphs for hoops first yielding are reported in Figure 7.43. The hoops' yielding is mainly related to in plane shear behaviour of the vessel web.

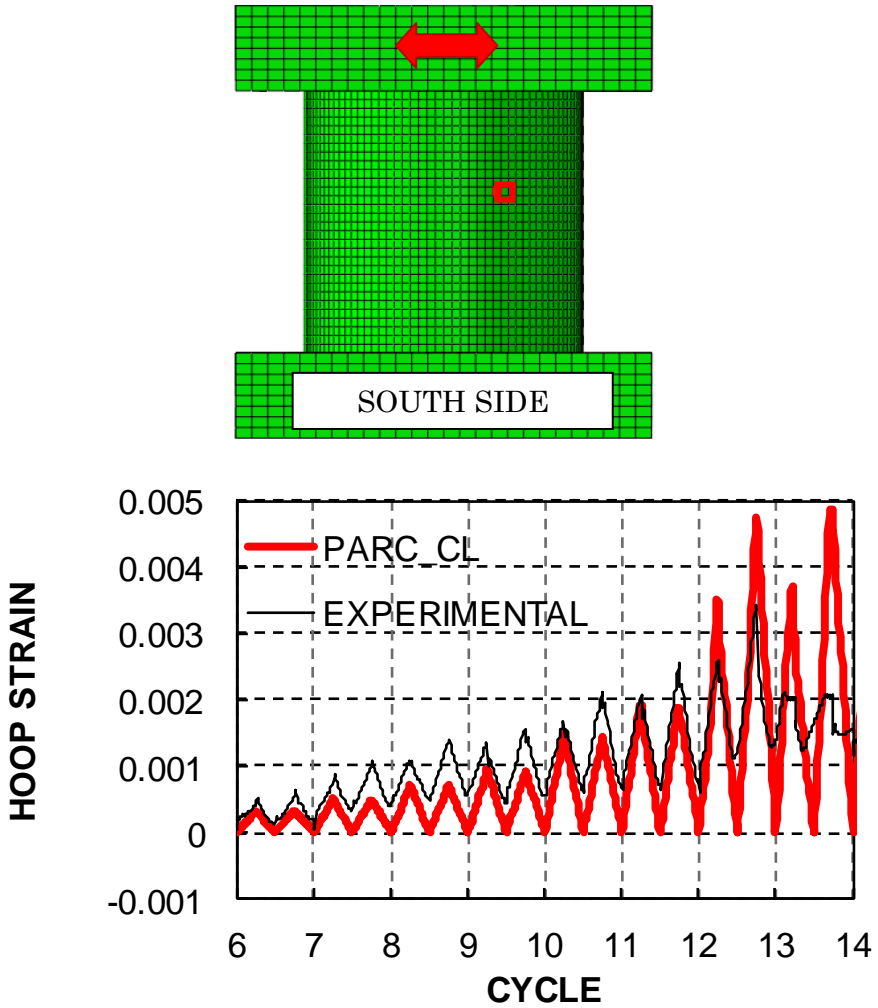


Figure 7.37 - Element 592, strain gage S3S1125E results comparison.

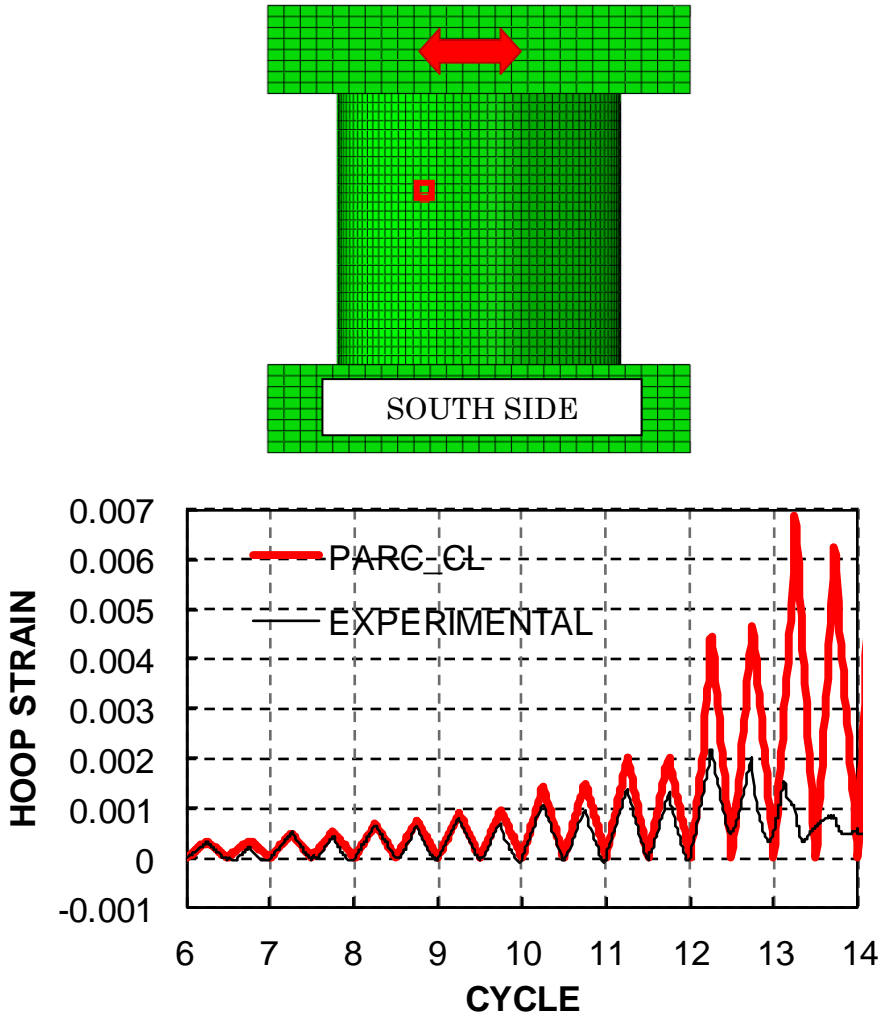


Figure 7.38 - Element 605, strain gage S3W7875S results comparison.

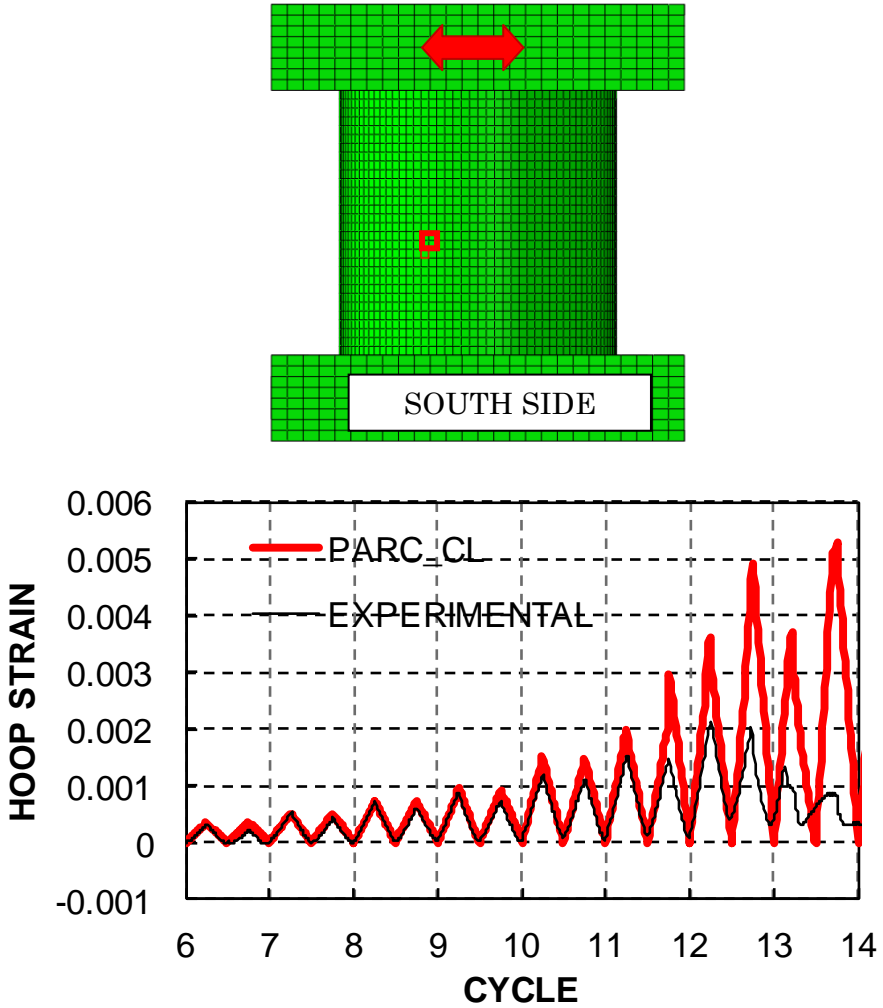


Figure 7.39 - Element 969, strain gage S4W7875S results comparison.

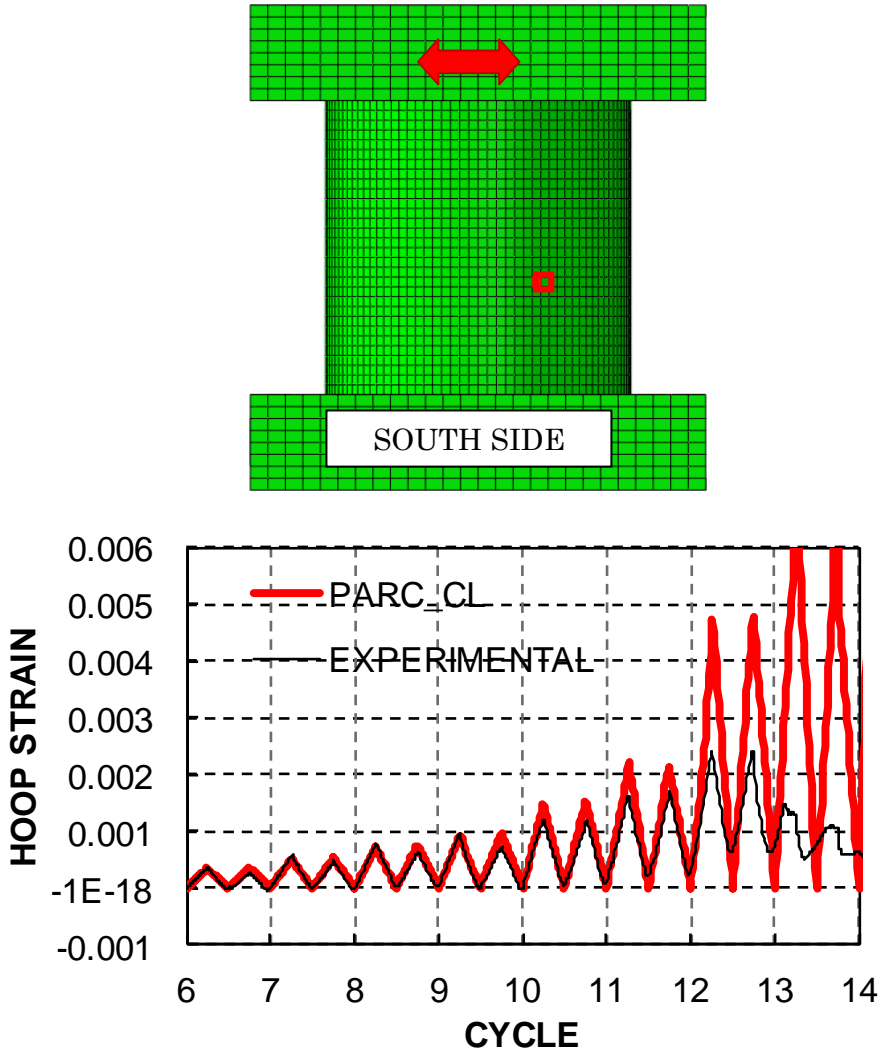


Figure 7.40 - Element 969, strain gage S4S1125E results comparison.

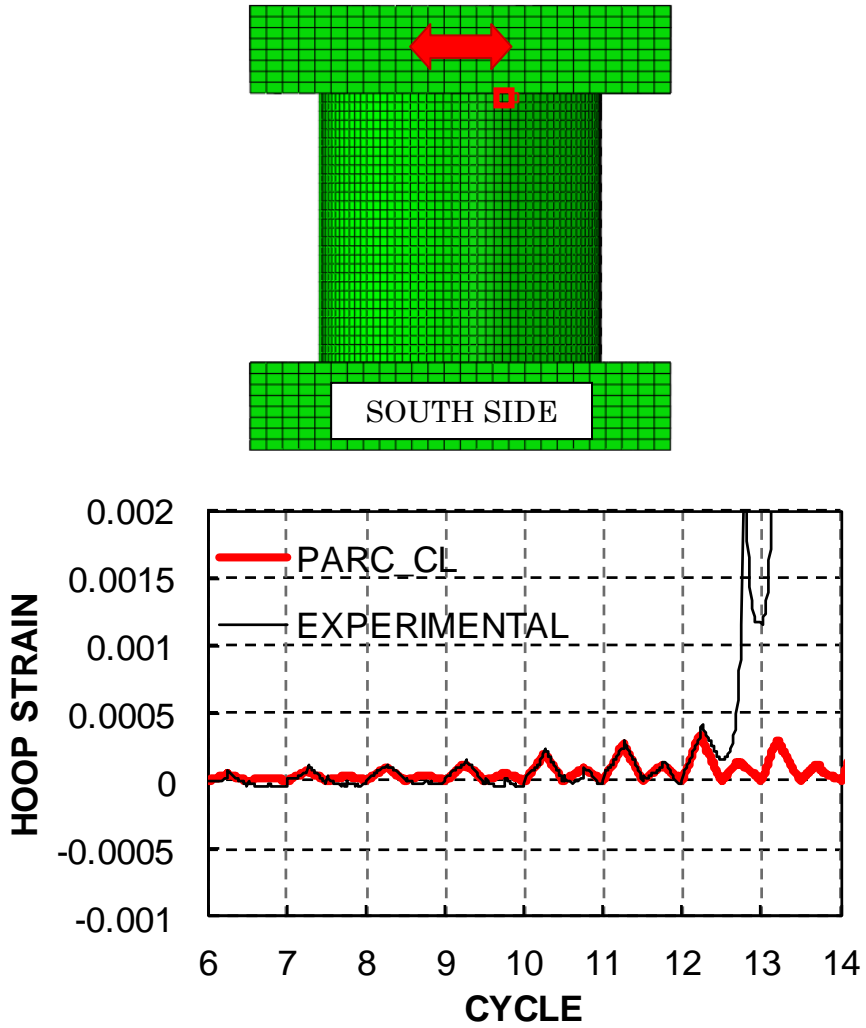


Figure 7.41 - Element 20, strain gage S1S1125E results comparison.



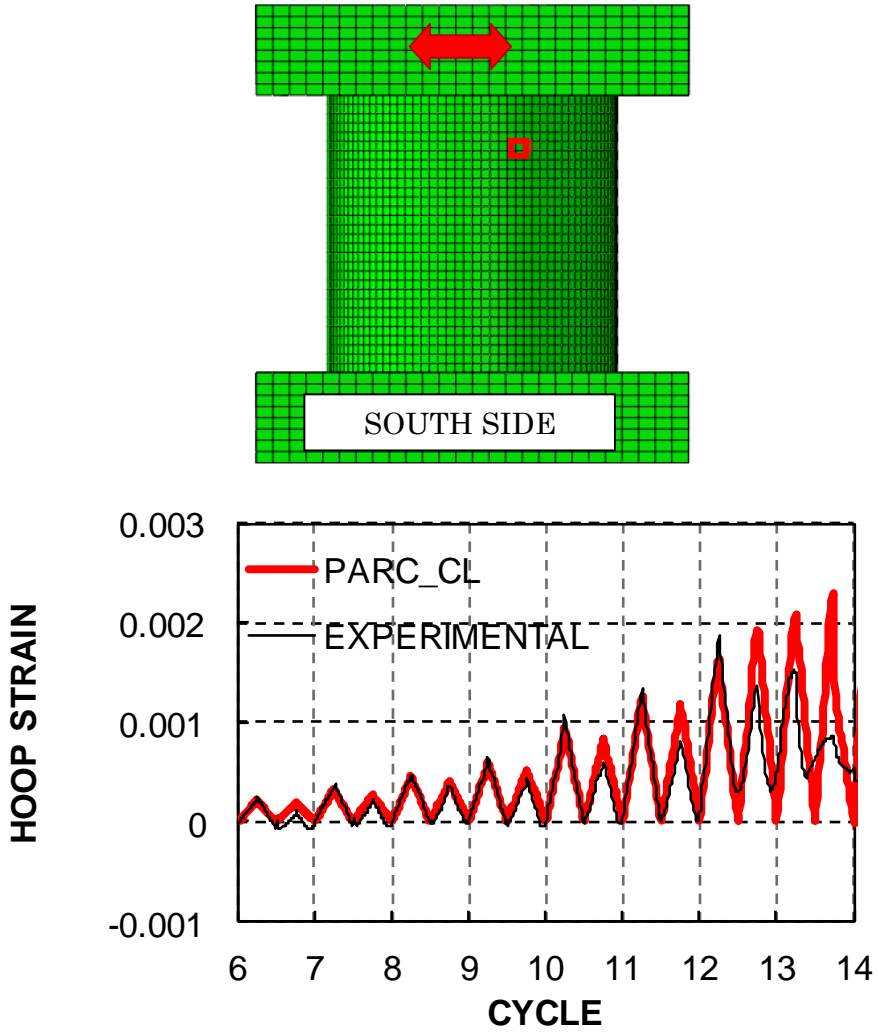
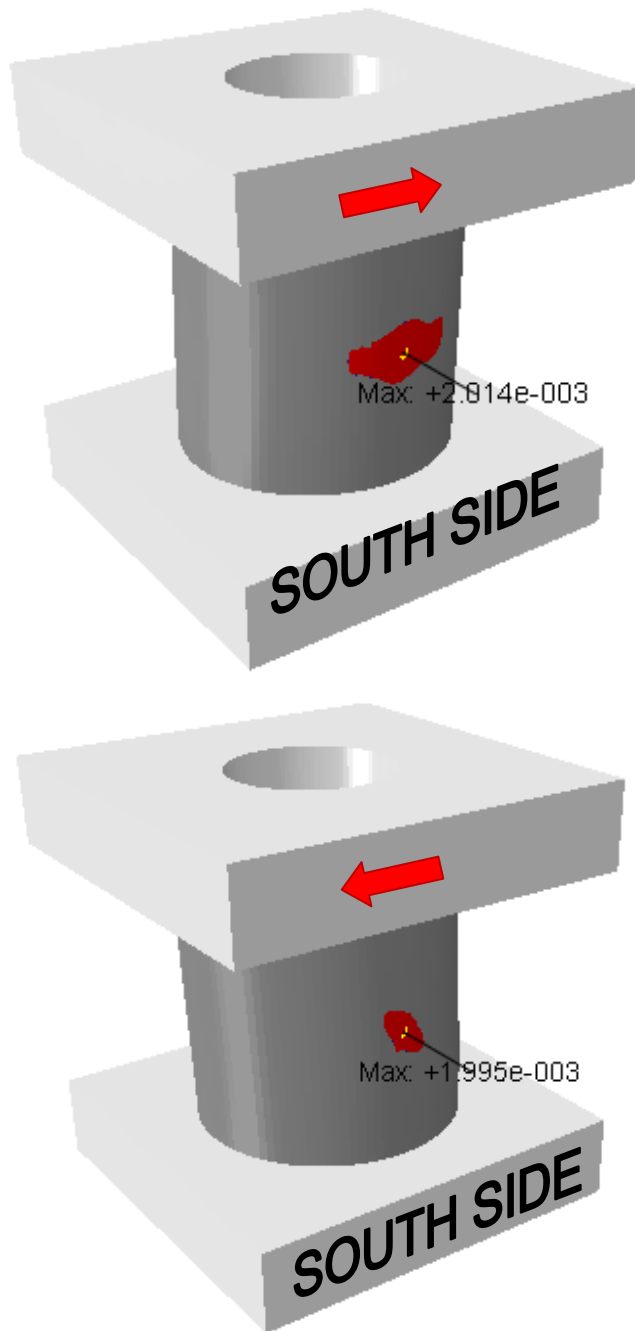


Figure 7.42 - Element 280, strain gage S2S1125E results comparison.

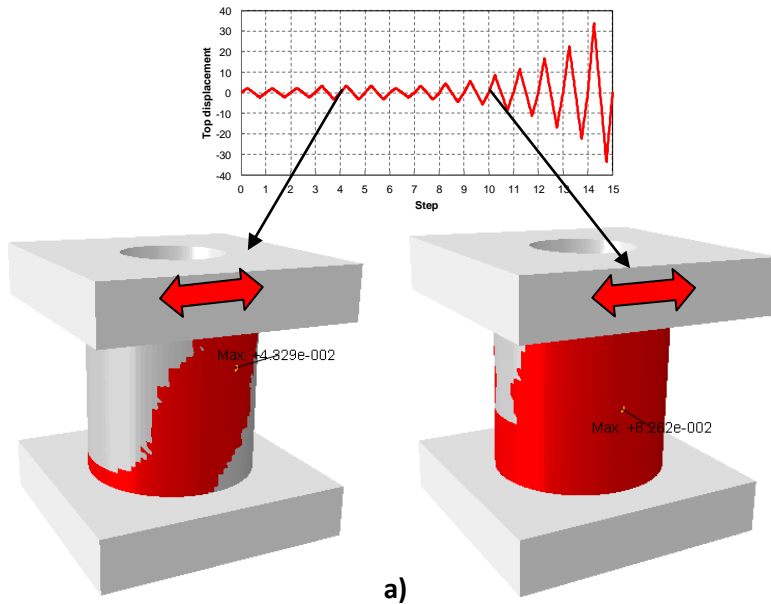


**Figure 7.43** - Hoops first yielding during cycle 12 in both directions (the area where  $\epsilon_s > \epsilon_y = 0.0019$  is displayed in red).

### 7.6.4 Crack opening

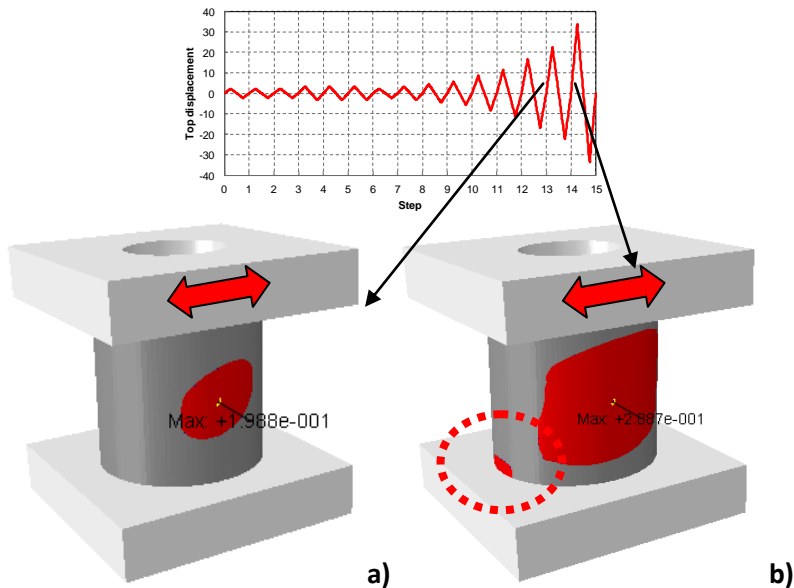
Visible crack openings were detected during the 7<sup>th</sup> cycle although evidences of non linear concrete behaviour can be found also at the first stage of loading. This can be explained by the fact that cracks occurred during the first loading stages could not be visible only to the naked eye. In fact, unfortunately, camera scanners observations were not available during the preliminary elastic test.

In Figure 7.44 a) it is reported the crack opening contour during the first cycle of the loading protocol (top displacement about 1 mm). The maximum crack opening is 0.04 mm. On the other hand, in Figure 7.44 b) a much larger crack pattern can be seen during stage 7 (which is formally equal to stage 1 in terms of loading protocol) and the maximum crack opening is now 0.08 mm, so twice the first stage value. This may be in accordance with what observed during the test (it must be considered that cracks are considered completely opened at a value equal to 0.19 mm).



**Figure 7.44** - Crack patterns for a) cycle 1, top displacement 1 mm and b) cycle 7, top displacement 1 mm. The vessel area affected by crack opening greater than zero is displayed in red, undamaged area is displayed in grey.

It is possible to observe that the vessel area affected by damage is very large even at early stage of loading although crack openings values are still quite small. Fully opened cracks develop during cycle 10 (the first within high intensity cycles, see 7.6.1.2) in correspondence of a top displacement equal to 5 mm. The crack pattern is evidence of shear behaviour, Figure 7.45 a). However, during cycle 11 it is possible also to observe fully opened cracks due to flexural behaviour, Figure 7.45 b).

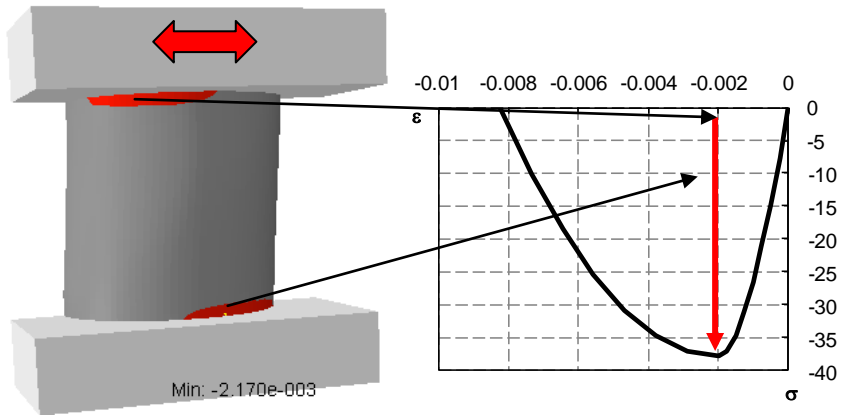


**Figure 7.45** - a) Crack pattern at cycle 10, top displacement 5 mm, and increment 738. Fully opened crack area is displayed in red ( $w > 0.19$  mm). b) Crack patterns during cycle 11, top displacement 7 mm, increment 817 (flexural cracking is put in evidence).

### 7.6.5 Concrete in compression

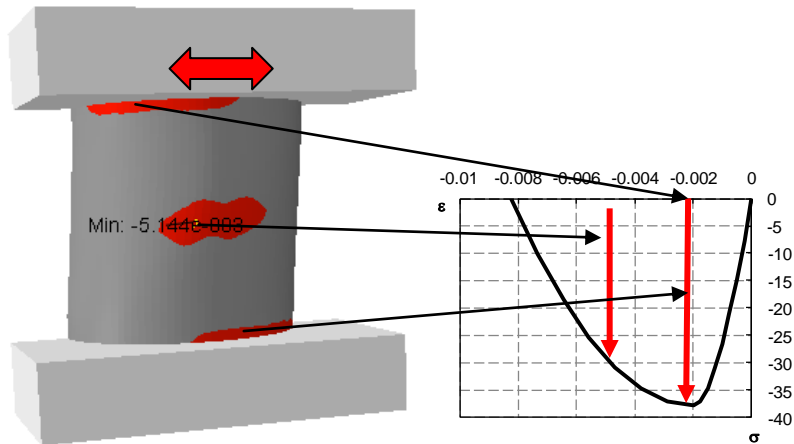
It is significant to analyse the behaviour of the concrete in compression. In fact, the FEA failure mode is due to crushing of concrete in the compressed strut related to in plane shear failure mode. The maximum concrete strain in compression is equal to  $-0.0083$  but a significant compression state can be observed for values greater (in absolute values) than about  $0.002$  (so stress  $f'_c$  has already been reached). During the 13<sup>th</sup> cycle it is possible to observe two compressed zones at the top and bottom interfaces between the vessel and the

slabs, Figure 7.46. These areas where strong compression is observed develop before the compressed strut in the central part of the vessel.



**Figure 7.46b** - Concrete in compression, cycle 13, top displacement 15 mm, increment 978. Compressive strain  $< -0.002$  are displayed in red.

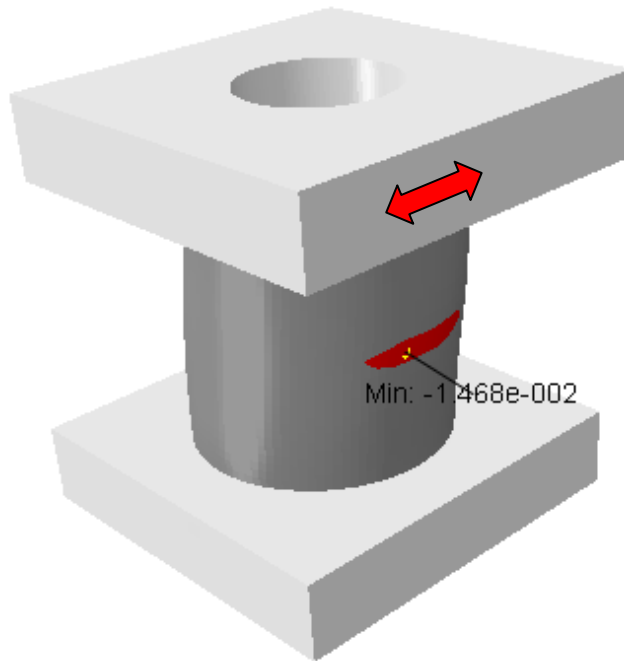
A few increments later it can be noted that a strong compressed area develops also in the central part of the specimen where maximum shear response is expected, Figure 7.47.



**Figure 7.47** - Concrete in compression, cycle 13, top displacement 15 mm, increment 980, step 12.26. Compressive strain  $< -0.002$  are displayed in red.

Finally during cycle 14 it is observed the crushing of concrete in compression, Figure 7.48. This is not in accordance with experimental observation where at the same step the specimen had already experienced a sliding shear type failure mode. However, as shown in Figure 7.47, the compression zone at the interface between slabs and specimen is subjected to

quite strong compression: this could be an evidence of a possible incipient sliding shear failure mode (it should be noted that dowel action is not still available in PARC\_CL). Moreover, further studies are required in order to evaluate the influence of the adopted modelling technique (especially boundary conditions and slab vessel interface modelling).



**Figure 7.48** - Concrete crushing in compression, cycle 14, top displacement 22 mm, increment 1058. The area where compression strain  $< -0.0083$  is displayed in red.

## 7.7 Vessel absolute displacements

During the test local displacements were measured at different height on the vessel body. Displacements were measured in the x-direction (west-east axis). Nodes identification codes of Linear Variable Differential *Transducers* LVDT position are reported in Figure 7.49. Displacements vs. cycle curves are reported in the following. It can be noted that the numerical model slightly overestimates the displacements.

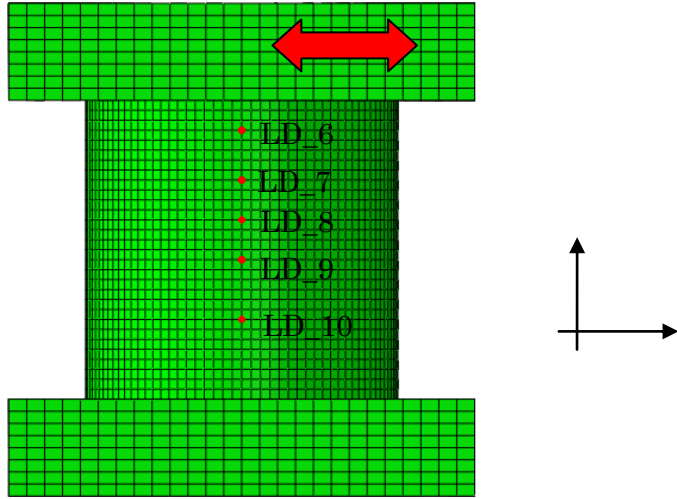
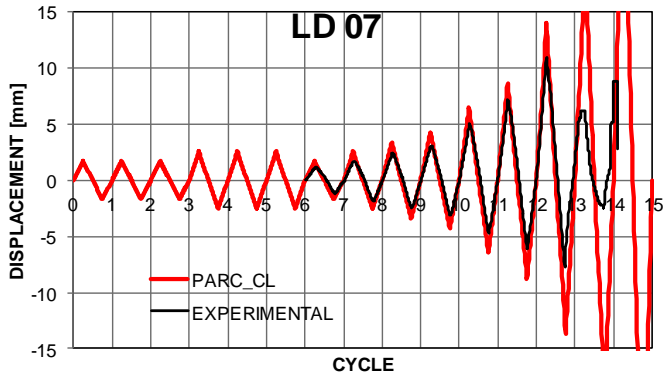
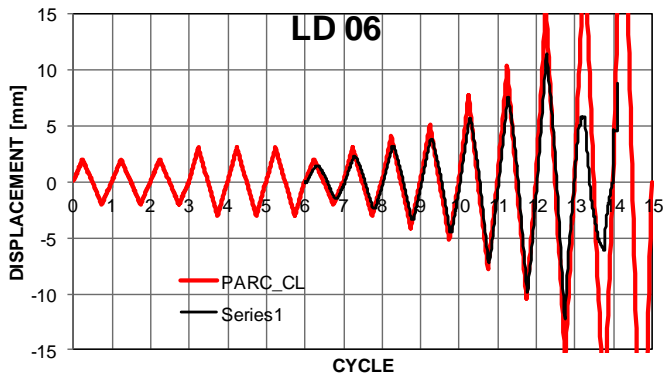


Figure 7.49 - LVDT location.



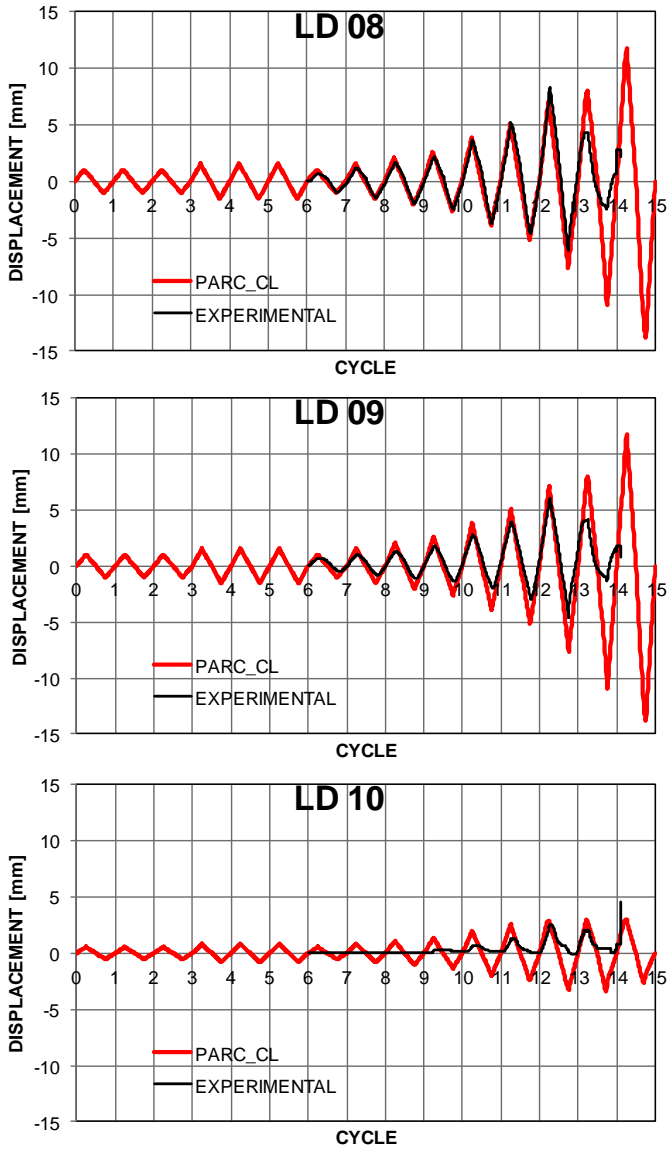


Figure 7.50 - Displacement vs. cycle comparison between experimental and numerical data.



## 7.8 Complete cycling test history

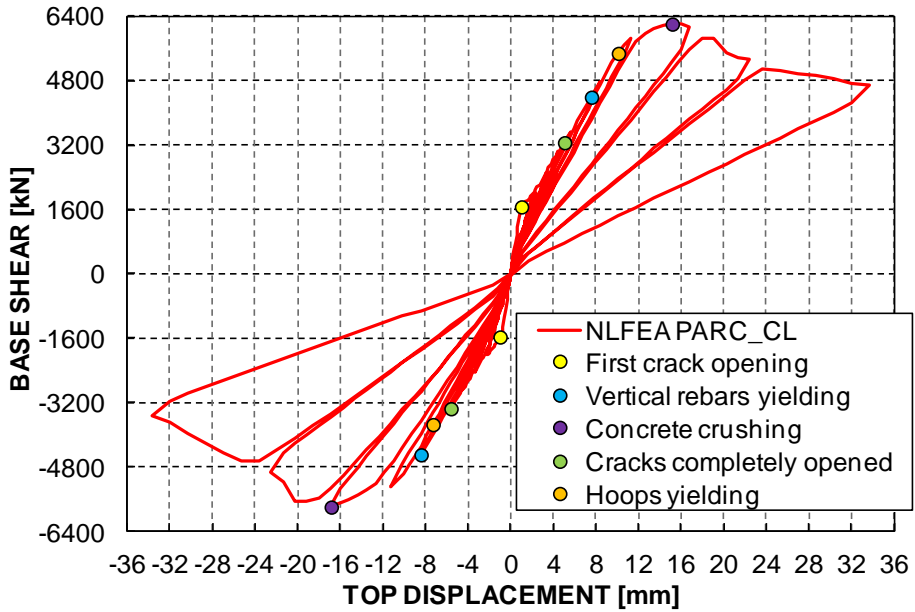
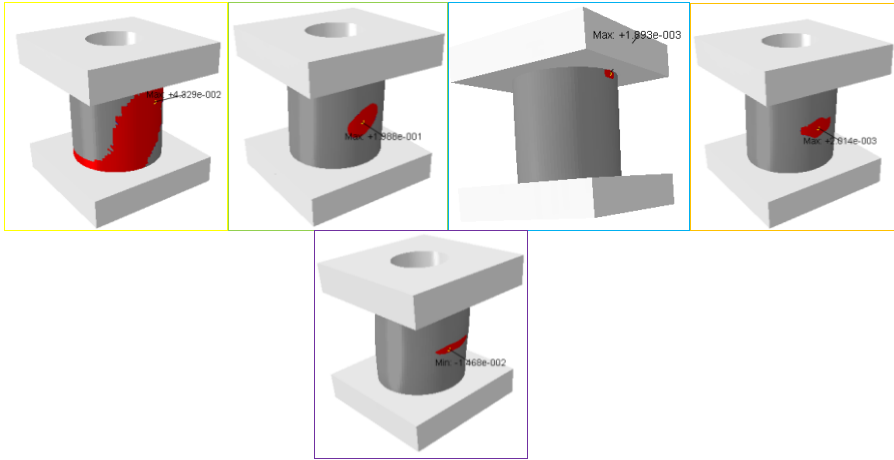
### 7.8.1 NLFEA results

Contour areas “greater than..” or “smaller than...” are always displayed in red. Variables and contour limits are reported in Table 7.3. The **concrete crushing** in compression is considered as the ultimate value of the numerical analysis.

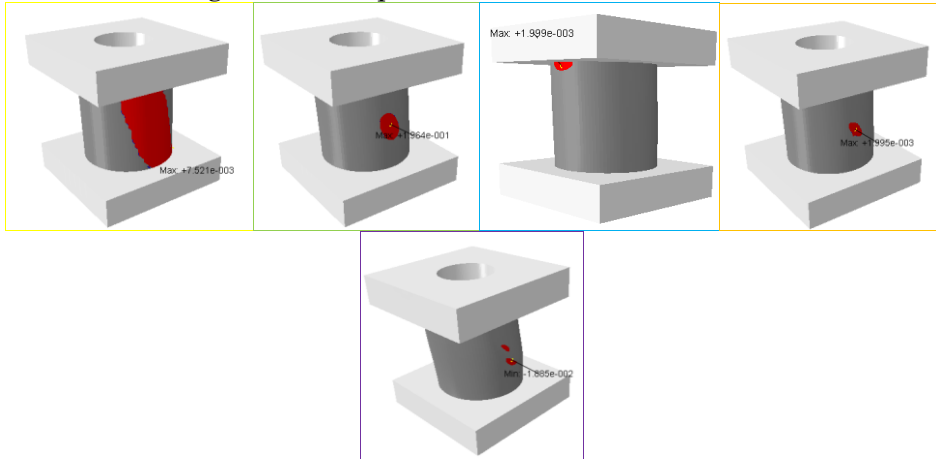
**Table 7.3** -Variables limits.

First crack opening	Crack opening	w	>0 mm
Cracks completely opened	Crack opening	w	>0.18 mm
Vertical bars yielding	Steel tensile strain	$\epsilon_s$	>0.0018
Hoops yielding	Steel tensile strain	$\epsilon_s$	>0.0019
Concrete crushing	Concrete strain in compression	$\epsilon_c$	<-0.0083

Positive +X displacement side contours view



Negative -X displacement side contours view



- NLFEA displacement history
- Cracks completely opened
- Hoops yielding
- First crack opening
- Vertical rebars yielding
- Concrete crushing

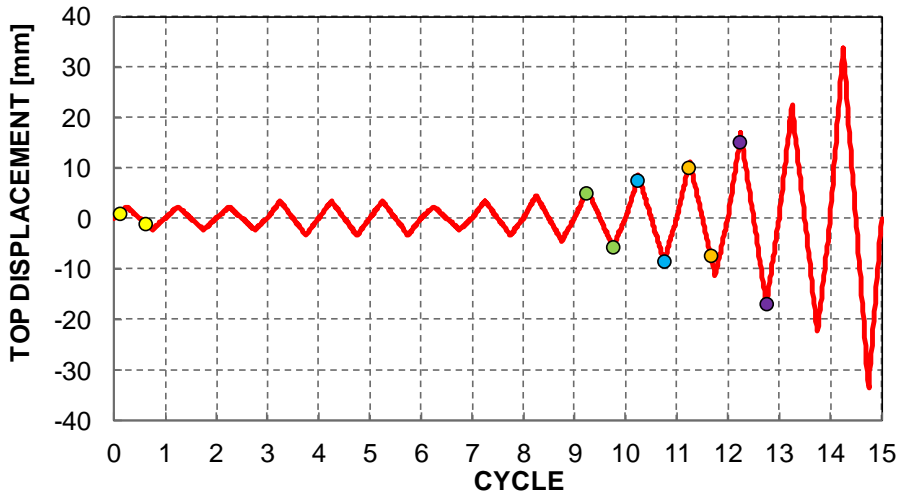


Figure 7.51 - Significant events during the numerical analysis.

## 7.9 Experimental results

In Figure 7.52 and Figure 7.53 the main events are put in evidence also for the experimental record data. By comparing Figure 7.51 and Figure 7.53 it can be noted that local engineer parameters are evaluated with good accuracy by shell modelling with PARC\_CL. Also the total base shear at each cycle (and so the structure stiffness at undamaged and damaged state) is evaluate with sufficient accuracy. On the other hand, further studies are required for the evaluation of the correct failure mode.

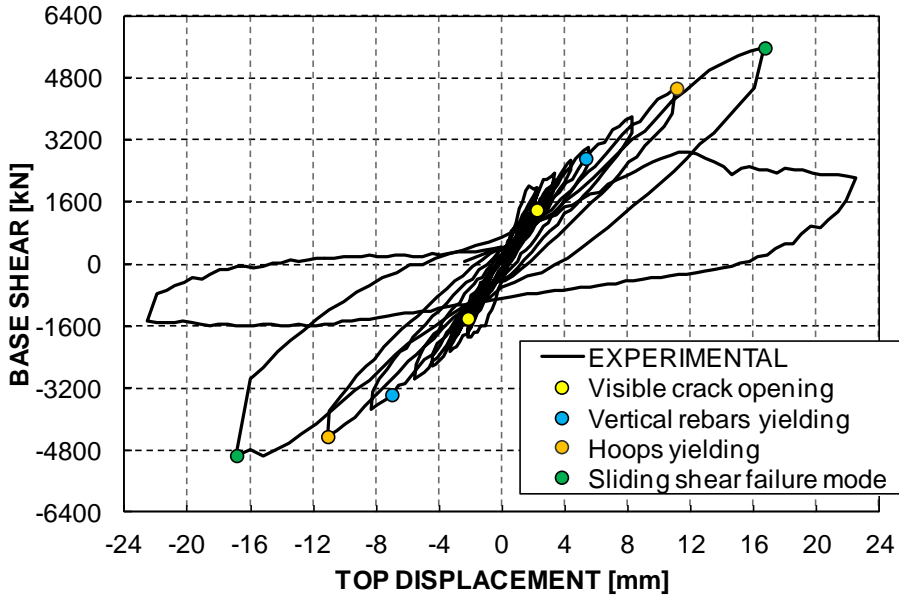


Figure 7.52 - Significant events during the experimental test.

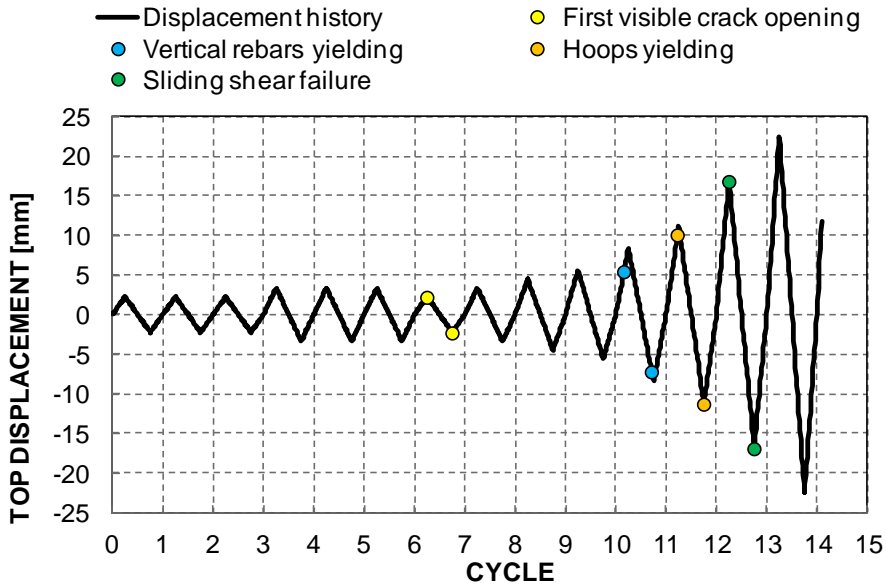


Figure 7.53 - Significant events during the experimental test on the cycle axis.

## 7.10 Pushover analysis

### 7.10.1 Total base shear vs. top displacement

In order to control the envelope curve a pushover analysis was carried out, Figure 7.54. Based on this analysis, a deeper look on damage is taken on the structure. For contour meanings please refer to Table 7.3.

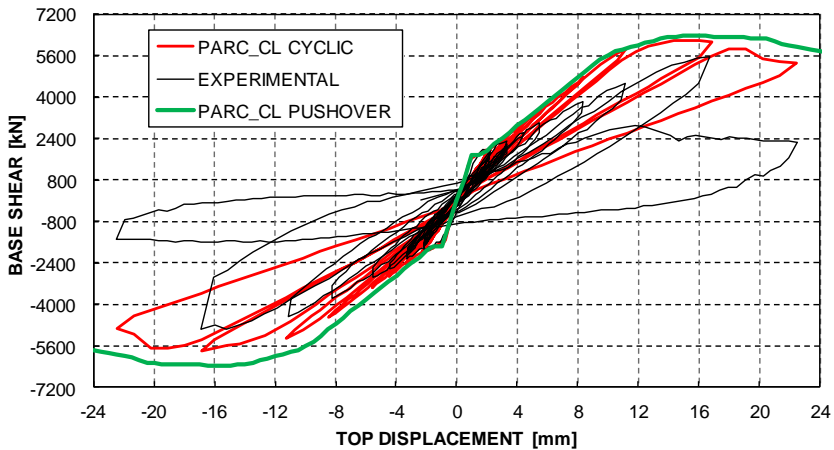


Figure 7.54 - Comparison between NLFEA pushover curve and cyclic curves.

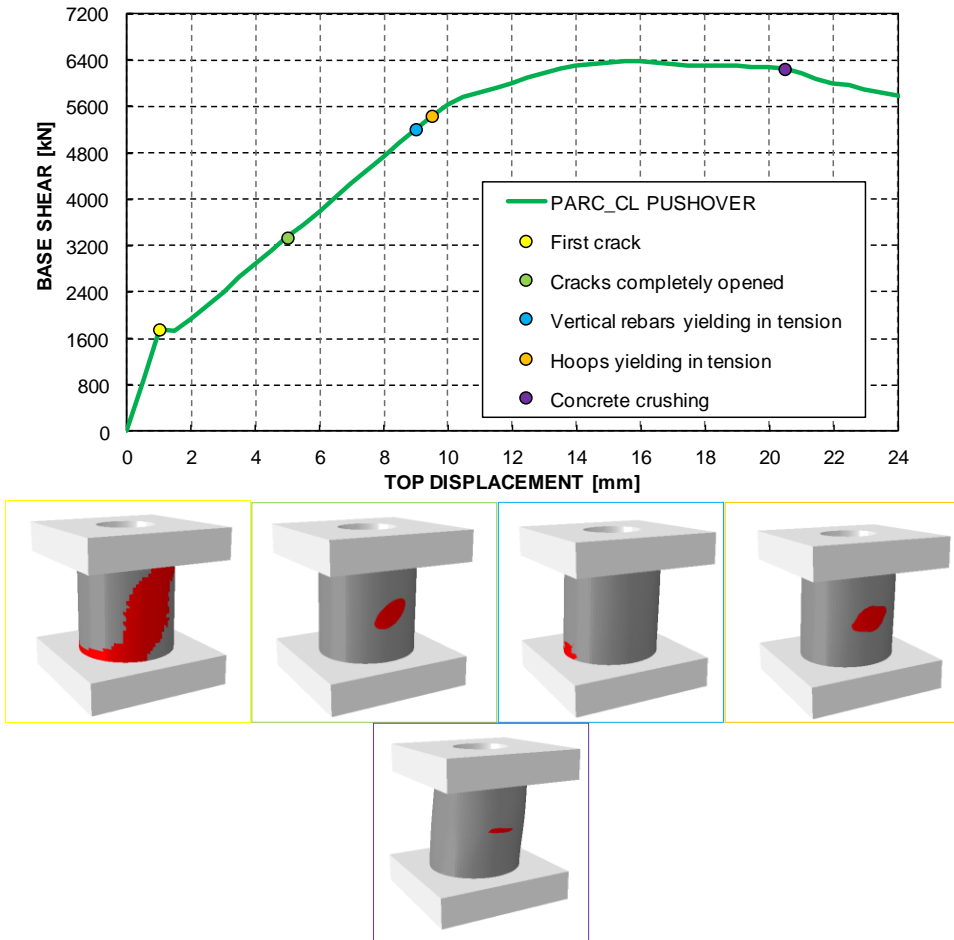


Figure 7.55 - NLFEA pushover curve with main events put in evidence.

## 7.11 Damage analysis

It has been showed that the vessel behaviour under cyclic loading is strongly conditioned by concrete cracking, high compression strains, and contemporary flexural and shear phenomena. It is useful to analyse the global damage by a numerical point of view and not only in terms of crack opening or compression strain contours. The damage level is conventionally defined using the following quantities.

$[D_c]$  = concrete stiffness matrix

$[D_s]$  = steel stiffness matrix

$[D]$  = reinforced concrete stiffness matrix

$[G_c]$  = concrete tangential stiffness matrix

Subscript  $_0$  = undamaged state

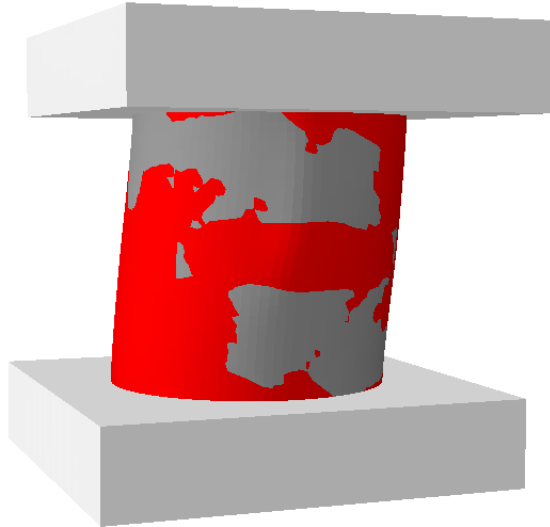
Subscript  $_i$  = current damage state

For each integration point the damage level is given by the ratio  $\det[X_i]/\det[X_0]$ . Ratios equal to 1 mean that the damaged and undamaged stiffness are equal, then the element is undamaged, ratios closed to 0 mean that the element is strongly damaged as  $\det[X_i] \ll \det[X_0]$ . Finally, it is possible to evaluate which parts of the vessel are more damaged because of contemporary compression, tension and shear contributions.

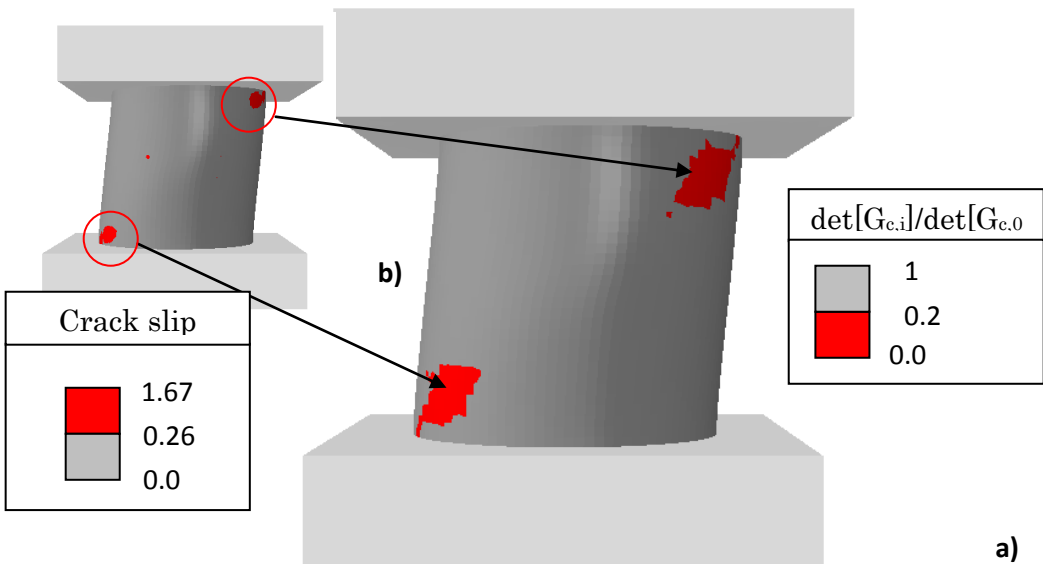
### 7.11.1 Damage in concrete

The ratio  $\det[D_{c,i}]/\det[D_{c,0}]$  shows the damage level in the concrete considering the contributes of tension, compression and shear. In Figure 7.56 it is showed the concrete damage at Step 41 of the pushover analysis correspondent to concrete crushing, (top displacement 20.5 mm). The area where  $\det[D_{c,i}]/\det[D_{c,0}] < 0.2$  is displayed in red. It can be noted that not only the web of the vessel (where crushing in compression first occurs) but also the interface regions are strongly subjected to degradation. For  $[G_c]$  it must be noted that the aggregate interlock effect is taken into account: if  $\det[G_i] \ll \det[G_0]$  it means that aggregate interlock is no more effective because of strong tangential slip or crack opening values. In Figure 7.53 the contour

shows the region where  $\det[G_{c,i}]/\det[G_{c,0}] < 0.2$  at ultimate displacement (concrete crushing). The damaged region seems to be correlated more to the crack slip highest values.



**Figure 7.56** - Damage in concrete at crushing. The red contour indicates  $\det[D_{c,i}]/\det[D_{c,0}] < 0.2$ . It is possible to notice that both the web and interface regions are strongly damaged.

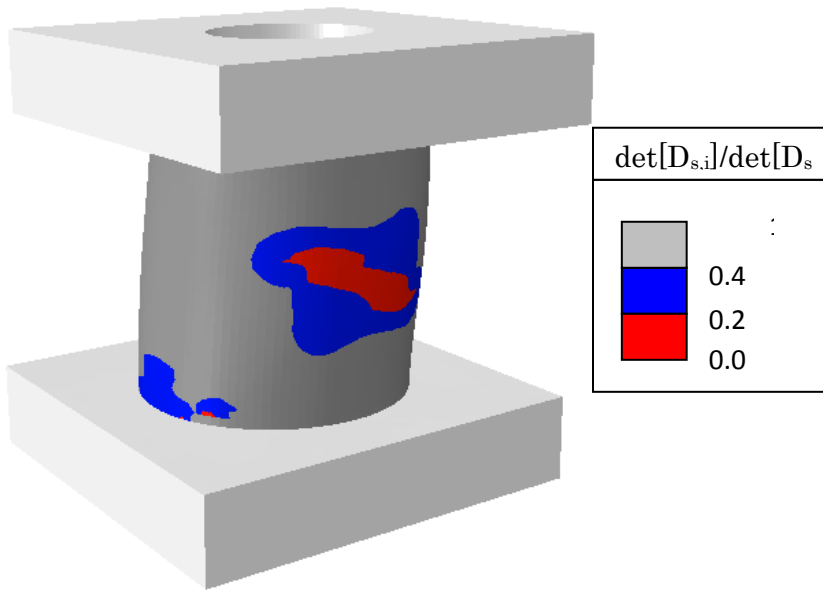


**Figure 7.57** - a) Tangential stiffness degradation and comparison with crack slip contour. The red contour indicates  $\det[G_{c,i}]/\det[G_{c,0}] < 0.2$ . b) Crack slip contour at the same step, highest values are showed in red.



### 7.11.2 Damage in steel

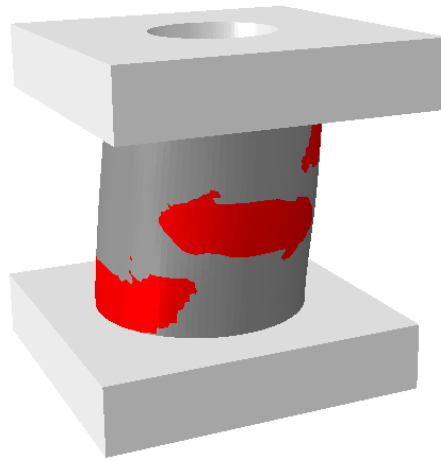
In Figure 7.58 it is showed the degradation in the steel matrix at ultimate displacement (concrete crushing, Figure 7.56). It can be noted that the strongest degradation occurs in the vessel web in association with the yielded hoops (see also Figure 7.43),  $\det[D_{s,i}]/\det[D_{s,0}] < 0.2$  (displayed in red). Vertical rebars are subjected to lower degradation,  $\det[D_{s,i}]/\det[D_{s,0}] < 0.4$  (displayed in blue).



**Figure 7.58** - Steel stiffness  $[D_s]$  degradation. The red contour indicates  $\det[D_{s,i}]/\det[D_{s,0}] < 0.2$  while the blue one  $0.2 < \det[D_{s,i}]/\det[D_{s,0}] < 0.4$ .

### 7.11.3 Global damage in reinforced concrete

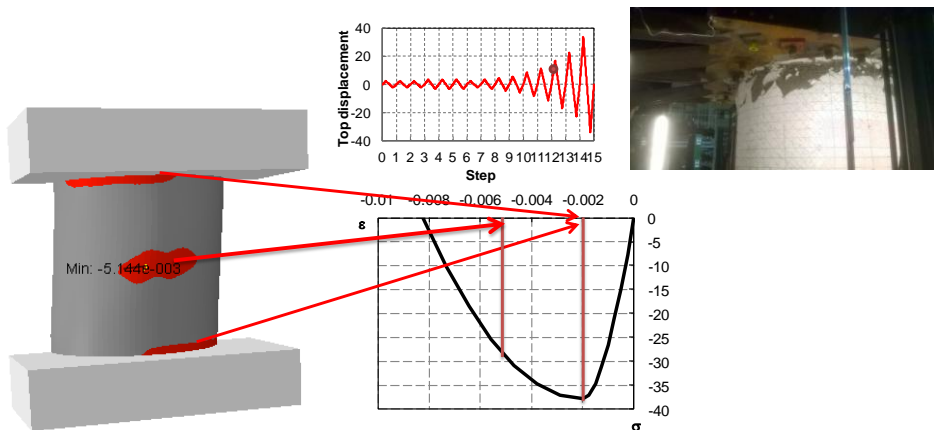
Matrix  $[D]$  is a combination of  $[D_c]$  and  $[D_s]$ . The  $\det[D_i]/\det[D_0] < 0.2$  contour reported in Figure 7.59 shows a strong degradation in the vessel web (crushing of concrete and hoop yielding, shear behaviour) and at the bottom west side (and also at the symmetric top east side) because of rebars yielding and concrete crack opening (flexural behaviour).



**Figure 7.59** - Reinforced concrete degradation,  $\det[D_i]/\det[D_0]<0.2$  contour in red.

### 7.12 Remarks

The experimental tested showed a sliding shear failure mode. Shell modelling was not able to detect such failure mode, further aspects about sliding shear will be discussed in chapter 8. However, strong compression level was detected both in the vessel web area and at the wall- foundation interface. This may be considered as an early evidence of a possible sliding shear mechanism.



**Figure 7.60** – Compression level in concrete and sliding shear failure mode observed (credits: Stocchi, courtesy of NCREE).





## **Chapter VIII. Further Applications and Future Developments**

## 8 Further applications and future developments: the RC interface problem

As described in chapters 6 and 7, the contact behaviour is an important aspect to be considered in the modelling. In the current chapter it will be described one modelling technique that can be used for the implementation of the contact problem for wall structures shell elements. The modelling technique then will need further validation in order to be properly introduced in complex models like the ones described in chapters 6 and 7. This chapter can be read also as a basic guideline for the description of the contact problem by other Abaqus code users.

The contact is given basically by two main contributions: friction at the foundation/wall interface and dowel action. The EC8 defines the sliding shear strength as the sum of three main contributions, Eq. (8.1).

$$V_{Rd,S} = V_{dd} + V_{id} + V_{fd} \quad (8.1)$$

where  $V_{dd}$  is the dowel action contribution,  $V_{id}$  is the shear strength provided by inclined rebars (which are usually not used in existing structure and are not always used in present design because of technical problems related to their set-up),  $V_{fd}$  is the concrete friction contribution.

The concrete friction can be introduced in FE models with surface to surface contact laws. For the description of the dowel action a spatial multi-spring element can be implemented in the user subroutine UEL.for for Abaqus code and can be introduced as a parallel system with concrete friction. Simpler zero length elements may be introduced as well in the model although they do not allow a full description of the non linear behaviour of dowels.

### 8.1 Contact behaviour

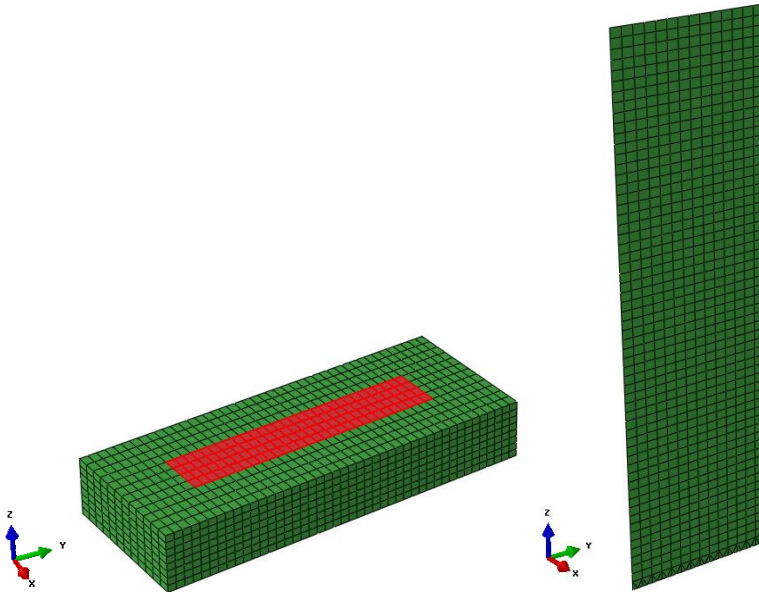
The modelling of wall to foundation friction only contact is described. In the chapter a simple no tension normal behaviour with tangential friction (both with zero and non-zero values) is investigated. Comparisons between different modelling techniques and analytical calculation are presented in terms of stress

distribution and total shear vs. top displacement curves.

### 8.1.1 Model description

#### *FOUNDATION and WALL*

The foundation is modelled by means of 8 nodes solid elastic elements. In the picture the master contact surface for the contact definition is also enlightened. The wall is modelled with 4 nodes elastic shell elements, Figure 8.1.



**Figure 8.1-** Foundation model with solid elements and the adopted reference system.

#### *WALL TO FOUNDATION INTERFACE*

As the shells wall are normal to the foundation an equivalent base section is introduced in order to take into account the contact problem. The nodes of the equivalent base section have the same displacements of the wall bottom nodes in order to uniformly distribute the normal force (beam multi point constraints are connecting the central row points to the lateral ones). The elements of the equivalent base section have small thickness (1 mm) and zero density. The Young modulus of the equivalent base elements has been defined by means of a parametric study (by checking stresses at the interface as shown in 8.1.3 and 8.1.4). The negative face of the equivalent base is the slave surface of the contact problem, Figure 8.2.

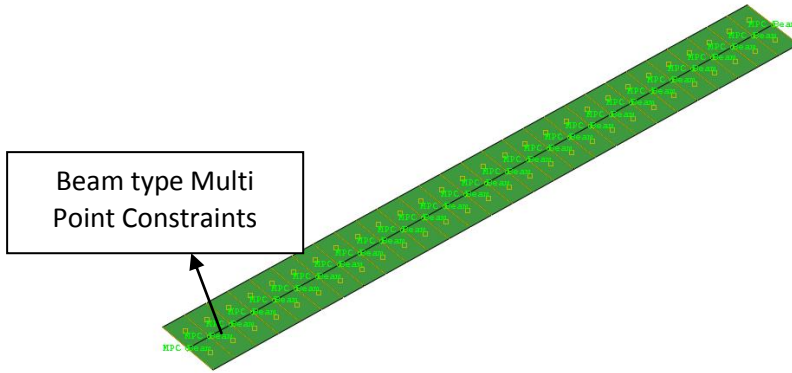


Figure 8.2- Equivalent base model with shell elements.

## 8.1.2 Global model

### 8.1.2.1 Boundary conditions

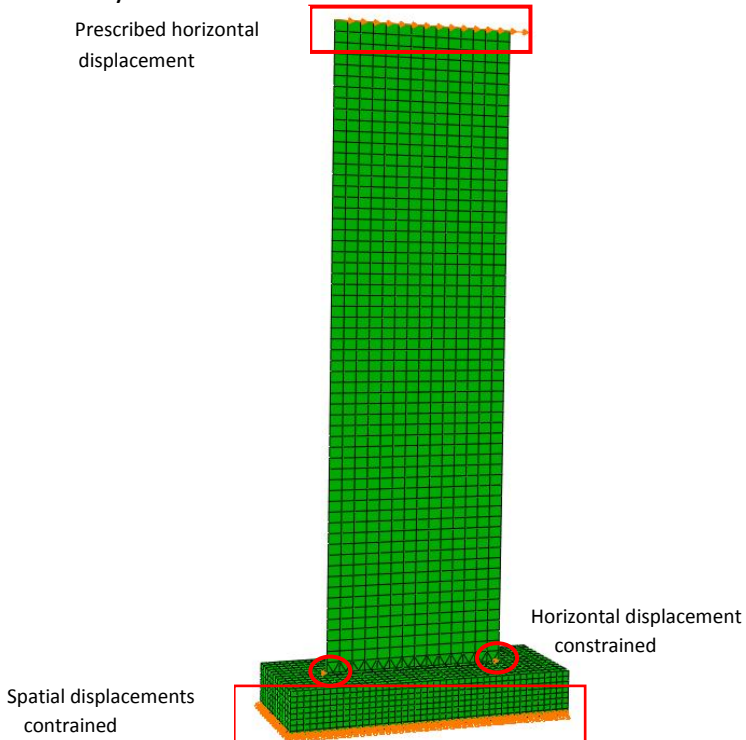


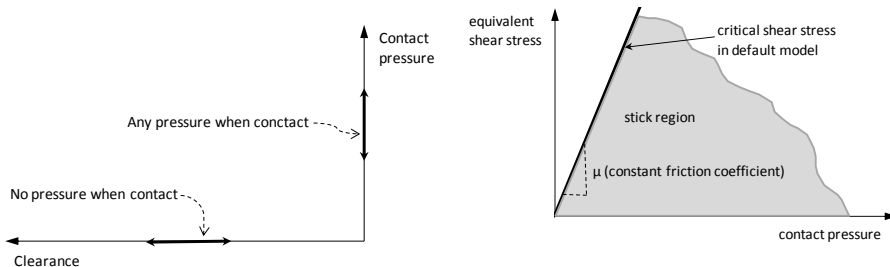
Figure 8.3- Equivalent global model with shell elements and boundary conditions.



The structure is subjected to self weight and to an additional load in order to enhance the compression response. A global 60 kN load is applied at top nodes.

### 8.1.2.2 Contact definition

The contact is defined as a surface to surface interaction. In order to enhance the contact the base mesh and the foundation mesh are slightly different and nodes adjustment is introduced in the contact definition. Two models are tested in this section: a frictionless model and a friction model with several coefficients too. The normal contact is defined with `PRESSURE-OVERCLOSURE=HARD` parameter. This means that as long as the surfaces are in contact pressure is transferred while when for non zero clearance pressure is zero. The model is as simple as possible so no contact enhancement controls and parameters are used. The tangential behaviour is defined with the default `*FRICTION` command which introduces the basic Coulomb friction in the model.



**Figure 8.4-** Hard pressure-overclosure model and Coulomb friction model in Abaqus code.

### 8.1.3 Frictionless model

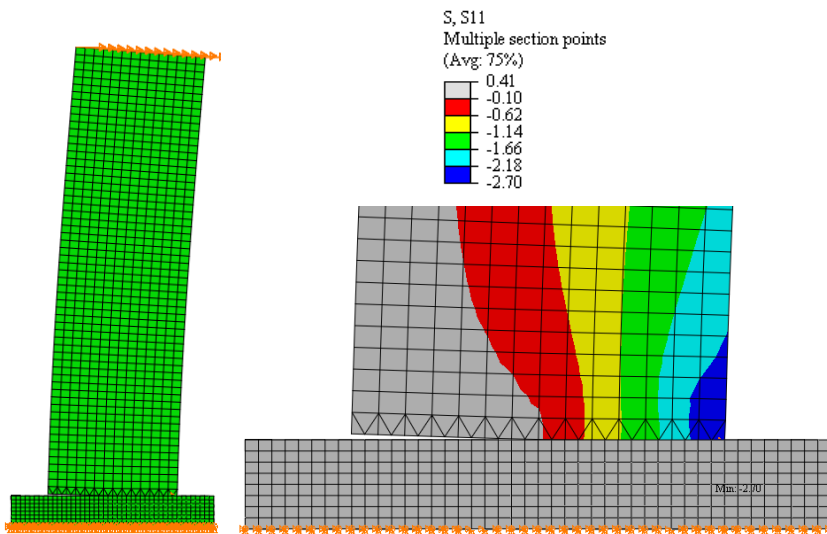
#### 8.1.3.1 Compression stresses distribution

In order to evaluate the reliability of the model stresses are compared to analytical calculation. The following parameters have been used for elastic materials:

- Wall:  $E_c=30000$  MPa ; Poisson=0.19
- Foundation:  $E_c=300000$  MPa ; Poisson=0.19
- Equivalent base:  $E_c=10000$  MPa ; Poisson=0.19

For the foundation it has been defined a stiffer material (Young modulus 10 times the modulus of the wall) in order to obtain a stress distribution at the wall base closer to analytical calculation. The equivalent base modulus has been calibrated via parametric analysis by introducing different Young modulus values and keeping the foundation modulus fixed.

The whole model is elastic so a triangular distribution of stresses is expected the base of the wall. As shown in Figure 8.5, paragraph 8.1.6, the model displays a global elastic behaviour until total shear is about equal to 6.5 - 7 kN. The principal stresses contour at the base of the wall is also reported. The stress distribution is also reported in Figure 8.6. It can be noted that the no tension model is behaving as expected (no tensile stress is transferred). The maximum stress at  $V=6.88$  kN is equal to  $-2.84$  N/mm<sup>2</sup>. Analytical data are provided in Table 8.1.



**Figure 8.5-** Deformed shape @  $V=6.9$  kN and  $d=0.6$  mm and Principal vertical stress at the base of the wall, frictionless interface.

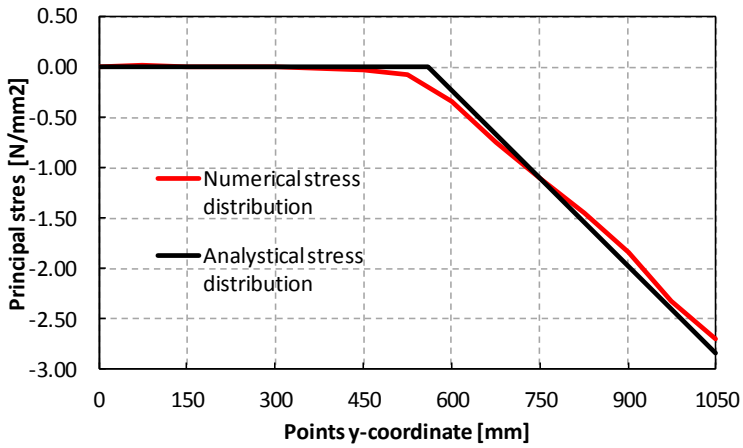


Figure 8.5- Stress triangular distribution at wall interface (no tension hypothesis) for total shear  $V=6.9$  kN.

Table 8.1 –Wall characteristics and stress values (frictionless model).

$H_{wall}$	3650	mm
$L_{wall}$	1050	mm
$t_{wall}$	100	mm
Volume	0.38325	$m^3$
Mass	958	kg
Self weight	9395	N
Additional weight	60000	N
$N_{tot}$	69395	N
Base Moment $M=VH$	25126600	Nmm
Total shear $V$	6884	N
$e=M/N_{tot}$	362	mm
$L_{wall}/2$	525	mm
<b><math>x</math></b>	<b>489</b>	<b>mm</b>
<b><math>\sigma_c</math></b>	<b>2.84</b>	<b><math>N/mm^2</math></b>
Total compression $C$	69395	N

Where:

$$x = 3 \left( \frac{L_{wall}}{2} - e \right) \text{ and } C = \frac{1}{2} \sigma_c \cdot x \cdot t_{wall}$$

It can be noted that, within the adopted hypotheses, the numerical curve fits the analytical one with good approximation.

### 8.1.4 Friction model

Lateral constraints on the wall base are removed and friction coefficient equal to 0.6 is introduced at the interface. As automatic increment method has been used in the static analysis in order to avoid convergence issues, results are presented for a slightly different value of total shear.

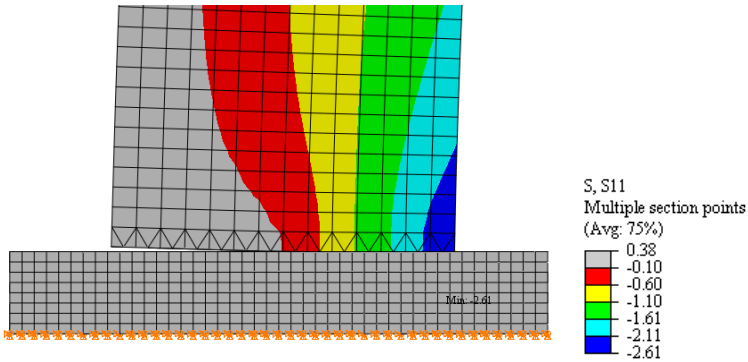


Figure 8.7- Principal vertical stress at the base of the wall,  $\mu=0.6$ .

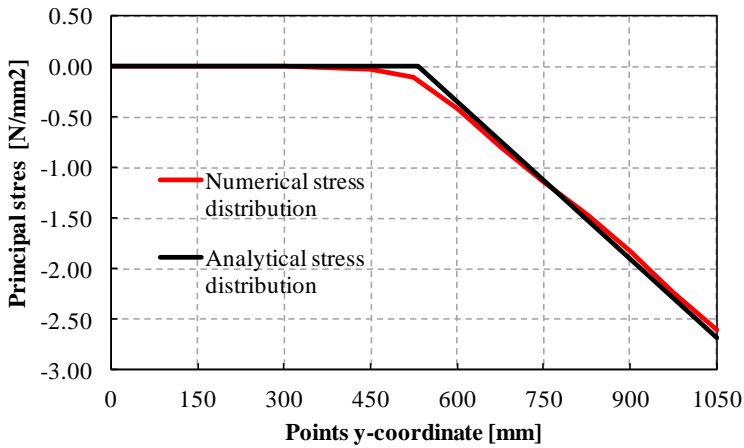


Figure 8.8- Stress triangular distribution at wall interface (no tension hypothesis) for total shear  $V=6.7$  kN.

**Table 8.2** – Wall characteristics and stress values (friction model).

$H_{\text{wall}}$	3650	mm
$L_{\text{wall}}$	1050	mm
$t_{\text{wall}}$	100	mm
Volume	0.38325	$\text{m}^3$
Mass	958	kg
Self weight	9395	N
Additional weight	60000	N
$N_{\text{tot}}$	69395	N
Base Moment $M=VH$	24455000	Nmm
Total shear $V$	6700	N
$a=M/N_{\text{tot}}$	352	mm
$L_{\text{wall}}/2$	525	mm
<b>x</b>	<b>518</b>	<b>mm</b>
<b><math>\sigma_c</math></b>	<b>2.68</b>	<b><math>\text{N}/\text{mm}^2</math></b>
Total compression $C$	69395	N

### 8.1.5 Solid model (frictionless)

In order to evaluate the influence of the equivalent base normal to the wall it was created a solid model, too. In this case the interface is defined between the solid faces of the bottom wall and of the top foundation. However, the PENALTY parameter was added to the contact definition in order to enforce convergence. The results are slightly different with respect to the shell model; however the solid modelling is used only to evaluate the reliability of the shell model with equivalent base.

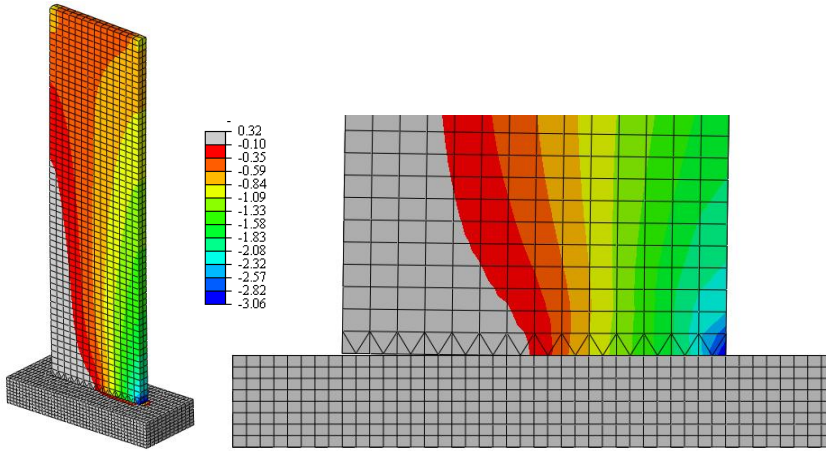


Figure 8.9- Principal vertical stress at the base of the wall, solid elements, frictionless contact

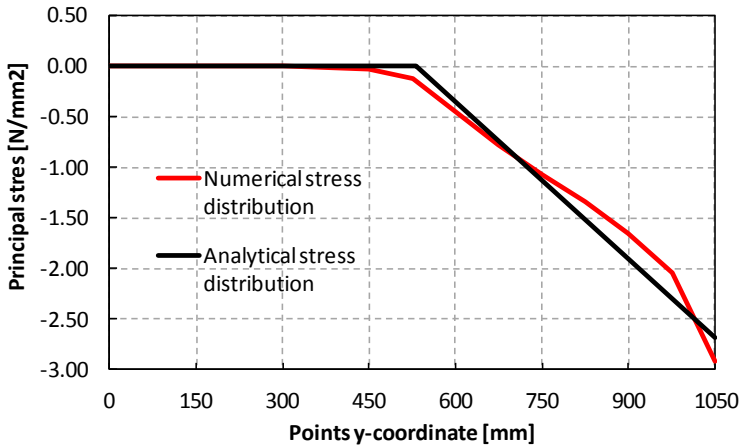


Figure 8.10- Stress triangular distribution at wall interface (no tension hypothesis) for total shear  $V=6.7$  kN (stresses are measured for the points in the middle of the wall thickness)

### 8.1.6 Global behaviour: total shear vs. top displacement

Simple pushover analyses have been performed in order to check the global behaviour of the models. In Figure 8.11 are reported curves for the shell models with and without tangential friction. The total normal force at the interface is equal to 69.4 kN. As expected, when friction coefficient is equal to 0.1 sliding occurs at about 6.9 kN. For higher friction values it is observed a rocking mechanism. It is possible to notice that the constrained frictionless model and the friction models (with  $\mu > 0.1$ ) give similar force displacement

curves. This means that the interface model is properly working. In Figure 8.12 it is reported the comparison between shell and solid frictionless modelling. The global response is the same also in this case.

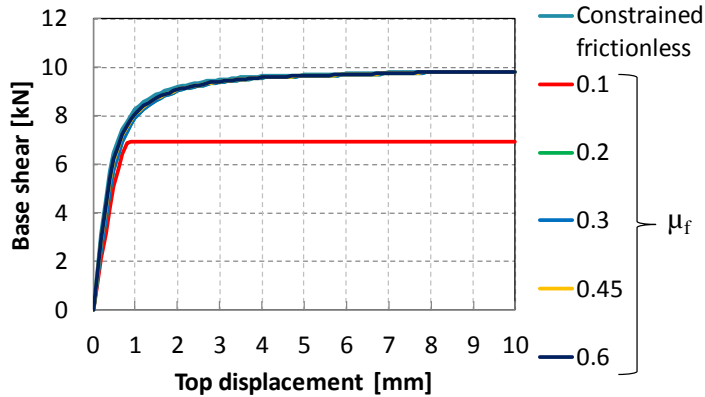


Figure 8.11- Shell modelling: force displacements curves for different friction models.

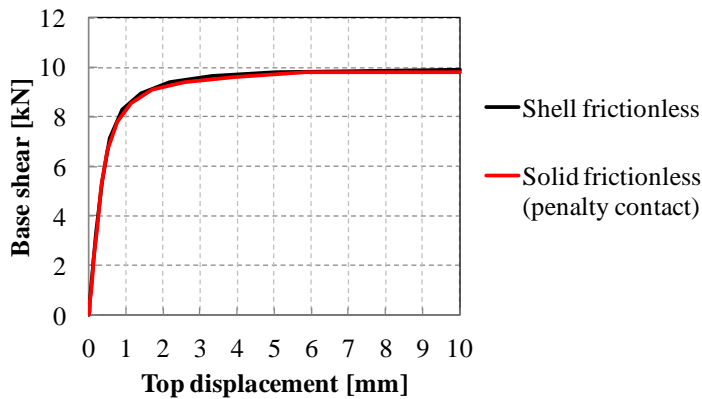


Figure 8.12- Shell modelling: force displacements curves for different friction models.

### 8.1.7 Cyclic behaviour

Cyclic analyses have been performed introducing the DIRECT parameter to the normal behaviour definition in order to reach convergence. This parameter allows choosing direct enforcement of contact constraints without approximation or use of augmentation iterations. The direct method can be used to strictly enforce a “hard” pressure-overclosure relationship. Lagrange multipliers are always used in this case. As the problem is completely elastic and

no energy dissipation is introduced in the friction model loading and unloading curves are coincident, Figure 8.13.

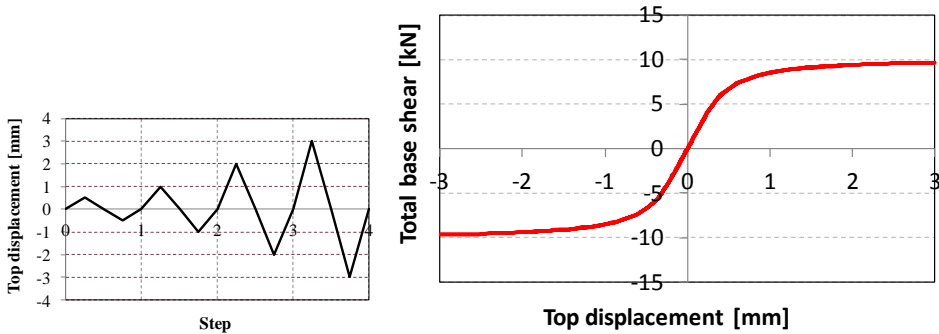


Figure 8.13- Loading protocol and cyclic response of the structure.

## 8.2 Dowel action

Dowel action can be modelled via connectors, which are special elements that can be used to model internal or external constraints by specifying a generalized force vs. displacement/rotation relationship. Such relationships can be linear, non linear, coupled and uncoupled. It is possible to use also zero length connectors which are very useful for the modelling of dowels crossing an interface. Even if ABAQUS offers a large amount of connectors, the dowel behaviour has then been implemented in a UEL.for subroutine in order to have more reliable and general model. The user element defined is then a zero-length spatial multi-spring.

### 8.2.1 ABAQUS zero-length connectors elements

The dowel behaviour could be easily implemented via built-in connectors elements; however the behaviour of such elements cannot be completely decided by the user.

#### 8.2.1.1 One direction loading, uncoupled behaviour

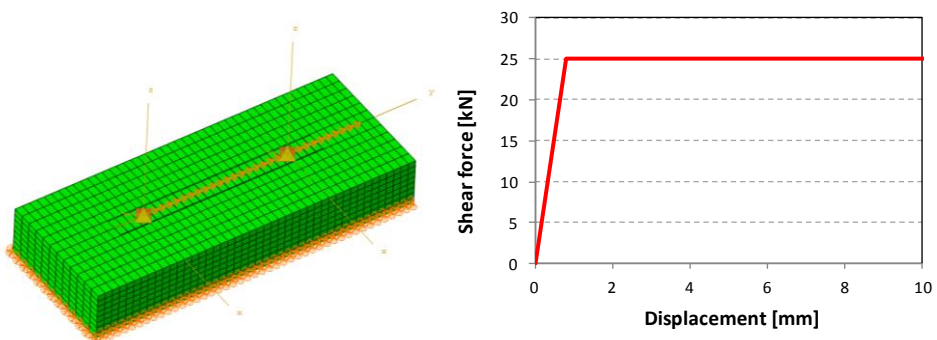
It is described a very simple model able to transfer shear across a section by means of two zero length Cartesian connectors simulating dowel action. In Figure 8.14 it is shown the adopted model. A rigid plate is connected by means of two Cartesian connectors to the foundation surface. Displacements are then



applied to the plate. The two connectors simulate  $\Phi 14$  rebars dowel action. A force/displacement relationship for dowels is introduced according to experimental results with a simplified bi linear curve. Connectors behaviour is defined by means of the following commands:

```
*CONNECTOR BEHAVIOR, NAME=CONNPROP-1_CONNSECT-4
*CONNECTOR ELASTICITY, COMPONENT=1
31250 "This is the elastic stiffness [N/mm]"
*CONNECTOR PLASTICITY, COMPONENT=1
*CONNECTOR HARDENING, DEFINITION=TABULAR
25000,25 "Plastic force [N] and the plastic
displacement [mm]"
*CONNECTOR ELASTICITY, COMPONENT=2
31250
*CONNECTOR PLASTICITY, COMPONENT=2
*CONNECTOR HARDENING, DEFINITION=TABULAR
25000,25
*CONNECTOR ELASTICITY, RIGID "In z direction connector
is set rigid"
3
```

In Figure 8.14 it is reported the global response in terms of total shear vs. displacement. It can be noticed that the global behaviour is given by the sum of the shear transferred by the two dowels. The model is then able to transfer prescribed dowel action values (in case of one-directional loading).



**Figure 8.14-** a) A rigid plate connected to an elastic foundation and b) shear displacement law in x and y direction for the connectors.

### 8.2.1.2 One direction loading: example of a simplified coupled behaviour

It is possible to specify a FAILURE parameter in the connector definition. In this way it is possible to release the constraint in x and y direction when yield force is reached in z direction.

```
*Connector Behavior, name=ConnProp-1_CONNSECT-4
*Connector Plasticity, component=1
*Connector Hardening, definition=TABULAR
25000.,25., 0.
*Connector Plasticity, component=2
*Connector Hardening, definition=TABULAR
25000.,25., 0.
*Connector Elasticity, component=1
31250.,
*Connector Elasticity, component=2
31250.,
*Connector Elasticity, component=3
300000
*Connector Failure, component=3, release=1
, , -69237., 69237. "Upper and lower limits of the failure force"
*Connector Failure, component=3, release=2
, , -69237., 69237.
```

The connector is given an elastic behaviour in z direction. The longitudinal elastic stiffness of a beam element is equal to  $EA/L$ . Young modulus and rebar area are known, for this early stage study  $L$  is fixed equal to 100 mm, so the resulting stiffness is approximated to 300000 N/mm. In the new model the horizontal displacement is applied together with a vertical displacement. If the connector failure command it is then specified the lower and upper bound of the elastic behaviour so it is sufficient to provide the value of the yielding force for the rebar (it is possible to specify displacement bounds too). It can be seen Figure 8.15 that as the connectors yields in vertical direction the other two directions are released and no more shear can be transferred.

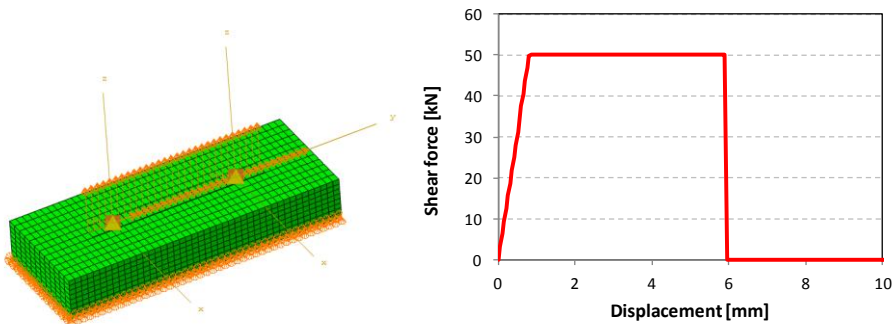


Figure 8.15- Connector model with vertical displacements and global response.

## 8.2.2 Implementation of a physical dowel action model in the user subroutine UEL.for: simplified elastic-plastic model

In order to have a better description of the dowel behaviour a physical model has been implemented in a user subroutine UEL.for. In this way it is possible to take into account several variables that may influence the problem: dowel diameter, surrounding concrete stiffness, cyclic degradation, vertical direction coupling.

A spatial multi-spring zero length element has been implemented. In the 1 and 2 horizontal direction a simple elastic plastic relationship is used while in direction 3 a linear elastic behaviour is introduced.

### 8.2.2.1 Monotonic loading

In order to test the functionality of the UEL subroutine a simplified elastic-plastic model has been implemented. The model provides full cyclic behaviour with loading and unloading at any point. The elastic stiffness and maximum shear transfer are tuned according to the monotonic experimental results of (Dei Poli et al., 1992).

It is necessary to provide the elastic stiffness and the elastic displacement in the input file. The experimental results refer to a  $\Phi 14$ mm dowel embedded in  $f_c=32.3$  N/mm<sup>2</sup> concrete. The user element is defined in the following:

```
*Node
1,      0,      0,      0
2,      0,      0,      0
*USER Element, NODES=2, TYPE=U1, PROPERTIES=1, COORDINATES=3,
VARIABLES=6
1,2,3
*ELEMENT, TYPE=U1 , ELSET=UTRUS
1,1,2
*UEL PROPERTY, ELSET=UTRUS
** TRANSVERSE K DOWEL , AXIAL K , ELASTIC DISPLACEMENT
   49000 , 30000 , 0.5
```

It is also reported the analytical calculation suggested in Model Code 2010:

$$V_F(s) = V_{F,\max} \cdot \left( \frac{s}{s_{\max}} \right)^{0.5} \cdot \sqrt{1 - k_1^2}$$

$k_1$  = interaction factor (degree of utilization) =  $\sigma_s/f_y = 0$

$s = \text{slip}$

$s_{max} = \text{slip when } V_{f,max} \text{ is reached } (\approx 0.1\Phi - 0.2\Phi) = 0.1 \times 14 = 1.4 \text{ mm}$

$$V_{F,max} = k \cdot A_s \cdot \sqrt{f_{cc} f_y} \approx 22.2 \text{ kN}$$

$k = \text{interaction coefficient for flexural resistance} \approx 1.6$

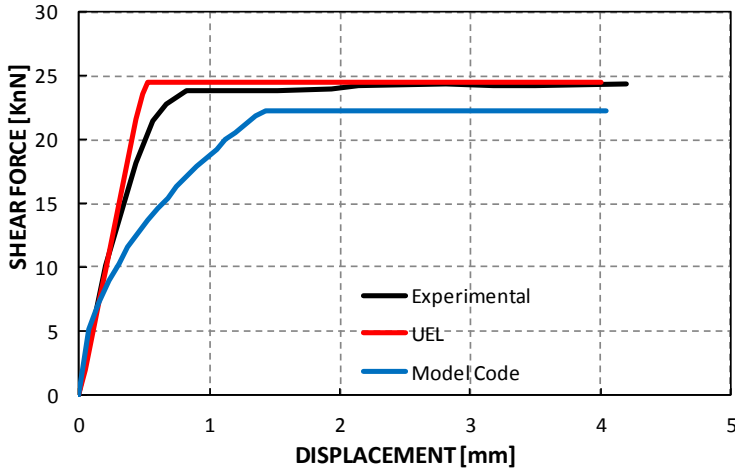


Figure 8.16- Simple elastic plastic behaviour; UEL vs. experimental results (Dei Poli) and analytical formulation.

### 8.2.2.2 Cyclic loading

A full cyclic loading has been implemented (Appendix A). Loading, reloading and unloading stiffness are considered equal (no cyclic degradation is considered in this first attempt). The loading protocol used for the test is reported in Figure 8.17, UEL vs. experimental results are reported in Figure 8.18.

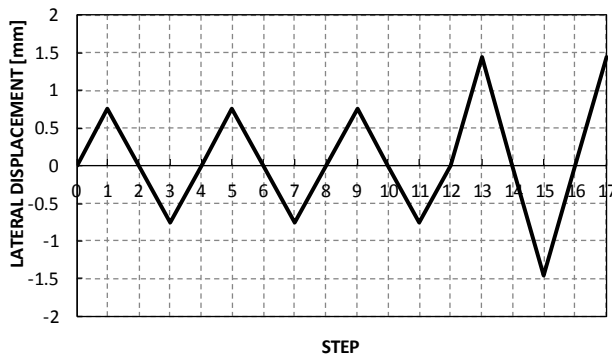
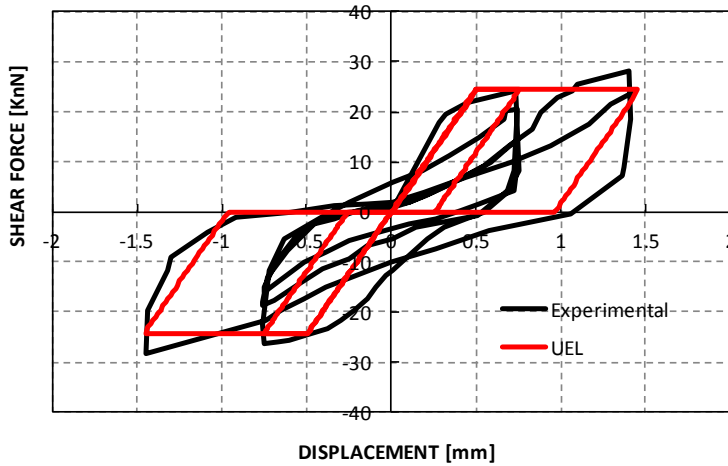


Figure 8.17- Cyclic loading protocol (Vintzeleou and Tassios, 1985).



**Figure 8.18-** Simple cyclic elastic plastic behaviour; UEL vs. experimental results (Vintzeleou and Tassios, 1985).

The model is obviously unable to take into account the proper reloading and unloading stiffness. However, residual plastic displacements and elastic loading although very rough are already able to provide some simplified results. The advantage of such model is its simplicity. This model can be easily extended to general loading protocols. It must be remarked that this kind of modelling strongly relies on available experimental data.

### 8.2.2.3 Cyclic loading: coupling with axial stress

As suggested by MC2010, the shear transferred by dowels is subjected to degradation not only to cyclic loading but also to axial stress degree of utilization. According to the following Eq.(8.2):

$$V_F(s) = V_{F,\max} \cdot \left( \frac{s}{s_{\max}} \right)^{0.5} \cdot \sqrt{1 - k_1^2} \quad (8.2)$$

where  $k_1$  = interaction factor (degree of utilization) =  $\sigma_s/f_y$

The reduction factor is then calculated at each increment taking into consideration also the axial behaviour. When the axial force is equal to yielding force the shear is equal to zero. A simple example analysis is reported in Figure

8.19. A vertical displacement equal to 2mm is gradually applied in order to observe the effect of the degradation coefficient on the numerical model.

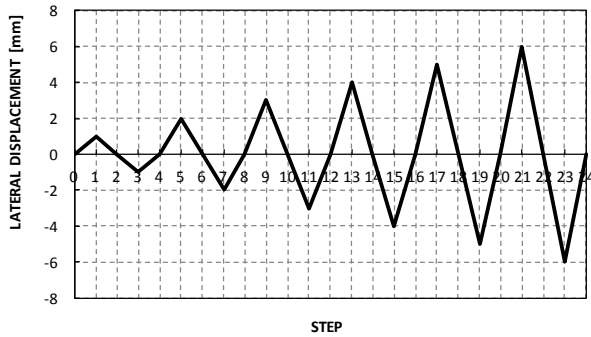


Figure 8.19- Cyclic loading protocol.

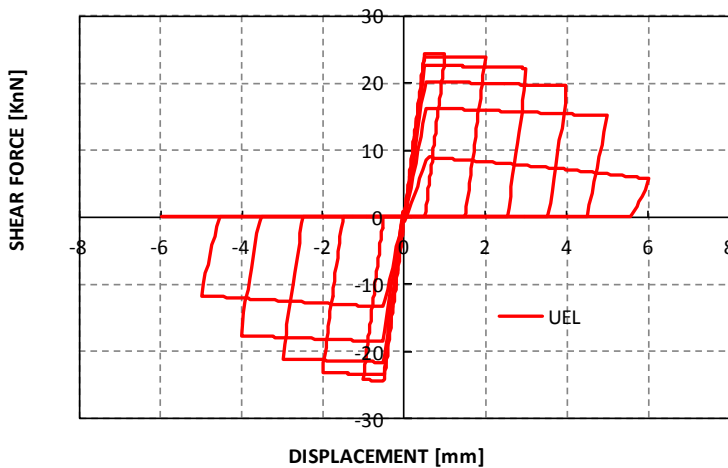


Figure 8.20- Numerical cyclic response with degradation due to axial coupling.

The same model could be used with any random loading protocol as it can consider partial loading/reloading phase.

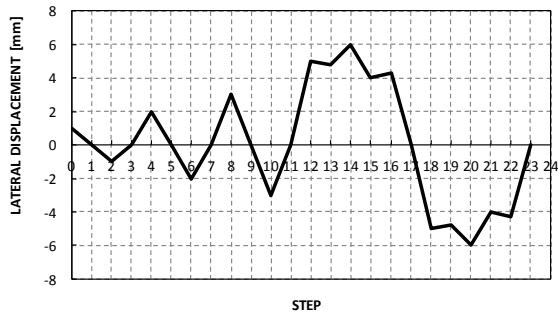


Figure 8.21- Cyclic protocol with partial unloading/reloading phases

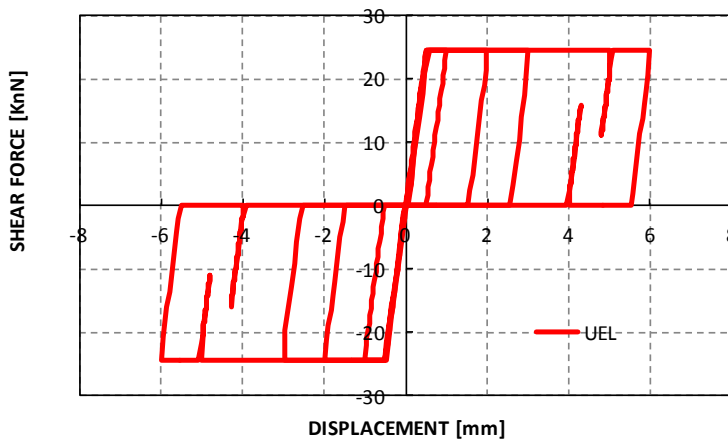


Figure 8.22- Spring response to a generic loading protocol with partial loading/unloading phases.

### 8.2.3 Implementation of a physical dowel action model in the user subroutine UEL.for: non linear BEF analogy

According to (Soltani and Maekawa, 2008), and (Vintzeleou and Tassios, 1987) studies a cyclic non linear model has been implemented in the UEL.for use subroutine. The model can take into account the stiffness degradation of reloading and unloading phase. Moreover, the model requires as input parameters only the concrete compression strength and the rebar diameter and is able to approximate interface problem for which experimental studies are not available. Thanks to the beam on elastic foundation analogy it is possible to take into account the degradation of the concrete surrounding the dowel and

consequent stiffness degradation. The beam on elastic foundation (BEF) scheme is reported in Figure 8.23.

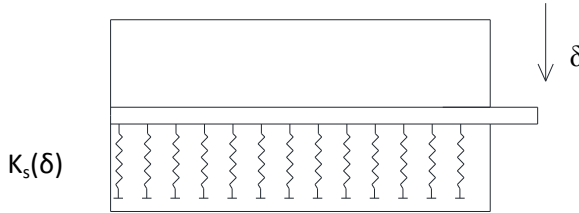


Figure 8.23- BEF analogy.

The soil stiffness can be calculated according to the model developed by (Soltani and Maekawa, 2008). At early loading stage the system response is linear. However, for larger displacements the surrounding concrete starts to crack and the stiffness quickly drops to a smaller value, Eq.(8.3).

$$k_s(\delta) = \begin{cases} 220f_c^{0.85} & DI \leq 0.02 \\ \frac{220f_c^{0.85}}{\left[1 + 3(DI - 0.02)^{0.8}\right]^4} & DI > 0.02 \end{cases} \quad (8.3)$$

where:

$$DI = \delta/\Phi$$

$\delta$  = lateral displacement

$\Phi$  = dowel diameter

Accordingly to the elastic line theory, for the considered boundary conditions (semi-infinite beam with concentrated load) the  $\delta$  displacement vs.  $V$  shear relationship can be written as Eq.(8.4):

$$V(\delta) = \frac{k_s(\delta)\delta}{2\lambda} \quad (8.4)$$

where:

$$\lambda = \sqrt[4]{\frac{k_s}{4E_s I_b}}$$

$E_s$  = rebar elastic modulus

$I_b$  = moment of inertia of the rebar section



It is then possible to notice that if one knows the geometrical and mechanical characteristics of rebars and concrete it is possible to define a monotonic model.

This simple non linear model can be easily implemented in a UEL.for. A numerical test is showed in figure. Results are compared with (Dei Poli et al., 1996). The BEF analogy can fit very well the monotonic load experimental data.

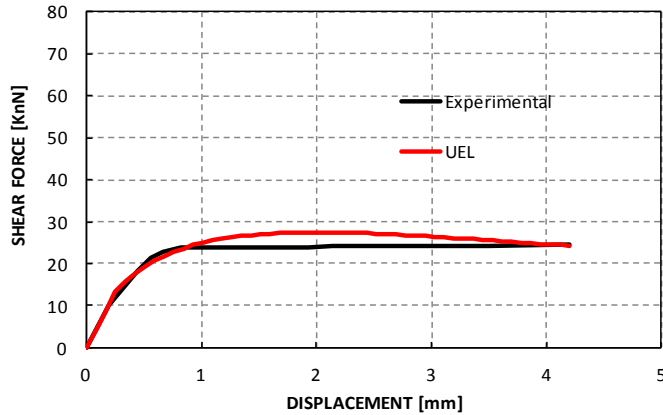


Figure 8.24- BEF analogy UEL vs. experimental test results.

The model has been extended to the case of cyclic loading test. In this case for the unloading/reloading branches the relationships derived from literature experimental data analyses have been used. The unloading branch has been implemented according to Eq.(8.5), Figure 8.25, (Soltani and Maekawa, 2008). while the reloading branch and cyclic deterioration have been taken into account according to Figure 8.26 (Vintzeleou and Tassios, 1985). Plastic displacements have been computed according to the analysis of (Soltani and Maekawa, 2008) on many experimental data by means of a quadratic data regression, Eq. (8.6).

$$V(\delta) = \frac{V_{d\max}(\delta - \delta_p)^2}{(\delta_{\max} - \delta_p)^2} \quad (8.5)$$

$$\delta_p(\delta_{\max}) = 0.1211\delta_{\max}^2 + 0.5209\delta_{\max} - 0.1289 \quad (8.6)$$

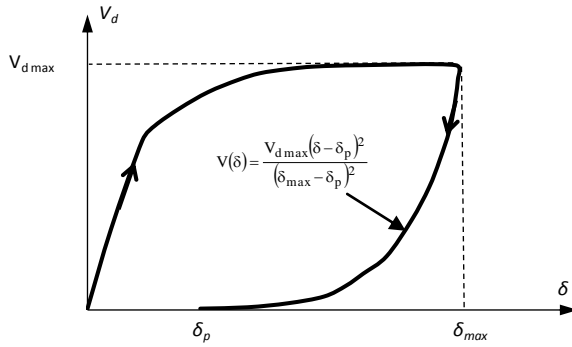


Figure 8.25- Unloading branch definition according to (Soltani and Maekawa, 2008).

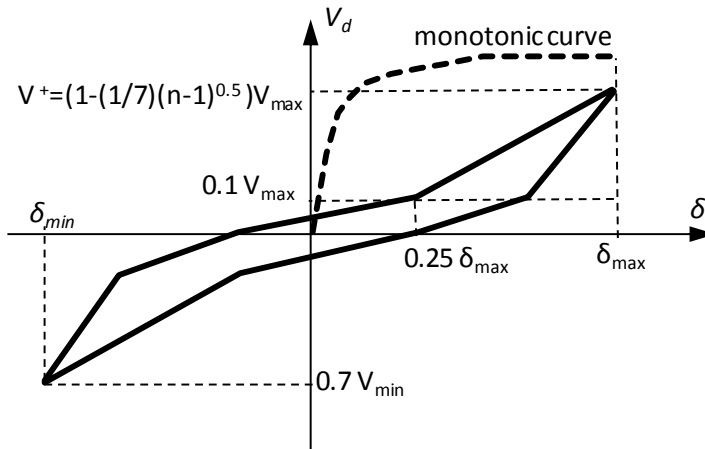


Figure 8.26- Unloading/reloading branches definition according to (Vintzeleou and Tassios, 1985).

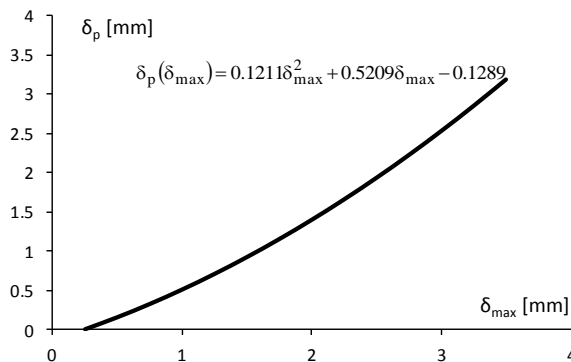


Figure 8.27- Evaluation of plastic displacement according to quadratic regression on available experimental data, (Soltani and Maekawa, 2008)..

The non linear UEL defined with the relationships given has then been

tested on a cyclic analysis (loading protocol Figure 8.28) as showed in Figure 8.29. The element has been defined in ABAQUS code as following:

```
*Node
1,      0,      0,      0
2,      0,      0,      0
*USER Element,  NODES=2,  TYPE=U1,  PROPERTIES=3,  COORDINATES=1,
VARIABLES=6
1
*ELEMENT, TYPE=U1 , ELSET=UTRUS
1,1,2
*UEL PROPERTY, ELSET=UTRUS
** DIAMETER, FC , ES
14 , 40 , 210000
```

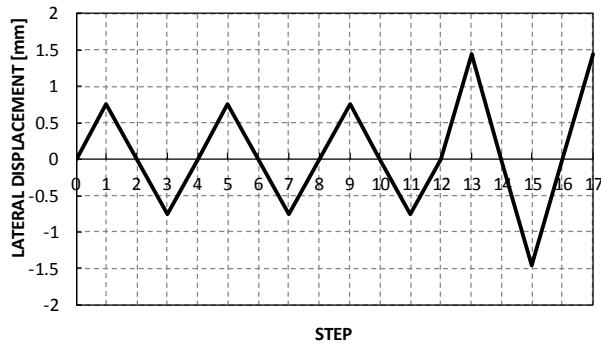


Figure 8.28- Cyclic loading protocol (Vintzeleou and Tassios).

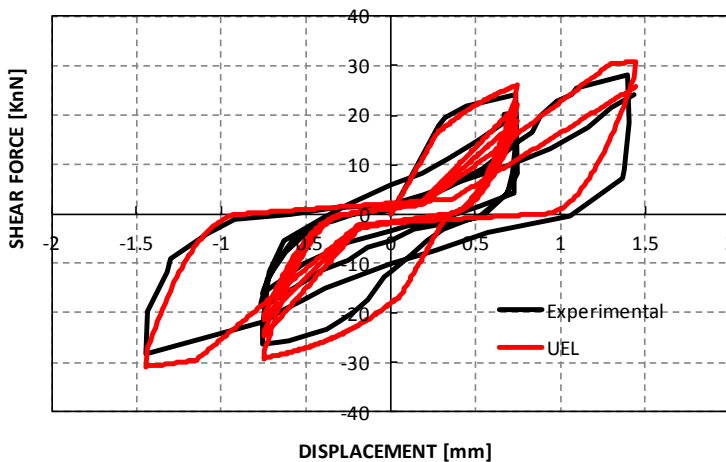


Figure 8.29- Shear displacement curve: UEL vs. experimental results.

The response of the spring seems to be good enough in order to catch the dowel shear response. The elastic stiffness degradation is adequately described as well as plastic displacements. However, the model cannot take into account the reduction due to axial coupling. The physical model implemented is summarized in Figure 8.30.

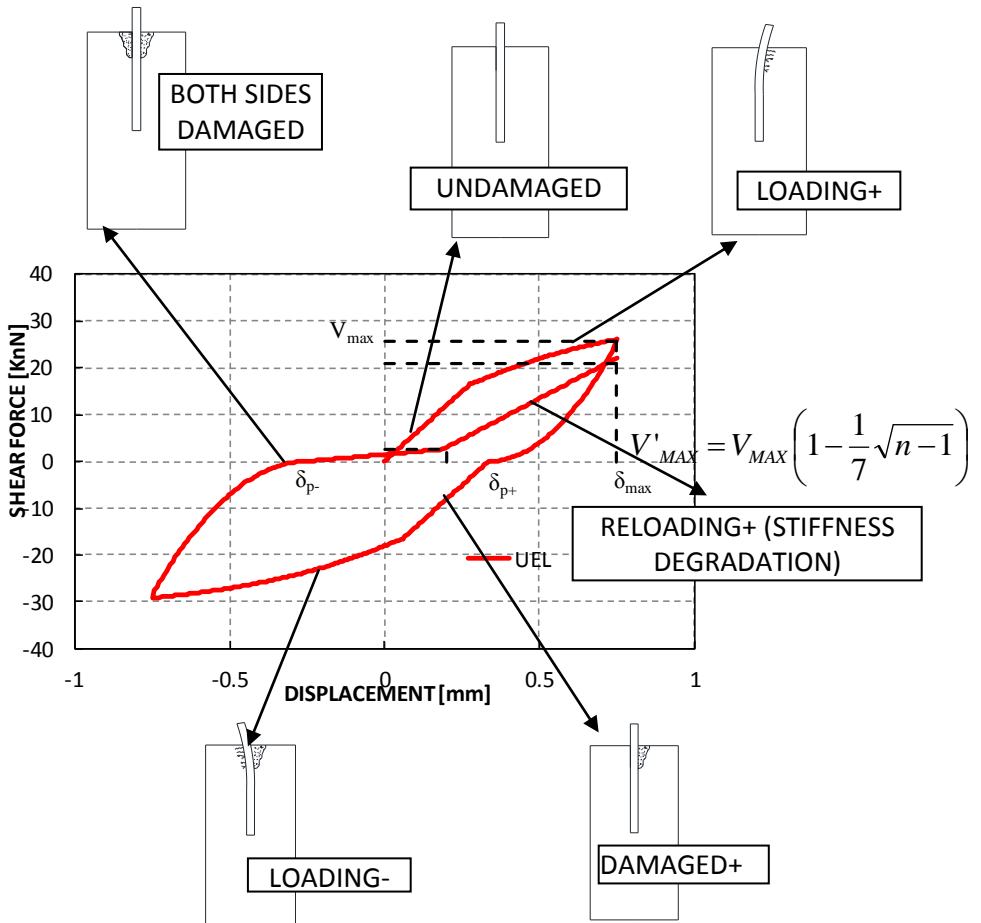


Figure 8.30- One cycle plus one reloading explanation scheme.





# Conclusions and Open Issues

天行健，君子以自強不息

*Whatever may happen, the nature never rests, so a gentleman should always work hard (for his knowledge).*

From "*The Book of Changes*", composed between the 10<sup>th</sup> and the 4<sup>th</sup> century B.C.



## Conclusions and open issues

In the current thesis the seismic assessment of RC wall structural systems was carried out by means of multi layered shell modelling and PARC\_CL fixed crack model. As wall structures are often used in NPPs design, it is of strong importance to develop reliable numerical tools able to predict the 3D behaviour of such structures in the non linear field. In particular, NLFE modelling was applied for the seismic assessment of two main case studies of wall structures. Two scaled NPPs RC structures were analyzed: an electric building facility for CPY power plants and a reinforced concrete containment vessel. In particular, attention was paid in order to assess the performances of such structures in terms of local and global engineering demand parameters. The importance of a proper evaluation of EDPs is closely correlated to the application of the modern performance based seismic engineering both for design of new buildings and structural assessment of existing ones. In fact, many NPPs will undergo a renewal process in the next year and this topic is actually of strong relevance. Moreover, it is strongly believed the importance of numerical model calibrations with real experimental tests, in order to acquire sufficient experience and then to transfer knowledge also to civil engineering non-academic applications, with the development of standards and guidelines.

For the dynamic modelling of the SMART2013 mock up described in chapter 6, the PARC\_CL shell modelling provided good results both in terms of global displacement and acceleration response spectrum in comparison with experimental results. Moreover, it was demonstrated that it was possible to catch in plane shear behaviour, rebars yielding and the complex torsional behaviour of the structure. The real slab stiffness was also considered and small cracking phenomena were observed in slabs area closed to walls. It is clear that the use of NLFEA for structural assessment needs a safety format different than that based on partial safety factors (e.g. probabilistic evaluation of the vulnerability, estimation of the fragility curves, etc). Moreover, the model uncertainties play an important role and have to be estimated. It was then observed though a probabilistic analysis that the model provided good performances especially when average spectral acceleration ASA40 intensity measure was taken into account (lower  $\beta$  values compared to the use of PGA and CAV). The eigen-frequency drop off EFDO demand parameter was also considered to be more efficient than maximum interstorey drift MID as the

latter may result less significant as a demand parameter in wall structures. In fact, spectral analysis demonstrated that the adopted model is able to catch the different modal frequencies both at undamaged and damaged state. On the other hand, MIDs values detected were very small and the MID parameter is not able in general to detect sliding shear phenomena. The research stressed the importance of the implementation of a wall to foundation local model to be introduced in the global model. Blind prediction and post analyses comparison demonstrated the importance of input signal manipulation, the improvement in boundary condition modelling (in this case, with or without shaking table model) and the correct description of damping. The damping ratio proved to be an important parameter to be set in case of dynamic analyses, especially for the evaluation of the post peak global response. In particular, attention must be paid also to the damping ratio value for modal frequencies in the damaged field. Although more research is required for the improvement of damping calibration in PARC\_CL model, the classical Rayleigh mass proportional damping was able to provide acceptable results. Further studies are also needed in order to evaluate the balance between damping energy dissipation and hysteretic energy dissipation: an energetic approach to the dynamic analysis would be useful also for design of new structures, for the seismic performances assessment of existing ones, and for retrofitting devices design. Further research will be carried out in order to investigate this issue. Moreover, computational efficiency should be improved in order to assess the quality of probabilistic results via robustness analyses.

The shell modelling with PARC\_CL was also applied to predict the behaviour of a 1/13 scaled RCCV subjected to quasi static cyclic loading in chapter 7. In this case the global load deflection cycles were predicted with good accuracy up to total base shear peak value. It was observed that the structure exhibited a non linear behaviour at early stage of loading (0.1% drift, top displacement equal to 2 mm). Local phenomena like cracking and rebars yielding were also detected. Strains in both vertical and horizontal reinforcement were adequately described by the smeared formulation. However, the model was not able to properly evaluate the experimental failure mode. In fact, the mock up failed because of sliding shear at the top wall to slab interface. It is remarked that strong compressive field were detected at the wall to foundation interface but no local crushing was observed in the numerical

model. This issue may be of strong relevance for the seismic assessment of existing structures, where the detailing level may be poor with respect to new buildings design. This is why a further development was proposed for the introduction of the interface problem in RC wall structures FEM shell modelling.

The results obtained put in light the importance of developing a local numerical tool able to catch shear failure and in general the interface problem for shell models and tailored on this kind of problem. A preliminary study on the problem was then provided in chapter 8 and further studies will be carried out for the calibration of the proposed model. Another research topic is relative to the extension of the modelling to other FE software codes in order to obtain a generally applicable crack model (now available only in UMAT format) and to provide with generality the results and to assess the reliability of this modelling technique through other solving techniques.

To conclude, multi-layered shell modelling with PARC\_CL can properly estimate damage indicators for the application of performance-based earthquake engineering in RC wall structures. However, it is remarked that the modelling with shell elements and crack models requires medium-high level of knowledge for users. It has also to be noticed that for the prediction of the non-linear behaviour of RC wall systems the “push-one-button” software user approach has to be avoided and this is why, in the civil engineering practice, guidelines and code prescriptions related to the use of this kind of modelling are needed. Moreover, the structural assessment is also depending on the knowledge of mechanical quantities involved and their uncertainties. The numerical tools now available require then a proper calibration in order to find out a rational approach to FEM seismic assessment of structures. The calibration of models based on real experimental tests was proved to be a key point of the problem.



## References and Glossary

## Selected References

### Scientific papers

*Scientific papers are in alphabetical order, first author surname at first place.*

- Akbas, B., Shen, J., & Hao, H. (2001). Energy approach in performance-based seismic design of steel moment resisting frames for basic safety objective. *The structural design of tall buildings* , 10 (3), 193-217.
- Akkar, S., Kale, {., Yenier, E., & Bommer, J. J. (2011). The high-frequency limit of usable response spectral ordinates from filtered analogue and digital strong-motion accelerograms. *Earthquake Engineering \& Structural Dynamics* , 40 (12), 1387-1401.
- Barda, F., Hanson, J. M., & Corley, W. G. (1977). Shear strength of low-rise walls with boundary elements. *ACI Special Publication* , 53.
- Bazant, Z. P., & Gambarova, P. (1980). Rough cracks in reinforced concrete. *Journal of the Structural Division* , 106 (4), 819-842.
- Belletti, B., Cerioni, R., & Iori, I. (2001). Physical approach for reinforced-concrete (PARC) membrane elements. *Journal of Structural Engineering* .
- Belletti, B., Damoni, C., & Gasperi, A. (2013)a. Modeling approaches suitable for pushover analyses of RC structural wall buildings. *Engineering Structures* , 57, 327-338.
- Belletti, B., Esposito, R., & Walraven, J. (2012). Shear capacity of normal, lightweight, and high-strength concrete beams according to Model Code 2010. II: Experimental results versus nonlinear finite element program results. *Journal of Structural Engineering* , 139 (9), 1600-1607.
- Belletti, B., Esposito, R., & Walraven, J. (2013)b. Shear Capacity of Normal, Lightweight, and High-Strength Concrete Beams according to Model Code 2010. II: Experimental Results versus Nonlinear Finite Element Program Results. *Journal of Structural Engineering* , 139 (9), 1600-1607.
- Benavent-Climent, A., Pujades, L., & Lopez-Almansa, F. (2002). Design energy input spectra for moderate-seismicity regions. *Earthquake engineering \& structural dynamics* , 31 (5), 1151-1172.

- Boore, D. M., & Bommer, J. J. (2005). Processing of strong-motion accelerograms: needs, options and consequences. *Soil Dynamics and Earthquake Engineering* , 25 (2), 93-115.
- Carpinteri, A., CERIONI, R., & Iori, I. (1996). Analisi del comportamento di calcestruzzi fibrorinforzati mediante la meccanica della frattura. *Studi e ricerche-Politecnico di Milano. Scuola di specializzazione in costruzioni in cemento armato* (17), 283-300.
- Chiu, H.-C. (1997). Stable baseline correction of digital strong-motion data. *Bulletin of the Seismological Society of America* , 87 (4), 932-944.
- Cedolin, L., Poli, S. D., & Iori, I. (1987). Tensile behavior of concrete. *Journal of engineering mechanics* , 113 (3), 431-449.
- Cerioni, R., & Iori, I. (1995). Sul comportamento di elementi bidimensionali a lastra, in conglomerato armato e soggetti ad azioni taglianti ai bordi. *Studi e ricerche-Politecnico di Milano. Scuola di specializzazione in costruzioni in cemento armato* (16), 151-171.
- Decanini, L. D., & Mollaioli, F. (2001). An energy-based methodology for the assessment of seismic demand. *Soil Dynamics and Earthquake Engineering* , 21 (2), 113-137.
- Dei Poli, S., Di Prisco, M., & Gambarova, P. (1992). Shear response, deformations, and subgrade stiffness of a dowel bar embedded in concrete. *ACI Structural Journal* , 89 (6).
- Douglas, J., & Boore, D. M. (2011). High-frequency filtering of strong-motion records. *Bulletin of Earthquake Engineering* , 9 (2), 395-409.
- Filippou, F. C., Popov, E. P., & Bertero, V. V. (1983). Modeling of R/C joints under cyclic excitations. *Journal of Structural Engineering* , 109 (11), 2666-2684.
- Gambarova, P. (1983). Sulla trasmissione del taglio in elementi bidimensionali piani di ca fessurati. *Proc., Giornate AICAP* , 141-156.
- Gupta, A., & Rangan, B. V. (1998). High-strength concrete (HSC) structural walls. *ACI structural journal* , 95 (2).
- Hendriks, M., den Uijl, J., de Boer, A., Feenstra, P., Belletti, B., & Damoni, C. (2012). Guidelines for non-linear finite element analyses of concrete structures. *Rijkswaterstaat Technisch Document (RTD), Rijkswaterstaat Centre for Infrastructure, RTD* , 1016, 2012.

- Huang, Y. N., Whittaker, A. S., & Luco, N. (2011). A probabilistic seismic risk assessment procedure for nuclear power plants:(I) Methodology. *Nuclear Engineering and Design*, 241(9), 3996-4003.
- Huang, Y. N., Whittaker, A. S., & Luco, N. (2011). A probabilistic seismic risk assessment procedure for nuclear power plants:(II) application. *Nuclear Engineering and Design*, 241(9), 3985-3995.
- Hwang, S.-J., Fang, W.-H., Lee, H.-J., & Yu, H.-W. (2001). Analytical Model for Predicting Shear Strength of Squat Walls. *Journal of Structural Engineering*, 127 (1), 43-50.
- Hwang, S.-J., Yu, H.-W., & Lee, H.-J. (2000). Theory of interface shear capacity of reinforced concrete. *Journal of Structural Engineering*, 126 (6), 700-707.
- Ile, N., & Reynouard, J. (2005). Behaviour of U-shaped walls subjected to uniaxial and biaxial cyclic lateral loading. *Journal of Earthquake Engineering*, 9 (01), 67-94.
- Iori, I., & Dei Poli, S. (1985). Sulla torsione di elementi strutturali in cemento armato. *L'Industria Italiana del Cemento*, 2, 121-129.
- Kabeyasawa, T., & Hiraishi, H. (1998). Tests and analyses of high-strength reinforced concrete shear walls in Japan. *ACI Special Publication*, 176.
- Kent, D. C., & Park, R. (1971). Flexural members with confined concrete. *Journal of the Structural Division*, 97 (7), 1969-1990.
- Lefas, I. D., Kotsovos, M. D., & Ambraseys, N. N. (1990). Behavior of reinforced concrete structural walls: strength, deformation characteristics, and failure mechanism. *ACI Structural Journal*, 87 (1).
- Leonhardt, F., & Schelling, G. (1974). Torsionsversuche an Stahlbetonbalken. *Deutscher Ausschuss für Stahlbeton* (239).
- Maier, J., & Thörlmann, B. (1985). Bruchversuche an Stahlbetonscheiben, IBK Bericht, 8003-1. Zürich: ETH.
- Mander, J. B., Priestley, M. J., & Park, R. (1988). Theoretical stress-strain model for confined concrete. *Journal of structural engineering*, 114 (8), 1804-1826.
- Manfredi, G. (2001). Evaluation of seismic energy demand. *Earthquake engineering & structural dynamics*, 30(4), 485-499.



- Mansour, M., & Hsu, T. T. (2005). Behavior of reinforced concrete elements under cyclic shear. I: Experiments. *Journal of Structural Engineering* .
- Mazars, J., Kotronis, P., & Davenne, L. (2002). A new modelling strategy for the behaviour of shear walls under dynamic loading. *Earthquake engineering & structural dynamics* , 31 (4), 937-954.
- Moradi, A. R., Soltani, M., & Tasnimi, A. A. (2012). A simplified constitutive model for dowel action across RC cracks. *Journal of Advanced Concrete Technology* , 10 (8), 264-277.
- Negro, P. (1997). Experimental assessment of the global cyclic damage of framed r/c structures. *Journal of Earthquake Engineering* , 1(03), 543-562.
- Negro, P., & Verzeletti, G. (1996). Effect of infills on the global behaviour of r/c frames: energy considerations from pseudodynamic tests. *Earthquake Engineering & Structural Dynamics* , 25 (8), 753-773.
- Ordaz, M., Huerta, B., & Reinoso, E. (2003). Exact computation of input-energy spectra from Fourier amplitude spectra. *Earthquake Engineering and Structural Dynamics* , 32(4), 597-606.
- Palermo, D., & Vecchio, F. J. (2002). Behavior of three-dimensional reinforced concrete shear walls. *ACI Structural Journal* , 99 (1).
- Palermo, D., & Vecchio, F. J. (2007). Simulation of cyclically loaded concrete structures based on the finite-element method. *Journal of Structural Engineering* , 133 (5), 728-738.
- Palieraki, V., & Vintzileou, E. (2009). Cyclic behaviour of interfaces in repaired/strengthened RC elements. *Architecture Civil Engineering Environment* , 2 (1), 97-108.
- Pilakoutas, K., & Elnashail, A. (1993). Interpretation of testing results for reinforced concrete panels. *ACI Structural Journal* , 90 (6).
- Riva, P., Meda, A., & Giuriani, E. (2003). Cyclic behaviour of a full scale RC structural wall. *Engineering Structures* , 25 (6), 835-845.
- Rinaldin, G., Amadio, C., & Fragiaco, M. (2013). A component approach for the hysteretic behaviour of connections in cross-laminated wooden structures. *Earthquake Engineering & Structural Dynamics* , 42 (13), 2023-2042.

- Salonikios, T. N., Kappos, A. J., Tegos, I. A., & Penelis, G. G. (1999). Cyclic load behavior of low-slenderness reinforced concrete walls: Design basis and test results. *ACI Structural Journal* , 96, 649-660.
- Soltani, M., & Maekawa, K. (2008). Path-dependent mechanical model for deformed reinforcing bars at RC interface under coupled cyclic shear and pullout tension. *Engineering Structures* , 30 (4), 1079-1091.
- Stevens, N., Uzumeri, S., & Collins, M. (1991). Reinforced concrete subjected to reversed cyclic shear--Experiments and constitutive model. *ACI Structural Journal* , 88 (2).
- Uang, C.-M., & Bertero, V. V. (1990). Evaluation of seismic energy in structures. *Earthquake Engineering & Structural Dynamics* , 19 (1), 77-90.
- Vecchio, F. J., & Collins, M. P. (1993). Compression response of cracked reinforced concrete. *Journal of Structural Engineering* , 119 (12), 3590-3610.
- Vintzeleou, E., & Tassios, T. (1986). Mathematical models for dowel action under monotonic and cyclic conditions. *Magazine of concrete research* , 38 (134), 13-22.
- Vintzeleou, E., & Tassios, T. (1987). Behavior of dowels under cyclic deformations. *ACI Structural Journal* , 84 (1).
- Walraven, J. C. (1981). Fundamental analysis of aggregate interlock. *Journal of the Structural Division* , 107 (11), 2245-2270.
- Walraven, J., & Reinhardt, H. (1981). Theory and experiments on the mechanical behaviour of cracks in plain and reinforced concrete subjected to shear loading. *HERON*, 26 (1A), 1981 .
- Whyte, C. A., & Stojadinovic, B. (2013). Effect of ground motion sequence on response of squat reinforced concrete shear walls. *Journal of Structural Engineering*, 140(8), A4014004.
- Wood, S. L. (1990). Shear strength of low-rise reinforced concrete walls. *ACI Structural Journal* , 87 (1).

## Books

- Boore, D. M. (1999). *Effect of baseline corrections on response spectra for two recordings of the 1999 Chi-Chi, Taiwan, earthquake*. US Department of the Interior, US Geological Survey.

- CEB-FIP (2010). *Model Code 2010 - Final draft: Volume 1*. International Federation for Structural Concrete (fib).
- CEB-FIP (1993). *Model Code 1990. Design of Concrete Structures*. International Federation for Structural Concrete (fib).
- Feenstra, P. H. (1993). *Computational aspects of biaxial stress in plain and reinforced concrete*. TU Delft, Delft University of Technology.
- Gulec, C. K., & Whittaker, A. S. (2009). *Performance-based assessment and design of squat reinforced concrete shear walls*. Multidisciplinary Center for Earthquake Engineering Research MCEER.
- Hsu, T., Wu, C., & Lin, J. (2013). *Infrastructure Systems for Nuclear Energy*. Wiley.
- Hsu, T & Mo, Y.L. (2010). *Unified Theory of Concrete Structures*. Wiley.
- Shing, P., & Tanabe, T. (2001). *Modeling of Inelastic Behavior of RC Structures Under Seismic Loads*. American Society of Civil Engineers.
- Nowak, A., & Collins, K. (2000). *Reliability of Structures*. McGraw-Hill.
- Oesterle, R., Association, P. C., & others. (1976). *Earthquake resistant structural walls: Tests of isolated walls*. Research and Development Construction Technology Laboratories, Portland Cement Association.
- Paulay, T., & Priestley, M. (1992). *Seismic Design of Reinforced Concrete and Masonry Buildings*. Wiley.
- Pitilakis, K., Crowley, H., & Kaynia, A. (2014). *SYNER-G: Typology Definition and Fragility Functions for Physical Elements at Seismic Risk: Buildings, Lifelines, Transportation Networks and Critical Facilities*. Springer Netherlands.

### In Proceedings

- Belletti, B., & Esposito, R. (2010). Un modello costitutivo per elementi in CA soggetti ad azioni cicliche. *Proc., 18th CTE Conf*, (p. 81-91).
- Belletti, B., & Riva, P. (2008). Alcune applicazioni del modello "PARC" all'analisi statica non lineare di edifici a pareti in calcestruzzo armato soggetti ad azioni sismiche. *Atti del 17° Congresso CTE Roma, 5-8 novembre 2008*.

- Belletti, B., Esposito, R., & Damoni, C. (2013). Numerical prediction of the response of a squat shear wall subjected to monotonic loading through PARC\_CL model. *FraMCoS-8: Proceedings of the 8th International Conference on Fracture Mechanics of Concrete and Concrete Structures, Toledo, Spain, 10-14 March 2013*.
- Cerioni, R., Ferretti, D., & Iori, I. (1998). 'Torsional behaviour of prestressed high-strength concrete beams. *Proc., EURO-C 1998 Conf. on Computational Modelling of Concrete Struct*, (p. 797-806).
- Damoni, C., Belletti, B., & Lilliu, G. (2013). Control of cracking in RC structures: numerical simulation of a squat shear wall. *8th International Conference on Fracture Mechanics of Concrete and Concrete Structures, FraMCoS-8 2013, Toledo, Spain, 11-14 March 2013/Edited by JGM Van Mier, G. Ruiz, C. Andrade, RC Yu and XX Zhang, 410-419*.
- Housner, G. W. (1956). Limit design of structures to resist earthquakes. In *Proceedings of 1st WCEE* (p. 5-1).
- Labbé, P. (2013). EDF Experience on Design and Construction of Nuclear Power Plants on Seismic Isolation Systems. *Technical Innovation in Nuclear Civil Engineering--TINCE 2013*.
- Menegotto, M. (1973). Method of analysis for cyclically loaded RC plane frames including changes in geometry and non-elastic behavior of elements under combined normal force and bending. *Proc. of IABSE symposium on resistance and ultimate deformability of structures acted on by well defined repeated loads*, (p. 15-22).
- Nazè, P.-A., & Sidaner, J.-F. (2001). Presentation and interpretation of SAFE tests: reinforced concrete walls subjected to shearing. *Proceedings of the 16th International Conference on Structural Mechanics in Reactor Technology*.
- Trost, B., Schuler, H., & Stojadinovic, B. (2014). Experimental investigation of sliding on compact sliding specimens under cyclic loads. *Proceedings of the 15th European Conference on Earthquake Engineering*.

### **Building Codes, Manuals and Standards**

- ABAQUS (2012). *Analysis User's Manual*, Version 6.12, ABAQUS Inc., Dassault Systèmes.
- ACI 318 (2008). Building Code Requirements for Structural Concrete (ACI 318-08) and Commentary. American Concrete Institute.

ASCE (2000). *Seismic Analysis of Safety-Related Nuclear Structures: (ASCE 4-98)*. American Society of Civil Engineers.

Eurocode 8 (2005). Design of Structures for earthquake resistance–Part 1: General rules, seismic actions and rules for buildings. UNI EN 1998-1:2005, 01 March 2005.

FEMA. (2012). FEMA P-58-1: Seismic Performance Assessment of Buildings. Volume 1--Methodology.

### Technical Reports and Presentations

Hsu, T. (2015). Keynote presentation, *OpenSees Day*, June 10-11, Salerno, Italy.

Richard, B., Fontan, M., Mazars, J., Voltaire, F., Chaudat, T., Bonfils, N., et al. (2014). *SMART 2013: Overview And Lessons Learnt From The International Benchmark*. CEA/DEN Tech. rep. CEA/DEN/DANS/DM2S/SEMT/EMSI/NT/14-037/A.

Thunell, B. (2014). *SMART 2013 - Low-Level Experimental Data Review And Elastic Model Calibration*. Scanscot Technology Tech.rep. 10506/R-01.

Negro, P., Caperan, P., Lamperti, M., Molina, F.J., Pegon, P., Peroni, M., Pett, P., Viaccoz, B., Toniolo, G., Biondini, F., Dal Lago, B., Titi, A. (2015). *SAFECLADDING Improved Fastening Systems Of Cladding Wall Panels Of Precast Buildings in Seismic Zones. Deliverable 5.3: Report of the test performed on the full-scale prototype* (limited distribution), ELSA, JRC.

### Theses

Emamy Farvashany, F. (2004). *Strength and deformation of high strength concrete shear walls*. Ph.D. dissertation, CURTIN UNIVERSITY OF TECHNOLOGY. DEPT. OF CIVIL ENGINEERING.

Greifenhagen, C. (2006). *Seismic behavior of lightly reinforced concrete squat shear walls*. Ph.D. dissertation, ECOLE POLYTECHNIQUE FEDERALE DE LAUSANNE.

Martinelli, P. (2007). *Shaking table tests on rc shear walls: significance of numerical modeling*. Ph.D. dissertation, POLITECNICO DI MILANO.

## Websites and Software Resources

SMART2013 project: [www.smart2013.eu](http://www.smart2013.eu)

Seismosignal tools: [www.seismosoft.com/seismosignal](http://www.seismosoft.com/seismosignal)

The European Strong Motion Database: [http://www.isesd.hi.is/ESD\\_Local/frameset.htm](http://www.isesd.hi.is/ESD_Local/frameset.htm)

The National Center for Research on Earthquake Engineering:  
<http://www.ncree.narlabs.org.tw/>

FreeMat resources: <http://freemat.sourceforge.net/>

MatLab resources: [www.mathworks.com/products/matlab/](http://www.mathworks.com/products/matlab/)

Maxima download resources: <http://maxima.sourceforge.net/>

Abaqus code: <http://www.3ds.com/products-services/simulia/products/abaqus/>

## Technical Glossary

### Acronyms and Abbreviations

**ASA.** Average Spectral Acceleration.

**CAV.** Cumulative Absolute Velocity.

**CDF.** Cumulative Distribution Function.

**CEA.** Commissariat à l'énergie atomique et aux énergies alternatives.

**CoV.** Covariance.

**DFT.** Discrete Fourier Transform.

**DM.** Damage measure.

**DOF.** Degree of Freedom.

**E.** Expected value.

**EDF.** Electricité de France.

**EDP.** Engineering Demand Parameters.

**ELSA.** European Laboratory for Structural assessment

**EFDO.** Eigen frequency drop off.

**FBD.** Friction Based Device.

**FFT.** Fast Fourier Transform.

**FEM.** Finite Element Method.

**IM.** Intensity Measure.

**MID.** Maximum Interstorey drift.

**NLFEA.** Non Linear Finite Element Analysis.

**NPP.** Nuclear Power Plant.

**NCREE.** National Center for Research on Earthquake Engineering.

**PARC.** Physical Approach for Reinforced Concrete.

**PARC\_CL.** Physical Approach for Reinforced Concrete\_subjected to Cyclic Loading.

**PDF.** Probability Density Function.  
**PGA.** Peak Ground Acceleration.  
**PWR.** Pressurized Water Reactor.  
**RC.** Reinforced Concrete.  
**RCCV.** Reinforced Concrete Containment Vessel.  
**UEL.** User Element subroutine (Abaqus code).  
**UMAT.** User MATerial subroutine (Abaqus code).  
**V.** Coefficient of variation.  
**Var.** Variance.

## Definitions

**Accelerogram.** Time series of acceleration during a seismic event.

**Aggregate interlock.** Shear transfer mechanism through concrete cracks by means of aggregates friction.

**Actuator.** A hydraulic mechanism that supplies and transmits a certain amount of force to a specimen.

**CPY type reactor.** French reactors built from the '70s and early '80s. They are subdivided in two classes: CP1 (two reactors with same machine and command room) and CP2 (two reactors with separate command rooms and machines).

**Dowel action.** Shear transfer mechanism through concrete cracks or interfaces by means of steel rebars or dowels.

**Engineering Demand Parameters.** EDPs are quantities of the structures response that may be used to predict and evaluate the damage of the system.

**Fragility function.** A fragility function express the probability that an undesirable event will occur as a function of the value of some environmental excitation (sometimes they are called *fragility curves*).

**Hoops (hoop reinforcement).** Hoops are circular steel rings. They are usually used to prevent buckling of reinforcing bars in column members.

**Intensity Measure.** IMs are quantities that should identify the earthquake most important characteristics which may affect the structural response.

**Pressurized water reactor.** In PWR reactors, the coolant is water, which is pumped under the core at high pressure. Then, heated water flows to a steam generator where its thermal energy is converted into mechanical energy by turbines.

**Pseudo-dynamic test.** During pseudo-dynamic test, the dynamic response is computed using the experimental result in each time step. During the analysis process, the computer calculates the structural response (displacement) in a time step.

**Quasi-static analysis.** In quasi-static analysis the load is applied slowly so that the structure deforms at low strain rate and therefore the inertia effects can be ignored.

**Random variables.** See “Uncertain quantities”.

**Response spectrum.** A response spectrum is a plot of the peak response (typically displacement, velocity or acceleration) of a series of oscillators of several natural frequency or period, which are excited by the same base time history acceleration, vibration or shock.

**Spectrum-compatible accelerogram.** Accelerogram which allows satisfying the compatibility conditions with a target elastic demand spectrum.

**Shaking table.** A device for shaking structural models or building components with a certain range of simulated ground motions.

**Sliding shear failure mode.** Brittle failure mode that may appear at wall base interface. Sliding shear strength of a RC interface is given by the sum of a friction contribution and dowel action of rebars across the interface.

**Strain Gauge (or strain gage).** A device for measuring strain on an object.

**Time history analysis.** A time history analysis provides the response of a structure over time during and after the application of a load. The structure equation of motion is solved at each time increment.

**Vessel.** In general, a vessel is a container designed to hold gases (or liquids) at a pressure which is different from the ambient pressure.

**Uncertain quantities (or Random variables).** Quantities that change unpredictably or that do not vary but are not known with certainty.







*to my family  
alla mia famiglia*



## Acknowledgements

I would like to thank all the people and institutions which provided precious help to the present work and to the entire research.

First, special thanks to prof. Ivo Iori, for all of his knowledge and passion he provided to me. Prof. Aldo De Poli is also gratefully acknowledged for the great efforts and enthusiasm he puts in the PhD school organization.

I would like to express my sincere and personal gratitude to prof. Beatrice Belletti, for the trust and strong support she has been always giving to me. Moreover, I would like to thank the professor for the passion and enthusiasm that she puts in all of her projects and researches.

The Cariparma Foundation is gratefully and sincerely acknowledged.

Prof. Thomas Hsu from the University of Houston is gratefully acknowledged for his precious help. Prof. Hwang from National Taiwan University is also acknowledged, together with the staff of NTU Office of International Affairs. I would like to thank the Minister of Science and Technology (MOST) of Taiwan for providing the Summer Program course and for the financial effort. Many thanks to dr. Wu for his great help and to the NCREE staff, especially to dr. Yang, Leo Chen and Ryo Lu for their help and friendship. The experimental data sets provided by the National Center for Research on Earthquake Engineering of Taiwan are gratefully acknowledged.

I would like to thank the SEISM institute for providing the financial supports required to carry out the SMART2013 program. CEA and EDF are also gratefully acknowledged. I would like especially to acknowledge dr. Richard (CEA), dr. Fontain (Oxand Consulting) and prof. Mazars (University of Grenoble) for their professionalism and for the precious advices.

The European Commission and JRC staff are also acknowledged. In particular, I would like to thank dr. Paolo Negro and mr. Marco Lamperti (JRC) for their help, guidance and friendship during the traineeship at the ELSA lab.

I would like to thank my friend Tse and the whole Hsu family for all the good time (and the food) we shared in Taiwan. I would like to thank also all the other friends of the epic NCREE nuclear team: Henry, Minh, Cynthia, Ray, Jimmy, and Maggie. I should also thank my Italian fellows in Taipei, Marco and Enrico.

Thanks also to the “TraineeLand” people of Ispra for their huge enthusiasm and contagious happiness.

My special thanks also to the dear colleagues and friends Cecilia and Matteo, who shared with me the sorrows and joys of this journey (and best wishes to Francesca, who has just joined the group) and always provided me with their sincere support. Thanks also to Fulvio who shared some of the path with us.

One more thanks to the musicians, especially Matteo, Nicholas, and Fabrizio, who I met and I will meet again “on the road”.

Finally, loving thanks to Lisa, who has been waiting with patience for a long time. Moreover, I would like to thank my family. Thanks to my sister, who will always be there for me, to my parents, who always trusted and supported my choices, and to my grandparents, who remind me who really I am.

## Ringraziamenti

Vorrei ringraziare tutte le persone e le istituzioni che hanno contribuito con il loro aiuto prezioso alla realizzazione della presente tesi e al completamento del percorso di studi.

Il primo ringraziamento è per il prof. Ivo Iori, per i suoi consigli scientifici, culturali e per la passione che è riuscito a trasmettere per la scienza (e l'arte) del costruire. Un ringraziamento va inoltre al prof. Aldo De Poli, per il grande e costante impegno che fornisce alla Scuola di Dottorato.

Vorrei inoltre esprimere i miei più sinceri ringraziamenti alla prof.ssa Beatrice Belletti, per la fiducia che ha sempre riposto nei miei confronti e per il grande supporto dato ai miei studi. Vorrei inoltre ringraziare la prof. per l'entusiasmo e la passione che trasmette a tutti noi suoi collaboratori in occasione di ogni progetto di ricerca.

Un sentito e doveroso ringraziamento va inoltre alla Fondazione Cariparma.

Un ringraziamento speciale ai miei amici, colleghi e compagni di viaggio Cecilia e Matteo, i quali hanno condiviso con me le fatiche e le gioie di un così lungo cammino, fornendomi sempre il loro sincero aiuto (e auguri a Francesca, che è da poco saltata a bordo). Grazie anche a Fulvio, col quale abbiamo condiviso parte del sentiero.

Un ringraziamento anche agli amici suonatori, in particolare Matteo, Nicholas e Fabrizio, che ho incontrato e incontrerò di nuovo "sulla strada".

Infine un affettuoso grazie a Lisa, che ha atteso a lungo e con pazienza. Grazie inoltre alla mia famiglia: a mia sorella, che ci sarà sempre per me, alla mamma e al papà, che hanno sempre supportato (e sopportato) le scelte del loro scapigliato figliolo, e ai miei nonni, che mi aiutano a ricordare chi sono veramente.

